DEVELOPMENT OF NEW LAYERED OXIDE AND OXYHALIDE TITANATES FOR SOLAR PHOTOCATALYSIS

Ph.D. THESIS

by

GOLLAPALLY NARESH

DEPARTMENT OF CHEMISTRY
INDIAN INSTITUTE OF TECHNOLOGY ROORKEE
ROORKEE – 247 667 (INDIA)

MARCH, 2016

DEVELOPMENT OF NEW LAYERED OXIDE AND OXYHALIDE TITANATES FOR SOLAR PHOTOCATALYSIS

A THESIS

Submitted in partial fulfilment of the requirements for the award of the degree

of

DOCTOR OF PHILOSOPHY

in

CHEMISTRY

by

GOLLAPALLY NARESH

DEPARTMENT OF CHEMISTRY
INDIAN INSTITUTE OF TECHNOLOGY ROORKEE
ROORKEE – 247 667 (INDIA)

MARCH, 2016

INDIAN INSTITUTE OF TECHNOLOGY ROORKEE
ROORKEE

CANDIDATE'S DECLARATION

I hereby certify that the work which is being presented in the thesis entitled **"DEVELOPMENT OF NEW LAYERED OXIDE AND OXYHALIDE TITANATES FOR SOLAR PHOTOCATALYSIS"** in partial fulfilment of the requirements for the award of the degree of Doctor of Philosophy and submitted in the Department of Chemistry of the Indian Institute of Technology Roorkee, Roorkee is an authentic record of my own work carried out during a period from December 2011 to March 2016 under the supervision of Dr. Tapas Kumar Mandal, Assistant Professor, Department of Chemistry, Indian Institute of Technology Roorkee, Roorkee.

The matter presented in the thesis has not been submitted by me for the award of any other degree of this or any other Institute.

(Gollapally Naresh)

This is to certify that the above statement made by the candidate is correct to the best of my knowledge.

(Tapas Kumar Mandal)
Supervisor

Date:

CONTENTS

ABSTRACT

Release of organic pollutants by various industries is of serious concern due to their harmful environmental and health effects. Development of novel semiconductor photocatalysts for rapid degradation of these pollutants by either complete mineralization or converting them into non-toxic fragments using solar energy may possibly render a sustainable solution. After the discovery of water-photolysis on TiO_2 semiconductor electrode by Fujishima-Honda in 1972, the world has seen an enormous amount of research on semiconductor photocatalysis that continue to grow even today, although, the use of TiO_2 and many other oxide semiconductors under solar irradiation is limited because of their UV active nature. Considering the abundance of 'visible' sunlight amounting to ~ 43% of incoming solar energy, there is an urgent need for the development of visible-light-active photocatalysts for efficient utilization of solar energy. Therefore, semiconductor photocatalysis driven by visible-light has emerged as an exciting area of research to address potential issues related to clean fuel production and environmental remediation. Hydrogen production by sunlight-driven water splitting is considered as a renewable way of clean fuel generation. Water disinfection by degradation of anthropogenic organic pollutants from industrial wastewater is indispensable for a cleaner environment. Ideally, an efficient sunlight-driven photocatalyst can find niche applications in some of the emergent areas of energy and environment.

Toward the development of visible-light-active photocatalysts, several approaches are adopted. For tuning the band gap, a metal or non-metal ion doping in either binary or complex oxides are being widely investigated. Besides, a solid-solution formation between a narrow and a wide band gap material has been exploited for the suitable tuning of band gap. Moreover, for improving upon the efficiencies of photocatalytic processes, use of multiple oxides in the form of semiconductor heterojunction, oxide composites or with graphene to form graphene-composites etc. have been investigated. Often, many of these systems have drawbacks with respect to high solution stability, resistance to photocorrosion and photoleaching, high efficiency and recyclability under visible-light/solar radiation. In quest for robust and efficient photocatalysts, research thrusts in single bulk semiconductors together with their nanostructured counterparts are in the rise. Among these, the perovskites constitute a major class both with the layered (2D) and

three-dimensional (3D) structures. In this regard, the role of layered perovskites in visible-light-driven photocatalytic activity is noteworthy.

A large body of research dealt with the formation and manipulation of layered perovskites for optimization and discovery of diverse properties including photocatalysis. It is observed that many oxides and oxyhalides studied for visible-light photocatalysis contain Bi^{3+} and among them the Aurivillius phases are noteworthy. The presence of Bi is known to push up the absorption band edge in the visible region and its dispersed valence band helps to generate high mobility holes. Recently, interest in these Aurivillius phase semiconductors has grown due to their superior activity as single bulk and nanostructured oxide photocatalysts. The most simple members of the Aurivillius family, namely, Bi_2MoO_6, Bi_2WO_6 (n = 1) and their solid-solution phases have been investigated for their photocatalytic activity under visible-light irradiation. Although, few reports on visible-light active photocatalysis over higher order members (n = 2, 3, 4) of the Aurivillius series were available, more complex systems remained largely unexplored. Recently, four (n = 4) and five-layer (n = 5) Aurivillius phases, $Bi_5Ti_3FeO_{15}$ and $Bi_6Ti_3Fe_2O_{18}$, respectively, have drawn attention for their ferroelectric, magnetic, optical and photocatalytic properties. Moreover, the rare earth (La, Sm, Gd and Dy) substituted $Bi_6Ti_3Fe_2O_{18}$ were investigated for their magnetic and magnetoelectric properties. Recognizing the effect of cation disorder in the stability of Aurivillius phases and recent reports on importance of ferroelectricity in photocatalysis, we have undertaken a systematic exploration of La substitution in the four- and five-layer Aurivillius phases towards phase formation, structure, band gap and photocatalytic activity. This has further been extended to develop new series of five-layer Aurivillius perovskites by both *A* and *B*-site cation co-substitution. Moreover, a strategy toward band gap alteration for developing new visible-light active semiconductors have been devised *via* intergrowth of Aurivillius oxides with Sillén phases forming a new series of hybrid layered perovskites. All the compounds were thoroughly characterized and their activities toward dye degradations were evaluated. Finally, for a better insight into the photocatalytic processes and mechanism of degradation detail studies involving energy level diagrams have been carried out. The outcomes of the present investigations are presented in the thesis consisting of seven chapters. **Chapter-1** gives an overview of various metal oxides and composite systems applied in the area of photocatalysis.

Chapter 2 gives the details of all the characterization techniques used, during the present course of investigation, along with their experimental procedures. The compounds were first synthesized by solid-state reactions employing simple metal carbonates / oxalates / oxides or oxychlorides. The progress of reactions and formation of final products were monitored by powder X-ray diffraction (PXD) and the morphological and compositional characterizations were carried out by Field Emission-Scanning Electron Microscopy (FE-SEM) and Energy Dispersive X-ray Spectroscopy (EDS) analysis. Further, the optical properties were studied by UV-vis Diffuse Reflectance Spectroscopy (UV-vis DRS) and the band gap energies were estimated by Tauc plots. Photocatalytic activity tests were performed following standard procedures under sunlight-irradiation using model dye solutions. For this, the catalyst-dye suspensions were equilibrated under stirring in the dark prior to photocatalytic degradations. In all cases, a control experiment was always performed in absence of catalysts to assess self-degradation of the dyes involved under the same experimental conditions. To obtain deep insights into the degradation mechanisms and reactive species involved, various scavenger tests were carried out. To elucidate the role of adsorption, surface charge and e^-- h^+ recombination processes, dye adsorption, ζ-potential and photoluminescence (PL) studies were carried out. The details of PXD, FE-SEM, EDS, UV-vis DRS, PL and ζ-potential techniques are discussed in this chapter.

Chapter 3 describes a systematic exploration on the solid-state synthesis and characterization of four-layer Aurivillius perovskites, $Bi_{5-x}La_xTi_3FeO_{15}$ (x = 1-3), together with theirs photocatalytic activity toward Rhodamine B (RhB) degradation under sunlight-irradiation. We report for the first time, to the best of our knowledge, the solid-state synthesis and characterization of $Bi_{5-x}La_xTi_3FeO_{15}$ (x = 1, 2). All the compounds crystallize in the orthorhombic $A2_1am$ space group. The analysis of lattice parameters obtained by least-squares refinement shows a slight increase in the c-parameter as x varies from 0 – 2 in the $Bi_{5-x}La_xTi_3FeO_{15}$ series, while the difference between a and b-parameter reduces and become nearly equal in $Bi_3La_2Ti_3FeO_{15}$. This clearly indicates a decrease in orthorhombic distortion and a shift toward tetragonal structure with progressive replacement of lone-pair active Bi^{3+} by La^{3+}. This has been attributed to the diminishing effect of out-of-center distortion which possibly leads to an increase in the c- parameter in the series with increasing La-substitution. The PXD simulation studies on

$Bi_3La_2Ti_3FeO_{15}$ indicated preferential occupation (~ 67-75 %) of La in *A*-site of the central perovskite layer and the residual La were distributed over the terminal perovskite layers with a minimal occupancy over the $[Bi_2O_2]^{2+}$ layers. UV-vis DRS data revealed that the compounds are visible light absorbing semiconductors with principal band gaps ranging from ~ 2.62 – 2.71 eV. Photocatalytic activity studies by RhB degradation under sunlight-irradiation showed that these layered oxides are very efficient photocatalysts in mild acidic medium. The activity of the catalysts toward RhB degradation is comparable or higher than many of the single-phase and composite catalysts with Aurivillius and perovskite structures in the bulk or nanostructured form reported recently. An enhanced charge separation rendering slow e^--h^+ recombination and efficient transport of photogenerated holes are attributed to high efficiency of the bulk catalysts irrespective of the degradation mechanisms involved. Moreover, the large positive ζ-potential led to enhanced dye adsorption and consequently a high rate of degradation in the acidic medium. Scavenger test experiments clearly indicated the dominant role of holes in the degradation process involving the Aurivillius layered oxides reported here. The positioning of VB and CB edges with respect to potentials of $^{\bullet}OH/H_2O$, $O_2/O_2^{\bullet-}$ and HOMO-LUMO levels of RhB clearly corroborated with the scavenger test results indicating no major role of hydroxyl species in the degradation.

In **Chapter 4**, we report the solid-state synthesis, characterization and photocatalytic activity studies of five-layered Aurivillius perovskites, $Bi_{6-x}La_xTi_3Fe_2O_{18}$ (x = 0, 1). The samples of $Bi_{6-x}La_xTi_3Fe_2O_{18}$ (x = 0, 1) were synthesized by conventional solid-state reactions. On La-substitution, the in-plane '*b*' parameter remains nearly the same while a slight contraction in the in-plane '*a*' and expansion in the '*c*' parameter was noticed. These are attributed to complex interplays between cation disorder and concomitant octahedral tilting distortions. The SEM images show homogeneous plate-like morphology as expected and often observed for layered compounds. The crystallites are mostly agglomerated and composed of plate-shaped crystallites with irregular sizes ranging from few hundred nanometers to a few micrometers. The UV-vis DRS established the compounds as visible-band-gap semiconductors. La-substitution appeared to help in the suppression of photogenerated e^-–h^+ recombination as evidenced by PL spectra. The photocatalytic RhB degradation in the acidic medium under sunlight-irradiation indicated $Bi_5LaTi_3Fe_2O_{18}$ as the most active catalyst among the two five-layered Aurivillius compounds

reported here. The enhanced activity of $Bi_5LaTi_3Fe_2O_{18}$ is attributed to the effective separation of photogenerated e^-–h^+ pairs and improved dye adsorption in the acidic medium. The predominant role of photogenerated holes in the RhB degradation has been established by reactive species trapping experiments. The conduction and valence band alignment of $Bi_5LaTi_3Fe_2O_{18}$ with respect to potentials of $^{\bullet}OH/H_2O$, $O_2/O_2^{\bullet-}$ and HOMO–LUMO levels of RhB supports the involvement of h^+ and formation of $O_2^{\bullet-}$ as reactive species. Furthermore, a large positive ζ-potential has been ascribed to improved dye adsorption which ultimately led to an enhanced photocatalytic activity and efficient COD removal by the catalysts. Moreover, the compounds are reusable and stable under the acidic medium even after five consecutive cycles of degradation without any noticeable loss in activity.

Chapter 5 deals with the synthesis and characterization of new five-layer Aurivillius perovskites, $Bi_5ATi_4FeO_{18}$ (A = Ca, Sr, Pb), and their photocatalytic activity toward selective dye degradation under sunlight. The compounds are synthesized for the first time by solid-state reaction. The UV-vis DRS confirmed that all the compounds have visible band gaps ranging from 2.61 – 2.72 eV. These catalysts exhibited highly selective degradation of Methylene Blue (MB) from aqueous mixture of MB and RhB in alkaline as well as neutral medium. The improved photocatalysis of $Bi_5SrTi_4FeO_{18}$ is attributed to a sluggish recombination of photoinduced e^-–h^+ pairs and enhanced adsorption of dye on the catalyst surfaces. Scavenger tests indicated h^+ and $O_2^{\bullet-}$ as active species involved in the photocatalytic degradation. The position of valence and conduction band edges of $Bi_5SrTi_4FeO_{18}$ with respect to potentials of $^{\bullet}OH/H_2O$, $O_2/O_2^{\bullet-}$ and HOMO–LUMO levels of RhB and MB also supports the role of h^+ and $O_2^{\bullet-}$ radicals in the sunlight-driven photocatalysis. The photocatalytic cycle tests and post-catalysis PXD analysis confirmed that the catalysts are reusable and stable.

In **Chapter 6**, we have devised a new strategy to make visible-light harvesting compounds from UV active compounds by designing new Sillén-Aurivillius intergrowth phases, namely, $Bi_{5-x}La_xBaTi_3O_{14}Cl$ (x = 0 – 2). For the synthesis of these hybrid phases a multi-step solid-state reaction strategy was adopted, where two pre-synthesized compounds, namely, $Bi_{4-x}La_xTi_3O_{12}$ (x = 0 – 2) and $BiBaO_2Cl$, were further reacted to prepare the hybrid phases. All the Sillén-Aurivillius hybrids are visible-light absorbers with band gap ranging from 2.66 to 2.87 eV and exhibit selective degradation of MB in neutral and alkaline media, where both RhB and

MB degradation is noticed in acidic medium with mixed RhB-MB dye solutions. Furthermore, these compounds showed excellent photodegradation of individual RhB and MB at different pH conditions. Among the three catalysts, $Bi_3La_2BaTi_3O_{14}Cl$ showed enhanced activity because of sluggish recombination of photogenerated e^-–h^+ pairs and superior dye adsorption. Based on the band edge position of catalysts, HOMO-LUMO levels of dyes and scavenger test results, $^{\bullet}OH$, $O_2^{\bullet-}$ and h^+ are perceived as active species at pH 2, whereas $O_2^{\bullet-}$ and h^+ are realized as active contributors at pH 7 and 11. These catalysts are reusable and stable after five photocatalytic cycles without showing any appreciable loss of activity.

The overall conclusions and future prospects of our current investigations are presented in **Chapter 7**. The present work has tremendous potential and gives insight for the development of various new types of layered oxides for sunlight-driven photocatalysis not only in the area of dye pollutant degradation but many other organic pollutant degradation, selective degradation, wastewater treatment and recovery of precious chemicals, to name a few.

ACKNOWLEDGEMENTS

First of all, I would like to take this opportunity to express my most sincere gratitude to my supervisor, Dr. Tapas Kumar Mandal. I consider myself immensely fortunate and privileged to be a first research scholar under his supervision. He is not only an example of best teacher but also a person with great soul and humanity. The entire research work carried out during the course of my Ph.D. would not have been possible without his innovative guidance and support coupled with encouragement. His training helped me a lot in thinking the research problems and designing the materials to solve them systematically. He has taught me not only enormous knowledge, but also how to become a proper researcher with broader vision in the long run. I particularly admire his enthusiasm for science and research. What I learned from him will benefit my whole life. I thank his family members for providing delicious food and homely environment during the festival time.

I am highly obliged and express my sincere thanks to Prof. M. R. Maurya, Head of the Department of Chemistry and all other faculty members for their kindness and help. I am grateful to the members of my SRC, Prof. M. R. Maurya (Chairman), Dr. P. Jeevanandam. (Internal member), Department of Chemistry and Dr. B. V. Manoj Kumar (External member), Department of Metallurgical and Materials Engineering, IIT Roorkee for their valuable suggestions and encouragement to carry out this work.

I am extremely indebted to Dr. Ramesh Chandra, Head, Institute Instrumentation Centre (IIC) for providing all the necessary instrumental facilities. I greatly appreciate Mr. Shiva for his help during the FE-SEM measurements. I am also thankful to Mr. Siva Kumar, in-charge of XRD and Mr. Mukesh, in-charge of TEM. I express my sincere thanks to Mr. Madan Pal, Department of Chemistry, who helped me a lot for the technical arrangements during my presentations in the department.

I would like to express my sincere thanks to Ministry of Human Resource Development, Government of India for providing me fellowship.

I am grateful to all members of solid state chemistry Lab who have offered support over the years. Thank you to Nishant Gautam for the early days we spent together ordering chemicals and setting up lab. Thanks to Vandana Meena, Sonia Rani and Saroj for creating an enjoyable work

environment when the lab was few in numbers. Your curious nature towards science will afford you great success in future endeavors. All the best to you. I thank rest of the lab members Lalit Kumar, Vijay, Jaideep, Anupam, Kamini, Rita, Anowar, Ambikeshwar, and Poonam for their support and good luck with your chemistry. Special thanks to Vandana Meena for her help in photocatalytic experiments and joyful moments with her.

I would like to thank my school friends Vinod, Naveen, Gabdu, Mujahid, Pranith, Sadiqu, Naresh, and Mustaque for their funny chatting to keep me refresh. I would like to thank my college friends Dasharath, Suresh, Jaganathula Sathish, Babu Rao, Ravi, Laxma Reddy, Mahesh, Mahender, Madhu, Chandraiah, Srinu, Naveen Reddy, Satayam and Kali Suresh for their support. Very special thanks to my best friend, Syam Kandula. You are a forever friend and I am extremely proud of all of your accomplishments. I thank my Gym partner Pankaj Gupta and Gym coach S. K. Dutta for making me strong. I thank my colleagues Govardhan, Rupam, Dr. Ravi, Monu, Aarthi, Soumita, Pallavi, Subrajyoshna, Dr. Kishor, Dr. Koteswara Rao, Dr. Naveen Mergu, Dr. Santhosh, Balu, Dr. Venkat, Rajendra, Karthik, Dr. Lokesh, Sudheer, Saurabh and Gulab for being around all the time.

I pay my perennial respect and gratitude to my father Sh. Rajalingu, my mother Smt. Sukkamma, my brother Suresh and his wife Latha, my elder sister Rajitha and her husband Raju, my nice Pooja and nephew Karthik who are always in tandem with me on my career aspirations. I thank all my gollapally family members Grandfather-Grandmother Late Mallaiah-Late Laxmi, Uncles-Aunts: Rajaiah-Late Badhramma, Komuraiah-Late Laxmi, Mogili-Sakkamma, Shanker-Renuka, Shekar-Laxmi, Sarangapani-Radha, Cousins-Cousin-in-laws: Ravinder-Komala, Bavanandam-Manjula, Krishnamurthy-Kavya, Srinu-Rajeshwari, Raju-Rajitha, Ramesh-Manasa, Raju-Sumalatha, Ramesh-Aruna, Vishnu, Chandhu, Kiran Nani, Kiran-Bhargavi, Krishna, Srikanth, Dr. Sathish, Vinod Srinu, Nieces-Nephews: Pragnya, Prudhvi, Bunty, Pinky, Sunny, Bunny, Lucky, Vicky, Sidhu, Sindhu, Hussy, Honey and Pravasthi.

(GOLLAPALLY NARESH)

List of Figures

List of Tables

List of Publications:

1. Gollapally Naresh and Tapas Kumar Mandal, Excellent Sun-Light-Driven Photocatalytic Activity by Aurivillius Layered Perovskites, $Bi_{5-x}La_xTi_3FeO_{15}$ (x = 1, 2). *ACS Appl. Mater. Interfaces* **2014**, *6*, 21000−21010.

2. Gollapally Naresh and Tapas Kumar Mandal, Efficient COD Removal Coinciding with Dye Decoloration by Five Layer Aurivillius Perovskites under Sunlight-Irradiation. *ACS Sustainable Chem. Eng.* **2015**, *3*, 2900−2908.

3. Gollapally Naresh and Tapas Kumar Mandal, Development of new five-layered Aurivillius perovskites, $Bi_5ATi_4FeO_{18}$ (A = Ca, Sr, Pb), for sunlight-driven selective photocatalysis (manuscript under preparation).

4. Gollapally Naresh and Tapas Kumar Mandal, New members of Sillén-Aurivillius layered oxyhalide hybrids and their selective photocatalysis (manuscript under preparation).

5. Kamini Gupta, **Gollapally Naresh** and Tapas Kumar Mandal, Novel perovskites in the Pb-La-Ti-Fe-O system: Synthesis, characterization and visible-light photocatalysis (manuscript under preparation).

6. Ambikeshwar Pandey, Gollapally Naresh and Tapas Kumar Mandal, New La-substituted Sillén-Aurivillius hybrid layered perovskites, Bi_3LaNbO_8X (X = Cl, Br), and their sunlight-driven photocatalytic activity (manuscript under preparation).

List of Conference Proceedings:

1. Gollapally Naresh and Tapas Kumar Mandal, Novel Transition Metal Incorporated Aurivillius Phases $Bi_{5-x}La_xTi_3FeO_{15}$ (x = 0 – 2) as Visible-Light Photocatalysts. Modern Trends in Inorganic Chemistry – XV, *Indian Institute of Technology Roorkee, Roorkee, India*, December 13-16, **2013**.

2. Kamini Gupta, Gollapally Naresh and Tapas Kumar Mandal, Novel Perovskites in the Pb-La-Ti-Fe-O System: Synthesis, Characterization and Visible-Light Photocatalysis. International Conference on Emerging Materials and Applications (ICEMA'14), *Indian Institute of Technology Roorkee, Saharanpur Campus, India*, April 5-6, **2014**.

3. Gollapally Naresh and Tapas Kumar Mandal, Sunlight-Driven Selective Dye Degradation over New Sillen-Aurivillius Layered Perovskites. *Modern Trends in Inorganic Chemistry – XVI, Jadavpur University, Kolkata, India*, December 3-5, **2015**.

CHAPTER -1

Introduction

1.1 Introduction.

Conversion of solar energy into clean hydrogen energy by water splitting reaction and degradation of organic and inorganic pollutants by solar photocatalysis is of immense interest for their potential application in renewable energy and environmental remediation [1-5]. The exponential increase in the global population and growth of industrialization and agricultural activities directed the demand of freshwater. In this context, the development of new techniques to protect clean water and rapid treatment of toxic pollutants from wastewater are important topics for environmental scientists [6]. On the other hand, decrease in the availability of fossil fuel and considering the environmental problems associated with the burning of fossil fuels modern society has been looking for clean, sustainable, inexpensive, renewable and feasible alternatives [2-4]. In the present decade, much attention has been focused on production of hydrogen that has been considered as a clean and sustainable energy source because it produces water vapors as byproduct during the energy generation process in fuel cells [7]. The key advantage of using hydrogen as a fuel is the significant reduction in the emission of greenhouse gases, which cause serious environmental problems, for example global warming and climate change.

1.2 Water Treatment.

Water is essential for life and it is one of the most important natural resources on the earth on which human and animals depend. Water is one of the most abundant resources on globe, shields nearly 75% of the earth's surface. In this, about 97% of the earth water is salt water, which is not useful for drinking and 3% of this water is fresh water contained in the poles, ground water, lakes and rivers, which is useful for human and animal needs. Approximately, 68.7% from the tiny 3% of global fresh water is locked up in glaciers and icecaps and 30.1% is in underground, mostly deep inside, hard to rich. Only 0.9% of freshwater (globally 0.027%) is contained in rivers and lakes (Figure 1.1), which is most available water source for human activities [8]. So saving this tiny accessible fresh water from contamination by pollutants is indispensable to save the planet and mankind. Due to the rapid growth in industrialization, modernization and population growth various pollutants are released into the clean water bodies, which are of serious concern due to their harmful environmental and health effects.

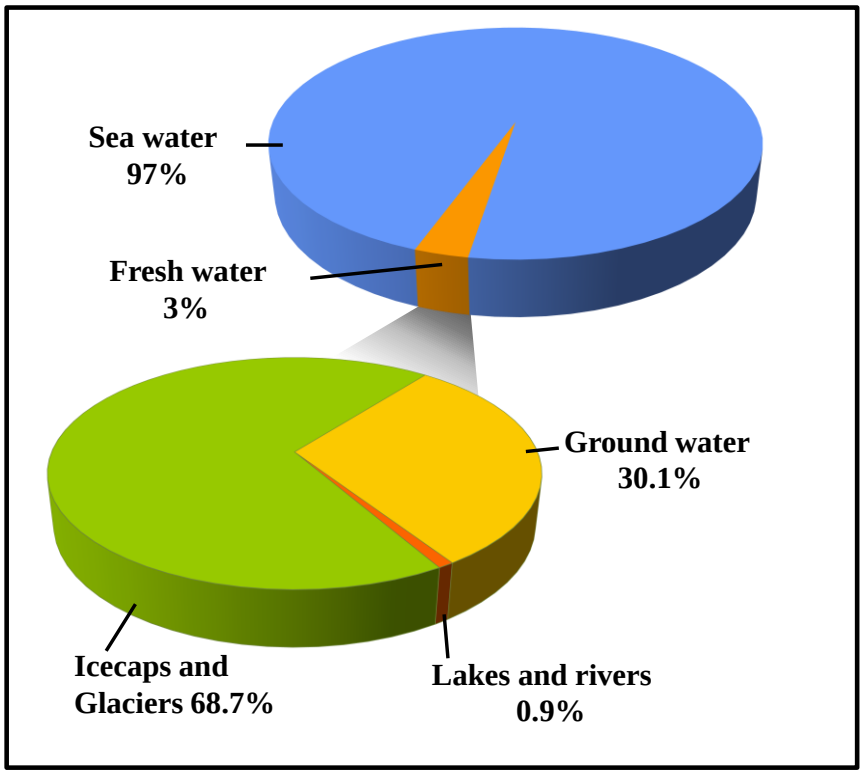

Figure 1.1 Global water content in sea, icecaps, glaciers, underground, lakes and rivers.

Improper management of effluents from industries, such as, textile, printing, plastic, cosmetics, coating, paper and rubber cause serious threat to environment in many countries [9, 10]. Rapid increase in the global population has resulted in the increase of fresh water demand for both domestic needs and agricultural activities to produce sufficient amount of food. The wastewater discharged from the household and agricultural activities contain large amount of pollutants. One of the major classes of the pollutants is organic dyes. The release of organic pollutants causing serious hazard to the surface and ground water systems, during manufacturing by various industries and application processes by humans, is of serious environmental concern [11, 12].

In addition, data show that 0.7 million tons of organic dyes are manufactured annually for use in the textile, leather goods, industrial painting, food, plastics, cosmetics, and consumer electronic sectors [13]. Nearly, 1-10% of the globally produced dyes are lost as industrial wastes during their manufacture and application process [14]. Rhodamine B (RhB) is one of the xanthene dyes which are used in textile industry as coloring agent and in biology as a staining fluorescent dye. During its natural anaerobic

degradation, RhB produces aromatic amines that are potentially toxic and carcinogenic. Therefore, removal of RhB and other organic effluents from industrial wastewater is important from health and environmental perspectives. The colored dye pollutants in the wastewater can shield the both sunlight penetration and oxygen dissolution, which are necessary for aquatic creatures. Moreover, the world health organization (WHO) has pointed out that 25% of diseases arise due to long term exposure of environmental pollutants present in soil, air and water [15]. Therefore, there is an urgent need of the hour for the removal of colored dye pollutants efficiently from the wastewater before releasing them to other water bodies.

Photocatalysis is promising and emerging technology to address the potential issues related to clean hydrogen fuel production and environmental remediation. During the photocatalysis, it is essential to activate the photocatalyst for degradation of pollutants and generation of hydrogen. As a renewable energy source, sunlight is the effective and attractive energy supplier for the activation of photocatalyst. The energy that reach to the earth surface per annum is 3×10^{24} J, which is nearly 4 orders of magnitude higher than the energy yearly used by human all over the world. In addition to its abundance, solar energy is also clean and safe [6].

1.3 Photocatalytic Dye Degradation by Semiconductor Oxides

One of the major applications of semiconductor photocatalysts is complete mineralization or partial conversion of toxic pollutants present in water and air to environmentally benign substances under solar irradiation. The reactive species generated during the photocatalytic experiments are $O_2^{\bullet-}$, $^{\bullet}OH$ and h^+, which are responsible for degradation of contaminants [16]. The advantages of semiconductor photocatalysts are summarized as follows: (i) the photocatalytic experiments can be performed under ambient condition (temperature and pressure); (ii) there is no need of adding expensive oxidizing chemicals; (iii) the reactive species generated in photocatalysis are strong oxidants which mineralizes almost all organic contaminants in wastewater; (iv) the photocatalysis process can also termed as green technology because the substances formed after photocatalysis are less toxic (CO_2, H_2O and mineral acids); (v) the photocatalysis can also be performed at different pH conditions and different dye concentrations and finally, (vi) the photocatalysts

could be low cost, environmentally benign, stable under ambient conditions, biologically and chemically inert, and reusable. Summing up all the above mentioned advantages, semiconductor photocatalysis offers an inexpensive and effective approach for industrial wastewater treatment and other environmental remediation processes [1, 6, 16-18].

1.4 Process Involved in Photocatalysis

In the photocatalytic dye degradation, toxic organic contaminants are either completely mineralized or converted into non-toxic fragments in presence of semiconductor photocatalysts under light irradiation. The photocatalysts are generally, semiconductors with a band gap either in UV or visible region, the conduction band (CB) and the valence band (VB) are separated by its band gap energy (E_g). The initial step for the photocatalytic dye degradation is the adsorption of light ($\lambda \geq E_g$) by semiconductor particles which results in the formation of electron-hole pairs in the semiconductor. The electrons in the VB are excited into the CB and leaves positive holes in the VB by the absorption of light. The photoinduced electrons in the CB and holes in the VB can follow several pathways (Figure 1.2) [19]. While the electrons in the CB can migrate to the surface of the semiconductor and reduce the electron acceptor (A) (pathway C), similarly, the holes can also migrate to the surface and oxidize the donor species (D) by taking electron from a donor species (pathway D).

The photogenerated electron-hole pair separation and their migration to the surface may depend on several factors that are intrinsic to the semiconductor including its crystal and band structure. The activity of the semiconductors can decrease by a faster recombination of the photogenerated electrons and holes. This recombination of electrons and holes may occur in the core of the semiconductor (pathway B) or on the surface of the semiconductor (pathway A) with release of heat. The dissolved oxygen can act as the electron acceptor to produce reactive species $O_2^{\bullet-}$ radicals in the photocatalysis pathway C [6]. In the same way the photogenerated holes can oxidize the electron donor (H_2O or OH^-) to yield reactive species $^{\bullet}OH$ radical or directly oxidize the adsorbed organic pollutants [6, 16]. All these reactive species, $O_2^{\bullet-}$, $^{\bullet}OH$ radicals and holes participate in the photodegradation process for the photocatalytic breakdown of organic pollutants.

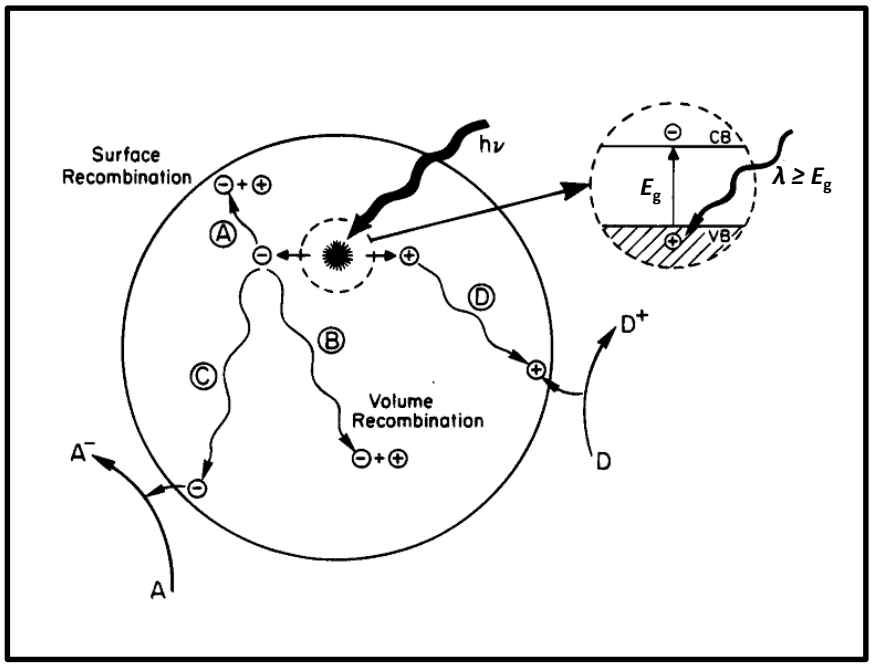

Figure 1.2 Main processes involved in photocatalytic dye degradation [19].

1.5 Mechanism of Generating Oxidizing Species

Photoinduced electrons and holes in the semiconductor react with O_2 and H_2O molecules to produce reactive species. The reaction mechanism involved in the production of reactive species on semiconductor (SC) surface is represented as follows:

$$SC + h\nu\ (\lambda \geq E_g) \rightarrow SC\ (e^-_{CB} \cdots h^+_{VB}) \quad (1.1)$$

$$SC\ (h^+_{VB}) + H_2O \rightarrow {}^\bullet OH + H^+ + SC \quad (1.2)$$

$$SC\ (h^+_{VB}) + OH^- \rightarrow {}^\bullet OH + SC \quad (1.3)$$

$$SC\ (e^-_{CB}) + O_2 \rightarrow O_2^{\bullet -} + SC \quad (1.4)$$

$$O_2^{\bullet -} + H_2O \rightarrow HO_2^\bullet + OH^- \quad (1.5)$$

$$HO_2^\bullet + H_2O \rightarrow {}^\bullet OH + H_2O_2 \quad (1.6)$$

$$H_2O_2 \rightarrow 2{}^\bullet OH \quad (1.7)$$

$$\left.\begin{array}{l}\text{Dye} + O_2^{\bullet-} \\ \text{Dye} + {}^{\bullet}OH \\ \text{Dye} + (h^+_{VB})\end{array}\right\} \longrightarrow \text{degraded products} \qquad (1.8)$$

where, e^-_{CB} refers to the conduction band electron and h^+_{VB} refers to the valence band hole.

Under light irradiation, e^- - h^+ pairs are generated within the semiconductor (Eq. 1.1). The holes in the VB can either oxidize adsorbed water or adsorbed hydroxyl groups (OH^-) on semiconductor surface to produce $^{\bullet}OH$ radicals (Eq. 1.2 and Eq. 1.3) [6, 16] The photogenerated electrons in the CB of the catalyst can reduce dissolved O_2 to yield $O_2^{\bullet-}$ anions (Eq. 1.4). The produced superoxide radical anions react with water to produce $HO_2^{\bullet}$ and hydroxyl anion species (OH^-) (Eq. 1.5). The $HO_2^{\bullet}$ species generated can further react with H_2O to produce H_2O_2 and $^{\bullet}OH$ radicals (Eq. 1.6). The H_2O_2 species can decompose and produce $^{\bullet}OH$ radicals (Eq. 1.7). It has been mentioned that $^{\bullet}OH$ radical production from $O_2^{\bullet-}$ radical anions involve several steps, but it involves a single step to form $^{\bullet}OH$ radicals from adsorbed water or hydroxyl group [20]. Therefore, most of the $^{\bullet}OH$ radicals are generated through VB holes [21]. The photocatalytic degradation of organic pollutants can be initiated by resulting $^{\bullet}OH$ and $O_2^{\bullet-}$. It has also been stated that the photoinduced holes in the VB of semiconductor can also directly participate in the degradation of pollutants [16].

1.6 Requirements for Photocatalytic Dye Degradation

One of the important parameters for semiconductor photocatalyst is the positioning of CB and VB with respect to the potentials of $^{\bullet}OH/H_2O$, $O_2/O_2^{\bullet-}$. The photocatalytic degradation ability and transfer of photogenerated charge carriers to the surface of the semiconductor and to any adsorbed species is directed by the relative positioning of the CB and VB of the photocatalyst and the redox potentials of $^{\bullet}OH/H_2O$ and $O_2/O_2^{\bullet-}$. For $O_2^{\bullet-}$ and $^{\bullet}OH$ radical generation, the respective potentials must lie within the band gap of the photocatalyst. The CB edge minima (E_{CB}) should be more negative than the potential for $O_2/O_2^{\bullet-}$ ($E_{O2/O2\bullet-}$ = +0.13 eV vs NHE), whereas the VB maxima (E_{VB}) should be more positive than the potential of $^{\bullet}OH/H_2O$ ($E_{\bullet OH/H2O}$ = +2.68 eV vs NHE) (Figure 1.3) [22].

Other factors, such as, charge separation, mobility, and lifetime of photoinduced charge carriers, affect the photocatalysis as well [2].

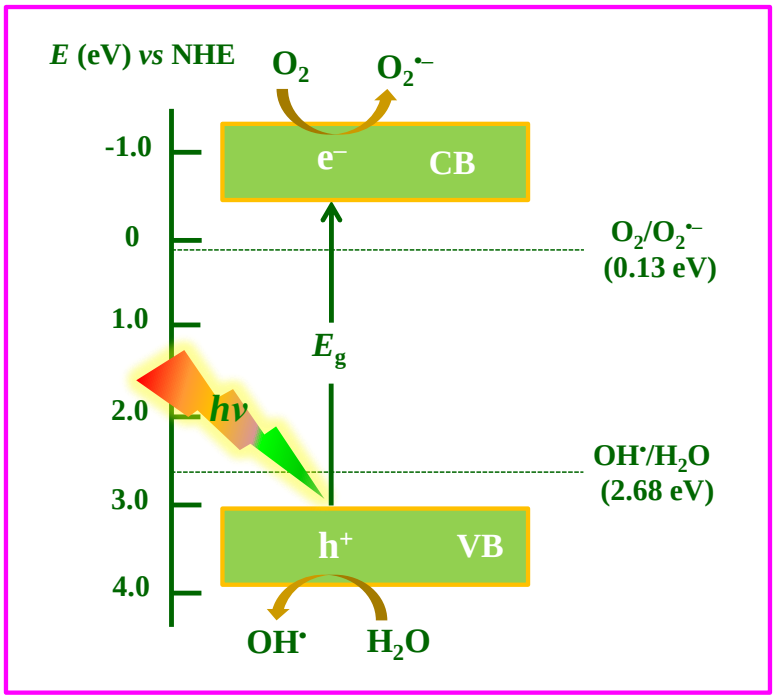

Figure 1.3 Band structure requirement of semiconductor for photocatalytic dye degradation reaction.

1.7 Wide Band Gap Metal Oxide Photocatalysts Working under UV Irradiation

Several titanate, niobate and tantalate semiconductors possessing layered perovskite structure have been effectively researched after the report of photocatalytic water splitting reaction over $K_2La_2Ti_3O_{10}$. $K_2La_2Ti_3O_{10}$ contain three octahedral thick perovskite layers separated by two K^+ ions. The uniqueness of this photocatalyst is that in its presence the H_2 evolution takes place with NiO_x co-catalyst, whereas O_2 evolution at the hydrated interlayer [23, 24]. The tailoring of the layered perovskite photocatalyst, $K_2La_2Ti_3O_{10}$, via ion-exchange reaction with divalent cations, such as, Ca^{2+}, Sr^{2+}, and Ba^{2+} was studied by Wang *et al.* The photocatalytic activities of these compounds were evaluated by methyl orange and phenol degradation in addition to the hydrogen evolution reaction. The enhanced activity of the ion-exchanged compounds were attributed to the decrease in the packing fraction leading to more interlayer spacing, which benefits the separation of charge carriers [25].

Teshima *et al.* successfully synthesized crystals of $K_4Nb_6O_{17}$ from potassium molybdate and tungstate fluxes and studied its photocatalytic activity. These colorless and transparent crystals of $K_4Nb_6O_{17}$ showed enhanced photocatalytic degradation and adsorption of methylene blue [26]. The semiconductor photocatalysts, $Ca_2Nb_{2-x}Ta_xO_7$ ($0 \leq x \leq 2$) prepared by a hydrothermal method has been studied for photocatalytic degradation of gaseous formaldehyde and Rhodamine B. An enhancement of degradation and photocurrent generation by Ta^{5+} substitution was achieved. The improved degradation was attributed to more effective photoelectron transfer in the conduction band with larger curvature [27].

Liang *et al.* synthesized $Sr_{0.25}H_{1.5}Ta_2O_6{\cdot}H_2O$ by a simple, facile, and mild hydrothermal reaction and studied its photocatalytic activity for the degradation of benzene and water splitting reaction (for evolution of H_2). The photocatalytic degradation of benzene and the rate of H_2 evolution were 4 and 81 times greater, respectively, than that found in case of TiO_2. A suitable electronic band structure is responsible for the enhanced photocatalysis [28]. The photocatalytic activity of hexagonal $BaTa_2O_6$ photocatalyst, synthesized by hydrothermal method at different temperature and time, has been studied by the way of RhB degradation. The compound synthesized at 270 °C for 72 h exhibited improved photocatalysis due to the reduction in the hydrogen related defects, which acts as recombination sites for charge carriers [29]. All the above mentioned metal oxides have band gaps greater than 3.0 eV, rendering these metal oxides inactive under visible-light/natural sunlight-irradiation.

1.8 Solar Spectrum

The photocatalysts having band gap more than 3.0 eV utilize only UV light for excitation of electrons from the VB and generation of charge carriers. But UV light accounts for only ~ 4% of the incoming solar energy and thus renders the photocatalytic process impractical under sunlight. However, considering the abundance of sunlight in the visible region (Figure 1.4) accounting for about ~ 43% of incoming solar energy, the development of visible-light-driven photocatalysts is in demand for efficient utilization of solar energy [30]. For harvesting of visible-light or the direct solar energy the band gap of the semiconductor should be narrower than 3.0 eV.

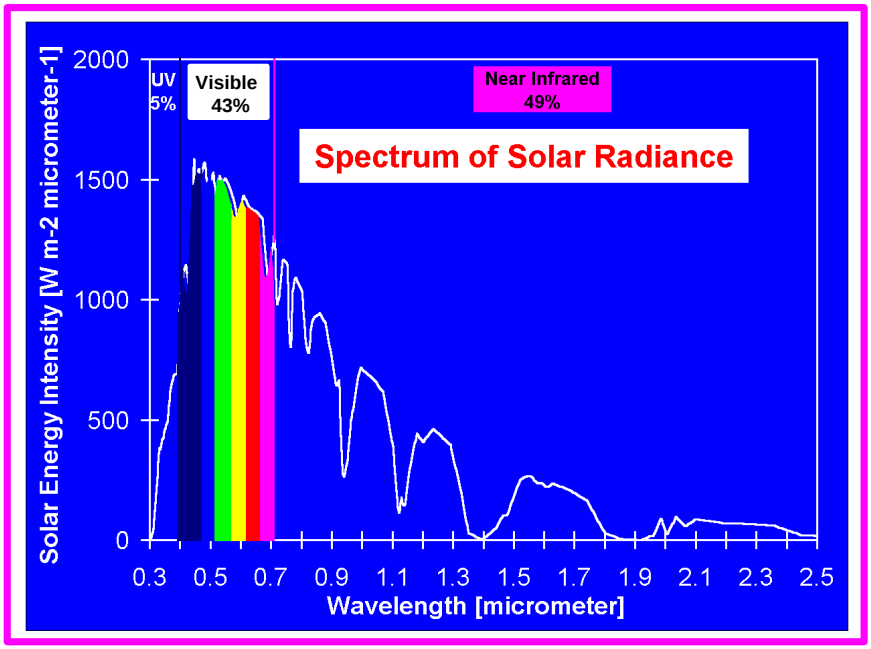

Figure 1.4 Solar spectrum showing the available amount of UV and visible light.

1.9 Approaches to Harvest Visible Light in Photocatalysis

Photocatalysis is initiated by light absorption of semiconductors, which forms charge carriers. The wide band gap semiconductors ($E_g \geq 3.0$ eV) absorb the light in the UV region of the solar spectrum, which is one of the major disadvantages of the UV-active semiconductor photocatalysts. Much effort has been devoted to develop visible-light-harvesting photocatalysts. Several common approaches that have been developed to narrow down the band gap for harvesting the visible light in photocatalysis include:

- Metal or/and non-metal ion doping
- Solid solution formation
- Dye sensitization
- New visible-light-active single photocatalysts

1.9.1 Metal or/ and Nonmetal Doping

1.9.1.1 Metal Doping

One of the most efficient approaches to develop visible-light active photocatalysts is to introduce impurity levels in the forbidden region by doping with cation. This impurity

level created in between the VB and CB can act as electron acceptor or electron donor, which makes the wide band gap semiconductor into a narrow band gap (comparatively) visible-light-active photocatalysts (Figure 1.5). Over few decades, there have been several literature reported on the development of visible-light-active photocatalysts by cation doping. Early in 1982, Borgarello *et al.* found that water decomposition reaction occurs on Cr^{3+}-doped TiO_2 under visible light irradiation (400−550 nm). The visible light absorption can be assigned to an electron transition from Cr^{3+} 3d level to CB of TiO_2 [31].

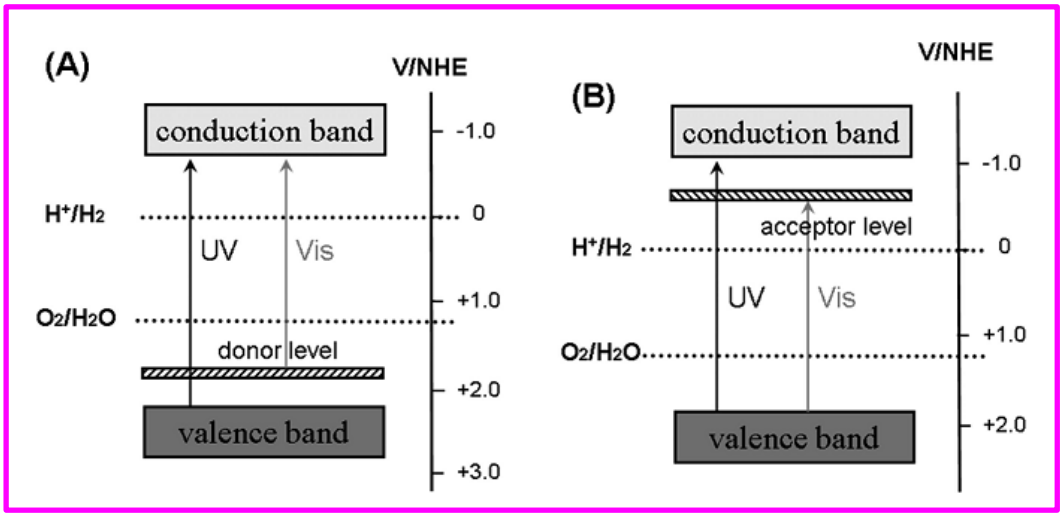

Figure 1.5 Schematic diagram showing the formation of donor level (A) and acceptor level (B) by doping with cation [2].

Liu and co-workers reported that Cr-doped $SrTi_{1-x}Cr_xO_3$ (x = 0.00, 0.02, 0.05, 0.10) exhibited increasing photocatalytic activities under both UV and visible light irradiation with increasing the amount of dopant. The parent compound $SrTiO_3$ shows the band gap at ~3.2 eV, which is UV active. The visible-light absorption in the Cr-doped $SrTi_{1-x}Cr_xO_3$ is attributed to band transition from the Cr 3d to the Cr 3d +Ti 3d hybrid orbital [32]. Lee *et al.* reported the photocatalytic activity of M-doped layered perovskite $La_2Ti_2O_7$ (M = Cr, Fe). The UV-active parent photocatalyst $La_2Ti_2O_7$ (E_g 3.6 eV) becomes visible light active photocatalyst on doping with Cr or Fe cation. Doping by Cr or Fe created donor levels in the band gap of $La_2Ti_2O_7$ and made it visible light active [33]. Suzuki and co-workers investigated the effect of Fe^{3+} and W^{6+} substitution for Ti^{4+} on photocatalytic properties of $K_2La_2Ti_{3-x}M_xO_{10+\delta}$. The pure $K_2La_2Ti_3O_{10}$ showed strong absorption edge in the UV-region (E_g 3.5 eV) and the transition metal substituted photocatalysts exhibited the absorption edge

in visible region. The substitution of a part of Ti^{4+} with Fe^{3+} remarkably increased the photocatalytic activity under visible-light-irradiation [34]. The Ni-doped $In_{1-x}Ni_xTaO_4$ showed enhanced photocatalytic performance in the splitting of water under visible-light-illumination with a quantum yield of ~ 0.66%. The reduction in the band gap of $In_{0.9}Ni_{0.1}TaO_4$ photocatalyst was attributed to the formation of Ni 3d donor level [30]. Interestingly, the $Bi_4Ti_{3-x}Cr_xO_{12}$ photocatalysts with Cr^{3+} doping at the Ti^{4+} sites exhibited higher photocatalytic performance towards hydrogen evolution under visible-light-irradiation. This was attributed to the existence of an impurity level of Cr 3d in both the CB and VB [35]. Kudo and co-workers demonstrated that Cr^{6+} -doped $PbMoO_4$ are efficient photocatalysts for the evolution of oxygen from water under visible-light-irradiation. The photocatalytic activity in the visible-light was attributed to the formation of impurity electron-acceptor level of Cr 3d orbitals below the CB of $PbMoO_4$ [36].

1.9.1.2 Non-metal-Ion Doping

Another approach to narrowing of band gap in wide band gap semiconductors and improving the visible-light harvesting property is by doping with non-metal ions (such as N, S, etc.). Non-metal ion dopants shift the VB edge upwards instead of forming new impurity level in between the VB and CB. This results in the band gap narrowing as shown in Figure 1.6. This method is mostly used to modify the UV-light active photocatalysts, such as, Ti, Nb and W-based oxides.

Domen and co-workers reported enhanced photocatalytic activity of $LaTiO_2N$ towards splitting of water under visible-light-irradiation. The band gap of the parent $La_2Ti_2O_7$ is estimated to be 3.9 eV and after doping with N the band gap narrowed to 2.1 eV. The narrowing of band gap was attributed to the formation of a new VB composed of O 2p and N 2p orbitals, shifting the VB edge upward [37]. Zou *et al.* reported excellent photocatalytic organic dye degradation by N-doped $SrTiO_3$ perovskite under visible-light-irradiation. They found that the N-doping narrowed the band gap by 0.3 eV and the absorption of visible light was enhanced [38]. Ji *et al.* reported that the N-doped layered perovskite oxides, $Sr_2Nb_2O_{7-x}N_x$, are visible-light-active photocatalysts for evolution of hydrogen from water [39]. After N-doping, the absorption edge of $Sr_2Nb_2O_7$ (UV region) was red shifted to visible region and subsequently induced visible-light-absorption.

Recently, it has been reported that S-doped ZrW_2O_8 shows the visible-light photocatalysis as compared to the UV-light in the undoped oxide. The band gap of host ZrW_2O_8 and S-doped ZrW_2O_8 are estimated to be 4.0 eV and 2.76 eV respectively. The visible-light-photocatalysis was due to the S 3p orbitals, which increased the width of VB and result in a narrow band gap [40].

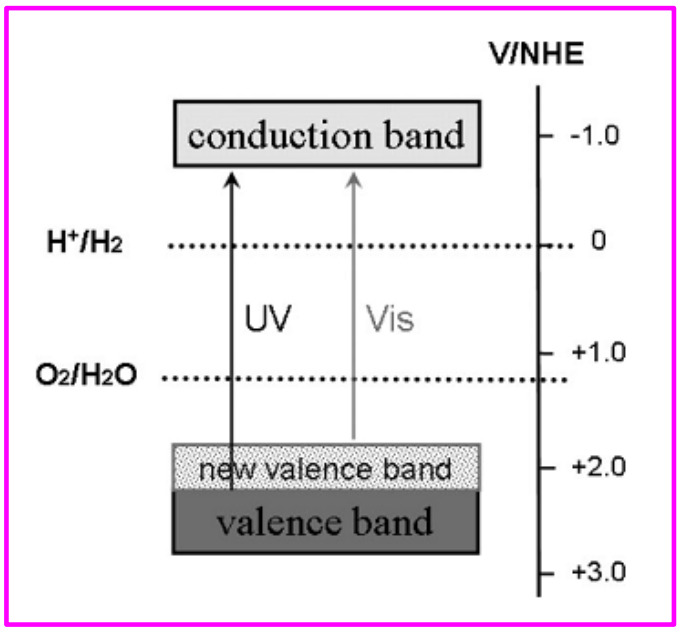

Figure 1.6 Schematic diagram showing the increase in the width of VB by doping with nonmetal ions [2].

1.9.1.3 Metal and Nonmetal-Ion Co-doping.

Another strategy toward narrowing of the band gap of the semiconductor oxides is co-doping with metal/non-metal-ions. Sasikala *et al.* investigated the co-doping of TiO_2 with In and N. It strongly reduced the band gap of TiO_2 than individual doping of In or N. The narrowing of the band gap in In and N co-doped TiO_2 was primarily due to the contribution of additional energy levels provided by In to the CB and that of N to the VB (Figure 1.7). As a result, enhanced photocatalytic activity was exhibited by In and N co-doped TiO_2 under visible-light-irradiation. Individual In or N doped TiO_2 can also exhibit enhanced visible-light-photocatalysis as compared to the undoped TiO_2. Co-doping of $SrTiO_3$ with N and La cation at O and Sr sites, respectively, resulted in the reduced band gap. Co-doped $SrTiO_3$

perovskites exhibited enhanced photocatalytic activity under visible-light-irradiation than the undoped oxide [41].

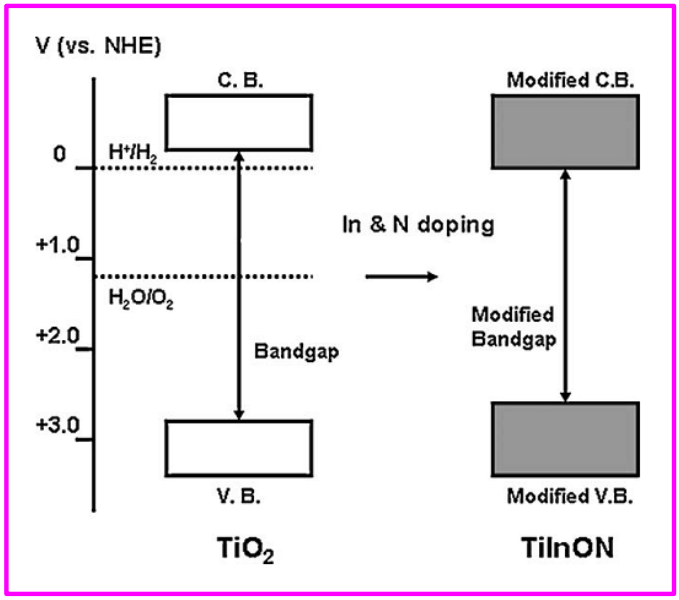

Figure 1.7 Schematic diagram showing the modification of the CB and VB of In and N codoped TiO_2 [2].

1.9.2 Solid Solution Formation

In addition to the metal and non-metal doping, making solid solutions between wide and narrow band gap semiconductors possessing same crystal structure is another approach to develop suitable band gap semiconductors for photocatalysis. Both, the band gap and band edge positions, of the solid solutions can be altered by changing the ratio of the narrow and the wide band gap semiconductors. Figure 1.8 shows the controllable band formation by making a solid solution.

The solid solutions formation in $Bi_xIn_{1-x}TaO_4$ ($0 < x < 1$), resulted in oxide with the band gap of 2.86, 2.71, and 2.74 eV for x = 0.2, 0.5 and 0.8, respectively. It was reported that while the CB was principally consisted of Ta 5d, In 5p and In 5s orbitals, the VB consisted of mainly O 2p, Bi 6s, and Bi 6p orbitals. These solid solutions showed efficient photocatalytic activity in presence of visible-light [42]. Wang *et al.* developed a novel visible-light-active solid-solution photocatalyst $(Ag_{0.75}Sr_{0.25})(Nb_{0.75}Ti_{0.25})O_3$ with the perovskite structure for the degradation of acetaldehyde. The enhanced photodegradation

was attributed to the modulated band structure where the CB was formed by the hybridization of Ti 3d with Nb 4d orbitals, while the VB was composed of O 2p and Ag 4d orbitals [43]. Maeda *et al.* reported new efficient visible-light induced GaN-ZnO solid solutions for stoichiometric splitting of water into hydrogen and oxygen. While the individual GaN and ZnO have band gap of 3.4 and 3.2 eV respectively, the solid solution formation, $(Ga_{1-x}Zn_x)(N_{1-x}O_x)$, resulted in smaller band gaps than those of GaN and ZnO alone. The estimated band gap for $x = 0.13$ solid solution was 2.58 eV. The reduction in the band gap was due to p-d repulsion between the N 2p and Zn 3d electrons that pushed the VB upwards [44].

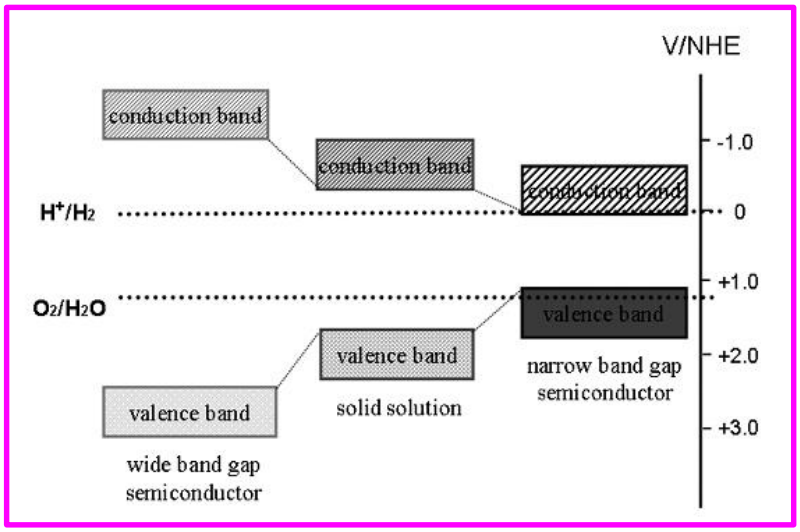

Figure 1.8 Schematic diagram showing the band gap narrowing by solid solution formation [2].

1.9.3 Dye Sensitization.

Dye sensitization is another powerful approach for visible-light absorption by wide band gap semiconductors. The proposed mechanism of dye sensitized photocatalysis is presented in Figure 1.9. The approach here is different from the band gap engineering. In this a dye molecules adsorbs visible-light and e^- excitation take place from HOMO to LUMO levels of the dye. Afterwards, the excited electrons in the LUMO of the dye molecules transfer to the CB of a semiconductor and then to a co-catalyst, which is loaded on the semiconductor. Finally, these electrons in the co-catalyst reduce the electron

acceptors. The excited sensitizer gets regenerated by the reaction with an electron donor (sacrificial reagent).

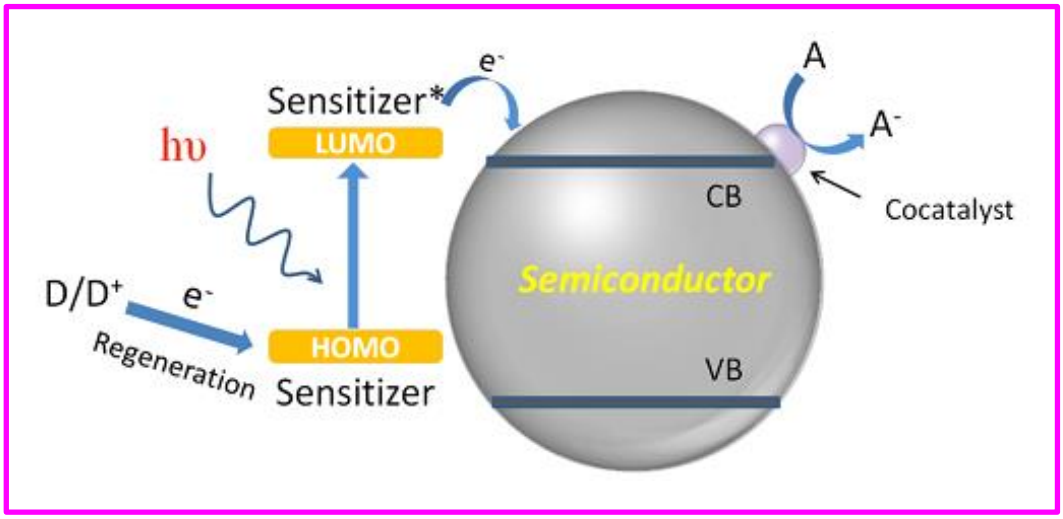

Figure 1.9 Schematic diagram representing the dye sensitized photocatalysis on wide band gap semiconductors [5].

In the year 1983, Houlding *et al.* used 8-hydroxyquinoline as sensitizer to harvest visible light on TiO_2 catalyst surface. This surface modified catalyst exhibited enhanced water splitting activity in the presence of EDTA scavenger under visible-light irradiation [45]. The use of Eosin Y dye as a sensitizer on TiO_2 surface for degradation of phenol in presence of visible-light was also reported. The catalyst showed efficient visible-light induced degradation in presence of triethanolamine as sacrificial reagent and a very low concentration of platinum co-catalyst [46]. Madras and co-workers also found that, when Eosin Y was used as visible light sensitizer, nano-TiO_2 exhibited higher activity for degradation of phenolic compounds. Here, the dye sensitized electrons in the CB of the TiO_2 first reacts with dissolved O_2 to form superoxide radical anions ($O_2^{\bullet-}$) and subsequently $^{\bullet}OH$ radicals, which later degraded the phenolic compounds into H_2O and CO_2 [47].

1.9.4 Developing novel visible-light-active single photocatalysts through band gap engineering

Besides the above mentioned techniques (ion doping, solid solution, dye sensitization), novel visible-light-active single photocatalysts, mostly heterometallic oxides, can be developed through metal mediated band gap engineering. The Bi 6s orbital in the Bi containing metal oxides hybridize with O 2p orbitals to form new VB. This hybridization shifts the VB upward, thus narrowing the band gap (Figure 1.10). $BiVO_4$ shows visible-light-active photocatalysis for O_2 evolution in presence of electron scavengers. The VB formation by Bi 6s orbitals was studied with the help of band structure calculations by DFT [47]. $BiVO_4$ was also used in the degradation of organic pollutants, such as Methylene Blue [49], Methyl Orange [50], Rhodamine B [51] and long chain alkylphenol [52]. Yin *et al.* reported the visible-light driven single photocatalysts, $MCrO_4$ (M = Sr, Ba), with calaulated band gap of 2.63 and 2.44 eV, for $BaCrO_4$ and $SrCrO_4$, respectively. Here the CB was formed by Cr^{6+} 3d orbitals and the VB was composed of O 2p orbitals [53].

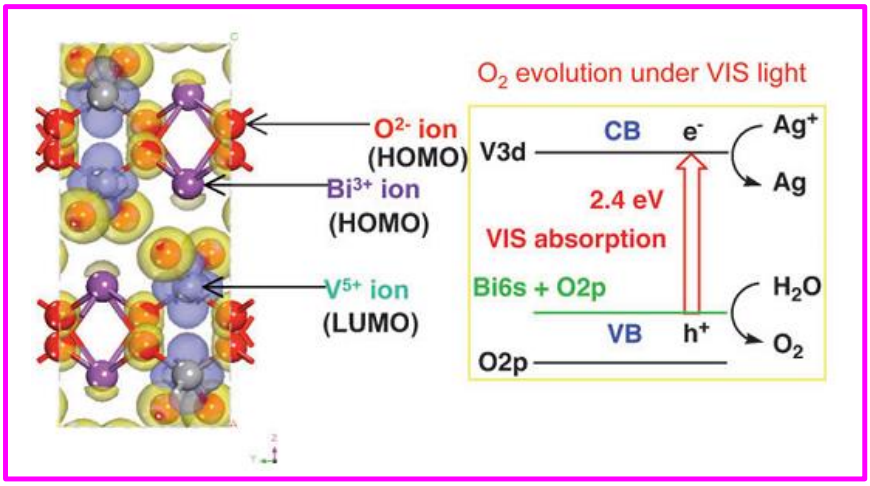

Figure 1.10 Band structure of $BiVO_4$ calculated by DFT calculations [48].

1.10 Photocatalysts Working under Visible Light Irradiation

From the perspective of efficient solar energy utilization, the development of visible-light-active photocatalysts is in great demand. Until middle of 1980s, only a few photocatalysts (chalcogenides and metal oxides), such as, CdS, CdSe and WO_3 were known to be visible-light-active photocatalysts [54]. Even though CdS and CdSe have suitable band position and band gap for visible-light photocatalysis these are not active for water splitting

reaction. The S^{2-} and Se^{2-} anions rather than water in the CdS and CdSe, respectively, are more susceptible to oxidation by photoinduced holes, according to the following reaction:

$$CdS + 2h^+ \rightarrow Cd^{2+} + S \quad (1.9)$$

$$CdSe + 2h^+ \rightarrow Cd^{2+} + Se \quad (1.10)$$

The above reactions are called photocorrosion. These catalysts (CdS or CdSe) themselves get oxidized and degraded [4, 55, 56]. On the other hand, WO_3 is visible-light-active photocatalyst for O_2 evolution in presence of an electron scavenger but it is not active for the production of H_2 from water because of lower CB potential level than the redox potential for H_2 evolution [57]. Therefore, suitable band levels with narrow band gap (E_g < 3.0 eV) and stable photocatalyst is necessary. To date, numerous attempts have been made to synthesize photocatalysts that effectively works under visible-light.

Lee and co-workers has synthesized novel Aurivillius phase perovskite, $PbBi_2Nb_2O_9$, and studied its photocatalytic activity for degradation of gaseous isopropyl alcohol, water splitting and photocurrent generation all under visible-light-irradiation. The Pt loaded, undoped, single oxide photocatalyst has exhibited much higher activity for H_2 (quantum yields with ca. 0.95%) and O_2 (quantum yields with ca. 29%) evolution in presence of scavengers. The quantum yield for generation of O_2 is higher than those reported previously under visible-light. In this compound, the hybridization of Bi 6s and Pb 6s with O 2p orbitals pushed up the position of VB maximum and narrowed the band gap, thereby extending the absorption in the visible-region [58].

The one octahedral thick Aurivillius phase perovskite, Bi_2WO_6, has been studied for visible-light-driven photodegradation of both $CHCl_3$ and CH_3CHO [59]. The substitution of Mo in Bi_2WO_6 has increased the photocatalytic activity towards RhB degradation under visible-light-irradiation. Bi_2WO_6 and $Bi_2Mo_{0.25}W_{0.75}O_6$ exhibited fairly higher degradation than those of other Mo substituted photocatalysts under visible-light and $Bi_2Mo_{0.25}W_{0.75}O_6$ showed much higher degradation than Bi_2WO_6 under visible-light. Since Mo substitution efficiently narrowed down the band gap of Bi_2WO_6, more photogenerated electrons were transferred in the CB with larger curvature [60].

The Aurivillius layered perovskite $Bi_5Ti_3FeO_{15}$ was investigated for the photodegradation of isopropyl alcohol (IPA) under visible-light-illumination. The enhanced activity for degradation of IPA than that of $TiO_{2-x}N_x$ was attributed to effective separation of charge carriers [61]. Tang *et al.* synthesized novel visible light active $CaBi_2O_4$ photocatalyst and first used it for the degradation of acetaldehyde and methylene blue. The activity and crystal structure of $CaBi_2O_4$ did not change after a series of degradation runs under different experimental conditions. The hybridized Bi 6s and O 2p levels makes the VB largely dispersed, which favored high mobility of photogenerated holes to degrade various organic pollutants [62].

Homogeneous $Bi_2Mo_xW_{1-x}O_6$ (x = 0.0, 0.25, 0.50, 0.75, and 1.0) solid solutions have been studied for degradation of methylene blue under visible-light-illumination. The photocatalyst $Bi_2Mo_{0.25}W_{0.75}O_6$ showed enhanced photodegradation. The intrinsic layered structure, nanosheet morphology, band gap engineering, and the W content play crucial roles in photodegradation [63]. The fluorination of Bi_2WO_6 enhanced the degradation rate of RhB and also changed the mechanistic pathway of RhB degradation via N-deethylation. The fluorinated surface acted as electron trapping site and enhanced the photocatalysis [64].

The visible light active Sillén-Aurivillius intergrowth (Bi_4NbO_8Cl) phase has been studied for methyl orange degradation. The polarizing fields in NbO_6 and BiO_8 local structures and the internal electrical fields between $[Bi_2O_2]$ and [Cl] slabs are responsible for efficient photogenerated carrier separation and thus an enhancement in degradation [65]. The layered compound of Pb-Bi-oxychloride $PbBiO_2Cl$ has been studied for methyl orange photodegradation under visible-light [66]. The enhanced visible-light-driven photodegradation of methyl orange and methylene blue was carried out over Bi-based $PbBiO_2Br$ as well [67].

1.11 Introduction to Perovskites

The general formula of perovskite oxides is ABO_3, where *A* and *B* represents two cations and *O* stands for an oxygen anion. The perovskite systems are probably the most researched mixed metal oxide system in the area of heterogeneous catalysis. The initial catalytic studies on perovskite metal oxides were reported in the beginning of 1970s, showing excellent catalytic activity in oxidation as well as NO reduction reaction, indicating

these perovskites as appropriate alternative for platinum-group metals (PGMs) in catalytic conversions [68]. Now, perovskite metal oxides are indeed considered as effective alternatives for PGMs in different catalytic reactions, mainly because of their easy synthesis and low-cost as compared to PGMs and the amazing ability of their structure to accommodate different elements thereby tailoring their properties to a large extend.

The perovskite structure can be considered to be formed by the corner shared octahedral framework of *B*-cation, which could be a 3*d*, 4*d*, or 5*d* series metal with both d^n (n = 1-9) or d^0 configuration. The *A* cation could be a lanthanide, alkaline, or alkaline-earth cation, which fits in the dodecahedral site of the corner connected octahedral framework. For the description and stability of perovskite structures, Goldschmidt had introduced a tolerance factor known as 'Goldschmidt tolerance factor', *t* and is given by the expression,

$$t = \frac{r_A + r_O}{\sqrt{2}(r_B + r_O)} \tag{1.11}$$

where, r_A, r_B and r_O are ionic radii of *A*, *B* and *O*, respectively. If *t* values are in between 0.8 to 1.0, perovskite structure gets stabilized. For *t* = 1, an ideal perovskite structure forms with no distortions. However, the structure distorts from an ideal perovskite when the value of *t* deviates from 1.0 [69]. Figure 1.11 shows an ideal perovskite structure of $SrTiO_3$.

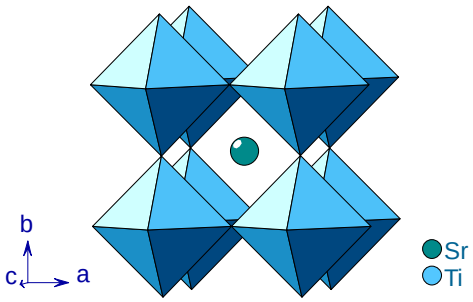

Figure 1.11 An ideal perovskite structure of $SrTiO_3$.

One of the benefits of perovskite structure is the possibility to tolerate a wide range of different compositions by substituting different metal ions at both the *A* and *B* sites, giving the general formula of a perovskite oxide as $A_{1-x}A'_xB_{1-y}B'_yO_{3\pm\delta}$. Since the perovskites

structure can be stabilized with a variety of compositions this emerges as an important research area in the field of solid state chemistry.

Due to the compositional and structural flexibility of perovskites, several perovskite derived structures are possible. For example, the intergrowth of perovskite and other related structures give rise to a series of layered perovskites. The most common layered perovskites are given below.

- Aurivillius phase [70]
- Ruddlesden-Popper (R-P) phase [71]
- Dion-Jacobson (DJ) phase [72]

All the three series of layered perovskites contain common two dimensional (2D) perovskite sheets of composition $[A_{n-1}B_nO_{3n+1}]$ as one of the blocks building the layered structure, where A denotes the 12 coordinated A-site cation of the perovskite structure, B is the octahedrally coordinated cation, and *n* represent the thickness of the octahedral slabs, i.e., $n = 1$ indicates one octahedral thick perovskite layer and $n = 2$, two octahedral thick perovskite layer, etc.

The Aurivillius phases are one of the most common class layered perovskite with the general composition, $[Bi_2O_2][A_{n-1}B_nO_{3n+1}]$, consisting of fluorite like $(Bi_2O_2)^{2+}$ units separated by the 2D perovskite slabs (Figure 1.12 (a)). More details of this class are discussed in the next section. The other familiar class of layered perovskite is the R-P phase, with a general composition, $A'_2[A_{n-1}B_nO_{3n+1}]$, which contain two alkali or alkaline earth cations in between the 2D perovskite slabs. Figure 1.12 (b) represent the $n = 3$ member of the R-P phase. Gopalakrishnan and co-workers presented the transformations of the R-P phase oxide, $K_2La_2Ti_3O_{10}$, to Aurivillius phase, $(Bi_2O_2)La_2Ti_3O_{10}$ by a novel metathesis reaction with BiOCl [73]. Subsequently, they were also successful in bridging the two layered perovskites, namely the Aurivillius and R-P and reported a new series of hybrid layered perovskites [74]. The remaining class of layered perovskite, namely, the D-J phase has only one interlayer cation between perovskite slabs, with the general formula, $A'[A_{n-1}B_nO_{3n+1}]$. Figure 1.12 (c) shows the structure of a representative $n = 3$ member of the DJ series, $RbCa_2Ti_3O_{10}$. The structure can be visualized as an intergrowth of perovskite and rock salt structure.

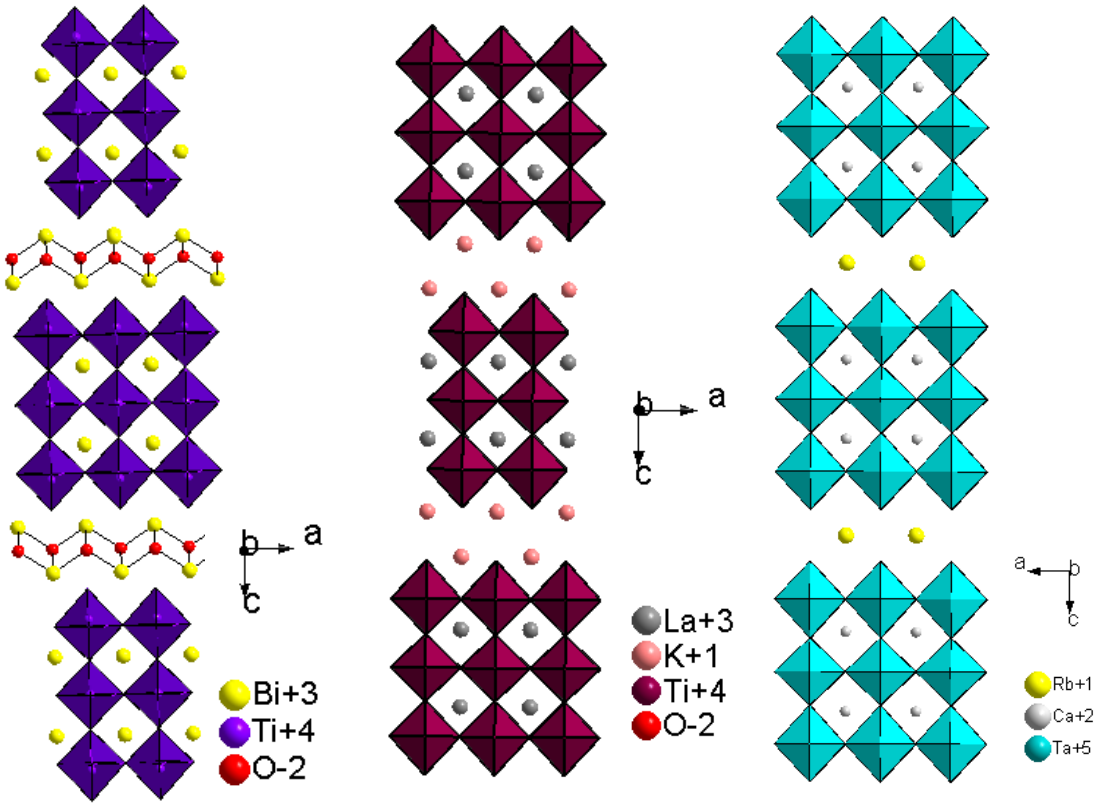

(a) $Bi_4Ti_3O_{12}$ **(b) $K_2La_2Ti_3O_{10}$** **(c) $RbCa_2Ta_3O_{10}$**

Figure 1.12 Structures of representative members of layered perovskites. Typical n = 3 members of (a) Aurivillius, (b) Ruddlesden-Popper and (c) Dion-Jacobson families of layered perovskites.

1.11.1 Layered Aurivillius Perovskite Phase

As stated earlier the Aurivillius phases are variants of layered perovskites having regular layered intergrowth structures composed of fluorite like $(Bi_2O_2)^{2+}$ blocks with perovskite $(A_{n-1}B_nO_{3n+1})^{2-}$ slabs, where A denotes the 12 coordinated A-site cation of the perovskite structure, which can be occupied by cations, such as Ca^{2+}, Sr^{2+}, Ba^{2+} and Bi^{3+}, in addition to the rare earth ions. The octahedrally coordinated B cation can be Ti^{4+}, Ta^{5+}, V^{5+}, Nb^{5+} or W^{6+}. Recently, interest in these Aurivillius phase semiconductors has grown due to their superior activity as single oxide photocatalysts. The most simple members of the Aurivillius family, namely, Bi_2WO_6 and Bi_2MoO_6 (n = 1), were investigated for their photocatalytic activity under visible-light irradiation [74, 75]. The replacement of W by Mo

or vice versa in the Aurivillius solid solution series, $Bi_2Mo_xW_{1-x}O_6$, enabled band gap alteration among the members with enhanced visible-light-induced photocatalytic activity [76, 77]. The n = 2 member, $PbBi_2Nb_2O_9$, has been reported for efficient photocatalytic degradation of isopropyl alcohol to CO_2, generation of photocurrent, and water splitting reaction, all under visible light irradiation [78]. Muktha *et al.* studied the synthesis, structure, and photocatalysis of three layered (n = 3) Aurivillius phase, $LiBi_4M_3O_{14}$ (M = Nb, Ta). These compounds have been confirmed to degrade specific dyes (Alizarine cyanine Green, Alizarin Red S, Orange G, Coomassie Brilliant Blue R250 and Methyl Violet) and phenolic compounds (phenol, 4-nitrophenol) [79].

Recently, the four layer (n = 4) Aurivillius phase, $Bi_5Ti_3FeO_{15}$, has drawn attention for its ferroelectric [80, 81] and photocatalytic [82, 83] properties. Photocatalytic activity of $Bi_5Ti_3FeO_{15}$ toward RhB [82], acetaldehyde [82] and isopropyl alcohol [83] degradation by visible-light irradiation has been reported, although very poor degradation (~6%) efficiencies were observed with the bulk $Bi_5Ti_3FeO_{15}$ in neutral aqueous solution. However, Sun et al. have shown enhanced RhB degradation with $Bi_5Ti_3FeO_{15}$ hierarchical microflowers as compared to the bulk oxide under similar conditions. The higher efficiency has been attributed to increased surface area and its nanocrystalline nature [82]. The five layer (n = 5) Aurivillius phase, $Bi_6Ti_3Fe_2O_{18}$, has also been investigated for its ferroelectric, magnetic, and optical properties [80, 84]. Moreover, the rare earth (La, Sm, Gd, and Dy) substituted $Bi_6Ti_3Fe_2O_{18}$ were explored for their magnetic and magnetoelectric properties [85, 86].

1.11.2 Sillén-Aurivillius Intergrowth Phases

In 1986, Ackerman first investigated the synthesis and structure of a new family of Sillén-Aurivillius phases, such as, Bi_3PbWO_8Cl and Bi_4NbO_8Cl [87]. As we know, an Aurivillius phase consist of fluorite-like $[Bi_2O_2]^{2+}$ blocks alternating with perovskite-like $[A_{n-1}B_nO_{3n+1}]^{2-}$ blocks, where n is the thickness of octahedral block and in Sillén phases, $[Bi_2O_2]^{2+}$ or $[BiPbO_2]^{+}$ blocks are sandwiched between halogen [X] layers. The general formula of a Sillén phases is $[M_2O_2]X_m$, where m = 1 or 2, M = Bi^{3+}, Pb^{2+}, Sr^{2+}, etc., and X is a halide [88]. Ackerman interconnected these two structurally similar families in a regular manner to produce the new intergrowth family of Sillén-Aurivillius phases and nicknamed

these intergrowth phases as 'Bipox' phases (*bi*smuth-*p*erovskite-*ox*yhalide). The Sillén-Aurivillius intergrowth phases have the general formula $[M_2O_2][A_{n-1}B_nO_{3n+1}][M_2O_2][X_m]$. The nomenclature A*n*X*m* is used for these phases to express the number of perovskite octahedral [A*n*] layers and halide [X*m*] layers.

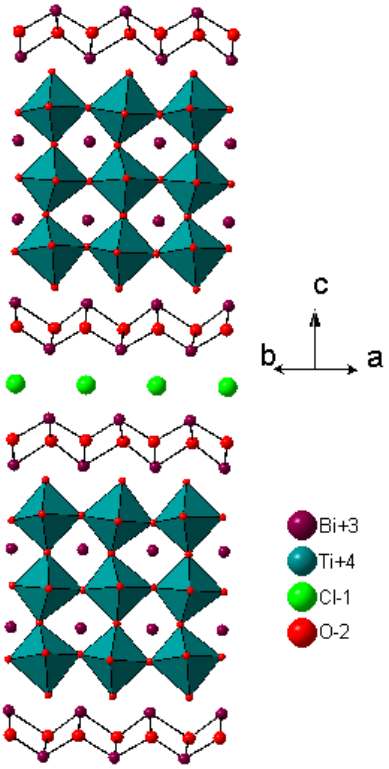

Figure 1.13 Structure of a Sillén-Aurivillius intergrowth phase $Bi_5PbTi_3O_{14}Cl$ with n = 3 perovskite block and m = 1 chloride layer.

The A1X1 phase Bi_4NbO_8Cl, have been reported for their excellent visible-light-induced photocatalytic activity for degradation of methyl orange (MO). The polarizing fields in NbO_6 and BiO_8 local structures, along with the internal electrical fields between $[Bi_2O_2]$ and [Cl] slabs, are responsible for effective separation of photogenerated electrons and holes, resulting enhanced photocatalysis [89]. The ferroelectric properties and crystal structure of an A2Xl member, $Bi_3Pb_2Nb_2O_{11}Cl$ has been reported [90]. The A3X1 phase $Bi_5PbTi_3O_{14}Cl$ (Figure 1.13) have been modified by substituting magnetic transition metals, such as, M^{3+} = Cr^{3+}, Mn^{3+} and Fe^{3+}, for 33.3% of the Ti^{4+} cations, accompanied by co-doping of Bi^{3+} for Pb^{2+}. The modified compounds, $Bi_6Ti_2MO_{14}Cl$ (M = Cr, Mn, Fe), showed naturally layered multiferroic properties [91, 92].

1.12 Methods to Synthesize Metal Oxides

A variety of synthetic methods is available in the literature for the synthesis of metal oxides. Some of the commonly used methods include the following.

- Ceramic
- Reactive grinding
- Hydrothermal
- Sol-gel
- Microwave
- Sonochemical

Among them the ceramic method or solid-state reaction method is the most common and widely employed method for the synthesis of inorganic solids [93]. In this method, stoichiometric quantities of solid starting materials, such as, binary / simple metal oxides / carbonates / oxides are weighed and ground thoroughly in an agate mortar for nearly an hour. The ground mixture is then placed in a platinum or silica or alumina containers (crucible / boat) and are heated in a muffle / tube furnace at high temperatures for variable durations. The requirement of high temperatures is due to fact that the reactions are diffusion controlled and the diffusion coefficients of the solids are very low (in the order of 10^{-12} cm^2s^{-1}). If any starting component is volatile or sensitive to the atmosphere, the reaction is performed in sealed evacuated capsules or controlled gas atmosphere (argon/nitrogen) to avoid the contact of O_2 or moisture. The reaction mixtures were ground thoroughly at each and every intermittent stage during the entire course of the reaction. The repeated grinding and heating steps involve in the ceramic method helps in breaking down the diffusion barrier between the grains of starting reactants and products formed during the course of a reaction. The nucleation step in the ceramic method is slightly difficult due to the structural differences between reactants and product and the huge amount of structural reorganization that take place to get the final product by bond braking, reforming and migration of constituent elements.

Although the ceramic method is a very common method for the preparation of various solid materials, it has few drawbacks, such as, (i) complete homogenous mixing of the starting compounds are not possible, (ii) large diffusion distance that makes the reactions

very slow, and (iii) reaction conditions are being worked out by trial and error method. Despite, the above drawbacks the ceramic method continues to exist for the exploratory synthesis of new mixed metal oxides even today. In our present study, we have extensively employed the ceramic method for the synthesis of new perovskite based layered oxides both by direct reactions (one pot) as well as multistep reactions where precursor oxides are initially synthesized and in subsequent stems they are reacted further to get the final target compound.

1.13 Objective of the Present Study

Besides the approaches that are already discussed in the previous sections, several other approaches have also been adopted toward the development of visible-light-active photocatalysts [94-118]. For tuning the band gap, besides, a metal/ non-metal ion doping and solid-solution formation, semiconductor heterojunction and oxide composites with graphene to form graphene-composites etc. have also been investigated [47, 94, 96, 99, 100, 102, 108-112]. Often, many of these systems have drawbacks with respect to high solution stability, resistance to photocorrosion and photoleaching, high efficiency and recyclability under visible-light/solar radiation. In quest for robust and efficient photocatalysts, research thrusts in single bulk semiconductors together with their nanostructured counterparts are in the rise. Among these, the perovskites constitute a major class both with the layered and three-dimensional (3D) structures. In this regard, the role of layered perovskites in visible-light driven photocatalytic activity is noteworthy.

A large body of research dealt with the formation and manipulation of layered perovskites for optimization and discovery of diverse properties including photocatalysis [35, 58-61, 74, 75, 79, 82, 119-127]. It is observed that many oxides and oxyhalides studied for visible-light photocatalysis contain Bi^{3+} [35, 48, 52, 58-61, 74, 75, 79, 82, 120-123, 133-137] and among them the Aurivillius phases are noteworthy [35, 58-61, 74, 75, 79, 82, 120-127]. Recognizing the effect of cation disorder in the stability of Aurivillius phases [138] and recent reports on importance of ferroelectricity in photocatalysis [139-141] we have undertaken a systematic exploration of La substitution in the four and five layer Aurivillius phases towards phase formation and its effect on structure, band gap and photocatalytic activity by way of dye degradation. This has further been extended to develop new series of

five-layer Aurivillius perovskites by both *A* and *B*-site co-substitution through cationic charge manipulation. Moreover, a strategy toward band gap alteration for developing new visible-light active semiconductors have been devised *via* intergrowth of Aurivillius oxides with Sillén oxyhalides forming a new series of hybrid layered perovskites. All the compounds were thoroughly characterized and their activities toward dye degradations were evaluated. Finally, for a better insight into the photocatalytic processes and mechanism of degradation detail studies involving energy level diagrams have been carried out. The outcomes of the present investigations are presented in subsequent chapters.

REFERENCES

1. Hoffmann, M. R.; Martin, S. T.; Choi, W.; Bahnemann, D. W. Environmental Applications of Semiconductor Photocatalysis. *Chem. Rev.* **1995**, *95*, 69-96.

2. Chen, X.; Shen, S.; Guo, L.; Mao, S. S. Semiconductor-Based Photocatalytic Hydrogen Generation. *Chem. Rev.* **2010**, *110*, 6503-6570.

3. Osterloh, F. E. Inorganic Materials as Catalysts for Photochemical Splitting of Water. *Chem. Mater.* **2008**, *20*, 35-54.

4. Kudo, A.; Miseki, Y. Heterogeneous Photocatalyst Materials for Water Splitting. *Chem. Soc. Rev.* **2009**, *38*, 253-278.

5. Ma, Y.; Wang, X.; Jia, Y.; Chen, X.; Han, H.; Li, C. Titanium Dioxide-Based Nanomaterials for Photocatalytic Fuel Generations. *Chem. Rev.* **2014**, *114*, 9987-10043

6. Chen, C.; Ma W.; Zhao, J. Semiconductor-mediated photodegradation of pollutants under visible-light irradiation. *Chem. Soc. Rev.* **2010**, *39*, 4206-4219.

7. Winter, M.; Brodd, R. J. What Are Batteries, Fuel Cells, and Supercapacitors ? *Chem. Rev.* **2004**, *104*, 4245-4269.

8. Kalogirou, S. A. Seawater desalination using renewable energy sources. *Prog. Energy Combust. Sci.* **2005**, *31*, 242-281.

9. Sinha, A. K.; Pradhan, M.; Sarkar, S.; Pal, T. Large-Scale Solid−State Synthesis of Sn−SnO_2Nanoparticles from Layered SnO by Sunlight: a Material for Dye Degradation in Water by Photocatalytic Reaction. *Environ. Sci. Technol.* **2013**, *47*, 2339−2345.

10. Subramanian, V.; Kamat, P. V.; Wolf, E. E. Mass−Transfer and Kinetic Studies during the Photocatalytic Degradation of an Azo Dye on Optically Transparent Electrode Thin Film. *Ind. Eng. Chem. Res.* **2003**, *42*, 2131−2138.

11. Dong, S.; Feng, J.; Fan, M.; Pi, Y.; Hu, L.; Han, X.; Liu, M.; Sun, J.; Sun, J. Recent Developments in Heterogeneous Photocatalytic Water Treatment using Visible Light Responsive Photocatalysts: A Review. *RSC Adv.* **2015**, *5*, 14610-14630.

12. Zhang, D.; Li, G.; Yu, J. C. Inorganic Materials for Photocatalytic Water Disinfection. *J. Mater. Chem.* **2010**, *20*, 4529-4536.

13. Rajeshwara, K.; Osugi, M. E.; Chanmanee, W.; Chenthamarakshan, C. R.; Zanoni, M. V. B. Kajitvichyanukul, P.; Ayer, R. K. Heterogeneous Photocatalytic Treatment of Organic Dyes in Air and Aqueous Media. *J. Photochem. Photobiol. C* **2008**, *9*, 171-192.

14. Forgacs, E.; Cserhati, T.; Oros, G. Removal of Synthetic Dyes from Wastewaters: a Review. *Environ. Int.* **2004**, *30*, 953-971.

15. Zhou, L.; Gao, C.; Xu, W. Magnetic Dendritic Materials for Highly Efficient Adsorption of Dyes and Drugs. *ACS Appl. Mater. Interfaces* 2010, *2*, 1483-1491.

16. Wang, W.; Tadé, M. O.; Shao, Z. Research Progress of Perovskite Materials in Photocatalysis- and Photovoltaics-Related Energy Conversion and Environmental Treatment. *Chem. Soc. Rev.* 2015, *44*, 5371-5408.

17. Chen, H.; Nanayakkara, C. E.; Grassian, V. H. Titanium Dioxide Photocatalysis in Atmospheric Chemistry. *Chem. Rev.* 2012, *112*, 5919-5948.

18. Aragay, G.; Pino, F.; Merkoçi, A. Nanomaterials for Sensing and Destroying Pesticides. *Chem. Rev.* 2012, *112*, 5317-5338.

19. Linsebigler, A. L.; Lu, G.; Yates, J. T. Photocatalysis on TiO_2 Surfaces: Principles, Mechanisms, and Selected Results. *Chem. Rev.* 1995, *95*, 735-758.

20. Kumar, S.; Khanchandani, S.; Thirumal, M.; Ganguli, A. K. Achieving Enhanced Visible-Light-Driven Photocatalysis Using Type-II $NaNbO_3$/CdS Core/Shell Heterostructures. *ACS Appl. Mater. Interfaces* **2014**, *6*, 13221-13233.

21. Chong, M. N.; Jin, B.; Chow, C. W. K.; Saint, C. Recent Developments in Photocatalytic Water Treatment Technology: A review. *Water Res.* **2010**, *44*, 2997-3027.

22. Kumar, S.; Surendar, T.; Baruah, A.; Shanker, V. Synthesis of a Novel and Stable g-C_3N_4–Ag_3PO_4 Hybrid Nanocomposite Photocatalyst and Study of the Photocatalytic Activity under Visible Light Irradiation. *J. Mater. Chem. A* **2013**, *1*, 5333-5340.

23. Takata, T.; Furumi, Y.; Shinohara, K.; Tanaka, A.; Hara, M.; Kondo, J. N.; Domen, K. Photocatalytic Decomposition of Water on Spontaneously Hydrated Layered Perovskites. *Chem. Mater.* **1997**, *9*, 1063-1064.

24. Ikeda, S.; Hara, M.; Kondo, J. N.; Domen, K.; Takahashi, H.; Okubo, T.; Kakihana, M. Preparation of $K_2La_2Ti_3O_{10}$ by Polymerized Complex Method and Photocatalytic Decomposition of Water. *Chem. Mater.* **1998**, *10*, 72-77.

25. Wang, Y.; Lai, X.; Lü, X.; Li, Y.; Liu, Q.; Lin, J.; Huang, F. Tailoring the Photocatalytic Activity of Layered Perovskites by Opening the Interlayer Vacancy via Ion-Exchange Reactions. *CrystEngComm* **2015**, *17*, 8703–8709.

26. Teshima, K.; Horita, K.; Suzuki, T.; Ishizawa, N.; Oishi, S. Flux Growth and Characterization of Layered $K_4Nb_6O_{17}$ Crystals. *Chem. Mater.* **2006**, *18*, 3693-3697.

27. Zhang, L.; Fu, H.; Zhang, C.; Zhu, Y. Effects of Ta^{5+} Substitution on the Structure and Photocatalytic Behavior of the $Ca_2Nb_2O_7$ Photocatalyst. *J. Phys. Chem. C* **2008**, *112*, 3126-3133.

28. Liang, S.; Shen, L.; Zhu, J.; Zhang, Y.; Wang, X.; Li, Z.; Wu, L.; Fu, X. Morphology-Controlled Synthesis and Efficient Photocatalytic Performances of a New Promising Photocatalyst $Sr_{0.25}H_{1.5}Ta_2O_6{\cdot}H_2O$. *RSC Adv.* **2011**, *1*, 458–467.

29. Xu, T.; Zhao, X.; Zhu, Y. Synthesis of Hexagonal $BaTa_2O_6$ Nanorods and Influence of Defects on the Photocatalytic Activity. *J. Phys. Chem. B* **2006**, *110*, 25825-25832.

30. Zou, Z.; Ye, J.; Sayama, K.; Arakawa, H. Direct Splitting of Water under Visible Light Irradiation with an Oxide Semiconductor Photocatalyst. *Nature* **2001**, *414*, 625-627.

31. Borgarello, E.; Kiwi, J.; Grätzel, M.; Pelizzetti, E.; Visca, M. Visible Light Induced Water Cleavage in Colloidal Solutions of Chromium-Doped Titanium Dioxide Particles. *J. Am. Chem. Soc.* **1982**, **104**, 2996-3002.

32. Liu, J.; Chen, G.; Lia, Z.; Zhang, Z. Electronic Structure and Visible Light Photocatalysis Water Splitting Property of Chromium-Doped $SrTiO_3$. *J. Solid State Chem.* **2006**, *179*, 3704-3708.

33. Hwang, D. W.; Kim, H. G.; Lee, J. S.; Kim, J.; Li, W.; Oh, S. H. Photocatalytic Hydrogen Production from Water over M-Doped $La_2Ti_2O_7$ (M = Cr, Fe) under Visible Light Irradiation (λ>420 nm). *J. Phys. Chem. B* **2005**, *109*, 2093-2102.

34. Wang, B.; Li, C.; Hirabayashi, D.; Suzuki, K. Hydrogen Evolution by Photocatalytic Decomposition of Water under Ultraviolet–Visible Irradiation over $K_2La_2Ti_{3-x}M_xO_{10+\delta}$ Perovskite. *Int. J. Hydrogen Energy* **2010**, *35*, 3306-3312.

35. Zhang, H.; Chen, G.; Li, X. Synthesis and Visible Light Photocatalysis Water Splitting Property of Chromium-Doped $Bi_4Ti_3O_{12}$. *Solid State Ionics* **2009**, *180*, 1599-1603.

36. Shimodaira, Y.; Kato, H.; Kobayashi, H.; Kudo, A. Investigations of Electronic Structures and Photocatalytic Activities under Visible Light Irradiation of Lead Molybdate Replaced with Chromium (VI). *Bull. Chem. Soc. Jpn.* **2007**, *80*, 885-893.

37. Kasahara, A.; Nukumizu, K.; Takata, T.; Kondo, J. N.; Hara, M.; Kobayashi, H.; Domen, K. $LaTiO_2N$ as a Visible-Light (≤600 nm)-Driven Photocatalyst. *J. Phys. Chem. B* **2003**, *107*, 791-797.

38. Zou, F.; Jiang, Z.; Qin, X.; Zhao, Y.; Jiang, L.; Zhi, J.; Xiao, T.; Edwards, P. P. Template-Free Synthesis of Mesoporous N-Doped $SrTiO_3$ Perovskite with High Visible-Light-Driven Photocatalytic Activity. *Chem. Commun.* **2012**, *48*, 8514–8516.

39. Ji, S. M.; Borse, P. H.; Kim, H. G.; Hwang, D. W.; Jang, J. S.; Bae, S. W.; Lee, J. S. Photocatalytic Hydrogen Production from Water–Methanol Mixtures using N-Doped $Sr_2Nb_2O_7$ under Visible Light Irradiation: Effects of Catalyst Structure. *Phys. Chem. Chem. Phys.* **2005**, *7*, 1315-1321.

40. Jiang, L.; Wang, Q.; Li, C.; Yuan, J.; Shangguan, W. ZrW_2O_8 Photocatalyst and Its Visible-Light Sensitization via Sulfur Anion Doping for Water Splitting. *Int. J. Hydrogen Energy* **2010**, *35*, 7043-7050.

41. Sasikala, R.; Shirole, A. R.; Sudarsan, V.; Sudakar, C.; Naik, R.; Rao, R.; Bharadwaj, S. R. Enhanced Photocatalytic Activity of Indium and Nitrogen Co-Doped TiO_2–Pd Nanocomposites for Hydrogen Generation. *Appl. Catal. A* **2010**, *377*, 47-54.

42. Luan, J.; Zou, Z.; Lu, M.; Chen, Y. Structural, Optical and Photocatalytic Properties of New

Solid Photocatalysts, $Bi_xIn_{1-x}TaO_4(0 < x < 1)$. *Mater. Chem. Phys.* **2006**, *98*, 434-441.

43. Wang, D.; Kako, T.; Ye, J. Efficient Photocatalytic Decomposition of Acetaldehyde over a Solid-Solution Perovskite $(Ag_{0.75}Sr_{0.25})(Nb_{0.75}Ti_{0.25})O_3$ under Visible-Light Irradiation. *J. Am. Chem. Soc.* **2008**, *130*, 2724-2725.

44. Maeda, K.; Takata, T.; Hara, M.; Saito, N.; Inoue, Y.; Kobayashi, H.; Domen, K. GaN:ZnO Solid Solution as a Photocatalyst for Visible-Light-Driven Overall Water Splitting. *J. Am. Chem. Soc.* **2005**, *127*, 8286-8287.

45. Houlding, V. H.; Gratzel, M. Photochemical H_2 Generation by Visible Light. Sensitization of TiO_2 Particles by Surface Complexation with 8-Hydroxyquinoline. *J. Am. Chem. Soc.* **1983**, *105*, 5695-5696.

46. Chowdhury, P.; Moreira, J.; Gomaa, H.; Ray, A. K. Visible-Solar-Light-Driven Photocatalytic Degradation of Phenol with Dye-Sensitized TiO_2: Parametric and Kinetic Study. *Ind. Eng. Chem. Res.* **2012**, *51*, 4523−4532.

47. Vinu, R.; Polisetti, S.; Madras, G. Dye Sensitized Visible Light Degradation of Phenolic Compounds. *Chem. Eng. J.* **2010**, *165*, 784–797.

48. Kudo, A.; Omori, K.; Kato, H. A Novel Aqueous Process for Preparation of Crystal Form-Controlled and Highly Crystalline $BiVO_4$ Powder from Layered Vanadates at Room Temperature and Its Photocatalytic and Photophysical Properties *J. Am. Chem. Soc.* **1999**, *121*, 11459-11467.

49. Zhang, X.; Ai, Z.; Jia, F.; Zhang, L.; Fan, X.; Zou, Z. Selective Synthesis and Visible-Light Photocatalytic Activities of $BiVO_4$ with Different Crystalline Phases. *Mater. Chem. Phys.* **2007**, *103*, 162-167.

50. Zhou, L.; Wang, W.; Liu, S.; Zhang, L.; Xu, H.; Zhu, W. A Sonochemical Route to Visible-Llight-Driven High-Activity $BiVO_4$ Photocatalyst. *J. Mol. Catal. A: Chem.* **2006**, *252*, 120-124.

51. Zhou, L.; Wang, W.; Zhang, L.; Xu, H.; Zhu, W. Single-Crystalline $BiVO_4$ Microtubes with Square Cross-Sections: Microstructure, Growth Mechanism, and Photocatalytic Property. *J. Phys. Chem. C* **2007**, *111*, 13659-13664.

52. Kohtani, S.; Hiro, J.; Yamamoto, N.; Kudo, A.; Tokumura, K.; Nakagaki, R. Adsorptive and Photocatalytic Properties of Ag-Loaded $BiVO_4$ on the Degradation of 4-n-Alkylphenols under Visible Light Irradiation. *Catal. Commun.* **2005**, *6*, 185-189.

53. Yin, J.; Zou, Z.; Ye, J. Photophysical and Photocatalytic Properties of New Photocatalysts $MCrO_4$ (M = Sr, Ba). *Chem. Phys. Lett.* **2003**, *378*, 24-28.

54. Maeda, K.; Domen, K. New Non-Oxide Photocatalysts Designed for Overall Water Splitting under Visible Light. *J. Phys. Chem. C* **2007**, *111*, 7851-7861.

55. Williams, R. Becquerel Photovoltaic Effect in Binary Compounds. *J. Chem. Phys.* **1960**, *32*, 1505-1514.

56. Ellis, A. B.; Kaiser, S. W.; Bolts, J. M.; Wrighton, M. S. Study of n-Type Semiconducting Cadmium Chalcogenide-Based Photoelectrochemical Cells Employing Polychalcogenide Electrolytes. *J. Am. Chem. Soc.* **1977**, *99*, 2839-2848.

57. Darwent, J. R.; Mills, A. Photo-Oxidation of Water Sensitized by WO_3 Powder. *J. Chem. Soc., Faraday Trans. 2* **1982**, *78*, 359-367.

58. Kim, H. G.; Hwang, D. W.; Lee, J. S. An Undoped, Single-Phase Oxide Photocatalyst Working under Visible Light. *J. Am. Chem. Soc.* **2004**, *126*, 8912-8913.

59. Tang, J.; Zou, Z.; Ye, J. Photocatalytic Decomposition of Organic Contaminants by Bi_2WO_6 under Visible Light Irradiation. *Catal. Lett.* **2004**, *92*, 53-56.

60. Zhang, L.; Man, Y.; Zhu, Y. Effects of Mo Replacement on the Structure and Visible-Light-Induced Photocatalytic Performances of Bi_2WO_6 Photocatalyst. *ACS Catal.* 2011, 1, 841-848.

61. Jang, J. S.; Yoon, S. S.; Borse, P. H.; Lim, K. T.; Hong, T. E.; Jeong, E. D.; Jung, O.-S.; Shim, Y. B.; Kim, H. G. Synthesis and Characterization of Aurivillius Phase $Bi_5Ti_3FeO_{15}$

Layered Perovskite for Visible Light Photocatalysis. *J. Ceram. Soc. Jpn.* **2009**, *117*, 1268-1272.

62. Tang, J.; Zou, Z.; Ye, J. Efficient Photocatalytic Decomposition of Organic Contaminants over $CaBi_2O_4$ under Visible-Light Irradiation. *Angew. Chem., Int. Ed.* **2004**, *43*, 4463-4466.

63. Zhou, L.; Yu, M.; Yang, J.; Wang, Y.; Yu, C. Nanosheet-Based $Bi_2Mo_xW_{1-x}O_6$ Solid Solutions with Adjustable Band Gaps and Enhanced Visible-Light-Driven Photocatalytic Activities. *J. Phys. Chem. C* **2010**, *114*, 18812-18818.

64. Fu, H.; Zhang, S.; Xu, T.; Zhu, Y.; Chen, J. Photocatalytic Degradation of RhB by Fluorinated Bi_2WO_6 and Distributions of the Intermediate Products. *Environ. Sci. Technol.* **2008**, *42*, 2085-2091.

65. Lin, X.; Huang, T.; Huang, F.; Wangac, W.; Shi, J. Photocatalytic activity of a Bi-based oxychloride Bi_4NbO_8Cl. *J. Mater. Chem.* **2007**, *17*, 2145-2150.

66. Shan, Z.; Lin, X.; Liu, M.; Ding, H.; Huang, F. A Bi-based Oxychloride $PbBiO_2Cl$ as a Novel Efficient Photocatalyst. *Solid State Sciences* **2009**, *11*, 1163-1169.

67. Shan, Z.; Wang, W.; Lin, X.; Ding, H.; Huang, F. Photocatalytic Degradation of Organic Dyes on Visible-Light Responsive Photocatalyst $PbBiO_2Br$. *J. Solid State Chem.* **2008**, *181*, 1361-1366.

68. Royer, S.; Duprez, D.; Can, F.; Courtois, X.; Dupeyrat, C. B.; Laassiri, S.; Alamdari, H. Perovskites as Substitutes of Noble Metals for Heterogeneous Catalysis: Dream or Reality. *Chem. Rev.* **2014**, *114*, 10292-10368.

69. Mitchell, R. H., *Perovskites: Modern and Ancient*; Almaz Press: Thunder Bay, Canada. (**2002**).

70. Aurivillius, B. Mixed Bismuth Oxides with Layer Lattices. I. Structure Type of $CaCb_2Bi_2O_9$. *Ark. Kemi* **1949**, *1*, 463; Aurivillius, B. Mixed Oxides with Layer Lattices. III. Structure of $BaBi_4Ti_4O_{15}$. *Ark. Kemi*, **1950**, *2*, 519.

71. Ruddlesden, S. N.; Popper, P. New Compounds of the K_2NiF_4 Type. *Acta. Crystallogr.* **1957**, *10*, 538-539; Ruddlesden, S. N.; Popper, P. The Compound $Sr_3Ti_2O_7$ and Its Structure. *Acta. Crystallogr.* **1958**, *11*, 54-55.

72. Dion, M.; Ganne, M.; Tournoux, M. Nouvells Familles De Phases $M^IM^{II}_2Nb_3O_{10}$ a Feuillets "Perovskites". *Mater. Res. Bull.* **1981**, *16*, 1429-1435; Jacobson, A. J.; Johnson, J. W.; Lewandowski, J. T. Interlayer Chemistry between Thick Transition-Metal Oxide Layers: Synthesis and Intercalation Reactions of $K[Ca_2Na_{x-3}Nb_xO_{3n+1}]$ ($3 \leq n \leq 7$). *Inorg. Chem.* **1985**, *24*, 3727-3729.

73. Gopalakrishnan, J.; Sivakumar, T.; Ramesha, K.; Thangadurai, V.; Subbanna, G. N. Transformations of Ruddlesden-Popper Oxides to New Layered Perovskite Oxides by Metathesis Reactions. *J. Am. Chem. Soc.* **2000**, 122, 6237-6241.

74. Kudo, A.; Hijii, S. H_2 or O_2 Evolution from Aqueous Solution on Layered Oxide Photocatalysts Consisting of Bi^{3+} with $6s^2$ Configuration and d^0 Transition Metal Ions. *Chem. Lett.* **1999**, *28*, 1103-1104.

75. Shimodaira, Y.; Kato, H.; Kobayashi, H.; Kudo, A. Photophysical Properties and Photocatalytic Activities of Bismuth Molybdates under Visible Light Irradiation. *J. Phys. Chem. B* **2006**, *110*, 17790-17797.

76. Zhou, L.; Yu, M.; Yang, J.; Wang, Y.; Yu, C. Nanosheet-Based $Bi_2Mo_xW_{1-x}O_6$ Solid Solutions with Adjustable Band Gaps and Enhanced Visible-Light-Driven Photocatalytic Activities. *J. Phys. Chem. C* **2010**, *114*, 18812-18818.

77. Zhang, L.; Man, Y.; Zhu, Y. Effects of Mo Replacement on the Structure and Visible-Light-Induced Photocatalytic Performances of Bi_2WO_6 Photocatalyst. *ACS Catal.* **2011**, *1*, 841-848.

78. Kim, H. G.; Hwang, D. W.; Lee, J. S. An Undoped, Single-Phase Oxide Photocatalyst Working under Visible Light. *J. Am. Chem. Soc.* **2004**, *126*, 8912-8913.

79. Muktha, B.; Priya, M. H.; Madras, G.; Guru Row, T. N. Synthesis, Structure, and Photocatalysis in a New Structural Variant of the Aurivillius Phase: $LiBi_4M_3O_{14}$ (M = Nb, Ta). *J. Phys. Chem. B* **2005**, *109*, 11442-11449.

80. Li, J.-B.; Huang, Y. P.; Rao, G. H.; Liu, G. Y.; Luo, J.; Chen, J. R.; Liang, J. K. Ferroelectric Transition of Aurivillius Compounds $Bi_5Ti_3FeO_{15}$ and $Bi_6Ti_3Fe_2O_{18}$. *Appl. Phys. Lett.* **2010**, *96*, 222903-222905.

81. Nakashima, S.; Fujisawa, H.; Ichikawa, S.; Park, J. M.; Kanashima, T.; Okuyama, M.; Simizu, M. Structural and Ferroelectric Properties of Epitaxial $Bi_5Ti_3FeO_{15}$ and Natural-Superlattice-Structured $Bi_4Ti_3O_{12}$−$Bi_5Ti_3FeO_{15}$ Thin Films. *J. Appl. Phys.* **2010**, *108*, 074106-074110.

82. Sun, S.; Wang, W.; Xu, H.; Zhou, L.; Shang, M.; Zhang, L. $Bi_5FeTi_3O_{15}$ Hierarchical Microflowers: Hydrothermal Synthesis, Growth Mechanism, and Associated Visible-Light-Driven Photocatalysis. *J. Phys. Chem. C* **2008**, *112*, 17835-17843.

83. Jang, J. S.; Yoon, S. S.; Borse, P. H.; Lim, K. T.; Hong, T. E.; Jeong, E. D.; Jung, O.-S.; Shim, Y. B.; Kim, H. G. Synthesis and Characterization of Aurivillius Phase $Bi_5Ti_3FeO_{15}$ Layered Perovskite for Visible Light Photocatalysis. *J. Cer. Soc. Jpn.* **2009**, *117*, 1268-1272.

84. Bai, W.; Xu, W. F.; Wu, J.; Zhu, J. Y.; Chen, G.; Yang, J.; Lin, T.; Meng, X. J.; Tang, X. D.; Chu, J. H. Investigations on Electrical, Magnetic and Optical Behaviors of Five-Layered Aurivillius $Bi_6Ti_3Fe_2O_{18}$ Polycrystalline Films. *Thin Solid Films* **2012**, *525*, 195-199.

85. Prasad, N. V.; Kumar, G. S. Magnetic and Magnetoelectric Measurements on Rare-Earth-Substituted Five-Layered $Bi_6Fe_2Ti_3O_{18}$ Compound. *J. Magn. Magn. Mater.* **2000**, *213*, 349-356.

86. Prasad, N. V.; Kumar, G. S. Low Temperature Magnetoelectric Measurements on Rare Earth Substituted Bismuth Layered Structure Ferroelectromagnetic Ceramic. *Mater. Sci. Eng. B* **2004**, *108*, 194-199.

87. Ackerman, J. F. The Structures of Bi_3PbWO_8Cl and Bi_4NbO_8Cl and the Evolution of the Bipox Structure Series. *J. Solid State Chem.* **1986**, *62*, 92-104.

88. Ketterer, J.; Krämer, V. Structural Characterization of the Synthetic Perites $PbBiO_2X$, X = I, *Mater. Res. Bull* **1985**, *20*, 1031-1036.

89. Lin, X.; Huang, T.; Huang, F.; Wang, W.; Shi, J. Photocatalytic Activity of a Bi-Based Oxychloride Bi_4NbO_8Cl. *J. Mater. Chem.* **2007**, *17*, 2145–2150.

90. Kusainova, A. M.; Lightfoot, P.; Zhou, W.; Stefanovich, S. Y.; Mosunov, A. V.; Dolgikh, V. A. Ferroelectric Properties and Crystal Structure of the Layered Intergrowth Phase $Bi_3Pb_2Nb_2O_{11}Cl$. *Chem. Mater.* **2001**, *13*, 4731-4737.

91. Kusainova, A. M.; Stefanovich, S. Y.; Irvine, J. T. S.; Lightfoot, P. Structure–Property Correlations in the New Ferroelectric $Bi_5PbTi_3O_{14}Cl$ and Related Layered Oxyhalide Intergrowth Phases. *J. Mater. Chem.* **2002**, *12*, 3413-3418.

92. Liu, S.; Miiller, W.; Liu, Y.; Avdeev, M.; Ling, C. D. Sillen−Aurivillius Intergrowth Phases as Templates for Naturally Layered Multiferroics. *Chem. Mater.* **2012**, *24*, 3932-3942.

93. West, A. R. Solid State Chemistry and Its Applications. Wiley Publishers, **2011**.

94. Khanchandani, S.; Kundu, S.; Parta, A.; Ganguli, A. K. Shell Thickness Dependent Photocatalytic Properties of ZnO/CdS Core−Shell Nanorods. *J. Phys. Chem. C* **2012**, *116*, 23653-23662.

95. Sayed, F. N.; Grover, V.; Mandal, B. P.; Tyagi, A. K. Influence of La^{3+} Substitution on Electrical and Photocatalytic Behavior of Complex $Bi_2Sn_2O_7$ Oxides. *J. Phys. Chem. C* **2013**, *117*, 10929-10938.

96. Satyapaul; Singh, A.; Madras, G. Photocatalytic degradation with combustion synthesized WO_3 and WO_3/TiO_2 mixed oxides under UV and visible light. Sep. Pur. Tech. **2013**, *105*, 79-89.

97. Jacob, N. M.; Madras, G.; Kottam, N.; Thomas, T. Multivalent Cu-Doped ZnO Nanoparticles with Full Solar Spectrum Absorbance and Enhanced Photoactivity. *Ind. Eng. Chem. Res.* **2014**, *53*, 5895-5904.

98. Eraiah, R. K.; Madras, G. Metal–metal charge transfer and interfacial charge transfer mechanism for the visible light photocatalytic activity of cerium and nitrogen co-doped TiO_2. *J. Sol-Gel Sci. Technol.* **2014**, *71*, 193–203.

99. Khanchandani, S.; Srivastava, P. K.; Kumar, S.; Ghosh, S.; Ganguli, A. K. Band Gap Engineering of ZnO using Core/Shell Morphology with Environmentally Benign Ag_2S Sensitizer for Efficient Light Harvesting and Enhanced Visible-Light Photocatalysis. *Inorg. Chem.* **2014**, *53*, 8902-8912.

100. Basu, N.; Garg, N.; Ganguli, A. K. A type-II semiconductor (ZnO/CuS heterostructure) for visible light photocatalysis. *J. Mater. Chem. A* **2014**, *2*, 7517-7525.

101. Bhattacharyya, K.; Majeed, J.; Dey, K. K.; Ayyub, P.; Tyagi, A. K.; Bharadwaj, S. R. Effect of Mo-Incorporation in the TiO_2 Lattice: A Mechanistic Basis for Photocatalytic Dye Degradation. *J. Phys. Chem. C*, **2014**, *118*, 15946-15962.

102. Singh, A.; Dutta, D. P.; Ballal, A.; Tyagi, A. K.; Fulekar, M. H. Visible light driven photocatalysis and antibacterial activity of $AgVO_3$ and $Ag/AgVO_3$ nanowires. *Mater. Res. Bull.* **2014**, *51*, 447-454.

103. Dutta, D. P.; Singh, A.; Tyagi, A. K. Ag doped and Ag dispersed nano $ZnTiO_3$: Improved photocatalytic organic pollutant degradation under solar irradiation and antibacterial activity. *J. Env. Chem. Eng.* **2014**, *2*, 2177-2187.\

104. Sayed, F. N.; Sasikala, R.; Jayakumar, O. D.; Rao, R.; Betty, C. A.; Chokkalingam, A.; Kadam, R. M.; Jagannath; Bharadwaj, S. R.; Vinu, A.; Tyagi, A. K. Photocatalytic hydrogen generation from water using a hybrid of graphene nanoplatelets and self doped TiO_2–Pd. *RSC Adv.* **2014**, 4, 13469-13476.

105. Fulekar, M. H.; Singh, A.; Dutta, D. P.; Roy, M.; Ballal, A.; Tyagi, A. K. Ag incorporated nano $BiPO_4$: sonochemical synthesis, characterization and improved visible light photocatalytic properties. *RSC Adv.* **2014**, 4, 10097-10107.

106. Roy, N.; Park, Y.; Sohn, Y.; Leung, K. T.; Pradhan, D. Green Synthesis of Anatase TiO_2 Nanocrystals with Diverse Shapes and their Exposed Facets-Dependent Photoredox Activity. *ACS Appl. Mater. Interfaces* **2014**, *6*, 16498-16507.

107. Roy, N.; Sohn, Y.; Leung, K. T.; Pradhan, D. Engineered Electronic States of Transition Metal Doped TiO_2 Nanocrystals for Low Overpotential Oxygen Evolution Reaction. *J. Phys. Chem. C* **2014**, *118*, 29499−29506.

108. Sharma, M.; Ojha, K.; Ganguly, A.; Ganguli, A. K. Ag_3PO_4 nanoparticle decorated on SiO_2 spheres for efficient visible light photocatalysis, *New J. Chem.* **2015**, *39*, 9242-9248.

109. Adhikari, S.; Sarkar, D.; Madras, G. Highly efficient WO_3–ZnO mixed oxides for Photocatalysis. *RSC Adv.* **2015**, 5, 11895-11904.

110. Rao, N. K.; Eswar; Ramamurthy, P. C.; Madras, G. Enhanced sunlight photocatalytic activity of Ag_3PO_4 decorated novel combustion synthesis derived TiO_2 nanobelts for dye and bacterial degradation. *Photochem. Photobiol. Sci.* **2015**, *14*, 1227-1237.

111. Rao, N. K.; Eswar; Ramamurthy, P. C.; Madras, G. High photoconductive combustion synthesized TiO_2 derived nanobelts for photocatalytic water purification under solar irradiation *New J. Chem.* **2015**, *39*, 6040-6051.

112. Rao, N. K.; Eswar; Katkar, V. V.; Ramamurthy, P. C.; Madras, G. Novel AgBr/Ag_3PO_4 Decorated Ceria Nanoflake Composites for Enhanced Photocatalytic Activity toward Dyes and Bacteria under Visible Light. *Ind. Eng. Chem. Res.* **2015**, *54*, 8031-8042.

113. Joshi, U. A.; Maggard, P. A. $CuNb_3O_8$: A p-Type Semiconducting Metal Oxide Photoelectrode *J. Phys. Chem. Lett.* **2012**, *3*, 1577−1581.

114. Sullivan, I.; Sahoo, P. P.; Fuoco, L.; Hewitt, A. S.; Stuart, S.; Dougherty, D.; Maggard, P. A. Cu-Deficiency in the p-Type Semiconductor $Cu_{5-x}Ta_{11}O_{30}$: Impact on Its Crystalline Structure, Surfaces, and Photoelectrochemical Properties. *Chem. Mater.* **2014**, *26*, 6711−6721.

115. Saha, D.; Madras, G.; Guru Row, T. N. Synthesis and structure of $Bi_2Ce_2O_7$: a new compound exhibiting high solar photocatalytic activity. *Dalton Trans.* **2012**, *41*, 9598-9600.

116. Sharma, V. M.; Saha, D.; Madras, G.; Guru Row, T. N. Synthesis, structure, characterization and photocatalytic activity of $Bi_2Zr_2O_7$ under solar radiation. *RSC Adv.* **2013**, *3*, 18938-18943.

117. Uma, S.; Singh, J.; Thakral, V. Facile Room Temperature Ion-Exchange Synthesis of Sn^{2+} Incorporated Pyrochlore-Type Oxides and Their Photocatalytic Activities. *Inorg. Chem.* **2009**, *48*, 11624–11630.

118. Singh, J.; Uma, S. Efficient Photocatalytic Degradation of Organic Compounds by Ilmenite $AgSbO_3$ under Visible and UV Light Irradiation. *J. Phys. Chem. C* **2009**, *113*, 12483–12488.

119. Wang, B.; Li, C.; Hirabayashi, D.; Suzuki, K. Hydrogen Evolution by Photocatalytic Decomposition of Water under Ultraviolet–Visible Irradiation over $K_2La_2Ti_{3-x}M_xO_{10+\delta}$ Perovskite. *Int. J. Hydrogen Energy* **2010**, *35*, 3306-3312.

120. Singh, A.; Dutta, D. P.; Roy, M.; Tyagi, A. K.; Fulekar, M. H. Sonochemical synthesis, characterization, and photocatalytic properties of $Bi_{2-2x}Sb_xWO_6$ nanorods, *J. Mater. Sci.* **2014**, *49*, 2085-2097.

121. Dutta, D. P.; Tyagi, A. K. Facile sonochemical synthesis of Ag modified $Bi_4Ti_3O_{12}$ nanoparticles with enhanced photocatalytic activity under visible light. *Mater. Res. Bull.* **2016**, *74*, 397-407.

122. Tang, J.; Zou, Z.; Ye, J. Photocatalytic Decomposition of Organic Contaminants by Bi_2WO_6 under Visible Light Irradiation. *Catal. Lett.* **2004**, *92*, 53-56.

123. Fu, H.; Pan, C.; Yao, W.; Zhu, Y. Visible-Light-Induced Degradation of Rhodamine B by Nanosized Bi_2WO_6. *J. Phys. Chem. B* **2005**, *109*, 22432-22439.

124. Mann, A. K. P.; Steinmiller, E. M. P.; Skrabalak, S. E. Elucidating the Structure-Dependent Photocatalytic Properties of Bi_2WO_6: A Synthesis Guided Investigation. *Dalton Trans.* **2012**, *41*, 7939-7945.

125. Martínez-de la Cruz, A.; Alfaro, S. O.; Cuellar, E. L.; Méndez, U. O. Photocatalytic Properties of Bi_2MoO_6 Nanoparticles Prepared by an Amorphous Complex Precursor. *Catal. Today*, **2007**, *129*, 194-199.

126. Zhou, L.; Yu, M.; Yang, J.; Wang, Y. Yu, C. Nanosheet-Based $Bi_2Mo_xW_{1-x}O_6$ Solid Solutions with Adjustable Band Gaps and Enhanced Visible-Light-Driven Photocatalytic Activities. *J. Phys. Chem. C* **2010**, *114*, 18812-18818.

127. Kim, H. G.; Borse, P. H.; Jang, J. S.; Jeong, E. D.; Lee, J. S. Enhanced Photochemical Properties of Electron Rich W-Doped $PbBi_2Nb_2O_9$ Layered Perovskite Material under Visible-Light Irradiation. *Mater. Lett.* **2008**, *62*, 1427-1430.

128. Yoshimura, J.; Ebana, Y.; Kondo, J.; Domen, K.; Tanaka, A. Visible Light Induced Photocatalytic Behavior of a Layered Perovskite Type Niobate, $RbPb_2Nb_3O_{10}$. *J. Phys. Chem.* **1993**, *97*, 1970-1973.

129. Arney, D.; Maggard, P. A. Effect of Platelet-Shaped Surfaces and Silver-Cation Exchange on the Photocatalytic Hydrogen Production of $RbLaNb_2O_7$. *ACS Catal.* **2012**, *2*, 1711-1717.

130. Boltersdorf, J.; Maggard, P. A. Silver Exchange of Layered Metal Oxides and Their Photocatalytic Activities. *ACS Catal.* **2013**, *3*, 2547-2555.

131. Kumar, V.; Govind; Uma, S.; Investigation of cation (Sn^{2+}) and anion (N^{3-}) substitution in favor of visible light photocatalytic activity in the layered perovskite $K_2La_2Ti_3O_{10}$. *J. Hazard. Mater.* **2011**, *189*, 502–508.

132. Schaak, R. E.; Mallouk, T. E. Perovskites by Design: A Toolbox of Solid-State Reactions. *Chem. Mater.* **2002**, *14*, 1455-1471.

133. Tokunaga, S.; Kato, H.; Kudo, A. Selective Preparation of Monoclinic and Tetragonal $BiVO_4$ with Scheelite Structure and Their Photocatalytic Properties. *Chem. Mater.* **2001**, *13*, 4624-4628.

134. Oshikiri, M.; Boero, M.; Ye, J.; Zou, Z.; Kido, G. Electronic Structures of Promising Photocatalysts $InMO_4$ (M = V, Nb, Ta) and $BiVO_4$ for Water Decomposition in the Visible Wavelength Region. *J. Chem. Phys.* **2002**, *117*, 7313-7318.

135. Kim, W. J.; Pradhan, D.; Min, B.-K.; Sohn, Y. Adsorption/photocatalytic activity and fundamental natures of BiOCl and $BiOCl_xI_{1-x}$ prepared in water and ethylene glycol environments, and Ag and Au-doping effects. *Appl. Cat. B: Env.* **2014**, *147*, 711-725.

136. Na, Y.; Kim, Y.-I.; Cho, D. W.; Pradhan, D.; Sohn, Y. Adsorption/photocatalytic performances of hierarchical flowerlike $BiOBr_xCl_{1-x}$ nanostructures for methyl orange, Rhodamine B and methylene blue. *Mater. Sci. Semicond. Process.* **2014**, *27*, 181-190.

137. Thakral, V.; Uma, S. Investigation of visible light photocatalytic behavior of $Bi_4V_2O_{11-\delta}$ and BIMEVOX (ME = Al, Ga) oxides. *Mater. Res. Bull.* **2010**, *45*, 1250–1254.

138. Hervoches, C. H.; Lightfoot, P. Cation Disorder in Three-Layer Aurivillius Phases: Structural Studies of $Bi_{2-x}Sr_{2+x}Ti_{1-x}Nb_{2+x}O_{12}$ ($0 < x < 0.8$) and $Bi_{4-x}La_xTi_3O_{12}$ ($x = 1$ and 2). *J. Solid State Chem.* **2000**, *153*, 66-73.

139. Cui, Y.; Briscoe, J.; Dunn, S. Effect of Ferroelectricity on Solar-Light-Driven Photocatalytic Activity of $BaTiO_3$-Influence on the Carrier Separation and Stern Layer Formation. *Chem. Mater.* **2013**, *25*, 4215-4223.

140. Li, L.; Salvador, P. A.; Rohrer, G. S. Photocatalysts with Internal Electric Fields. *Nanoscale* **2014**, *6*, 24-42.

141. Grinberg, I.; West, D. V.; Torres, M.; Gou, G.; Stein, D. M.; Wu, L.; Chen, G.; Gallo, E. M.; Akbashev, A. R.; Davis, P. K.; Spanier, J. E.; Rappe, A. M. Perovskite Oxides for Visible-Light-Absorbing Ferroelectric and Photovoltaic Materials. *Nature* **2013**, *503*, 509-512.

CHAPTER -2

Characterization Techniques

Characterization Techniques

All the synthesized metal oxides and oxyhalides reported in the present study were thoroughly characterized using a variety of analytical techniques. These include powder X-ray diffraction (PXD), field-emission scanning electron microscopy (FE-SEM), energy dispersive X-ray spectroscopy (EDS), transmission electron microscopy (TEM), selected area electron diffraction (SAED), UV-visible diffuse reflectance spectroscopy (UV-vis DRS), photoluminescence (PL) spectroscopy and ζ-potential measurements. The photocatalytic dye degradations were monitored with the help of absorption measurements using UV−visible spectrophotometer. A brief description of the above mentioned analytical techniques, sample preparation and methods of analysis have been discussed in this chapter.

2.1 Powder X-ray Diffraction (PXD)

PXD is the most widely used technique for characterization of solid compounds. It is a non-destructive technique useful for the differentiation of crystalline and amorphous compounds, identification of phase purity (each crystalline compound has its own characteristic PXD pattern) and determination of crystal structure of compounds. The diffraction from a three dimensional periodic structure, such as atoms in a crystal is described by Bragg's diffraction law. When monochromatic X-rays fall on crystalline compounds possessing long range order (periodicity) constructive or destructive interference take place. Constructive interference occurs when the Bragg's condition as given in equation (2.1) is satisfied.

$$n\lambda = 2dSin\theta \tag{2.1}$$

where n is an integer known as the order of diffraction, λ refers to the wavelength of X-ray, d stands for interplanar distance and θ is the diffraction angle [1].

In the present work, PXD measurements were carried out using a Bruker AXS D8 Advance diffractometer operating at 40 kV and 30 mA with graphite monochromatized CuK_α (1.5406 Å) radiation in the angular range 5−90°. The software DIFFRAC^{plus} and EVA$^{®}$ were used for input instrumental parameters and data evaluation, respectively. For

PXD analysis, nearly 1 g of powder sample was placed in sample holder and leveled the sample surface with a gentle press by a glass slide.

The phase purity of the synthesized compounds was ascertained by comparing the observed diffraction pattern with the standard PDFs available in the JCPDS (Joint Committee on Powder Diffraction Standards) database. Indexing of the PXD patterns and least-squares refinement of lattice parameters were carried out using the PROSZKI program [2]. The PXD pattern simulations were carried out by the POWDERCELL program [3] using the refined lattice parameters. The positional, thermal and occupancy parameters were used from reference structural models. For changes in cation distribution and occupancy appropriate adjustments were made as per the compositions.

For Rietveld refinements, the PXD data were collected in 10-90° angular range at 40 kV and 30 mA with a data collection time 6 h. For the refinement runs, first the background coefficients along with zero-shift and cell parameters were refined. In the subsequent runs, the profile and shape parameters were refined. In case, where the program diverged, the profile and shape parameters were refined one by one. The positional and thermal parameters were refined in the later stages of the refinement by systematically starting with heavier atoms first and the lighter atoms toward the end. Moreover, to avoid divergence, the thermal parameters of oxygen were fixed to the value reported for the model system. Finally the cation disorder was examined by using the refined position and thermal parameters and refining the varying occupancy of the atoms.

2.2 Field-Emission Scanning Electron Microscopy and Energy Dispersive X-ray Spectroscopy (FE-SEM and EDS)

FE-SEM is the most versatile and widely utilized electron microscopic technique for the determination of morphology and composition of solid samples [4, 5]. In this technique, a focused beam of high energy electron is used to scan the sample to generate an image and analyze the specimen. The interaction of the electron beam with the sample generates secondary electrons, backscattered electrons, characteristic X-rays and optical radiation in addition to many other signals. The secondary electrons are used to produce the image of the sample. The resolution and magnification in the SEM is far higher than optical microscope due to the utilization of short wavelength electron beam in SEM. The emitted X-rays can

give two types of information; (1) qualitative information by measuring the energy of each characteristic X-rays generated from the elements present in the sample and (2) quantitative information by measuring the intensity of X-rays emitted by each element present in the sample.

In present work, morphological studies of the samples were investigated with the aid of a Zeiss FE-SEM, Ultra plus55, operating at an accelerating voltage of 20 kV. The elemental composition and mapping analysis of the compounds were performed by EDS. A large scanning area was initially selected for the analysis of elemental composition. Then slowly the scan area was reduced and finally reached to individual crystallites. Spot and area analyses were carried out to find the elemental compositions in several locations of the sample to ascertain local and overall compositional homogeneity. Moreover, several spots within a crystallite were also analyzed for checking its compositional homogeneity. The elemental mapping analysis helped in establishing evenly distribution of all elements present in a sample throughout an imaging area. For the preparation of samples, aluminum stubs were cleaned with isopropyl alcohol followed by hot drying. The powder samples were smeared on a carbon tape pasted on the aluminum stub and gold sputtering was carried out under argon atmosphere to form a thin layer of gold for electrical conductivity.

2.3 Transmission Electron Microscopy (TEM)

In TEM, high energy electrons emitted from a tungsten filament of the electron gun, operating at an accelerating voltage of 50-300 kV, is allowed to pass through a thin sample deposited on carbon coated copper grid [6]. The electron gun contains several electromagnetic lenses and these lenses are used to regulate the size and angular spread of the electron beam which is focused on the sample. The transmitted electrons from the thin sample on copper grid are used for imaging. Selected area electron diffraction (SAED) patterns were recorded and diffraction spots were indexed to confirm the crystal structures and lattice spacing as ascertained from PXD analysis. HR-TEM images were also taken to look at the lattice fringes and determine the lattice periodicity.

For the present investigation, TEM images and SAED patterns were recorded with FEI TECNAI G^2 microscope, operated at an acceleration voltage of 200 kV. For the TEM analysis, about 5 mg of finely powdered sample was dispersed in 5 mL of ethanol and

sonicated for 15 min. Then, 20 µL of above suspension was put on a carbon coated copper grid with the help of a micropipette and allowed to dry in air.

2.4 UV-Visible Diffuse Reflectance Spectroscopy (UV-vis DRS)

UV-vis DRS is one of the most efficient and widely used techniques for measuring the optical properties of solid materials. It involves the measurement of diffuse reflected light in all possible directions from the particles oriented in all directions. In the present work, UV-vis DRS of the synthesized compounds were recorded using a Shimadzu UV-2450 UV-vis spectrophotometer within the wavelength range 200-800 nm. $BaSO_4$ was used as a reference material for baseline correction. For this, approximately 40 mg of the powder sample was ground thoroughly with about 4 g of $BaSO_4$ in agate mortar for ~20 min. Then, the mixture was packed in the groove of the sample holder by using cylindrical glass slide. The sample holder was placed in the spectrophotometer to measure the reflectance spectrum. The reflectance data were converted to absorption according to the Kubelka-Munk (K-M) theory [7]:

$$F(R_\infty) = (1 - R_\infty)^2 / 2R_\infty \tag{2.2}$$

where R_∞ is reflectance of the sample and $F(R_\infty)$ is the K-M function. The band gap of the samples was estimated by Tauc plot. For this, the following expression given by Tauc was used [8].

$$(\alpha h\nu)^{1/n} = A(h\nu - E_g) \tag{2.3}$$

where α, $h\nu$, A and E_g are the absorption coefficient, incident light frequency, proportionality constant and band gap, respectively. The value of the exponent, n determines the nature of electronic transition; for a direct transition, n = ½ and for indirect transition, n = 2 were used [9, 10]. The linear extrapolation of $(\alpha h\nu)^{1/n}$ to the energy axis gave the band gap energies of the samples.

2.5 Photoluminescence (PL) Spectroscopy

The process of photon excitation followed by photon emission is called photoluminescence (fluorescence and phosphorescence). PL measurements were carried out on Shimadzu RF-5301PC specrtofluorophotometer at room temperature. The sample for PL study was prepared by dispersing ~ 10 mg of solid sample in 10 mL of methanol and sonicating the resulting suspension for 10 minutes. Then, the above suspension was taken in a quartz cuvette and the PL spectra were recorded.

PL measurements to detect hydroxyl radical ($^{\bullet}$OH) generation for the oxide photocatalysts under sunlight-irradiation were carried out using terephthalic acid (TA) as a probe molecule. For this, 0.1 g of the catalyst powder was dispersed in 100 mL of 5×10^{-4} M aqueous TA solution in alkaline medium (2×10^{-3} M in NaOH). The resulting catalyst-TA suspension was magnetically stirred in the dark for 60 min and then it was exposed to the sunlight. At regular time intervals, 5 mL of the suspension was taken out, centrifuged to remove the catalyst particles. The PL intensity of the filtrates was then measured by a fluorescence spectrophotometer at an excitation wavelength of 315 nm.

2.6 Electrochemical Impedance Spectroscopy (EIS)

Electrochemical impedance measurements were carried out using a galvanostate (model; Versastat 3, PAR) based on a conventional three electrode assembly consisting of $Bi_{5-x}La_xBaTi_3O_{14}Cl$ ($x = 0 – 2$) catalyst (Chapter 6) mixed with graphite paste as the working electrode, Pt wire as the counter electrode, Ag/AgCl (3 M KCl) as the reference electrode and 10 mM $K_3[Fe(CN)_6]$ solution containing 0.1 M KCl as the electrolyte. All measurements were performed in the frequency ranging from 0.02 Hz to 100 kHz at 0.24 V and the amplitude of the applied sinusoidal potential perturbation of ±5 mV.

2.7 ζ-potential Measurements

The surface charge of the photocatalyst particles were measured *via* ζ-potential measurements using Malvern Zeta Sizer Nano ZS90. The experiments were carried out by dispersing 10 mg of solid catalyst in 10 mL aqueous solution of different pH (2, 3, 5, 7, 9, 11 and 14). The pH of the solutions was adjusted by adding dilute hydrochloric acid or

sodium hydroxide. The catalyst suspensions were sonicated for 10 min prior to each measurement.

2.8 Photocatalytic Activity Test

Photocatalytic activities of the as prepared compounds were tested by way of dye degradation under natural sunlight at different pH. For this, the dye solution was prepared in aqueous medium and the required pH (2, 3, 7 and 11) of the solutions was adjusted by addition of dilute hydrochloric acid or sodium hydroxide. The degradation experiments were carried out at IIT Roorkee (29°51′ N; 77°53′ E) under natural sunlight-irradiation [having solar Direct Normal Irradiance (DNI) ~ 187 W/m^2 in the month of February, 2014 (Chapter-3), DNI ~ 204 W/m^2 during the month of September, 2014 (Chapter 4), DNI ~ 212 W/m^2 during the month of October, 2015 (Chapter 5) and DNI ~137 W/m^2 during the month of December, 2014 (Chapter 6)] keeping all other conditions identical. In a typical degradation study, 0.1 g of the powder photocatalyst was added into 100 mL of dye solution (1×10^{-5} M) of appropriate pH taken in a 250 mL beaker. Then, the dye-catalyst suspensions were magnetically stirred at 350 rpm for 60 min in the dark to ensure adsorption-desorption equilibrium between the photocatalyst and dye. After this, the beaker containing dye-catalyst suspension was exposed to the direct sunlight-irradiation. For measuring dye concentration during the degradation experiments, 5 mL suspension were sampled at regular time intervals, centrifuged at 8500 rpm to remove the catalyst particles and absorption measurements were carried out with the filtrates using a Shimadzu 2450 UV-visible spectrophotometer. After recording the absorbance at each time interval, the dye solution was put back into the beaker to maintain the constant volume of dye solution so that the errors due to loss of dye and catalysts are minimized. A blank test was also performed with the dye solution of same concentration without the catalyst under identical condition for self-degradation correction and calculation of degradation efficiency. The photocatalytic degradation efficiencies of the catalysts were calculated using the following expression:

$$\text{Degradation (\%)} = (1 - C/C_0) \times 100 \qquad (2.4)$$

where C_0 is the initial dye concentration and C is the concentration of the dye at different time intervals.

2.8.1 Catalyst Stability and Photocatalytic Cycle Test

The stability of the catalyst in the acidic medium on photocatalytic dye degradation was investigated by carrying out several cycles of photodegradation with the same catalyst and recording its PXD pattern. For this, a fixed quantity of catalyst (0.1 g) were taken in 100 mL of 1×10^{-5} M dye solution and the photocatalytic degradation studies were performed by the same procedure as mentioned in the activity test. For cycle studies, the catalyst was separated by centrifuging it after the first cycle and recovered from the centrifuge tube into a beaker with the help of a fresh 100 mL of 1×10^{-5} M dye solution. Then, the dye-catalyst suspension was subjected to magnetic stirring for 60 min in the dark and subsequently exposed to the direct sunlight-irradiation for the second cycle test. The same procedure was repeated for other cyclic runs and at the end of the fifth cycle, the catalyst was separated, dried and subjected to PXD studies.

2.8.2 Detection of Reactive Species

To understand the role of various reactive species (h^+, $^\bullet OH$ and $O_2^{\bullet-}$) on the photocatalytic dye degradation, different scavengers was added to the dye solution prior to the addition of the catalyst. The experimental procedure for the active species determination was similar to that described above during photodegradation studies. In our experiments, ethylenediaminetetraacetic acid (EDTA), isopropyl alcohol (IPA) and Ar gas purging was employed as hole (h^+) [11], $^\bullet OH$ [12] and $O_2^{\bullet-}$scavenger, respectively (Chapter 3). Ammonium oxalate (AO), benzoquinone (BQ) and tertiary butyl alcohol (*t*-BuOH) was used as h^+, $O_2^{\bullet-}$ and $^\bullet OH$ scavengers, respectively [13,14] (Chapter 4-6).

2.9 Chemical Oxygen Demand (COD) Test

COD of the dye solution before, during and after the photocatalysis was analyzed by using a digestion unit (DRB 200, HACH, USA) and UV-visible spectrophotometer. The following expression was used to calculate the photocatalytic degradation efficiency.

$$\text{Potodegradation efficiency} = \frac{\text{Initial COD}-\text{Final COD}}{\text{Initial COD}} \times 100 \qquad (2.5)$$

2.10 Cyclic Voltammetry (CV)

CV measurements were performed with an electrochemical analyzer (CH Instruments) using a conventional three electrode assembly consisting a glassy carbon working electrode, a platinum wire counter electrode, and a Ag/AgCl (3 M KCl) reference electrode. pH of the dyes were adjusted by adding appropriate buffer solutions to the dye solution in 1 : 1 ratio.

REFERENCES

1. West, A. R. Solid State Chemistry and Its Applications. Wiley Publishers, **2011**.

2. Losocha, W.; Lewinski, K. PROSZKI- A System of Programs for Powder Diffraction Data Analysis. *J. Appl. Crystallogr.***1994**, *27*, 437-438.

3. Kraus, W.; Nolze, G. *POWDER CELL* - A Program for the Representation and Manipulation of Crystal Structures and Calculation of the Resulting X-ray Powder Patterns. *J. Appl. Crystallogr.***1996**, *29*, 301-303.

4. Wetzig, K.; Schulze, D. *In Situ* Scanning Electron Microscopy in Materials Research. *AkademieVerlag* **1995**.

5. Chandler, G. W.; Seraphin, S.; Ed. Kaufmann, E. N. Scanning Electron Microscopy. *Characterization of Materials* **2003**, *2*, 1050-1063.

6. Pennycook, S. J.; Eds. Williams, D. B.; Carter, C. B. Transmission Electron Microscopy: A Text Book for Materials Science. *Microscopy and Microanalysis* **2010**, *16*, 111-111.

7. Kubelka, P.; Munk, F. EinBeitragzurOptik der Farbanstriche. *Z. Tech. Phys.***1931**, *12*, 593-601.

8. Tauc, J.; Grigorovic, R.; Vancu, A.Optical Properties and Electronic Structure of Amorphous Germanium. *Phys. Status Solidi* **1966**, *15*, 627-637.

9. Kim, M. R.; Kang, Y.; Jang, D. Synthesis and Characterization of Highly Luminescent CdS@ZnS Core−Shell Nanorods. *J. Phys. Chem. C* **2007**, *111*, 18507-18511.

10. Joshi, U. A.; Maggard, P. A. $CuNb_3O_8$: A p-Type Semiconducting Metal Oxide Photoelectrode. *J. Phys. Chem. Lett.* **2012**, *3*, 1577-1581.

11. Zhang, H.; Zong, R.; Zhao, J.; Zhu, Y. Dramatic Visible Photocatalytic Degradation Performances Due to Synergetic Effect of TiO_2 with PANI. *Environ. Sci. Technol.* **2008**, *42*, 3803-3807.

12. Yang, H.; Li, G.; An, T.; Gao, Y.; Fu, J. Photocatalytic Degradation Kinetics and Mechanism of Environmental Pharmaceuticals in Aqueous Suspension of TiO_2: A Case of Sulfa Drugs. *Catal. Today* **2010**, *153*, 200-207.

13. Wang, Y.; Deng, K.; Zhang, L. Visible Light Photocatalysis of BiOI and Its Photocatalytic Activity Enhancement by in Situ Ionic Liquid Modification. *J. Phys. Chem. C* **2011**, *115*, 14300-14308.

14. Kumar, S.; Khanchandani, S.; Thirumal, M.; Ganguli, A. K. Achieving Enhanced Visible-Light-Driven Photocatalysis Using Type-II $NaNbO_3$/CdS Core/Shell Heterostructures. *ACS Appl. Mater. Interfaces* **2014**, *6*, 13221-13233.

CHAPTER -3

Four-Layer Aurivillius Perovskites Exhibiting Excellent Sunlight-Driven Photocatalytic Activity

Four-Layer Aurivillius Perovskites Exhibiting Excellent Sunlight-Driven Photocatalytic Activity

3.1 INTRODUCTION

In recent years, there has been tremendous research thrust in harvesting solar energy by visible-light-driven photocatalysis utilizing bulk and nanostructured metal oxides [1-5]. Among them, perovskites constitute a major class both with two-dimensional (layered) and three-dimensional structures [2-4]. It is observed that many oxides studied for visible-light photocatalysis contain Bi^{3+} [1, 2, 6-14]. The presence of Bi plays a crucial dual role in these materials. First, it pushes the absorption band edge in the visible region because of the formation of a hybridized valence band comprising of Bi 6s and O 2p states [6] and second, the dispersed valence band facilitates oxidation reaction because of high mobility of photogenerated holes [1, 2, 15].

Among the Bi^{3+} containing compounds that exhibit visible-light-driven photocatalytic activity, the Aurivillius phases are noteworthy [8-11, 13, 14]. The Aurivillius phases are variants of layered perovskites where the layered structure is formed by alternating stacks of perovskite slabs, with a general composition $[A_{n-1}B_nO_{3n+1}]^{2-}$ (where *n* represents *n*-octahedra thick perovskite block), and the fluorite-like $[Bi_2O_2]^{2+}$ units (Figure 3.1) [16]. Preparation and photocatalytic activities of single-layer (*n* = 1) Aurivillius type perovskite oxides, such as Bi_2MoO_6 [17, 18], Bi_2WO_6 [8, 10, 19] and their solid solution [20, 21] phases have been investigated. Recently, the four layer (*n* = 4) Aurivillius phase, $Bi_5Ti_3FeO_{15}$, has drawn attention for its ferroelectric [22, 23] and photocatalytic [11, 13] properties. Photocatalytic activity of $Bi_5Ti_3FeO_{15}$ toward Rhodamine B (RhB) [11], acetaldehyde [11] and isopropyl alcohol [13] degradation by visible-light irradiation has been reported, although very poor degradation (~ 6%) efficiencies were observed with the bulk $Bi_5Ti_3FeO_{15}$ in neutral aqueous solution. However, Sun *et al.* have shown enhanced RhB degradation with $Bi_5Ti_3FeO_{15}$ hierarchical microflowers as compared to the bulk oxide under similar conditions. The higher efficiency has been attributed to increased surface area and its nanocrystalline nature [11]. Synthesis of $Bi_4LaTi_3FeO_{15}$ by a molten-salt flux method was reported, but the structural parameters and photocatalytic activities are not known [24].

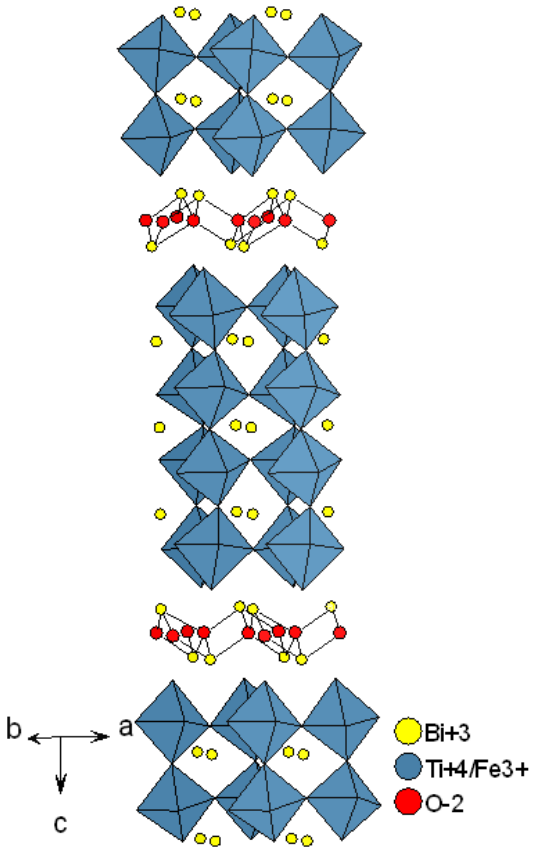

Figure 3.1 Structure of four layer Aurivillius layered perovskite, $Bi_5Ti_3FeO_{15}$, showing alternate stacks of $[Bi_2O_2]^{2+}$ and $[Bi_3Ti_3FeO_{13}]^{2-}$.

We undertook a systematic exploration on the solid state synthesis and characterization of four layer Aurivillius perovskites, $Bi_{5-x}La_xTi_3FeO_{15}$ (x = 1-3). We report here for the first time, to the best of our knowledge, the solid-state synthesis and characterization of $Bi_{5-x}La_xTi_3FeO_{15}$ (x = 1, 2). Besides, the effectiveness of these bulk photocatalysts toward RhB degradation under sunlight-irradiation at different solution pH and their photostability on recycling are reported in this chapter in comparison to that with parent $Bi_5Ti_3FeO_{15}$ bulk oxides. The details of synthesis, characterization and sunlight-driven RhB degradation together with a mechanistic insight into dye degradation over $Bi_{5-x}La_xTi_3FeO_{15}$ (x = 1, 2) are described.

3.2 EXPERIMENTAL SECTION

3.2.1 Materials and Synthesis

Bi_2O_3 (Sigma-Aldrich, ≥ 98.0%), La_2O_3 (Sigma-Aldrich, 99.99%), TiO_2 (Sigma-Aldrich, 99.8%) $FeCl_2{\cdot}4H_2O$ (Sigma-Aldrich, ≥ 99.0%) and oxalic acid (Merck ≥ 99.0%) were used as received. All other reagents used in our work were of analytical grade and used without any further purification. Double distilled water was used throughout the degradation experiments.

The compounds, $Bi_{5-x}La_xTi_3FeO_{15}$ (x = 1, 2), were synthesized by solid-state reactions. For this purpose, stoichiometric quantities of Bi_2O_3, La_2O_3 (preheated at 950 °C), TiO_2 and $FeC_2O_4{\cdot}2H_2O$ were ground thoroughly in an agate mortar for 1 h and the powder mixture was heated at 900 °C for 12 h followed by 1000 °C for 6 h with intermittent grinding. $FeC_2O_4{\cdot}2H_2O$ was prepared by co-precipitation method in aqueous medium by mixing equimolar quantities of $FeCl_2{\cdot}4H_2O$ and oxalic acid. $Bi_5Ti_3FeO_{15}$ was also synthesized by a solid-state reaction, starting with a stoichiometric mixture of Bi_2O_3, TiO_2 and $FeC_2O_4{\cdot}2H_2O$, similar to that reported in the literature [25].

3.2.2 Dye Adsorption Studies

To determine the adsorption of RhB on the catalyst surface at different pH, the catalyst suspensions in RhB solution were magnetically stirred in the dark for 6 h. The initial and final dye concentrations were measured by absorption experiments carried out with a Shimadzu UV-2450 UV-vis spectrophotometer. The percentage adsorption was calculated from the difference between the final and initial dye concentrations.

3.2.3 Photocatalytic Activity Test

Photocatalytic activities of the as prepared compounds were tested by RhB degradation under natural sunlight at different pH. For this, the RhB solution was prepared in aqueous medium and the required pH (2, 3, 7 and 11) of the solutions was adjusted by addition of dilute hydrochloric acid or sodium hydroxide. The degradation experiments were carried out at IIT Roorkee (29°51′ N; 77°53′ E) under similar conditions in the month of February, 2014 (having solar Direct Normal Irradiance ~ 187 W/m^2 during the month). In a

typical degradation study, 0.1 g of powder photocatalyst was added into 100 mL of RhB solution (1×10^{-5} M) of appropriate pH taken in a 250 mL beaker. Then, the dye-catalyst suspensions were magnetically stirred at 350 rpm for 60 min in the dark to ensure adsorption-desorption equilibrium between the photocatalyst and RhB. After this, the beaker containing dye-catalyst suspension was exposed to the direct sunlight-irradiation. For measuring dye concentration during the degradation experiments, 5 mL of suspension were sampled at regular time intervals, centrifuged at 8500 rpm to remove the catalyst particles and absorption measurements were carried out with the filtrates using a Shimadzu 2450 UV-visible spectrophotometer. After recording the absorbance at each time interval, the dye solution was put back into the beaker to maintain the constant volume of dye solution so that the errors due to loss of RhB and catalysts are minimized. A blank test was also performed with the RhB solution of same concentration without the catalyst under sunlight-irradiation for self-degradation correction and calculation of degradation efficiency. The photocatalytic degradation efficiencies of the catalysts were calculated using the following expression

$$\text{Degradation (\%)} = (1 - C/C_0) \times 100 \qquad (3.1)$$

where C_0 is the initial dye concentration and C is the concentration of the dye at different time intervals.

3.2.4 Catalyst Stability and Photocatalytic Cycle Test

The stability of the catalyst in the acidic medium on photocatalytic RhB degradation was investigated by carrying out several cycles of photodegradation with the same catalyst and recording its PXD pattern. For this, a fixed quantity of catalyst (0.1 g) were taken in 100 mL of 1×10^{-5} M RhB solution and the photocatalytic degradation studies were performed by the same procedure as mentioned in the activity test. For cycle studies, the catalyst was separated by centrifuging it after the first cycle and recovered from the centrifuge tube into a beaker with the help of a fresh 100 mL of 1×10^{-5} M RhB solution. Then, the dye-catalyst suspension was subjected to magnetic stirring for 60 min in the dark and subsequently exposed to the direct sunlight-irradiation for the second cycle test. The same procedure was repeated for other cyclic runs and at the end of the fifth cycle, the catalyst was separated, dried and subjected to PXD studies.

3.3.5 Detection of Reactive Species

To investigate the active species responsible for photodegradation, different scavenger tests were carried out. For this purpose, an appropriate scavenger was added to the catalyst-dye suspension and the photodegradation experiment was carried out in the same way as mentioned in the activity test. In our experiments, ethylenediaminetetraacetic acid (EDTA, 1 mM), isopropyl alcohol (IPA, 1 mM) and Ar gas purging was employed as hole (h^+) [26], $^{\bullet}OH$ [27] and $O_2^{\bullet-}$ scavenger, respectively. For scavenger tests, 29.2 mg of solid EDTA and 76.4 μL of IPA were used for 100 mL of dye-catalyst suspension to make the required concentration of the scavenger as mentioned above.

3.2.6 Chemical Oxygen Demand (COD) Test

COD of the RhB solution before, during and after the photocatalysis was analyzed by using a digestion unit (DRB 200, HACH, USA) and UV-visible spectrophotometer (HACH, DR 5000, USA). For this, multiple degradation experiments were carried out with the same set of dye and catalyst. The dye-catalyst suspensions were exposed to different time intervals and the aliquots were collected for COD analysis. The following expression was used to calculate the photocatalytic degradation efficiency.

$$\text{Potodegradation efficiency} = \frac{\text{Initial COD} - \text{Final COD}}{\text{Initial COD}} \times 100 \qquad (3.2)$$

3.3 RESULTS AND DISCUSSION

3.3.1 PXD Analysis

The PXD patterns of the as prepared compounds, $Bi_{5-x}La_xTi_3FeO_{15}$ (x = 0 - 2) are shown in Figure 3.2. A comparison of the observed PXD data with that of the standard JCPDS data of the parent $Bi_5Ti_3FeO_{15}$ (JCPDS PDF # 89-8545) indicated formation of single phase four-layer Aurivillius perovskites, excepting for $Bi_3La_2Ti_3FeO_{15}$, where a small impurity of $LaFeO_3$ was detected. All the peaks observed in the PXD pattern of $Bi_4LaTi_3FeO_{15}$ are indexable in the orthorhombic $A2_1am$ space group [28]. In case of $Bi_3La_2Ti_3FeO_{15}$, all the diffraction peaks except those assigned to $LaFeO_3$ (Figure 3.2c) are

indexable in the same $A2_1am$ space group. The least-squares refined lattice parameters for the compounds are given in Table 3.1. The lattice parameters for the parent $Bi_5Ti_3FeO_{15}$ are in good agreement with the literature data [28]. The indexed PXD data for $Bi_5Ti_3FeO_{15}$, $Bi_4LaTi_3FeO_{15}$ and $Bi_3La_2Ti_3FeO_{15}$ are given in Tables 3.2, 3.3 and 3.4, respectively.

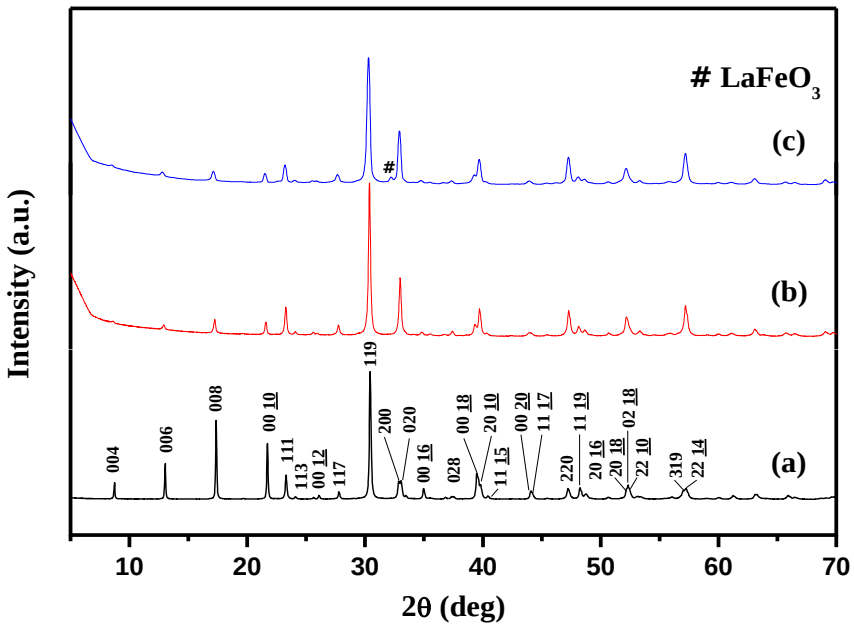

Figure 3.2 PXD patterns of (a) $Bi_5Ti_3FeO_{15}$, (b) $Bi_4LaTi_3FeO_{15}$, and (c) $Bi_3La_2Ti_3FeO_{15}$.

Table 3.1 Lattice Parameters and Band Gap of $Bi_{5-x}La_xTi_3FeO_{15}$ (x = 0 - 2)

Compound	Lattice parameters (Å)			Band Gap (eV)	
	a	*b*	*c*	E_g (1)	E_g (2)
$Bi_5Ti_3FeO_{15}$	5.458(3)	5.421(3)	41.02(2)	2.09	2.62
$Bi_4LaTi_3FeO_{15}$	5.436(1)	5.420(2)	41.19(1)	2.08	2.67
$Bi_3La_2Ti_3FeO_{15}$	5.437(1)	5.436(1)	41.29(1)	2.01	2.71

A closer look at the lattice parameters (Table 3.1) of $Bi_{5-x}La_xTi_3FeO_{15}$ series shows a slight increase in the *c*-parameter as *x* varies from 0 to 2, while *a* and *b*-parameter approach each other and become nearly equal in $Bi_3La_2Ti_3FeO_{15}$. This clearly indicates a decrease in orthorhombic distortion and a shift toward tetragonal structure with progressive replacement of lone-pair active Bi^{3+} by La^{3+} (having no lone-pair of electrons). It is reported that the La-incorporation in the perovskite *A*-site diminishes the out-of-center distortion [29], which possibly leads to an increase in the *c*- parameter of the compounds with increasing La-substitution.

The PXD simulation studies on $Bi_3La_2Ti_3FeO_{15}$ indicated La-substitution at the $[Bi_2O_2]^{2+}$ layers. The simulation result also showed preferential occupation (~ 67-75 %) of La in *A*-site of the central perovskite layer and the residual Bi and La, apart from those occupied central perovskite and $[Bi_2O_2]^{2+}$ layers, were located in the terminal perovskite layers. The simulated PXD pattern is compared with the observed data in Figure 3.3 and the positional parameters, occupancy and thermal factors used in the simulation are given in Table 3.5. Now, as shown in Figure 3.1, due to intergrowth nature of the Aurivillius phases by alternate layering of fluorite-type $[Bi_2O_2]^{2+}$ and $[A_{n-1}B_nO_{3n+1}]^{2-}$ perovskite sheets, a mismatch in the in-plane lattice parameters of the units would induce a strain in the structure. Moreover, changes in the Bi/La distribution over the $[Bi_2O_2]$ layer and *A*-site of perovskite blocks would give rise to subtle changes in the in-plane lattice parameter as well. Therefore, the Bi/La cation disorder takes place in such a way that this mismatch strain is reduced and an Aurivillius phase is stabilized. A cation disorder mediated relief of mismatch strain is attributed for monoclinic to orthorhombic structural transition in $Bi_{4-x}La_xTi_3O_{12}$ [30]. The trend of lattice parameter variation and cation distribution observed in $Bi_{5-x}La_xTi_3FeO_{15}$ series are similar to those observed in La-substituted $Bi_{4-x}La_xTi_3O_{12}$ with increase in La^{3+} substitution. We were not been able to synthesize $Bi_2La_3Ti_3FeO_{15}$ (*x* = 3 member of the general composition $Bi_{5-x}La_xTi_3FeO_{15}$). The destabilization of the Aurivillius phase, $Bi_2La_3Ti_3FeO_{15}$, could probably be due to an expected large mismatch strain that would have resulted by the larger amount of La present in the composition, thereby giving only a mixed phase with large quantities of $LaFeO_3$ impurity.

Table 3.2 Indexed PXD Data for $Bi_5Ti_3FeO_{15}$

h k l	d_{obs} (Å)	d_{calc} (Å)	I_{obs}
0 0 4	10.146	10.255	13
0 0 6	6.792	6.837	28
0 0 8	5.107	5.128	62
0 0 10	4.085	4.102	44
1 1 1	3.816	3.829	19
1 1 3	3.692	3.703	2
0 0 12	3.413	3.418	3
1 1 7	3.209	3.216	6
1 1 9	2.937	2.939	100
2 0 0	2.725	2.729	14
0 2 0	2.710	2.711	14
0 0 16	2.564	2.564	8
0 2 8	2.399	2.397	1
0 0 18	2.281	2.279	12
2 0 10	2.275	2.272	20
1 1 15	2.230	2.229	2
0 0 20	2.053	2.051	6
1 1 17	2.043	2.044	6
2 2 0	1.924	1.923	8
1 1 19	1.885	1.883	9
2 0 16	1.867	1.869	4
2 0 18	1.750	1.749	11
0 2 18	1.746	1.744	11
2 2 10	1.743	1.741	10
3 1 9	1.615	1.613	1
2 2 14	1.608	1.608	8

$a = 5.458(3)$, $b = 5.421(3)$, $c = 41.02(2)$ Å.

Table 3.3 Indexed PXD Data for $Bi_4LaTi_3FeO_{15}$

h *k* *l*	d_{obs} (Å)	d_{calc} (Å)	I_{obs}
0 0 4	10.304	10.298	2
0 0 6	6.848	6.865	3
0 0 8	5.139	5.149	9
0 0 10	4.114	4.119	8
1 1 1	3.818	3.821	18
1 1 3	3.695	3.696	2
0 0 12	3.431	3.433	1
1 1 7	3.212	3.215	6
1 1 9	2.940	2.941	100
2 0 0	2.717	2.718	38
0 2 0	2.712	2.710	38
0 0 16	2.575	2.575	2
0 2 8	2.398	2.398	3
0 0 18	2.289	2.289	7
2 0 10	2.268	2.269	18
1 1 15	2.234	2.233	2
0 0 20	2.060	2.060	2
1 1 17	2.052	2.049	2
2 2 0	1.921	1.919	7
1 1 19	1.890	1.888	5
2 0 16	1.869	1.869	3
2 0 18	1.752	1.751	12
0 2 18	1.747	1.748	12
2 2 10	1.738	1.739	10
3 1 9	1.609	1.609	1
2 2 14	1.606	1.607	20

a = 5.436(1), b = 5.420(2), c = 41.19(1) Å.

Table 3.4 Indexed PXD Data for $Bi_3La_2Ti_3FeO_{15}$

h *k* *l*	d_{obs} (Å)	d_{calc} (Å)	I_{obs}
0 0 4	10.326	10.322	2
0 0 6	6.889	6.881	3
0 0 8	5.167	5.161	8
0 0 10	4.128	4.129	7
1 1 1	3.831	3.828	14
1 1 3	3.703	3.703	2
0 0 12	3.439	3.440	1
1 1 7	3.221	3.221	6
1 1 9	2.948	2.946	100
2 0 0	2.720	2.719	43
0 0 16	2.581	2.580	2
0 2 8	2.404	2.405	3
0 0 18	2.295	2.294	6
2 0 10	2.270	2.270	19
1 1 15	2.238	2.238	1
0 0 20	2.064	2.064	2
1 1 17	2.054	2.053	2
2 2 0	1.922	1.922	19
1 1 19	1.892	1.892	4
2 0 16	1.871	1.872	2
2 0 18	1.753	1.753	10
3 1 9	1.609	1.609	1
2 2 14	1.610	1.610	23

a = 5.437(1), b = 5.436(1), c = 41.29(1) Å.

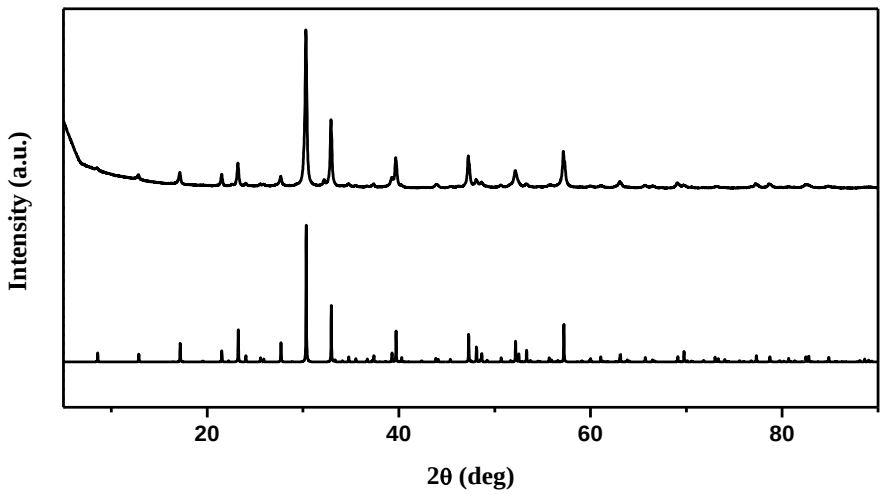

Figure 3.3 Observed (top) and simulated (bottom) PXD pattern of $Bi_3La_2Ti_3FeO_{15}$.

Table 3.5 Atomic Position, Site Occupancy and Thermal Parameters used for PXD Pattern Simulation of $Bi_3La_2Ti_3FeO_{15}$*

Atom	*x*	*y*	*z*	occ.	U_{iso}(×100)
Bi(1)/La(1)	0.25	0.2495	0	0.33/0.67	1.28
Bi(2)/La(2)	0.2395	0.2447	0.1043	0.42/0.58	0.73
Bi(3)/La(3)	0.2312	0.2679	0.2190	0.91/0.09	1.07
Ti(1)/Fe(1)	0.3169	0.1891	0.4534	0.75/0.25	0.50
Ti(2)/Fe(2)	0.2596	0.2771	0.3532	0.75/0.25	0.50
O(1)	0.3382	0.1772	0.4989	1	0.33
O(2)	0.6111	0.5463	0.0517	1	1.23
O(3)	0.3270	0.3062	0.4042	1	0.72
O(4)	0.5358	0.4856	0.1381	1	0.57
O(5)	0.2929	0.2035	0.3043	1	1.36
O(6)	0.5076	0.4890	0.2501	1	0.44
O(7)	0.0336	-0.0299	0.0393	1	1.16
O(8)	0.0837	0.0323	0.1466	1	0.43

* Space group $A2_1am$, a = 5.437(1), b = 5.436(1), c = 41.29(1) Å.

3.3.2 FE-SEM and EDS Analysis

FE-SEM images of $Bi_{5-x}La_xTi_3FeO_{15}$ (x =1, 2) are shown in Figure 3.4. The images show homogeneous morphology over the entire region of imaging with plate-like crystallites having a quite large variation in their sizes ranging from few hundred nanometers to few micrometers. Moreover, there appears to be fairly large degree of agglomeration among the crystallites. Elemental ratio as obtained from EDS analyses, both on spot and area basis, were in excellent agreement with the nominal compositions.

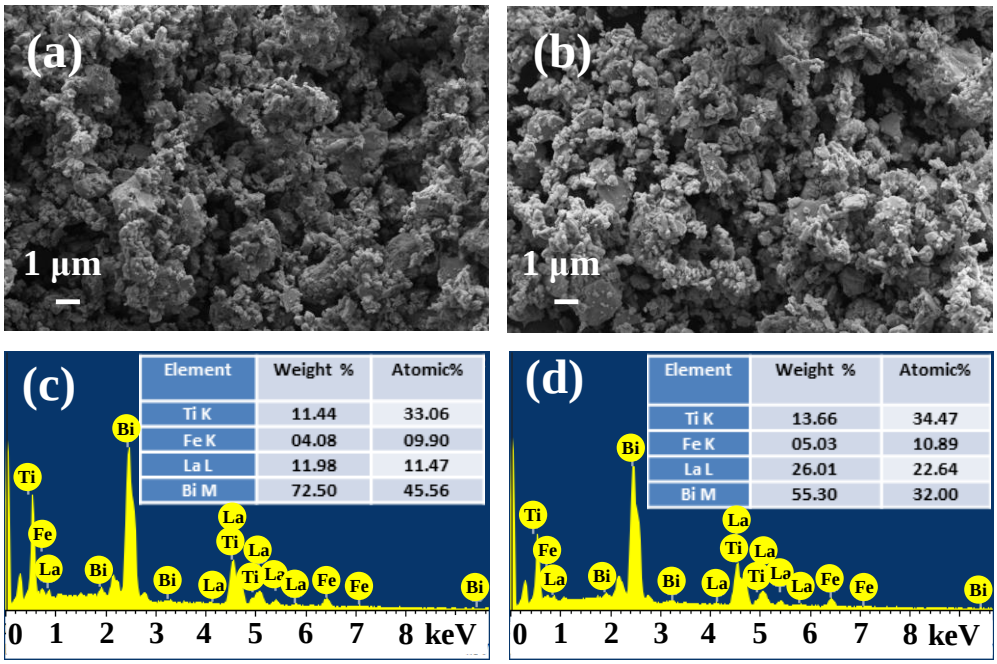

Figure 3.4 FE-SEM images of (a) $Bi_4LaTi_3FeO_{15}$ and (b) $Bi_3La_2Ti_3FeO_{15}$. Corresponding EDS data are shown in (c) and (d).

3.3.3 FE-SEM-EDS Elemental Mapping Analysis

To analyze the elemental distribution in $Bi_{5-x}La_xTi_3FeO_{15}$ (x = 1, 2), EDS elemental mapping was conducted. The mapping shows (Figure 3.5) uniform distribution of all elements throughout the selected area of FE-SEM image. It clearly shows that the amount of La has increased and that of Bi has decreased in going from $Bi_4LaTi_3FeO_{15}$ to $Bi_3La_2Ti_3FeO_{15}$ while the amount of Ti and Fe remained largely unchanged as expected for the nominal compositions. The bright spot observed in Figure 3.5 (h) could probably be due to the impurity phase $LaFeO_3$ showing accumulation of Fe.

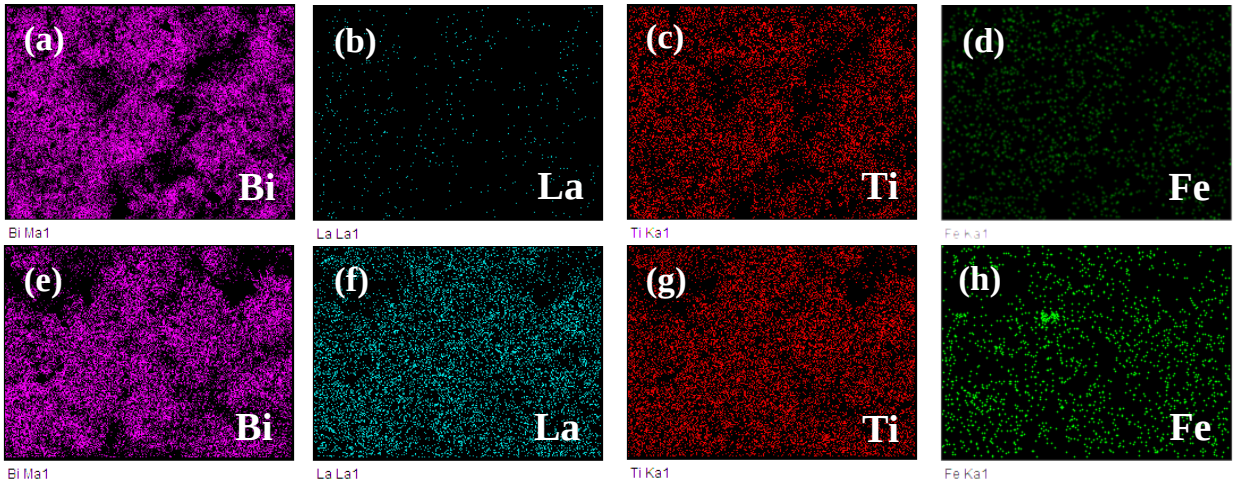

Figure 3.5 EDS elemental mapping of (a) Bi, (b) La, (c) Ti and (d) Fe in $Bi_4LaTi_3FeO_{15}$, and (e)-(h) elemental mapping for $Bi_3La_2Ti_3FeO_{15}$ in the same order.

3.3.4 UV-vis DRS Analysis

The UV-vis DRS (Figure 3.6) for all the compounds show absorption edges in the visible region (λ > 400 nm). Assuming $Bi_4LaTi_3FeO_{15}$ and $Bi_3La_2Ti_3FeO_{15}$ to be indirect band gap semiconductors, like $Bi_5Ti_3FeO_{15}$ [31], band gap energies (E_g) were estimated from the plot of $(\alpha h\nu)^{1/2}$ versus $h\nu$ (Figure 3.6 (b)). The E_g for the compounds are given in Table 3.1. Two absorption edges could be observed in $Bi_{5-x}La_xTi_3FeO_{15}$ (Figure 3.6 (a)); the first band is ascribed to the transition from the hybridized O 2p + Bi 6s + Fe t_{2g} valence band (VB) states to Fe e_g conduction band (CB) states with the corresponding band gap E_g (1) and the other from the same VB to Ti 3d CB states with the corresponding band gap E_g (2). The interband transitions are shown schematically in the inset of Figure 3.6 (a) [11]. Because all the compounds reported here are visible light absorbers with band gaps ranging from ~ 2.0 to 2.7 eV, it suggested their potential use in visible-light-driven photocatalysis.

3.3.5 PL Analysis

PL spectra of $Bi_{5-x}La_xTi_3FeO_{15}$ (x = 0 - 2) were recorded with an excitation wavelength of 350 nm. All the compounds show broad emission spectra (410–580 nm) with a peak around 470 nm (Figure 3.7). Because the PL intensity is an indicator of electron-hole recombination rate, a lower PL intensity indicates slow recombination; therefore, longer lifetime of electron-hole pairs [32]. This would suggest a higher efficiency of photocatalytic

dye degradation for the catalyst having lower PL intensity. On the basis of the PL data (Figure 3.7), one would expect lowest photocatalytic activity for $Bi_4LaTi_3FeO_{15}$, if all other factors are considered to remain fixed. To our surprise, we observed highest degradation rate for $Bi_4LaTi_3FeO_{15}$ (see the photocatalytic activity section). This suggests that other factors such as adsorption of the dye on the catalyst surface, the position of valence and conduction band edges of the catalyst and the relative positioning of the HOMO-LUMO states of the dye must be responsible for enhanced activity.

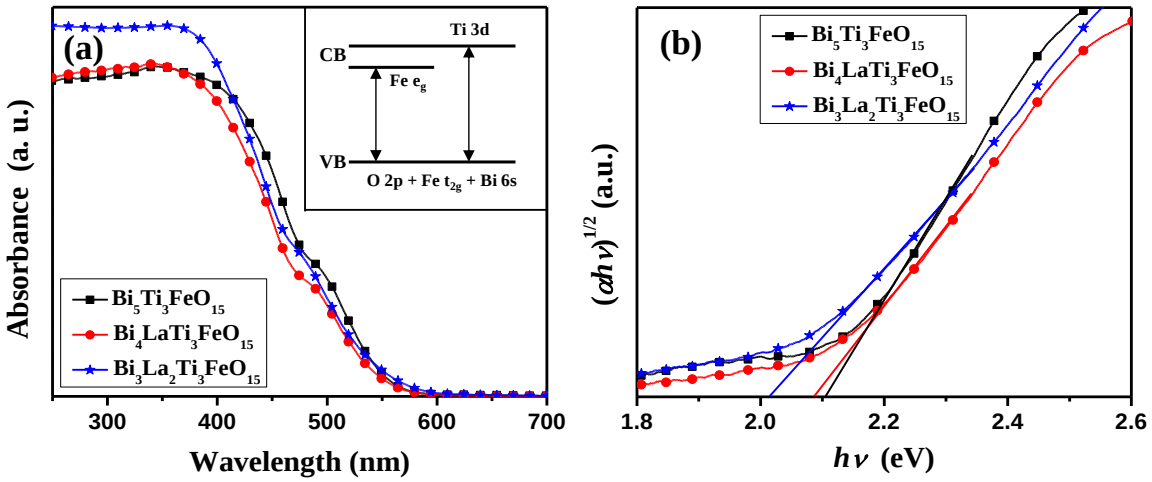

Figure 3.6 (a) UV-vis diffuse reflectance spectra (DRS). A schematic diagram showing interband transitions in $Bi_{5-x}La_xTi_3FeO_{15}$ (x = 0 - 2) is given in the inset. (b) Tauc plot for the band gap calculation of $Bi_{5-x}La_xTi_3FeO_{15}$ (x = 0 - 2).

3.3.6 Sun-Light-Driven Photocatalytic Activity

The photocatalytic activity of the compounds, $Bi_{5-x}La_xTi_3FeO_{15}$ (x = 0 - 2), was evaluated by RhB degradation under natural sunlight at various pH (2, 3, 7, and 11). Enhanced photocatalytic degradation of RhB was observed over all the catalysts at pH 2. The RhB was degraded almost completely within 25-40 min of solar illumination (Figure 3.8 (a)). Our results have been compared with blank runs carried out at same pH and identical solar illuminations conditions in absence of catalysts to show photostability (no self-degradation) of the dye.

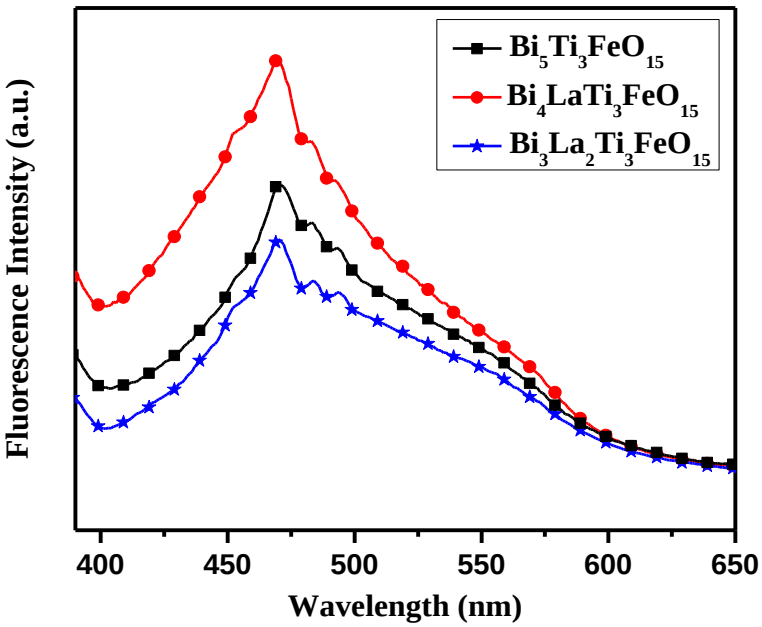

Figure 3.7 Photoluminescence spectra of $Bi_{5-x}La_xTi_3FeO_{15}$ (x = 0 - 2) at room temperature (excitation at 350 nm).

The kinetics of the photocatalytic RhB degradation over $Bi_{5-x}La_xTi_3FeO_{15}$ (x = 0 - 2) catalysts was fitted with Langmuir-Hinshelwood rate expression [33]

$$\ln(C_0/C) = kt \qquad (3.3)$$

where C_0 is the initial dye concentration, C is the dye concentration at time t and k is the pseudo-first-order rate constant. The linear plot between $\ln(C_0/C)$ and irradiation time (t) for $Bi_{5-x}La_xTi_3FeO_{15}$ (x = 0 - 2) compounds indicated the photocatalytic RhB degradation to follow a first-order kinetics. The degradation rate constants (k) are calculated from the slope of $\ln(C_0/C)$ versus t plot. Among all the compounds, $Bi_4LaTi_3FeO_{15}$ shows the highest degradation rate constant (Figure 3.8 (b)) and follows the order; $Bi_4LaTi_3FeO_{15}$ (k = 0.18853 min^{-1}) > $Bi_3La_2Ti_3FeO_{15}$ (k = 0.13143 min^{-1}) > $Bi_5Ti_3FeO_{15}$ (k = 0.11002 min^{-1}).

Degradation studies at pH 3 also showed near complete degradation of the dye but required longer illumination time ranging from 30 to 90 min (Figure 3.9). However, the degradation studies at higher pH such as, 7 and 11 did not show any appreciable degradation of the dye indicating almost no photocatalysis.

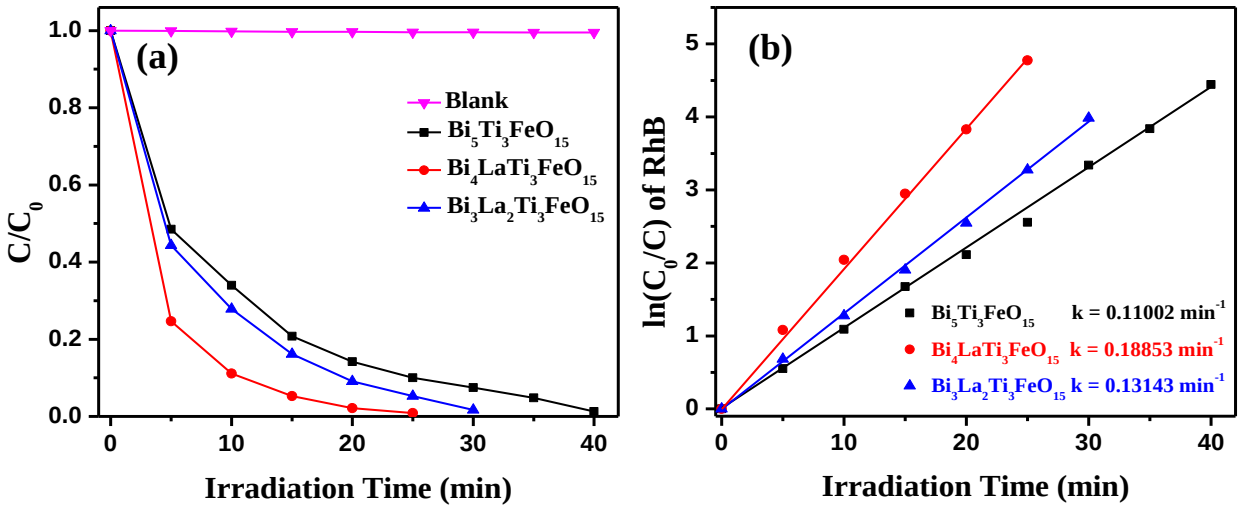

Figure 3.8 (a) Photocatalytic degradation of RhB with time by $Bi_{5-x}La_xTi_3FeO_{15}$ (x = 0 - 2) under sunlight. (b) The plot of ln(C_0/C) as a function of time over $Bi_{5-x}La_xTi_3FeO_{15}$ (x = 0 - 2).

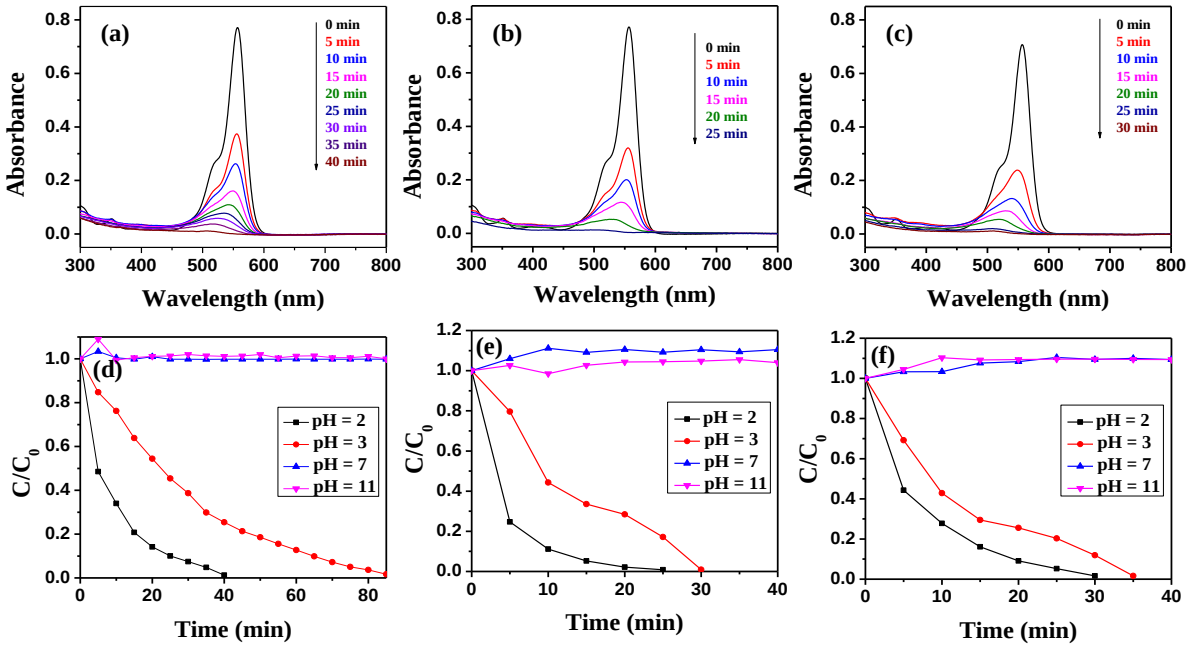

Figure 3.9 UV-vis absorption spectral changes of the aqueous RhB solutions over (a) $Bi_5Ti_3FeO_{15}$, (b) $Bi_4LaTi_3FeO_{15}$ and (c) $Bi_3La_2Ti_3FeO_{15}$ under sunlight-irradiation at pH 2. The course of photodegradation at different pH for (d) $Bi_5Ti_3FeO_{15}$, (e) $Bi_4LaTi_3FeO_{15}$ and (f) $Bi_3La_2Ti_3FeO_{15}$.

The RhB degradation at pH 2 was further confirmed by measuring the chemical oxygen demand (COD) of RhB solution. The COD decreased by 94 - 99% within 30-60 min of solar illumination depending on the catalysts used (Figure 3.10). This indicated a high degree of dye mineralization within a shorter period of time under solar irradiation.

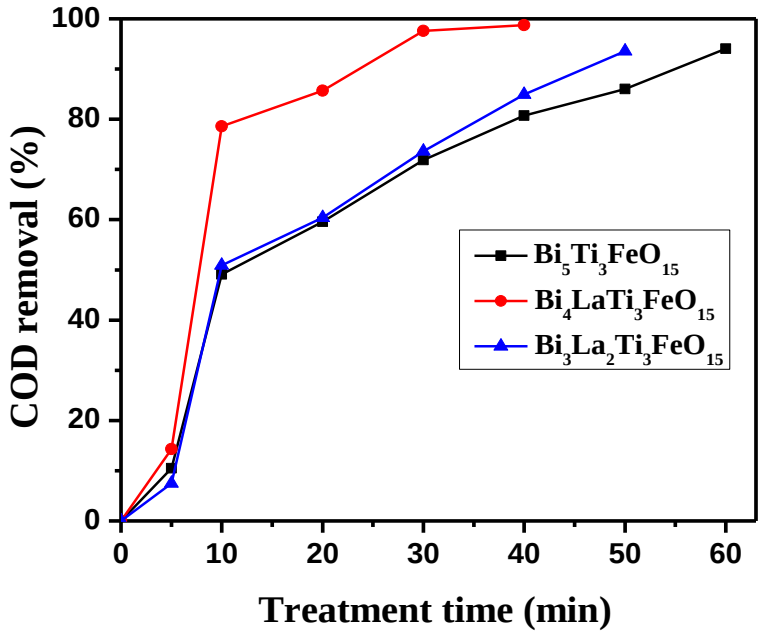

Figure 3.10 COD removal efficiency of $Bi_{5-x}La_xTi_3FeO_{15}$ (x = 0 - 2) with time.

3.3.7 Catalyst Stability and Photocatalytic Cycle Studies

To evaluate the stability and reusability of the photocatalysts, the RhB degradation process was repeated for five cycles (see Experimental Section). Figure 3.11 shows a typical UV-vis absorption data of RhB over $Bi_4LaTi_3FeO_{15}$ along with the degradation profiles for five successive catalytic cycles. In every cycle ~ 99 % of RhB were degraded within 25 min of sunlight-irradiation with complete decolorization of the dye solution, indicating no observable loss of activity of the catalyst (Figure 3.11 (b)). The dye degradation profiles for $Bi_3La_2Ti_3FeO_{15}$ and parent $Bi_5Ti_3FeO_{15}$ over five catalytic cycles are shown in the Figure 3.12. The PXD patterns recorded for all the catalysts recovered after the fifth cycle of photocatalysis run are shown in Figure 3.13. The PXD data did not show any impurity due to decomposition or phase separation indicating no photocorrosion or photoleaching during dye degradation. Moreover, the crystallinity of the postdegradation catalysts was almost

retained showing excellent stability and robustness of the catalysts under the reaction condition.

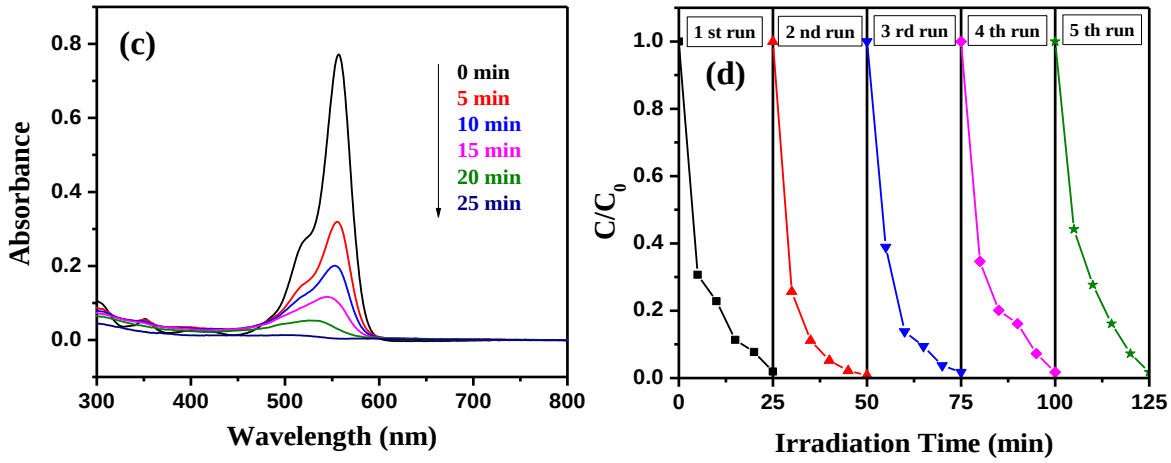

Figure 3.11 (a) UV-vis absorption spectra of RhB as a function of irradiation time for $Bi_4LaTi_3FeO_{15}$. (b) Time profiles of RhB degradation for five successive cycles with $Bi_4LaTi_3FeO_{15}$ under sunlight-irradiation.

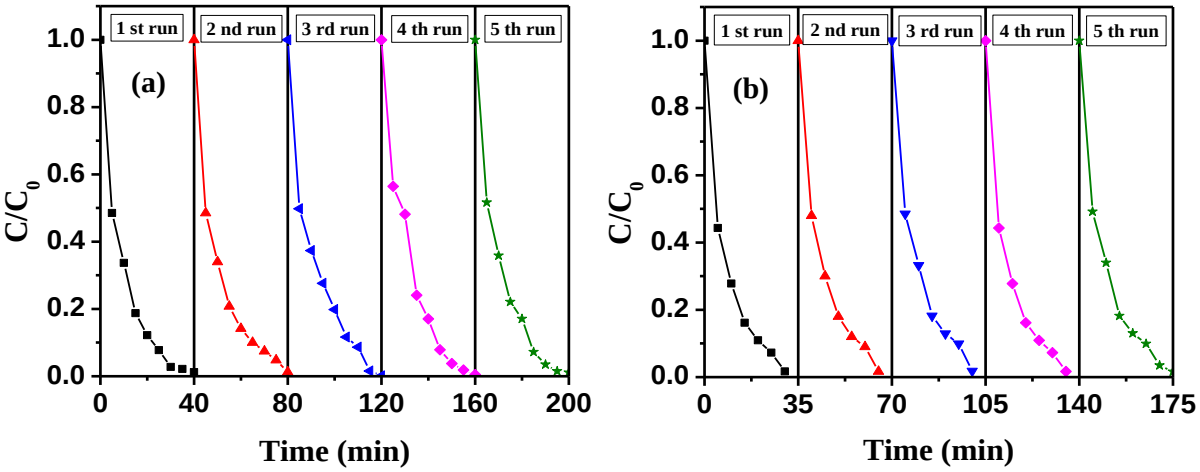

Figure 3.12 Time profiles of RhB degradation over five successive cycles for (a) $Bi_5Ti_3FeO_{15}$ and (b) $Bi_3La_2Ti_3FeO_{15}$ under sunlight-irradiation.

3.3.8 Detection of Reactive Species

The radical and hole trapping experiments (scavenger tests) with different scavenger molecules were carried out to elucidate the photocatalytic degradation mechanism of RhB under sunlight-irradiation over $Bi_4LaTi_3FeO_{15}$. Generally, the reactive species such as, hydroxyl radicals ($^{\bullet}OH$), superoxide radical anions ($O_2^{\bullet-}$) and holes (h^+) are expected to

be involved in the photocatalytic dye degradation processes [34]. The photocatalytic activity of RhB is drastically suppressed in a controlled experiment when EDTA was used as a hole scavenger (Figure 3.14 (a)). Moreover, when Argon purging was conducted during degradation, the RhB degradation is inhibited (Figure 3.14 (a)) to a moderate extent. However, no significant change in the degradation of RhB is observed upon the addition of IPA (a $^{\bullet}OH$ scavenger) as compared to uncontrolled experiments carried out in absence of scavengers under similar conditions. This indicates that h^+ and $O_2^{\bullet-}$ are playing a dominant role in the photocatalytic degradation of RhB over $Bi_4LaTi_3FeO_{15}$ under sunlight.

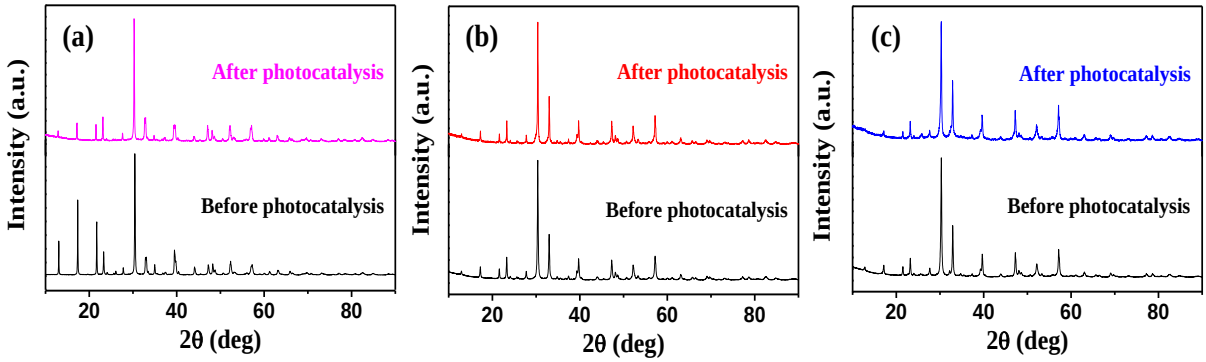

Figure 3.13 PXD patterns of (a) $Bi_5Ti_3FeO_{15}$, (b) $Bi_4LaTi_3FeO_{15}$ and (c) $Bi_3La_2Ti_3FeO_{15}$ before and after the photocatalytic RhB degradation.

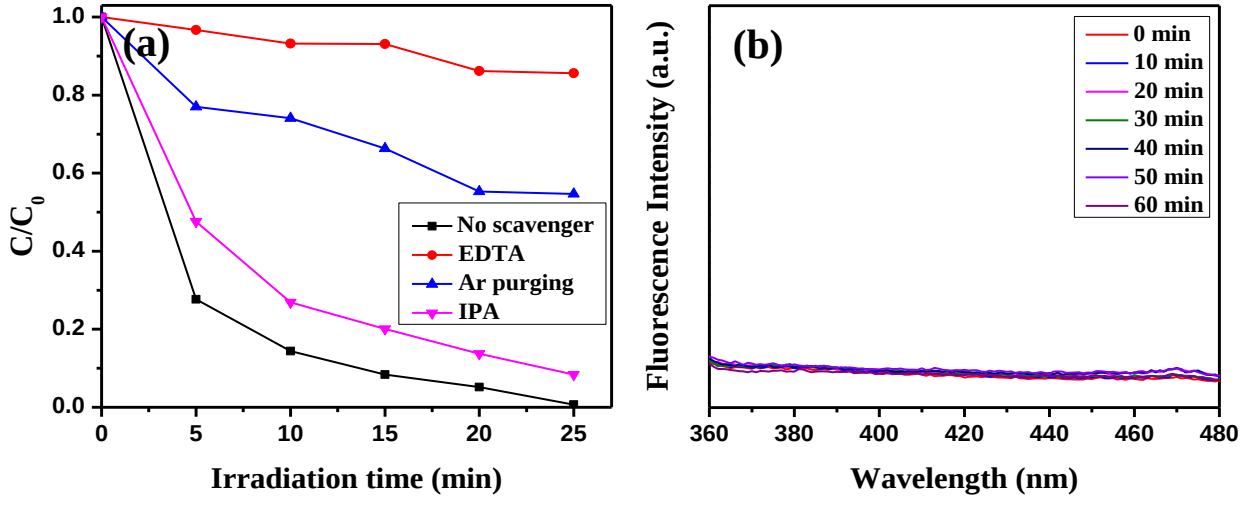

Figure 3.14 (a) Effects of different scavengers on the degradation of RhB in presence of $Bi_4LaTi_3FeO_{15}$ under sunlight-irradiation. (b) $^{\bullet}OH$ trapping PL spectra of $Bi_4LaTi_3FeO_{15}$ with excitation at 315 nm.

Moreover, the PL spectra did not show any indication of $^{\bullet}OH$ generation, when terephthalic acid (TA) was used as a probe molecule [35], which readily reacts with $^{\bullet}OH$ to produce highly fluorescent 2-hydroxyterephthelic acid (HTA) having a λ_{max} at ~ 425 nm. The absence of a PL emission peak for HTA at ~ 425 nm (Figure 3.14 (b)) indicated no $^{\bullet}OH$ formation with time. This, however, confirmed that $^{\bullet}OH$ does not play any role in the photodegradation of RhB with $Bi_4LaTi_3FeO_{15}$ under the reaction condition reported here.

3.3.9 Mechanistic Insights for Enhanced Photocatalytic Activity

The semiconductor photocatalysis with dyes is known largely to occur through dye adsorption on the surface of the photocatalyst, followed by e^{-}-h^{+} generation on photoexcitation and oxidative breakdown of the dye molecule on action of reactive species generated. To investigate further into the degradation process and to find out the reason for high activity of the catalyst, we have looked into the energy level alignment of the photocatalyst with respect to the potential of $^{\bullet}OH/H_2O$, $O_2/O_2^{\bullet-}$ and HOMO-LUMO levels of RhB. The conduction band minima (E_{CB}) and valence band maxima (E_{VB}) of the semiconductor photocatalysts were calculated empirically using the following expressions [36]

$$E_{CB} = \chi(A_aB_bC_c) - \tfrac{1}{2} E_g + E_0 \quad (3.4)$$

$$E_{VB} = E_{CB} + E_g \quad (3.5)$$

where, E_g is the band gap of the semiconductor, E_{CB} is the conduction band potential, E_{VB} is the valence band potential, E_0 is the scale factor taken as –4.5 eV with respect to the normal hydrogen electrode (*NHE* scale) and $\chi(A_aB_bC_c)$ is the absolute electronegativity (*AE*) of the semiconductor, $A_aB_bC_c$. The *AE* of a compound semiconductor is calculated as the geometric mean of the *AE* of the constituent atoms. For our calculation, the *AE* values for Bi, La, Ti, Fe and O are taken as 4.69, 3.1, 3.45, 4.06 and 7.54, respectively [37]. The calculated values of valence and conduction band positions of $Bi_{5-x}La_xTi_3FeO_{15}$ (x = 0 - 2) are given in Table 3.6. The potential of $^{\bullet}OH/H_2O$ (+ 2.68 eV *vs. NHE*), $O_2/O_2^{\bullet-}$ (+ 0.13 eV *vs. NHE*) and HOMO-LUMO levels of RhB (E_{HOMO} = 0.95 eV and E_{LUMO} = – 1.42 eV that matches fairly well with the λ_{max} of 553 nm) were taken from the literature [35, 38]. Figure 3.15 shows the

energy level diagram of $Bi_4LaTi_3FeO_{15}$ with respect to the potential of $^{\bullet}OH/H_2O$, $O_2/O_2^{\bullet-}$ and HOMO-LUMO levels of RhB.

Table 3.6 Calculated Values of Valence and Conduction Band Positions of $Bi_{5-x}La_xTi_3FeO_{15}$ (*x* = 0 - 2)

compound	valence band (eV)	conduction band-1 (eV)	conduction band-2 (eV)
$Bi_5Ti_3FeO_{15}$	2.58	0.49	– 0.04
$Bi_4LaTi_3FeO_{15}$	2.47	0.39	– 0.20
$Bi_3La_2Ti_3FeO_{15}$	2.34	0.33	– 0.37

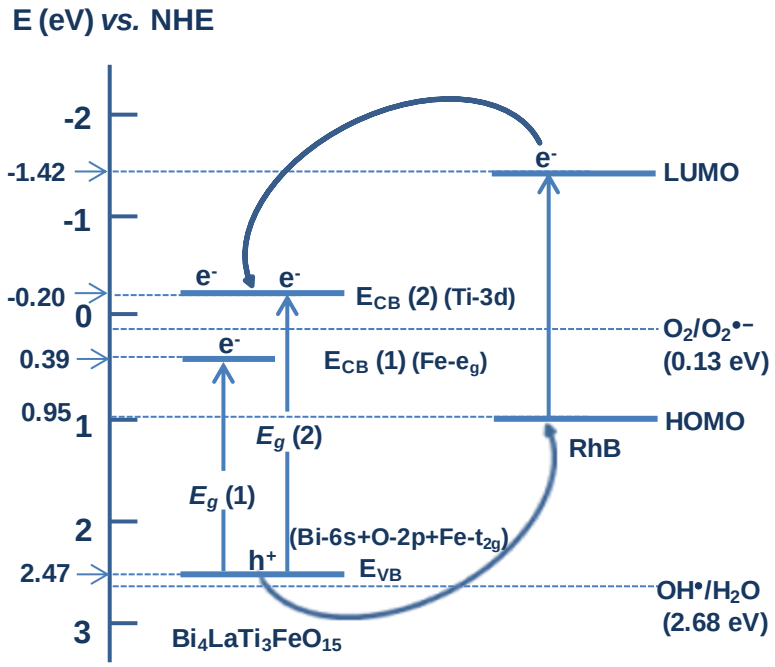

Figure 3.15 Schematic energy level diagram of $Bi_4LaTi_3FeO_{15}$ with respect to potential (vs *NHE*) of $^{\bullet}OH/H_2O$, $O_2/O_2^{\bullet-}$ and the HOMO-LUMO levels of RhB.

As it is evident from the UV-vis DRS of the semiconductors and according to earlier discussions, there exists two CB edges (one primarily of Ti 3d character and the other

Fe e_g character) and a VB edge (hybridized states of O 2p + Bi 6s + Fe t_{2g}). Apparently, this would give rise to two absorption edges arising out of the transitions from the VB to both the CBs as shown in Figure 3.6. These two transitions correspond to the band gap energies of 2.08 and 2.67 eV for $Bi_4LaTi_3FeO_{15}$. It is clear from the potential (vs *NHE*) energy level diagram that the position of E_{VB} above the potential of $^{\bullet}OH/H_2O$ is not suitable for $^{\bullet}OH$ formation. Similarly, the position of E_{CB} (1) below the potential of $O_2/O_2^{\bullet-}$ is not in favor of $O_2^{\bullet-}$ generation. However, the position of E_{CB} (2), which lies above the potential of $O_2/O_2^{\bullet-}$, is suitable for the $O_2^{\bullet-}$ formation. Although, the passage of electron from E_{CB} (2) to E_{CB} (1), an alternate and competing pathway for electron transfer, would diminish the probability of $O_2^{\bullet-}$ formation. Since both the electronic states are part of the same single-phase semiconductor photocatalyst, the e^- transfer from E_{CB} (2) to E_{CB} (1) will be at ease. The above facts explain the results of Argon purging test, to show a moderate role of $O_2^{\bullet-}$ and the IPA scavenger test, to signify only a marginal or no role of $^{\bullet}OH$ in the RhB degradation. The later was further confirmed by the PL studies (Figure 3.14 (b)). Moreover, the positioning of E_{VB} below the HOMO levels of RhB in the energy level diagram is suitable for h^+ transfer from semiconductor to adsorbed dye molecules and supportive for the role of h^+ in RhB degradation. The drastic decrease in degradation rate in presence of an h^+ scavenger (EDTA) further confirmed that the RhB degradation over $Bi_4LaTi_3FeO_{15}$ was largely mediated by holes. On the basis of our experimental results, a plausible mechanism for the photocatalytic RhB degradation over $Bi_4LaTi_3FeO_{15}$ catalyst under sunlight-irradiation is shown in Figure 3.16.

3.3.9.1 *Role of Adsorption*

It is believed that for h^+-mediated dye degradation, the adsorption of the dye molecule with the catalyst surface plays an important role. To elucidate the role of dye adsorption on the photocatalytic activity, we have performed adsorption experiments on dye-catalyst suspensions at different pH in the dark (see the Experimental Section). Interestingly, the adsorption data indicates that nearly 50% of dye molecules are adsorbed on the surface of $Bi_4LaTi_3FeO_{15}$ at pH 2 and a marked decrease in adsorption in neutral and alkaline pH (Figure 3.17). The corresponding adsorption data for $Bi_5Ti_3FeO_{15}$ and $Bi_3La_2Ti_3FeO_{15}$ are 37 and 47%, respectively, at pH 2 and a similar decrease is observed in neutral and alkaline medium. This indeed, explains the enhanced activity of the catalyst in

acidic pH and very poor performance in neutral and alkaline pH. Moreover, the activity of the catalysts follows the adsorption order making $Bi_4LaTi_3FeO_{15}$ as the most active and decreases in the order $Bi_4LaTi_3FeO_{15}$ > $Bi_3La_2Ti_3FeO_{15}$ > $Bi_5Ti_3FeO_{15}$ (Figure 3.8).

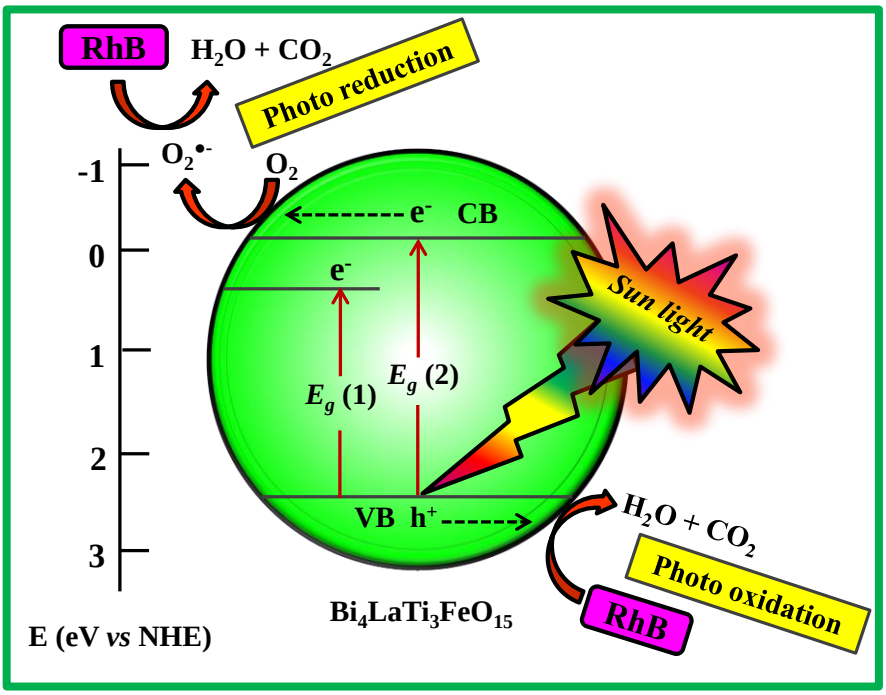

Figure 3.16 Schematic diagram showing the photocatalytic RhB degradation over $Bi_4LaTi_3FeO_{15}$ catalyst under sunlight-irradiation.

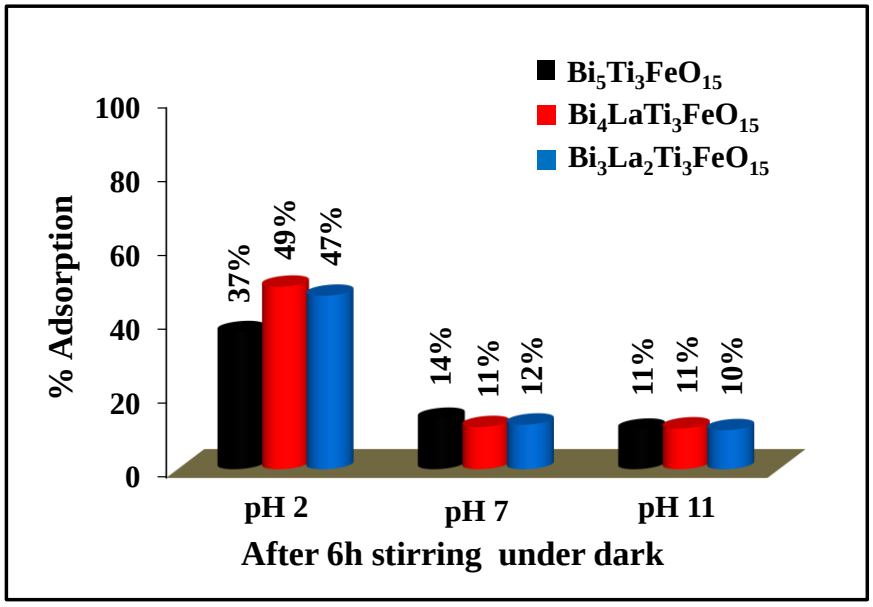

Figure 3.17 Influence of pH on RhB adsorption onto $Bi_{5-x}La_xTi_3FeO_{15}$ (x = 0-2) catalysts.

3.3.9.2 *Role of ζ- Potential*

The ζ- potential of the catalysts plays important role in the adsorption process. The surface charge of the photocatalysts is determined by measuring the ζ- potential. Figure 3.18 shows the variation of ζ- potential for $Bi_{5-x}La_xTi_3FeO_{15}$ (x = 0 - 2) catalysts as a function of pH. The highest positive ζ- potentials are seen at pH 2. As the pH increases, the ζ- potential shows a decreasing trend from more positive to less positive and finally to negative potentials in the alkaline pH. This is largely due to the action of H^+ and OH^- ions on the surface hydroxyl groups of the semiconductor.

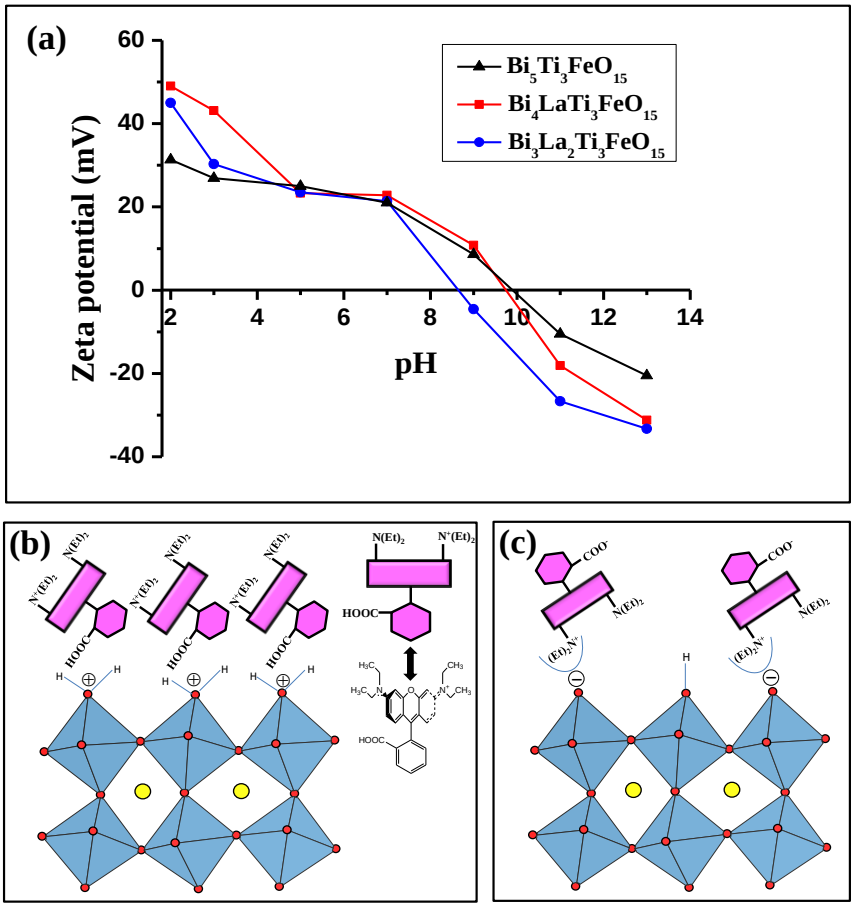

Figure 3.18 (a) ζ- potential of $Bi_{5-x}La_xTi_3FeO_{15}$ (x = 0 - 2) catalysts at different pH. Adsorption schemes of RhB on the catalyst surface at (b) acidic (pH = 2) and (c) alkaline (pH 11) media.

It is interesting to note that the biggest adsorption of RhB took place in case of $Bi_4LaTi_3FeO_{15}$, which had the highest ζ- potential (+ 49.1 mV) among all the members, $Bi_{5-x}La_xTi_3FeO_{15,}$ at pH 2. The ζ- potentials for $Bi_3La_2Ti_3FeO_{15}$ and $Bi_5Ti_3FeO_{15}$ were + 45.0 and + 31.3 mV, respectively, at pH 2. Indeed, the value of ζ- potential was reflected in the adsorption data for $Bi_3La_2Ti_3FeO_{15}$ and $Bi_5Ti_3FeO_{15}$ being the highest at pH 2 and then a decrease in adsorption with decreasing positive ζ- potential.

The adsorption of RhB under acidic pH may be explained on the basis of a schematic diagram (Figure 3.18), where the positive charge generated on the catalyst surface can effectively accommodate RhB molecules through electrostatic interaction with carboxylic acid groups of the dye molecule. At higher pH (pH 11) the catalyst surface acquires a negative charge and the carboxylate anionic group of the RhB would be repelled. However, the RhB molecule can get adsorbed on the negatively charged surface through electrostatic interaction with the positively charged N-diethyl end. But, the steric bulkiness of the N-diethyl group would not allow effective adsorption of RhB. Moreover, the magnitude of negative ζ- potential (–10 to – 31 mV) is significantly lower as compared to that of positive potential at pH 2. These above two factors, in fact, would reduce the extent of dye adsorption considerably. This observation led us to believe that a different mode together with a very low amount of dye adsorption is responsible for nearly zero photocatalytic RhB degradation in the alkaline medium.

Lastly, considering the possible ferroelectric nature of the compounds [22, 23], ($Bi_4LaTi_3FeO_{15}$ and $Bi_3La_2Ti_3FeO_{15}$ also crystallizes in the noncentrosymmetric space group, $A2_1am$) the internal electric fields from ferroelectric domains and surface polarizations might be playing important role for enhanced dye adsorption and concomitant high photocatalytic activity of these catalysts. Enhanced photocatalytic activity of ferroelectric oxides has been accounted in the recent literature [39, 40]. Moreover, the internal electric fields of the semiconductor catalysts might also be helping in efficient charge carrier separation [41], which in turn, would enhance the photocatalytic dye degradation. Further work is required to fully understand the precise role of ferroelectric domains and charge polarization on adsorption, zeta potential and photocatalytic activity in these layered Aurivillius perovskites.

In summary, a highly efficient sunlight-driven RhB degradation by a series of Aurivillius layered perovskites, $Bi_{5-x}La_xTi_3FeO_{15}$ (x = 0 - 2), in aqueous acidic solution has been demonstrated. The compounds, $Bi_4LaTi_3FeO_{15}$ and $Bi_3La_2Ti_3FeO_{15}$ were synthesized for the first time in the bulk form by solid state reaction. The activity of the catalysts toward RhB degradation is comparable or higher than many of the single and composite catalysts with Aurivillius and perovskite structures in the bulk or nanostructured form reported recently. An enhanced charge separation rendering slow e^- - h^+ recombination and efficient transport of photogenerated holes could possibly be the rationale for high efficiency of the bulk catalysts irrespective of the degradation mechanisms involved. Moreover, the large positive ζ-potential led to enhanced dye adsorption and consequently a high rate of degradation. Scavenger test experiments clearly indicated the dominant role of holes in the degradation process involving the Aurivillius layered oxides reported here. The positioning of VB and CB edges with respect to potentials of $^{\bullet}OH/H_2O$, $O_2/O_2^{\bullet-}$ and HOMO-LUMO levels of RhB clearly corroborated with the scavenger test results indicating no major role of hydroxyl species in the degradation. Considering the effect of ferroelectricity for enhanced photocatalytic activity in the recent literature, the role of internal electric fields and surface polarizations of these polar Aurivillius oxides for enhanced dye adsorption and photocatalytic activity may not be ruled out. Lastly, due to their high activity, these compounds may find practical applications in the area of organic contaminant detoxification, indoor air purification (VOC control), photocurrent generation and hydrogen production by water-splitting reaction, all under sunlight-irradiation.

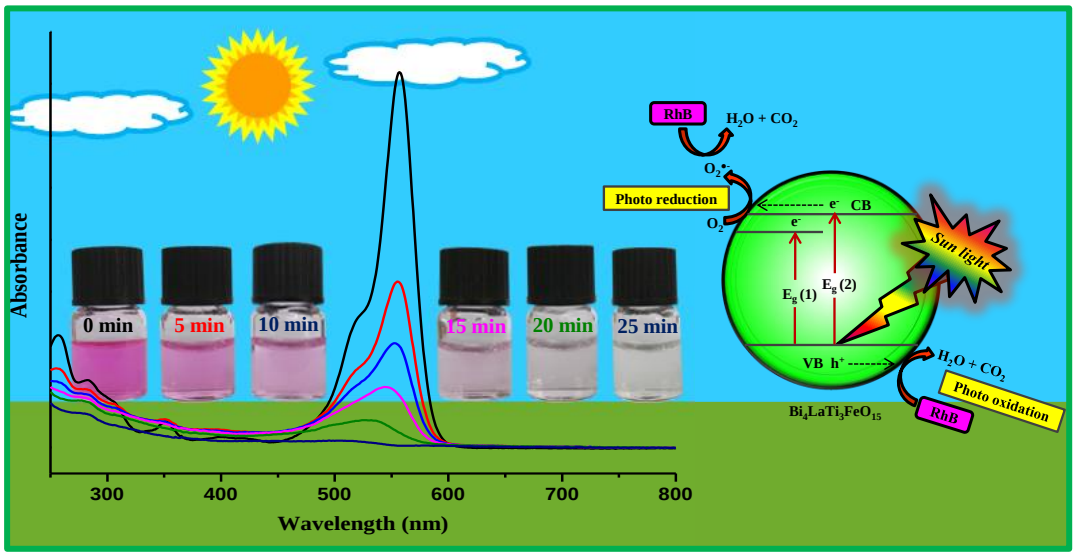

REFERENCES

1. Tang, J.; Zou, Z.; Ye, J. Efficient Photocatalytic Decomposition of Organic Contaminants over $CaBi_2O_4$ under Visible-Light Irradiation. *Angew. Chem. Int. Ed.* **2004**, *43*, 4463-4466.

2. Kim, H. G.; Hwang, D. W.; Lee, J. S. An Undoped, Single-Phase Oxide Photocatalyst Working under Visible Light. *J. Am. Chem. Soc.* **2004**, *126*, 8912-8913.

3. Wang, D.; Kako, T.; Ye, J. Efficient Photocatalytic Decomposition of Acetaldehyde over a Solid-Solution Perovskite $(Ag_{0.75}Sr_{0.25})(Nb_{0.75}Ti_{0.25})O_3$ under Visible-Light Irradiation. *J. Am. Chem. Soc.* **2008**, *130*, 2724-2725.

4. Kim, H. G.; Borse, P. H.; Jang, J. S.; Ahn, C. W.; Jeong, E. D.; Lee, J. S. Engineered Nanorod Perovskite Film Photocatalysts to Harvest Visible Light. *Adv. Mater.* **2011**, *23*, 2088-2092.

5. Colón, G.; López, S. M.; Hidalgo, M. C.; Navío, J. A. Sunlight Highly Photoactive Bi_2WO_6–TiO_2 Heterostructures for Rhodamine B Degradation. *Chem. Commun.* **2010**, *46*, 4809-4811.

6. Kudo, A.; Omori, K.; Kato, H. A Novel Aqueous Process for Preparation of Crystal Form-Controlled and Highly Crystalline $BiVO_4$ Powder from Layered Vanadates at Room Temperature and Its Photocatalytic and Photophysical Properties. *J. Am. Chem. Soc.* **1999**, *121*, 11459-11467.

7. Tokunaga, S.; Kato, H.; Kudo, A. Selective Preparation of Monoclinic and Tetragonal $BiVO_4$ with Scheelite Structure and Their Photocatalytic Properties. *Chem. Mater.* **2001**, *13*, 4624-4628.

8. Tang, J.; Zou, Z.; Ye, J. Photocatalytic Decomposition of Organic Contaminants by Bi_2WO_6 under Visible Light Irradiation. *Catal. Lett.* **2004**, *92*, 53-56.

9. Muktha, B.; Priya, M. H.; Madras, G.; Guru Row, T. N. Synthesis, Structure, and Photocatalysis in a New Structural Variant of the Aurivillius Phase: $LiBi_4M_3O_{14}$ (M = Nb, Ta) *J. Phys. Chem. B* **2005**, *109*, 11442-11449.

10. Fu, H.; Pan, C.; Yao, W.; Zhu, Y. Visible-Light-Induced Degradation of Rhodamine B by Nanosized Bi_2WO_6. *J. Phys. Chem. B* **2005**, *109*, 22432-22439.

11. Sun, S.; Wang, W.; Xu, H.; Zhou, L.; Shang, M.; Zhang, L. $Bi_5FeTi_3O_{15}$ Hierarchical Microflowers: Hydrothermal Synthesis, Growth Mechanism, and Associated Visible-Light-Driven Photocatalysis. *J. Phys. Chem. C* **2008**, *112*, 17835-17843.

12. Yu, K.; Yang, S.; He, H.; Sun, C.; Gu, C.; Ju, Y. Visible Light-Driven Photocatalytic Degradation of Rhodamine B over $NaBiO_3$: Pathways and Mechanism. *J. Phys. Chem. A* **2009**, *113*, 10024-10032.

13. Jang, J. S.; Yoon, S. S.; Borse, P. H.; Lim, K. T.; Hong, T. E.; Jeong, E. D.; Jung, O.-S.; Shim, Y. B.; Kim, H. G. Synthesis and Characterization of Aurivillius Phase $Bi_5Ti_3FeO_{15}$ Layered Perovskite for Visible Light Photocatalysis. *J. Cer. Soc. Jpn.* **2009**, *117*, 1268-1272.

14. Mann, A. K. P.; Steinmiller, E. M. P.; Skrabalak, S. E. Elucidating the Structure-Dependent Photocatalytic Properties of Bi_2WO_6: A Synthesis Guided Investigation. *Dalton Trans.* **2012**, *41*, 7939-7945.

15. Oshikiri, M.; Boero, M.; Ye, J.; Zou, Z.; Kido, G. Electronic Structures of Promising Photocatalysts $InMO_4$ (M = V, Nb, Ta) and $BiVO_4$ for Water Decomposition in the Visible Wavelength Region. *J. Chem. Phys.* **2002**, *117*, 7313-7318.

16. Subbarao, E. C. Crystal Chemistry of Mixed Bismuth Oxides with Layer-Type Structures. *J. Am. Ceram. Soc.* **1962**, *45*, 166-169.

17. Shimodaira, Y.; Kato, H.; Kobayashi, H.; Kudo, A. Photophysical Properties and Photocatalytic Activities of Bismuth Molybdates under Visible Light Irradiation. *J. Phys. Chem. B* **2006**, *110*, 17790-17797.

18. Martínez-de la Cruz, A.; Alfaro, S. O.; Cuellar, E. L.; Méndez, U. O. Photocatalytic Properties of Bi_2MoO_6 Nanoparticles Prepared by an Amorphous Complex Precursor. *Catal. Today*, **2007**, *129*, 194-199.

19. Kudo, A.; Hijii, S. H_2 or O_2 Evolution from Aqueous Solution on Layered Oxide Photocatalysts Consisting of Bi^{3+} with $6s^2$ Configuration and d^0 Transition Metal Ions. *Chem. Lett.* **1999**, *28*, 1103-1104.

20. Zhang, L.; Man, Y.; Zhu, Y. Effects of Mo Replacement on the Structure and Visible-Light-Induced Photocatalytic Performances of Bi_2WO_6 Photocatalyst. *ACS Catal.* **2011**, *1*, 841-848.

21. Zhou, L.; Yu, M.; Yang, J.; Wang, Y. Yu, C. Nanosheet-Based $Bi_2Mo_xW_{1-x}O_6$ Solid Solutions with Adjustable Band Gaps and Enhanced Visible-Light-Driven Photocatalytic Activities. *J. Phys. Chem. C* **2010**, *114*, 18812-18818.

22. Li, J.-B.; Huang, Y. P.; Rao, G. H.; Liu, G. Y.; Luo, J.; Chen, J. R.; Liang, J. K. Ferroelectric Transition of Aurivillius Compounds $Bi_5Ti_3FeO_{15}$ and $Bi_6Ti_3Fe_2O_{18}$. *Appl. Phys. Lett.* **2010**, *96*, 222903-222905.

23. Nakashima, S.; Fujisawa, H.; Ichikawa, S.; Park, J. M.; Kanashima, T.; Okuyama, M.; Simizu, M. Structural and Ferroelectric Properties of Epitaxial $Bi_5Ti_3FeO_{15}$ and Natural-Superlattice-Structured $Bi_4Ti_3O_{12}$ – $Bi_5Ti_3FeO_{15}$ Thin Films. *J. Appl. Phys.* **2010**, *108*, 074106-074110.

24. Porob, D. G.; Maggard, P. A. Synthesis of Textured $Bi_5Ti_3FeO_{15}$ and $LaBi_4Ti_3FeO_{15}$ Ferroelectric Layered Aurivillius Phases by Molten-Salt Flux Methods. *Mater. Res. Bull.* **2006**, *41*, 1513-1519.

25. Morozov, M. I.; Gusarov, V. V. Synthesis of $A_{m-1}Bi_2M_mO_{3m+3}$ Compounds in the $Bi_4Ti_3O_{12}$–$BiFeO_3$ System. *Inorg. Mater.* **2002**, *38*, 723-729.

26. Zhang, H.; Zong, R.; Zhao, J.; Zhu, Y. Dramatic Visible Photocatalytic Degradation Performances Due to Synergetic Effect of TiO_2 with PANI. *Environ. Sci. Technol.* **2008**, *42*, 3803-3807.

27. Yang, H.; Li, G.; An, T.; Gao, Y.; Fu, J. Photocatalytic Degradation Kinetics and Mechanism of Environmental Pharmaceuticals in Aqueous Suspension of TiO_2: A Case of Sulfa Drugs. *Catal. Today* **2010**, *153*, 200-207.

28. Hervoches, C. H.; Snedden, A.; Riggs, R.; Kilcoyne, S. H.; Manuel, P.; Lightfoot, P. Structural Behavior of the Four-Layer Aurivillius-Phase Ferroelectrics $SrBi_4Ti_4O_{15}$ and $Bi_5Ti_3FeO_{15}$. *J. Solid State Chem.* **2002**, *164*, 280-291.

29. Halasyamani, P. S. Asymmetric Cation Coordination in Oxide Materials: Influence of Lone-Pair Cations on the Intra-Octahedral Distortion in d^0 Transition Metals. *Chem. Mater.* **2004**, *16*, 3586-3592.

30. Chu, M.-W.; Caldes, M.-T.; Brohan, L.; Ganne, M.; Marie, A.-M.; Joubert, O.; Piffard, Y. Bulk and Surface Structures of the Aurivillius Phases: $Bi_{4-x}La_xTi_3O_{12}$ ($0 \leq x \leq 2.00$). *Chem. Mater.* **2004**, *16*, 31-42.

31. Wu, M.; Tian, Z.; Yuan, S.; Huang, Z. Magnetic and Optical Properties of the Aurivillius Phase $Bi_5Ti_3FeO_{15}$. *Mater. Lett.* **2012**, *68*, 190-192.

32. Fujihara, K.; Izuni, S.; Ohno, S.; Matsumura, M. Time-resolved Photoluminescence of Particulate TiO2 Photocatalysts Suspended in Aqueous Solution. *J. Photochem. Photobiol. A* **2000**, *132*, 99-104.

33. Fu, H.; Pan, C.; Yao, W.; Zhu, Y. Visible−Light−Induced Degradation of Rhodamine B by Nanosized Bi_2WO_6. *J. Phys. Chem. B* **2005**, *109*, 22432-22439.

34. Kumar, S.; Surendar, T.; Baruah, A.; Shanker, V. Synthesis of a Novel and Stable g-C_3N_4–Ag_3PO_4 Hybrid Nanocomposite Photocatalyst and Study of the Photocatalytic Activity under Visible Light Irradiation. *J. Mater. Chem. A* **2013**, *1*, 5333-5340.

35. Hirakawa, T.; Nosaka, Y. Properties of $O_2^{\bullet-}$ and $OH^{\bullet}$ Formed in TiO_2 Aqueous Suspensions by Photocatalytic Reaction and the Influence of H_2O_2 and some Ions. *Langmuir*, **2002**, *18*, 3247-3254.

36. Lv, J.; Kako, T.; Zou, Z.; Ye, J. Band Structure Design and Photocatalytic Activity of In_2O_3/N−$InNbO_4$ Composite. *Appl. Phys. Lett.* **2009**, *95*, 032107-032109.

37. Pearson, R. G. Absolute Electronegativity and Hardness: Application to Inorganic Chemistry. *Inorg. Chem.* **1988**, *27*, 734-740.

38. Pan, L.; Zou, J.; Liu, X.; Liu, X.; Wang, S.; Zhang, X.; Wang, L. Visible-Light-Induced Photodegradation of Rhodamine B over Hierarchical TiO_2: Effects of Storage Period and Water-Mediated Adsorption Switch. *Ind. Eng. Chem. Res.* **2012**, *51*, 12782-12786.

39. Cui, Y.; Briscoe, J.; Dunn, S. Effect of Ferroelectricity on Solar-Light-Driven Photocatalytic Activity of $BaTiO_3$-Influence on the Carrier Separation and Stern Layer Formation. *Chem. Mater*. **2013**, *25*, 4215-4223.

40. Li, L.; Salvador, P. A.; Rohrer, G. S. Photocatalysts with Internal Electric Fields. *Nanoscale* **2014**, *6*, 24-42.

41. Grinberg, I.; West, D. V.; Torres, M.; Gou, G.; Stein, D. M.; Wu, L.; Chen, G.; Gallo, E. M.; Akbashev, A. R.; Davis, P. K.; Spanier, J. E.; Rappe, A. M. Perovskite Oxides for Visible-Light-Absorbing Ferroelectric and Photovoltaic Materials. *Nature* **2013**, *503*, 509-512.

CHAPTER -4

Five-Layer Aurivillius Perovskites for Efficient COD Removal under Sunlight-Irradiation

Five-Layer Aurivillius Perovskites for Efficient COD Removal under Sunlight-Irradiation

4.1 INTRODUCTION

Layered perovskites have drawn considerable research attention in visible-light-driven photocatalysis in recent years [1-10]. Amongst them, the Aurivillius phases [11], which inevitably contain Bi as one of its constituent element, are notable due to their superior catalytic activity under visible-light [5-8]. A reduction in the band gap of Bi-containing compounds was attributed to the hybridization of O 2*p* with Bi 6*s* that pushes up the valence band edge has been discussed in Chapter 1 [4, 5]. Moreover, the reason for their high activity was also pointed out in the previous chapters [12, 13].

Recently, the interest in Aurivillius phase semiconductors has grown due to their superior activity as single oxide photocatalysts [5, 14-18]. The most simple members of the Aurivillius family, namely, Bi_2WO_6 and Bi_2MoO_6 (n = 1) were investigated for their photocatalytic activity under visible-light irradiation [14, 15]. The replacement of W by Mo or vice-versa in the Aurivillius solid solution series, $Bi_2Mo_xW_{1-x}O_6$, enabled band gap alteration among the members with enhanced visible-light-induced photocatalytic activity [16, 17]. Although, few reports on visible-light active photocatalysis over higher order members (n = 2, 3, 4) of the Aurivillius series were available [5, 7, 8, 18], more complex systems remained largely unexplored. Recently, the five layer (n = 5) Aurivillius phase, $Bi_6Ti_3Fe_2O_{18}$, has drawn attention for its ferroelectric, magnetic and optical properties [19, 20]. Moreover, the rare earth (La, Sm, Gd and Dy) substituted $Bi_6Ti_3Fe_2O_{18}$ were explored for their magnetic and magnetoelectric properties [21, 22]. The only structural report available on $Bi_6Ti_3Fe_2O_{18}$ projected it as an ordered Aurivillius phase where the central octahedral layer is fully occupied by Fe (Figure 4.1) [23]. Recognizing the effect of cation disorder in the stability of Aurivillius phases [24] and recent reports on importance of ferroelectricity in photocatalysis [25-27], we envisaged the effect of La-substitution on the phase formation, structure and its consequences on photophysical and photocatalytic properties in $Bi_6Ti_3Fe_2O_{18}$.

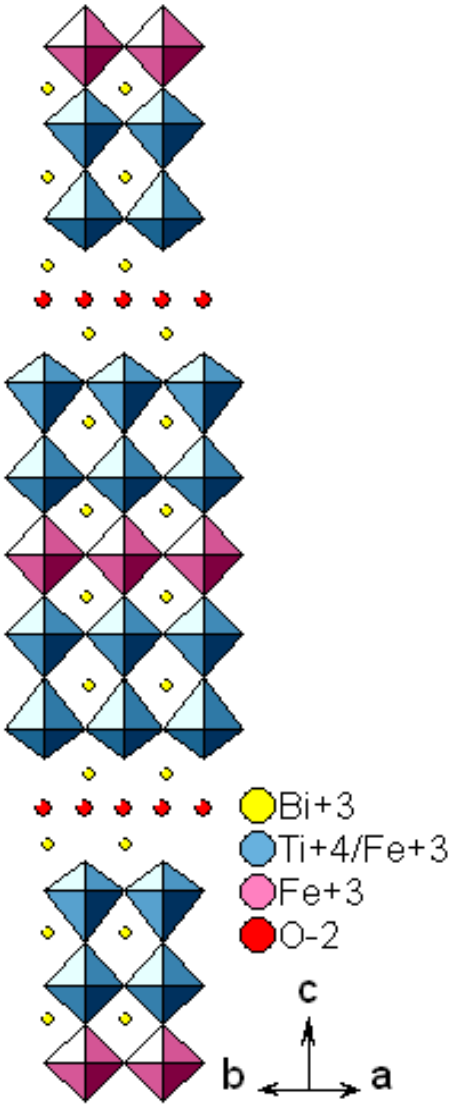

Figure 4.1 Structure of five layer (n = 5) Aurivillius phase perovskite $Bi_6Ti_3Fe_2O_{18}$.

In this chapter, we report the bulk solid-state synthesis, characterization and photocatalytic activity studies of five layered Aurivillius perovskites, $Bi_{6-x}La_xTi_3Fe_2O_{18}$ (x = 0, 1). The photocatalytic degradation of Rhodamine B (RhB) at different pH was examined under sunlight-irradiation. Both the compounds show highly efficient photocatalysis in acidic medium. The efficacy of photogenerated e^- and h^+ separation in the compounds were compared with the help PL studies. Scavenger tests were performed to elucidate the role of reactive species in the dye decoloration and COD removal process. Moreover, the photocatalytic cycle tests were performed to ascertain the stability, cyclability and sustainability of the catalysts in sunlight-driven photocatalysis.

4.2 EXPERIMENTAL SECTION

4.2.1 Materials and Synthesis

The chemical reagents were same as those used in Chapter 3. All other reagents used in our work were of analytical grade and used without any further purification. Double distilled water was used throughout the degradation experiments.

Powder samples of $Bi_{6-x}La_xTi_3Fe_2O_{18}$ (x = 0, 1) were synthesized by conventional solid–state reactions under similar conditions as reported in the literature [19]. For this purpose, Bi_2O_3, La_2O_3 (preheated at 950 °C), TiO_2 and $FeC_2O_4{\cdot}2H_2O$ were weighed in stoichiometric ratios and ground thoroughly in an agate mortar for 1 h. The mixed powders were heated at 780 °C for 2 h. Then, the mixture was ground and pressed into 8 mm diameter, ~ 2 mm thick pellets at a pressure of 120 MPa. The pellets were heated at 1000 °C for 6 h. The pellets thus obtained were ground into fine powders and used for characterization and photocatalytic experiments. $FeC_2O_4{\cdot}2H_2O$ was prepared by the same procedure as discussed in Chapter 3.

4.2.2 Photocatalytic Activity Test

RhB was chosen as a model dye pollutant for degradation under natural sunlight-irradiation at different pH. All the photocatalytic experiments were carried out during the same time on consecutive days in the month of September, 2014 (having solar Direct Normal Irradiance ~ 204 W/m^2 during the month) at IIT Roorkee (29°51′ N; 77°53′ E). In a typical degradation experiment, 0.1 g of photocatalyst was dispersed in 100 mL of RhB solution (1×10^{-5} M) of appropriate pH taken in a 250 mL beaker. The catalyst-dye suspensions were magnetically stirred at 350 rpm for 60 min in the dark to achieve equilibrium adsorption. After this, the dye–catalyst suspension was exposed to the natural sunlight. The dye degradation was monitored by periodically withdrawing 5 mL of suspensions at regular intervals and measuring its absorbance. For this, the suspension was first centrifuged at 8500 rpm to remove the suspended catalyst particles, and then, the absorbance spectra was recorded using a Shimadzu 2450 UV–visible spectrophotometer. After recording the absorbance at each time interval, the RhB solution was transferred back to the beaker to maintain the constant volume of the dye solution. A blank test was also

performed with RhB solution of same concentration without the catalyst under similar conditions to assess self-degradation of the dye. The dye degradation efficiency was calculated by using the absorbance data.

4.2.3 Chemical Oxygen Demand (COD) Test

COD of the RhB solution at different stages of the photocatalysis was analyzed by using a digestion unit (DRB 200, HACH, USA) and a UV–visible spectrophotometer. For this, multiple degradation experiments were carried out with the same set of dye and catalyst. The dye-catalyst suspensions were exposed to different time intervals and the aliquots were collected for COD analysis. The photocatalytic degradation efficiency from the COD data was calculated using the following expression:

$$\text{Photodegradation efficiency} = \frac{\text{Initial COD} - \text{Final COD}}{\text{Initial COD}} \times 100 \quad (4.1)$$

4.2.4 Scavenger Study

To understand the role of various reactive species (h^+, $^{\bullet}OH$ and $O_2^{\bullet-}$) in photocatalytic RhB degradation, different scavengers were added to the RhB solution prior to the addition of the catalyst. The experimental procedure for the active species determination was similar to that described above during photodegradation studies. In our experiments, 10 mM scavenger species were added to the RhB solution. Ammonium oxalate (AO), benzoquinone (BQ) and tertiary butyl alcohol (*t*-BuOH) was used as h^+, $O_2^{\bullet-}$ and $^{\bullet}OH$ scavengers, respectively [28, 29]. For scavenger tests, 0.14 g of solid AO, 0.18 g of BQ and 0.96 mL of *t*-BuOH were added to 100 mL dye solution to make a scavenger concentration of 10 mM in each case.

4.2.5 Stability and Reusability Study of Catalysts

The photostability and reusability of the catalysts in acidic RhB solution were performed with five consecutive cyclic runs using the same catalyst and recording the PXD pattern of the recovered catalyst at the end of the fifth cycle. For this experiment, the catalyst (0.1 g) was taken in 100 mL of RhB (1×10^{-5} M) solution, and the photocatalytic dye degradations were carried out by the same procedure as that mentioned in the activity test. After the first cycle, the catalyst was separated by centrifugation, and the recovered catalyst

was transferred to another beaker with the help of a fresh 100 mL RhB (1×10^{-5} M) solution. Then, the dye–catalyst suspension was magnetically stirred for 60 min in the dark before irradiating with sunlight. This procedure was repeated for 5 times, and at the end of the fifth cycle, the solid catalyst was separated, dried, and subjected to PXD studies.

4.2.6 Dye Adsorption Studies

To determine the adsorption of RhB on the catalyst surface at different pH, the catalyst-RhB suspension was magnetically stirred at 350 rpm in the dark for 6 h. The adsorption efficiency was monitored by evaluating the change in intensity of the characteristic absorption peak of RhB at 554 nm using a Shimadzu 2450 UV-visible spectrophotometer.

4.3 RESULTS AND DISCUSSION

4.3.1 PXD Analysis

The PXD patterns of the pristine oxides, $Bi_{6-x}La_xTi_3Fe_2O_{18}$ (x = 0, 1), are shown in Figure 4.2. A comparison of the PXD patterns with the JCPDS files reported in the literature indicated formation of five layered Aurivillius phases (JCPDS PDF # 21–0101). All the diffraction peaks in the PXD patterns were indexed in the orthorhombic space group *B*2*cb* (No. 41). The least-squares refined lattice parameters (Table 4.1) of the parent compound, $Bi_6Ti_3Fe_2O_{18}$, are in fairly good agreement with the literature values [19]. The indexed PXD data for $Bi_6Ti_3Fe_2O_{18}$ and $Bi_5LaTi_3F_2eO_{18}$ are given in Table 4.2. In the La-substituted phase, while the in-plane '*b*' parameter remains nearly the same, a slight contraction in the in-plane '*a*' and expansion in the '*c*' was noticed (Table 4.1). These are presumably due to complex interplays between cation disorder and concomitant octahedral tilting distortions [24, 30]. Similar contraction of the in-plane lattice parameters and expansion in the perpendicular direction has been observed in other La-substituted Aurivillius phases [30].

Our efforts to prepare other La-substituted (x = 2, 3, 4) five layer compounds were unsuccessful. This could possibly be rationalized on the basis of cation disorder and consequent lattice mismatch [24, 30]. With progressive La-substitution, an increased cation disorder would result in larger discrepancy in the in-plane lattice parameters, thereby rendering the five layer compound unstable and ensuing in multiphase products. In fact, we

have observed $LaFeO_3$-type perovskite impurity along with a five layer Aurivillius phase at $x = 2$. Moreover, at higher La content ($x = 3, 4$), the products were ended up in an admixture of $LaFeO_3$-type perovskite and a $Bi_{4-x}La_xTi_3O_{12}$-like three layer Aurivillius perovskite, with a growing contribution of the perovskite phase for higher La contents.

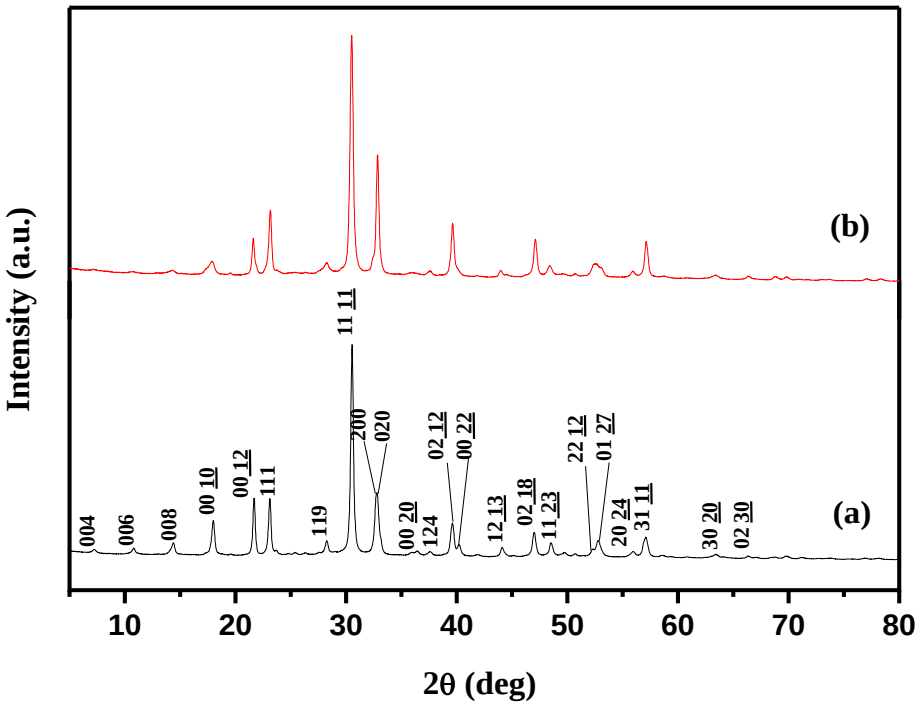

Figure 4.2 PXD patterns of (a) $Bi_6Ti_3Fe_2O_{18}$ and (b) $Bi_5LaTi_3Fe_2O_{18}$.

Table 4.1 Lattice Parameters and Band Gap of $Bi_{6-x}La_xTi_3Fe_2O_{18}$ ($x = 0, 1$)

compound	lattice parameters (Å)			band gap (eV)	
	a	*b*	*c*	E_g (1)	E_g (2)
$Bi_6Ti_3Fe_2O_{18}$	5.465(1)	5.454(1)	49.332(6)	2.05	2.54
$Bi_5LaTi_3Fe_2O_{18}$	5.445(1)	5.453(1)	49.469(9)	2.02	2.57

Table 4.2 Indexed PXD Data for $Bi_6Ti_3Fe_2O_{18}$ and $Bi_5LaTi_3Fe_2O_{18}$

$Bi_6Ti_3Fe_2O_{18}$				$Bi_5LaTi_3Fe_2O_{18}$			
h k l	d_{obs} (Å)	d_{calc} (Å)	I_{obs}	*h k l*	d_{obs} (Å)	d_{calc} (Å)	I_{obs}
0 0 8	6.155	6.166	6	0 0 8	6.183	6.184	2
0 0 10	4.924	4.933	17	0 0 10	4.946	4.947	6
0 0 12	4.109	4.111	27	0 0 12	4.123	4.122	15
1 1 1	3.844	3.848	27	1 1 1	3.840	3.842	27
1 1 9	3.155	3.156	6	1 1 9	3.155	3.155	4
1 1 11	2.925	2.926	100	1 1 11	2.928	2.926	100
0 2 0	2.730	2.728	29	0 2 0	2.725	2.726	50
1 2 4	2.392	2.394	2	1 2 4	2.389	2.392	2
0 2 12	2.273	2.273	16	0 2 12	2.273	2.274	22
1 2 13	2.052	2.053	4	1 2 13	2.053	2.053	3
0 2 18	1.932	1.933	11	0 2 18	1.928	1.935	15
1 1 23	1.875	1.875	6	1 1 23	1.880	1.878	4
0 3 4	1.799	1.799	10	0 3 4	1.800	1.798	3
2 2 12	1.748	1.747	3	2 2 12	1.743	1.744	5
0 1 27	1.732	1.733	8	0 1 27	1.724	1.724	3
2 0 24	1.642	1.643	20	2 0 24	1.643	1.643	2
3 1 11	1.612	1.612	9	3 1 11	1.611	1.608	31
3 0 20	1.465	1.465	2	3 0 20	1.464	1.463	2
0 2 30	1.408	1.408	1	0 2 30	1.411	1.411	1

$Bi_6Ti_3Fe_2O_{18}$; a = 5.465(1), b = 5.454(1), c = 49.332(6) Å

$Bi_5LaTi_3Fe_2O_{18}$; a = 5.445(1), b = 5.453(1), c = 49.469(9) Å

4.3.2 FE-SEM and EDS Analysis

The morphology and elemental composition of $Bi_{6-x}La_xTi_3Fe_2O_{18}$ (x = 0, 1) were investigated by FE-SEM and EDS analysis, respectively. Figure 4.3 shows FE-SEM images and corresponding EDS spectra of the as-synthesized compounds. The SEM images show homogeneous plate like morphology, often observed for layered compounds, throughout the imaging area. The crystallites are mostly agglomerated and composed of plate-shaped crystallites with irregular sizes ranging from few hundred nanometers to few micrometers. The elemental percentages as obtained from EDS analysis, both in spot and area basis, are in good agreement with the nominal compositions.

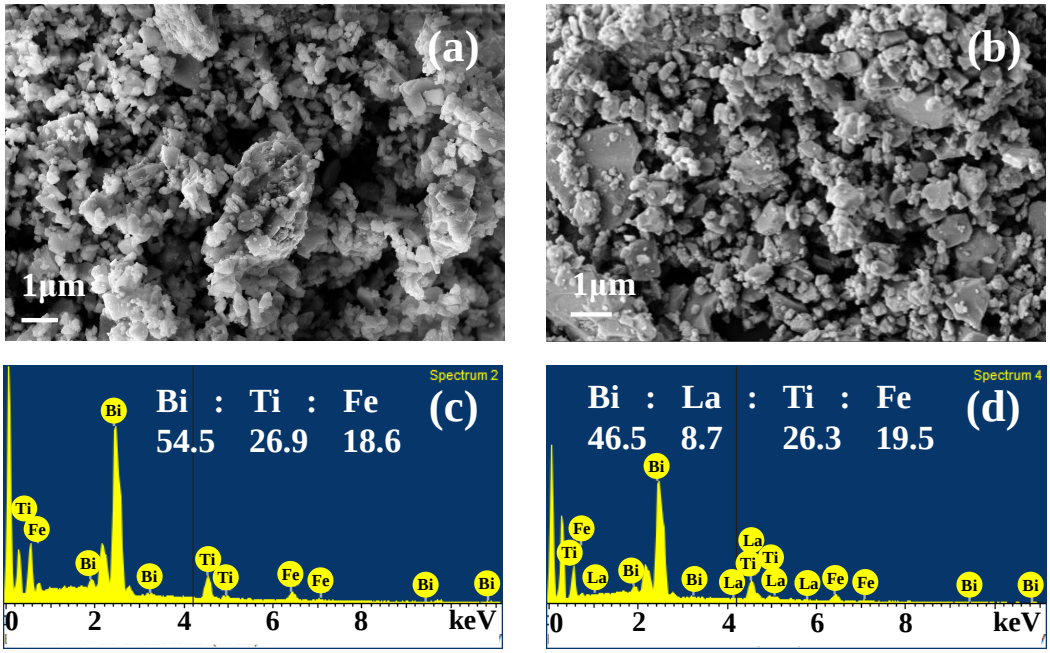

Figure 4.3 FE-SEM images of (a) $Bi_6Ti_3Fe_2O_{18}$ and (b) $Bi_5LaTi_3Fe_2O_{18}$. Corresponding EDS data are shown in (c) and (d), respectively.

Additionally, EDS elemental mapping analysis was performed to study the elemental distribution in the compounds. The mapping of selected rectangular area of FE-SEM images (Figure 4.4) of $Bi_{6-x}La_xTi_3Fe_2O_{18}$ (x = 0, 1) clearly show uniform and homogeneous distribution of all the elements in the compound. Moreover, the presence of La in the x = 1 member and a slight decrease in the amount of Bi as compared to the parent

compound (x = 0) while maintaining the elemental percentage of Ti and Fe constant, is clearly evident from the mapping analysis.

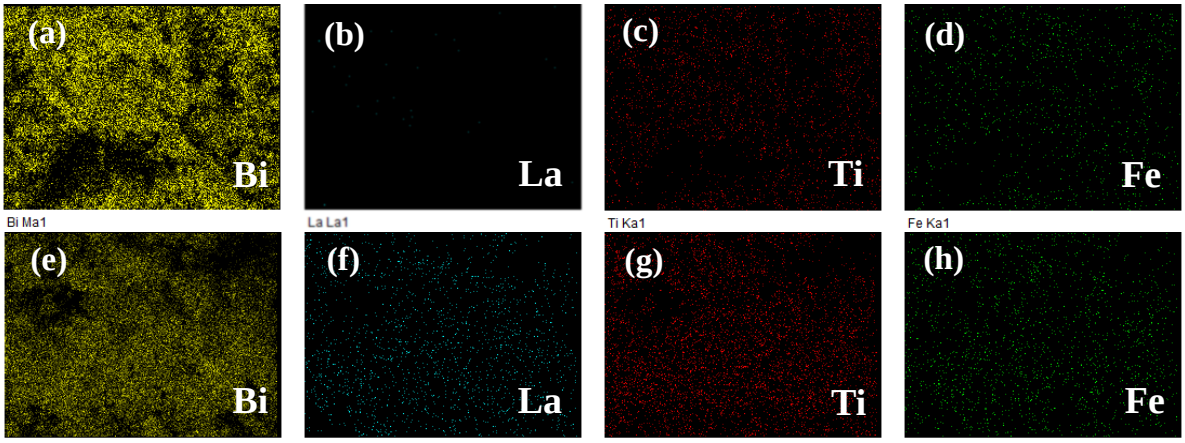

Figure 4.4 EDS elemental mapping of (a) Bi, (b) La, (c) Ti and (d) Fe in $Bi_6Ti_3Fe_2O_{18}$, and (e)–(h) show the elemental mapping for $Bi_5LaTi_3Fe_2O_{18}$ in the same order.

4.3.3 UV-vis DRS Analysis

The band gaps of $Bi_{6-x}La_xTi_3Fe_2O_{18}$ (x = 0, 1) were determined by UV-vis DRS. Figure 4.5 (a) portrays the UV-vis DRS of the compounds and confirms that they are visible light absorbers (λ_{edge} > 400 nm). The compounds show two absorption edges similar to $Bi_{5-x}La_xTi_3FeO_{15}$ (x = 1, 2) as discussed in Chapter 3. The optical bang gap (E_g) was estimated considering the semiconductors as indirect (Figure 4.5 (b) and Table 4.1). The origin of the band edges is schematically shown in the inset of Figure 4.5 (a).

4.3.4 Photocatalytic Activity

RhB was used as a model dye for degradation experiments over $Bi_{6-x}La_xTi_3Fe_2O_{18}$ (x = 0, 1) under sunlight-irradiation at various pH (2, 7, and 11). At pH 2, the ratio of residual dye concentration (C) to initial concentration (C_0) against irradiation time (Figure 4.6) plot has unveiled complete RhB degradation after 30 min of solar irradiation in presence of $Bi_5LaTi_3Fe_2O_{18}$, whereas the degradation took 35 min for $Bi_6Ti_3Fe_2O_{18}$. Moreover, the % COD removal (Figure 4.6) data for $Bi_{6-x}La_xTi_3Fe_2O_{18}$ (x = 0, 1) confirms the photocatalytic degradation of the dye at pH = 2. It is interesting to note that, the COD

removal kinetics is more or less concomitant with the decolorization kinetics indicating excellent mineralization of the dye within 30-35 min of solar irradiation.

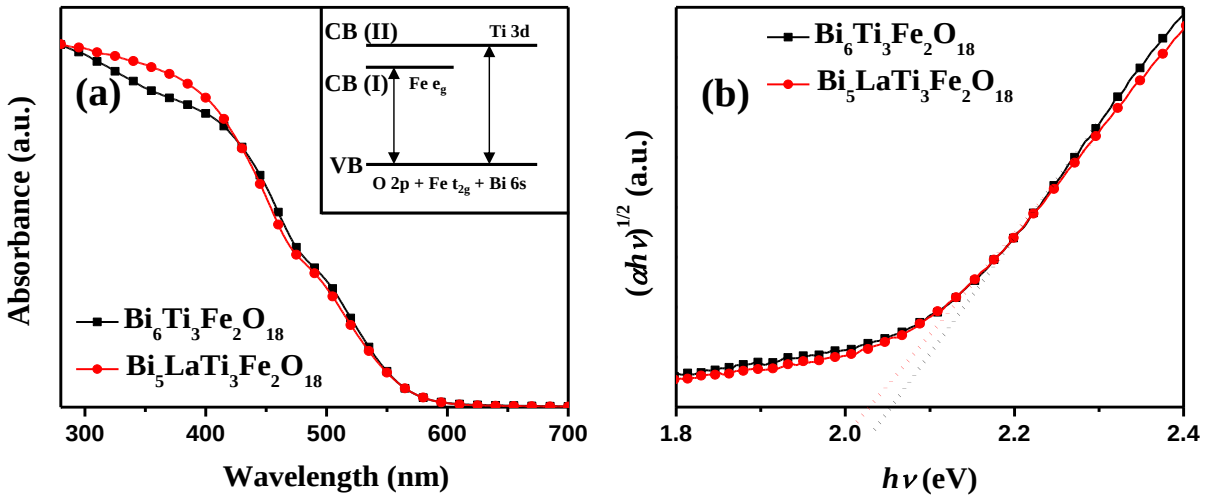

Figure 4.5 (a) UV–vis DRS of $Bi_{6-x}La_xTi_3Fe_2O_{18}$ (x = 0, 1). Inset shows a schematic of inter-band transitions. (b) Corresponding Tauc plots for band gap determination.

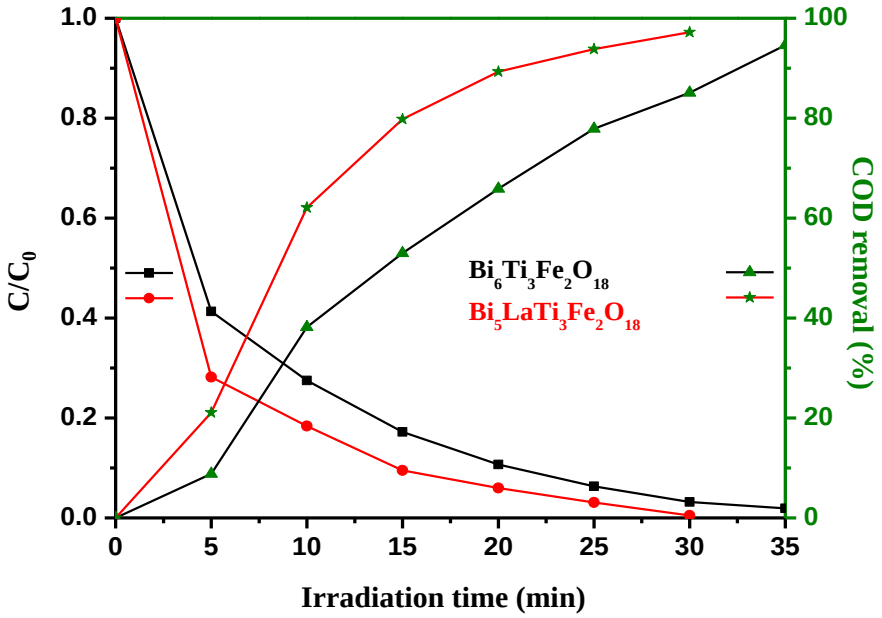

Figure 4.6 Photocatalytic degradation of RhB and COD removal efficiency with time by $Bi_{6-x}La_xTi_3Fe_2O_{18}$ (x = 0, 1) under sunlight.

It has been observed that while more than 99% of RhB is degraded over $Bi_5LaTi_3Fe_2O_{18}$, up to ~ 97% is degraded with $Bi_6Ti_3Fe_2O_{18}$ after 30 min solar irradiation

(Figure 4.7 (a)). The photocatalytic degradation kinetics of RhB over $Bi_{6-x}La_xTi_3Fe_2O_{18}$ (x = 0, 1) is fitted with a Langmuir–Hinshelwood rate expression [31].

$$\ln(C_0/C) = kt \qquad (4.2)$$

where, C_0 is the initial dye concentration, C is the dye concentration at time t and k is the rate constant. The plot between $\ln(C_0/C)$ and irradiation time (t) for the compounds is found to follow a pseudo-first-order kinetics. The rate constant (k) is calculated (Figure 4.7 (b)) to be 0.11094 and 0.13957 min^{-1} for $Bi_6Ti_3Fe_2O_{18}$ and $Bi_5LaTi_3Fe_2O_{18}$, respectively.

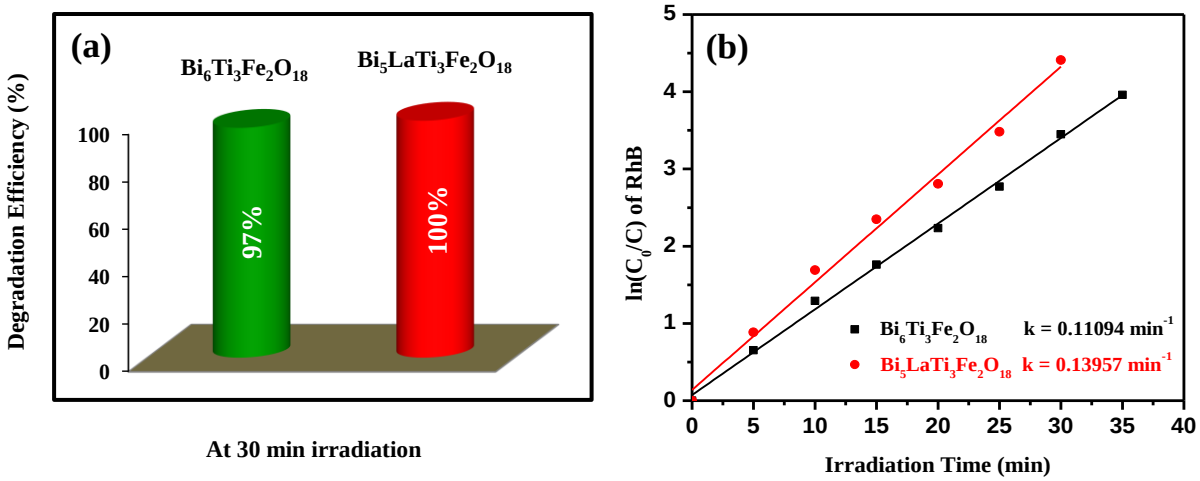

Figure 4.7 (a) RhB degradation efficiency of $Bi_{6-x}La_xTi_3Fe_2O_{18}$ (x = 0, 1) at 30 min sunlight-irradiation. (b) The plot of $\ln(C_0/C)$ as a function of time over $Bi_{6-x}La_xTi_3Fe_2O_{18}$ (x = 0, 1).

The stability of RhB was also checked with a blank run in absence of any catalyst and it was found to be resistant to any self-degradation under the reaction conditions (Figure 4.8). However, the degradation experiments carried out at higher pH, such as, neutral (pH = 7) and alkaline (pH = 11), did not show any significant degradation of the dye indicating almost zero photocatalysis (Figure 4.8).

4.3.5 PL Analysis

It is apparent that the life time and recombination rate of photogenerated e^- - h^+ pairs in the semiconductor catalysts will directly impact upon its photocatalytic activity. Since, the intensity of PL spectra is an indicator of photogenerated charge carrier's recombination rate, while a lower PL intensity indicates slower recombination rate and longer lifetime of the photogenerated e^- - h^+ pair [32], the activity of a photocatalyst can a

priori be predicted from PL spectra, in principle. An enhanced e^- - h^+ recombination would adversely affect the concentrations of reactive species generated and thus the photocatalytic activity. Figure 4.9 shows the experimental PL data for $Bi_{6-x}La_xTi_3Fe_2O_{18}$ (x = 0, 1). The compounds exhibit broad emission ranging from 410 to 650 nm with a peak around 470 nm. The higher wavelength emission edge (~ 600 nm) agrees well with the inter-band recombination. A lower PL intensity for $Bi_5LaTi_3Fe_2O_{18}$ clearly indicates a larger concentration and lifetime of electron hole pairs. Thus, based on PL studies, $Bi_5LaTi_3Fe_2O_{18}$ is expected to show higher photocatalytic degradation efficiency than the parent, $Bi_6Ti_3Fe_2O_{18}$. The PL data are consistent with the results of dye degradation experiment (see later) showing enhanced activity over $Bi_5LaTi_3Fe_2O_{18}$.

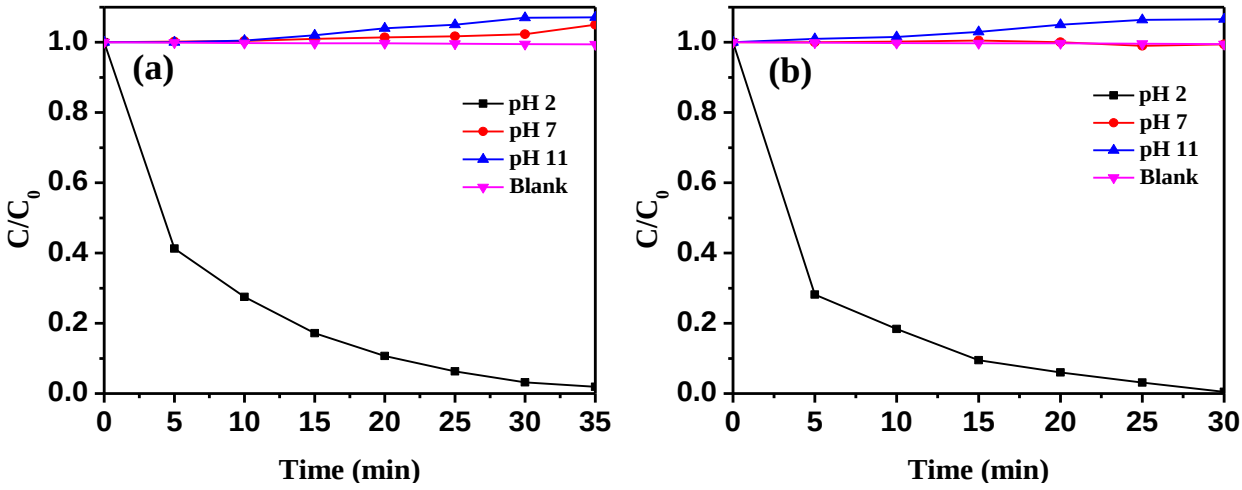

Figure 4.8 Photocatalytic degradation of RhB with time by (a) $Bi_6Ti_3Fe_2O_{18}$ and (b) $Bi_5LaTi_3Fe_2O_{18}$ under sunlight at different pH.

4.3.6 Scavenger Study

Generally, photogenerated reactive species, such as, $^{\bullet}OH$, $O_2^{\bullet-}$ and h^+ are expected to take part in the photocatalytic dye degradation process. To understand the mechanism and detect the main reactive species responsible for photocatalytic RhB degradation in presence of $Bi_5LaTi_3Fe_2O_{18}$, scavenger tests were carried out employing benzoquinone (BQ), ammonium oxalate (AO) and *tert*-butanol (*t*-BuOH). In the experiment with addition of AO (hole scavenger) to the catalyst-dye suspension, the RhB degradation was drastically suppressed as compared to that in absence of scavenger (Figure 4.10), conforming to h^+ being the active player in the dye degradation. Moreover, on introduction of BQ ($O_2^{\bullet-}$

scavenger), the dye degradation was inhibited to a moderate extent. However, the addition of *t*-BuOH ($^{\bullet}$OH scavenger) affected the degradation rate only to a small extent. On the basis of the above findings, it appears that h^+ and $O_2^{\bullet-}$ play predominant role in photocatalytic RhB degradation over $Bi_5LaTi_3Fe_2O_{18}$ in the acidic medium under sunlight-irradiation, although a minor role of $^{\bullet}$OH cannot be completely ruled out.

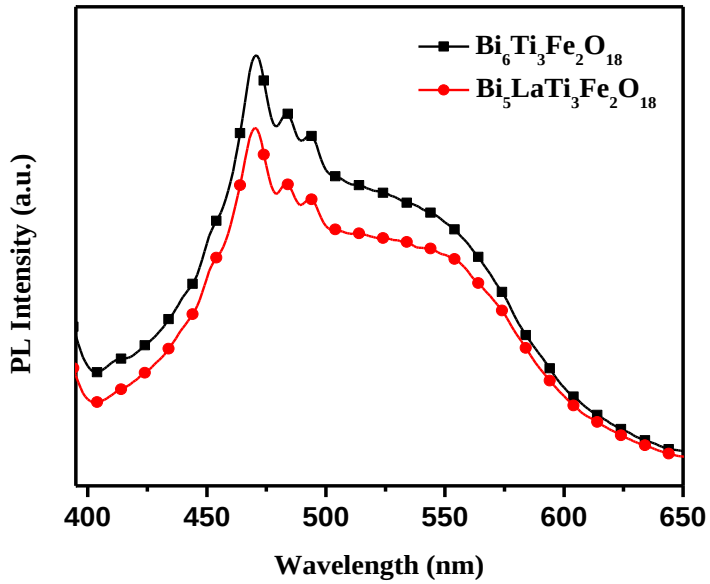

Figure 4.9 PL spectra of $Bi_{6-x}La_xTi_3Fe_2O_{18}$ (x = 0, 1) at room temperature (excitation at 350 nm).

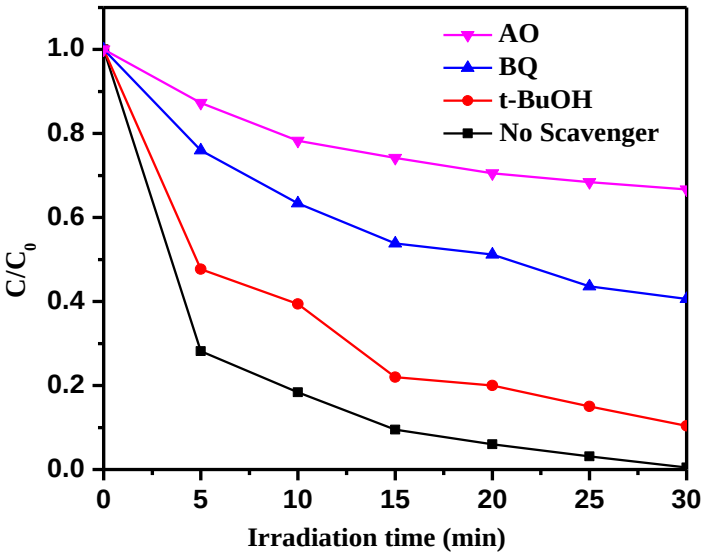

Figure 4.10 RhB degradation over $Bi_5LaTi_3Fe_2O_{18}$ in the presence of different scavengers under sunlight-irradiation.

4.3.7 Photocatalytic Cycle and Catalyst Stability

The photocatalyst stability and reusability is an important issue for their practical use. For this purpose, the photocatalytic degradation of RhB over $Bi_5LaTi_3Fe_2O_{18}$ was carried out for five consecutive cycles (Figure 4.11 (a)). It has been observed that ~ 96 % of RhB is degraded even after four successive cyclic runs within 30 min of solar irradiation, demonstrating no noticeable loss in the activity of the catalyst.

Figure 4.11 (b) shows the PXD pattern of recovered $Bi_5LaTi_3Fe_2O_{18}$ catalyst powder at the end of fifth degradation cycle. It retains good crystallinity like the original compound. The absence of any impurity reflection in the PXD pattern demonstrates that the parent phase remains intact without showing any sign of catalyst decomposition. This seems consistent with the excellent photostability of the catalyst under acidic pH. Therefore, it is evident that $Bi_5LaTi_3Fe_2O_{18}$ does not undergo any photocorrosion or photoleaching during the dye degradation experiments. The dye degradation cycle test results and post-catalysis PXD pattern of the parent $Bi_6Ti_3Fe_2O_{18}$ also demonstrates its excellent recyclability and stability even under acidic reaction conditions (Figure 4.12).

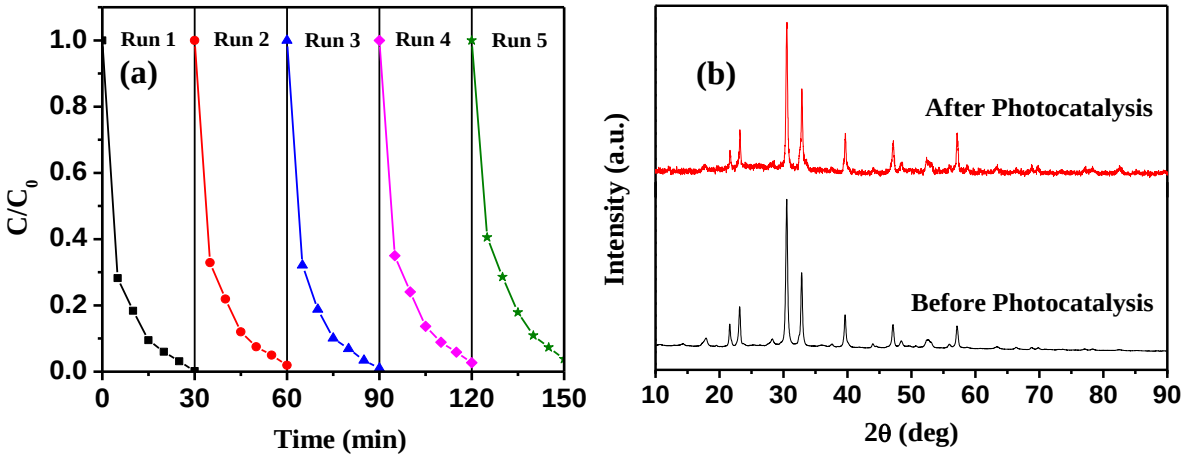

Figure 4.11 (a) Time profiles of RhB degradation for five successive cycles with $Bi_5LaTi_3Fe_2O_{18}$. (b) PXD pattern of $Bi_5LaTi_3Fe_2O_{18}$ before and after five successive cyclic photocatalytic RhB degradation.

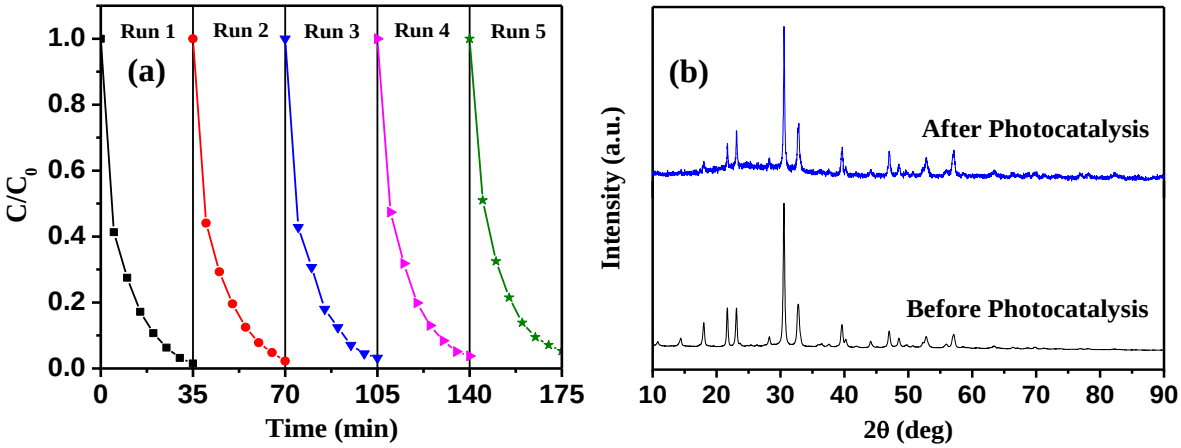

Figure 4.12 (a) Time profiles of RhB degradation for five successive cycles with $Bi_6Ti_3Fe_2O_{18}$ under sunlight-irradiation. (b) PXD pattern of $Bi_6Ti_3Fe_2O_{18}$ before and after the photocatalytic RhB degradation.

4.3.8 Energy Level Diagram (ELD) and Mechanism of Photocatalysis

To understand the enhanced photocatalytic activity of the catalysts, we have calculated empirically the valence and conduction band edges of the photocatalyst and analyzed their band energy alignment with respect to the potential of $^{\bullet}OH/H_2O$, $O_2/O_2^{\bullet-}$ and HOMO–LUMO levels of RhB. The band edge positions of the semiconductor photocatalyst were calculated using the following empirical formula [33] and in a similar manner as detailed in Chapter 3.

$$E_{CB} = \chi(A_aB_bC_c) - \tfrac{1}{2}\, E_g + E_0 \quad (4.3)$$

$$E_{VB} = E_{CB} + E_g \quad (4.4)$$

Using the calculated χ value (5.95 eV) and following the above formulas, the bottom of the conduction bands, E_{CB} (1) and E_{CB} (2) for $Bi_5LaTi_3Fe_2O_{18}$ are calculated to be 0.44 and –0.11 eV, respectively. Correspondingly, the top of the valence band is 2.46 eV. The band edges of $Bi_6Ti_3Fe_2O_{18}$ are summarized in Table 4.3. Figure 4.13 shows the band alignment diagram of $Bi_6LaTi_3Fe_2O_{18}$ with respect to the potential of $^{\bullet}OH/H_2O$, $O_2/O_2^{\bullet-}$ and HOMO-LUMO levels of RhB. The literature reported potentials for the generation of $^{\bullet}OH$ ($E_{\bullet OH/H2O}$= +2.68 eV *vs. NHE*), $O_2^{\bullet-}$ ($E_{O2/O2\bullet-}$= +0.13 eV *vs. NHE*) and HOMO–LUMO levels of RhB (E_{HOMO} = 0.95 eV and E_{LUMO} = –1.42 eV) are used to construct the energy level diagram [34, 35].

According to the ELD, the photogenerated electrons in E_{CB} (2) of $Bi_5LaTi_3Fe_2O_{18}$ could reduce the dissolved O_2 to produce $O_2^{\bullet-}$ radicals because the E_{CB} (2) (–0.11 eV *vs. NHE*) is higher than E ($O_2/O_2^{\bullet-}$) (+0.13eV *vs. NHE*). However, the position of E_{CB} (1) (0.44 eV *vs. NHE*) below the potential of $O_2/O_2^{\bullet-}$ is not in favor of $O_2^{\bullet-}$ generation. Moreover, the photoinduced holes (h^+) in E_{VB} cannot produce $^{\bullet}OH$ radicals by oxidizing H_2O because E_{VB} (+2.46 eV *vs. NHE*) is above E ($^{\bullet}OH/H_2O$) (+2.68eV *vs. NHE*) in the ELD. The above facts explains the results of BQ scavenger test, to show a moderate role of $O_2^{\bullet-}$ and the *t*-BuOH scavenger test, to indicate only a minor role of $^{\bullet}OH$ in the RhB degradation. Although the band diagram is not in favor of $^{\bullet}OH$ formation, there is a possibility of $^{\bullet}OH$ formation through a secondary process mediated by superoxide radicals [36]. This can probably explain the marginal effect in the degradation behavior of RhB in presence of *t*-BuOH scavenger.

Table 4.3 Calculated Values of Valence and Conduction Band Positions of $Bi_{6-x}La_xTi_3Fe_2O_{18}$ (x = 0, 1)

Compound	valence band (eV)	conduction band-1 (eV)	conduction band-2 (eV)
$Bi_6Ti_3Fe_2O_{18}$	2.57	0.52	0.03
$Bi_5LaTi_3Fe_2O_{18}$	2.46	0.44	–0.11

Furthermore, the positioning of E_{VB} below the HOMO levels of RhB favors h^+ transfer from the photocatalyst to adsorbed dye molecule and thereby RhB degradation. The drastic decrease in the activity in presence of an h^+ scavenger (AO) further confirmed the active role of holes in the RhB degradation. Moreover, the minor role of $O_2^{\bullet-}$ radicals indicates that the dye degradation is mostly driven by photocatalysis rather than sensitization mechanism.

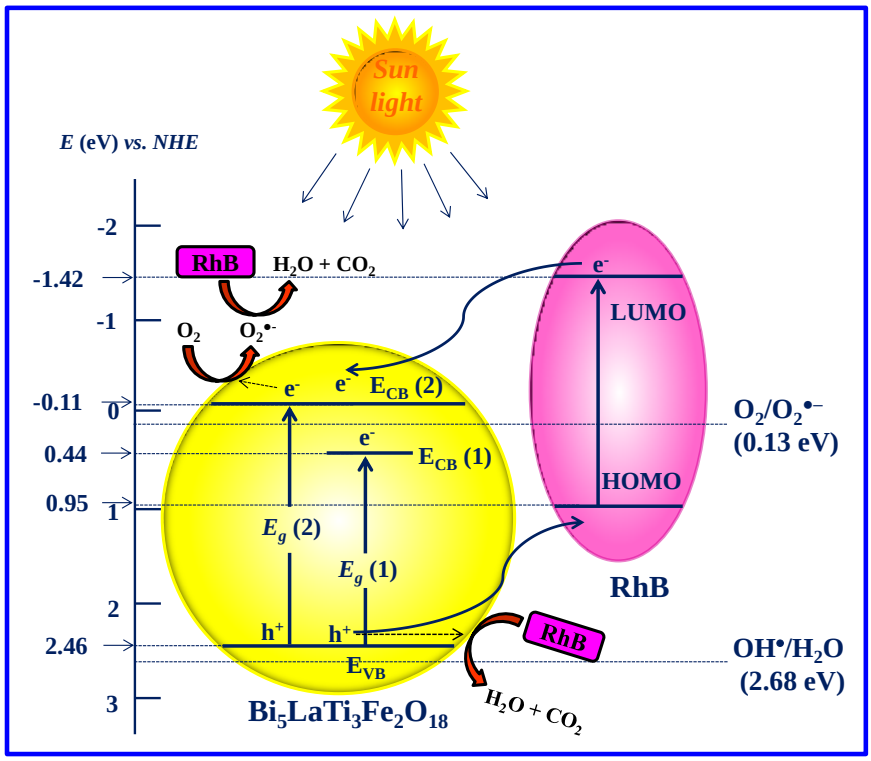

Figure 4.13 Schematic energy level diagram of $Bi_5LaTi_3Fe_2O_{18}$ with respect to potential (vs. *NHE*) of $^{\bullet}OH/H_2O$, $O_2/O_2^{\bullet-}$ and the HOMO–LUMO levels of RhB.

4.3.9 Adsorption, ζ-Potential and COD Removal Efficiency

To probe into the excellent dye mineralization concomitant with decoloration by the catalysts, dye adsorption and ζ-potential measurements were carried out. We believed that the attachment of the RhB molecule with photocatalyst surface plays a key role in h^+ mediated RhB degradation. To evaluate the role of RhB adsorption on the degradation rate, we have carried out adsorption tests at various pH in the dark. Interestingly, the adsorption results indicate that the maximum adsorption took place in acidic medium and that a large decrease in the adsorption was found in neutral and alkaline media (Figure 4.14 (a)). These results are in good agreement with the enhanced activity of the photocatalyst in acidic medium and very poor degradation in neutral and alkaline media. Moreover, the degradation rate of the photocatalysts follows the adsorption order resulting $Bi_5LaTi_3Fe_2O_{18}$ as more efficient than the parent $Bi_6Ti_3Fe_2O_{18}$.

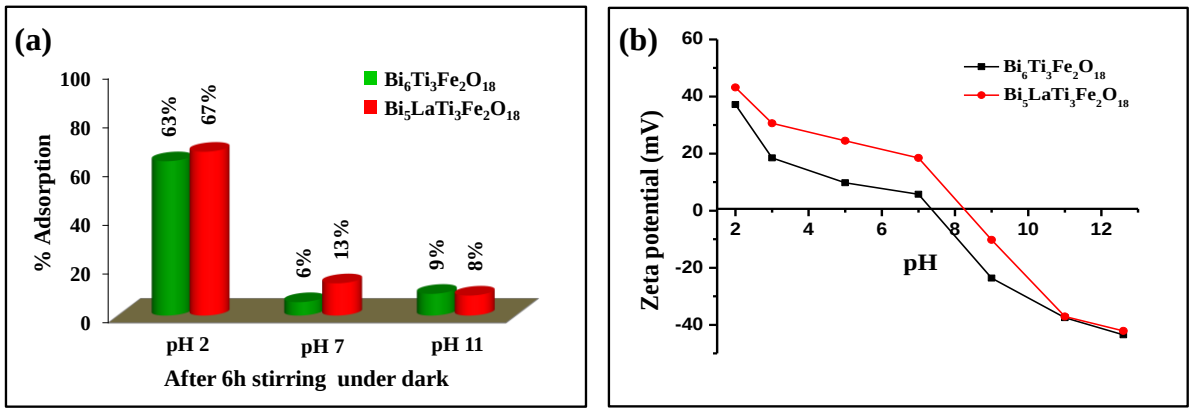

Figure 4.14 (a) Influence of pH on RhB adsorption onto $Bi_{6-x}La_xTi_3Fe_2O_{18}$ (x = 0, 1) catalyst surfaces. (b) ζ-potential of $Bi_{6-x}La_xTi_3Fe_2O_{18}$ (x = 0, 1) catalysts at different pH.

Realizing that the photocatalyst surface charge plays an important role in the dye adsorption, ζ-potential measurements were conducted to determine the surface charge of the photocatalysts. Figure 4.14 (b) displays the difference in ζ-potential of the compounds, $Bi_{6-x}La_xTi_3Fe_2O_{18}$ (x = 0, 1), at various pH. While, more positive ζ-potentials are observed in acidic medium, a decreasing trend is prevalent with increasing pH and finally negative ζ-potentials are exhibited in the alkaline medium. This trend is due to the adsorption of H^+ and OH^- ions on the surface hydroxyl groups of the photocatalyst.

Interestingly, the magnitude of the ζ-potential is reflected in the dye adsorption at pH 2. The maximum adsorption of dye molecules took place on $Bi_5LaTi_3Fe_2O_{18}$, which contain the highest ζ-potential (+ 43.2 mV) followed by $Bi_6Ti_3Fe_2O_{18}$ which had a ζ-potential +37.2 mV. The adsorption of RhB decreases while going from acidic to alkaline pH due to decreasing positive ζ and ultimately negative potentials. The extent of adsorption is explained on the basis of electrostatic interaction of the dye molecules with the charged surfaces depending on their modes of adsorption as discussed in Chapter 3. It is believed that a large surface charge mediated adsorption of the dye molecules help in efficient h^+ transfer from the semiconductor surface thereby enhancing the COD removal efficiency. This is consistent with the fact that the La-substituted analog, $Bi_5LaTi_3Fe_2O_{18}$, shows highest activity and COD removal which is almost coincident with the dye decoloration kinetics, having the maximum extent of dye adsorption in comparison to the parent compound.

Nevertheless, at this juncture it is noteworthy to point out that La-substitution in $Bi_6Ti_3Fe_2O_{18}$ has resulted in enhanced photocatalytic activity with more or less a subtle or no change in the visible band gap and structure. This can primarily be attributed to improved separation of photogenerated e^-–h^+ pairs as evidenced by PL data of the semiconductors. It is believed that La-substitution can be an effective strategy in layered Aurivillius compounds for enhanced photocatalytic activity. Similar enhanced activity of La-substituted pyrochlore type oxides are recently reported in the literature [37]. Considering the fact that the compounds crystallize in noncentrosymmetric space groups and are polar, further studies are required to investigate any possible role of ferroelectricity and internal electric fields for exhibiting enhanced photocatalytic activity.

In summary, solid-state bulk synthesis of single-phase five-layered Aurivillius perovskites, $Bi_{6-x}La_xTi_3Fe_2O_{18}$ (x = 0, 1) are reported in this chapter. The UV-vis DRS established the compounds as visible-band-gap semiconductors. The La-substitution was appeared to help in the suppression of photogenerated e^-–h^+ recombination as evidenced by PL spectra. The photocatalytic Rhodamine B degradation in the acidic medium under sunlight-irradiation indicated $Bi_5LaTi_3Fe_2O_{18}$ as the most active catalyst among the two five layered Aurivillius compounds reported here. The enhanced activity of $Bi_5LaTi_3Fe_2O_{18}$ is attributed to the effective separation of photogenerated e^-–h^+ pairs and improved dye adsorption in the acidic medium. The predominant role of photogenerated holes in the RhB degradation has been established by reactive species trapping experiments. The conduction and valence band alignment of $Bi_5LaTi_3Fe_2O_{18}$ with respect to potentials of $^{\bullet}OH/H_2O$, $O_2/O_2^{\bullet-}$ and HOMO–LUMO levels of RhB supports the involvement of h^+ and formation of $O_2^{\bullet-}$ as reactive species. Furthermore, a large positive ζ-potential has been ascribed to improved dye adsorption which ultimately led to an enhanced photocatalytic activity and efficient COD removal by the catalysts. Moreover, the compounds are reusable and stable under the acidic medium even after five consecutive cycles of degradation without any noticeable loss in activity.

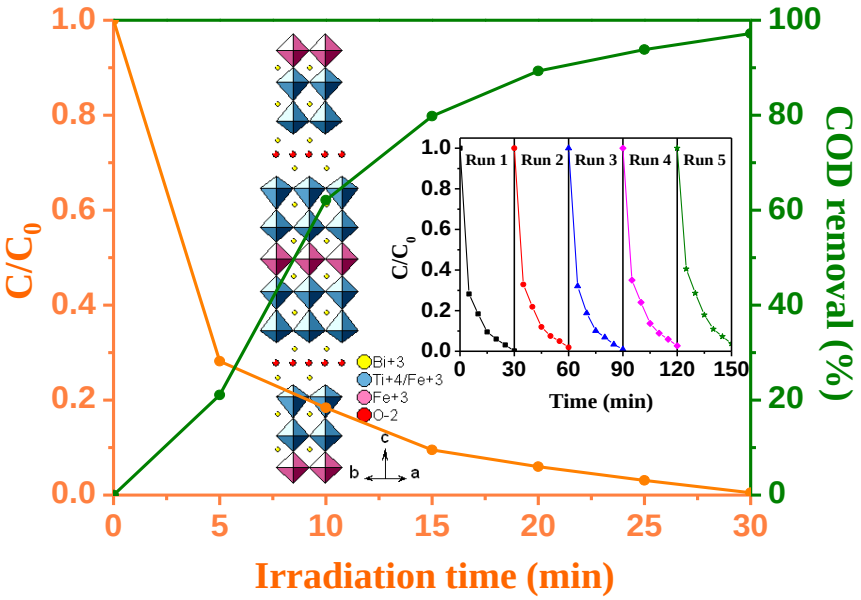
C/C0
COD removal (%)
Irradiation time (min)
Run 1
Run 2
Run 3
Run 4
Run 5
Time (min)
Bi+3
Ti+4/Fe+3
Fe+3
O-2
c
b
a

REFERENCES

1. Osterloh, F. E. Inorganic Materials as Catalysts for Photochemical Splitting of Water. *Chem. Mater.* **2008**, *20*, 35-54.

2. Kudo, A.; Miseki, Y. Heterogeneous Photocatalyst Materials for Water Splitting. *Chem. Soc. Rev.* **2009**, *38*, 253-278.

3. Chen, X.; Shen, S.; Guo, L.; Mao, S. S. Semiconductor-Based Photocatalytic Hydrogen Generation. *Chem. Rev.* **2010**, *110*, 6503-6570.

4. Yoshimura, J.; Ebana, Y.; Kondo, J.; Domen, K.; Tanaka, A. Visible Light Induced Photocatalytic Behavior of a Layered Perovskite Type Niobate, $RbPb_2Nb_3O_{10}$. *J. Phys. Chem.* **1993**, *97*, 1970-1973.

5. Kim, H. G.; Hwang, D. W.; Lee, J. S. An Undoped, Single-Phase Oxide Photocatalyst Working under Visible Light. *J. Am. Chem. Soc.* **2004**, *126*, 8912-8913.

6. Tang, J.; Zou, Z.; Ye, J. Photocatalytic Decomposition of Organic Contaminants by Bi_2WO_6 under Visible Light Irradiation. *Catal. Lett.* **2004**, *92*, 53-56.

7. Muktha, B.; Priya, M. H.; Madras, G.; Guru Row, T. N. Synthesis, Structure, and Photocatalysis in a New Structural Variant of the Aurivillius Phase: $LiBi_4M_3O_{14}$ (M = Nb, Ta) *J. Phys. Chem. B* **2005**, *109*, 11442-11449.

8. Jang, J. S.; Yoon, S. S.; Borse, P. H.; Lim, K. T.; Hong, T. E.; Jeong, E. D.; Jung, O.-S.; Shim, Y. B.; Kim, H. G. Synthesis and Characterization of Aurivillius Phase $Bi_5Ti_3FeO_{15}$ Layered Perovskite for Visible Light Photocatalysis. *J. Cer. Soc. Jpn.* **2009**, *117*, 1268-1272.

9. Arney, D.; Maggard, P. A. Effect of Platelet-Shaped Surfaces and Silver-Cation Exchange on the Photocatalytic Hydrogen Production of $RbLaNb_2O_7$. *ACS Catal.* **2012**, *2*, 1711-1717.

10. Boltersdorf, J.; Maggard, P. A. Silver Exchange of Layered Metal Oxides and Their Photocatalytic Activities. *ACS Catal.* **2013**, *3*, 2547-2555.

11. Subbarao, E. C. Crystal Chemistry of Mixed Bismuth Oxides with Layer-Type Structures. *J. Am. Ceram. Soc.* **1962**, *45*, 166-169.

12. Oshikiri, M.; Boero, M.; Ye, J.; Zou, Z.; Kido, G. Electronic Structures of Promising Photocatalysts $InMO_4$ (M = V, Nb, Ta) and $BiVO_4$ for Water Decomposition in the Visible Wavelength Region. *J. Chem. Phys.* **2002**, *117*, 7313-7318.

13. Tang, J.; Zou, Z.; Ye, J. Efficient Photocatalytic Decomposition of Organic Contaminants over $CaBi_2O_4$ under Visible-Light Irradiation. *Angew. Chem. Int. Ed.* **2004**, *43*, 4463-4466.

14. Kudo, A.; Hijii, S. H_2 or O_2 Evolution from Aqueous Solution on Layered Oxide Photocatalysts Consisting of Bi^{3+} with $6s^2$ Configuration and d^0 Transition Metal Ions. *Chem. Lett.* **1999**, *28*, 1103-1104.

15. Shimodaira, Y.; Kato, H.; Kobayashi, H.; Kudo, A. Photophysical Properties and Photocatalytic Activities of Bismuth Molybdates under Visible Light Irradiation. *J. Phys. Chem. B* **2006**, *110*, 17790-17797.

16. Zhou, L.; Yu, M.; Yang, J.; Wang, Y.; Yu, C. Nanosheet-Based $Bi_2Mo_xW_{1-x}O_6$ Solid Solutions with Adjustable Band Gaps and Enhanced Visible-Light-Driven Photocatalytic Activities. *J. Phys. Chem. C* **2010**, *114*, 18812-18818.

17. Zhang, L.; Man, Y.; Zhu, Y. Effects of Mo Replacement on the Structure and Visible-Light-Induced Photocatalytic Performances of Bi_2WO_6 Photocatalyst. *ACS Catal.* **2011**, *1*, 841-848.

18. Kim, H. G.; Borse, P. H.; Jang, J. S.; Jeong, E. D.; Lee, J. S. Enhanced Photochemical Properties of Electron Rich W-Doped $PbBi_2Nb_2O_9$ Layered Perovskite Material under Visible-Light Irradiation. *Mater. Lett.* **2008**, *62*, 1427-1430.

19. Li, J.-B.; Huang, Y. P.; Rao, G. H.; Liu, G. Y.; Luo, J.; Chen, J. R.; Liang, J. K. Ferroelectric Transition of Aurivillius Compounds $Bi_5Ti_3FeO_{15}$ and $Bi_6Ti_3Fe_2O_{18}$. *Appl. Phys. Lett.* **2010**, *96*, 222903-222905.

20. Bai, W.; Xu, W. F.; Wu, J.; Zhu, J. Y.; Chen, G.; Yang, J.; Lin, T.; Meng, X. J.; Tang, X. D.; Chu, J. H. Investigations on Electrical, Magnetic and Optical Behaviors of Five-Layered Aurivillius $Bi_6Ti_3Fe_2O_{18}$ Polycrystalline Films. *Thin Solid Films* **2012**, *525*, 195-199.

21. Prasad, N. V.; Kumar, G. S. Magnetic and Magnetoelectric Measurements on Rare-Earth-Substituted Five-Layered $Bi_6Fe_2Ti_3O_{18}$ Compound. *J. Magn. Magn. Mater.* **2000**, *213*, 349-356.

22. Prasad, N. V.; Kumar, G. S. Low Temperature Magnetoelectric Measurements on Rare Earth Substituted Bismuth Layered Structure Ferroelectromagnetic Ceramic. *Mat. Sci. Eng. B* **2004**, *108*, 194-199.

23. García-Guaderrama, M.; Fuentes-Montero, L.; Rodriguez, A.; Fuentes, L. Structural Characterization of $Bi_6Ti_3Fe_2O_{18}$ Obtained by Molten Salt Synthesis. *Integrated Ferroelectrics* **2006**, *83*, 41-47.

24. Hervoches, C. H.; Lightfoot, P. Cation Disorder in Three-Layer Aurivillius Phases: Structural Studies of $Bi_{2-x}Sr_{2+x}Ti_{1-x}Nb_{2+x}O_{12}$ ($0 < x < 0.8$) and $Bi_{4-x}La_xTi_3O_{12}$ ($x = 1$ and 2). *J. Solid State Chem.* **2000**, *153*, 66-73.

25. Cui, Y.; Briscoe, J.; Dunn, S. Effect of Ferroelectricity on Solar-Light-Driven Photocatalytic Activity of $BaTiO_3$-Influence on the Carrier Separation and Stern Layer Formation. *Chem. Mater.* **2013**, *25*, 4215-4223.

26. Li, L.; Salvador, P. A.; Rohrer, G. S. Photocatalysts with Internal Electric Fields. *Nanoscale* **2014**, *6*, 24-42.

27. Grinberg, I.; West, D. V.; Torres, M.; Gou, G.; Stein, D. M.; Wu, L.; Chen, G.; Gallo, E. M.; Akbashev, A. R.; Davis, P. K.; Spanier, J. E.; Rappe, A. M. Perovskite Oxides for Visible-Light-Absorbing Ferroelectric and Photovoltaic Materials. *Nature* **2013**, *503*, 509-512.

28. Wang, Y.; Deng, K.; Zhang, L. Visible Light Photocatalysis of BiOI and Its Photocatalytic Activity Enhancement by in Situ Ionic Liquid Modification. *J. Phys. Chem. C* **2011**, *115*, 14300-14308.

29. Kumar, S.; Khanchandani, S.; Thirumal, M.; Ganguli, A. K. Achieving Enhanced Visible-Light-Driven Photocatalysis Using Type-II $NaNbO_3$/CdS Core/Shell Heterostructures. *ACS Appl. Mater. Interfaces* **2014**, *6*, 13221-13233.

30. Chu, M.-W.; Caldes, M.-T.; Brohan, L.; Ganne, M.; Marie, A.-M.; Joubert, O.; Piffard, Y. Bulk and Surface Structures of the Aurivillius Phases: $Bi_{4-x}La_xTi_3O_{12}$ ($0 \leq x \leq 2.00$). *Chem. Mater.* **2004**, *16*, 31-42.

31. Fu, H.; Pan, C.; Yao, W.; Zhu, Y. Visible−Light−Induced Degradation of Rhodamine B by Nanosized Bi_2WO_6. *J. Phys. Chem. B* **2005**, *109*, 22432-22439.

32. Fujihara, K.; Izuni, S.; Ohno, S.; Matsumura, M. Time-resolved Photoluminescence of Particulate TiO_2 Photocatalysts Suspended in Aqueous Solution. *J. Photochem. Photobiol. A* **2000**, *132*, 99-104.

33. Lv, J.; Kako, T.; Zou, Z.; Ye, J. Band Structure Design and Photocatalytic Activity of In_2O_3/N−$InNbO_4$ Composite. *Appl. Phys. Lett.* **2009**, *95*, 032107-032109.

34. Kumar, S.; Surendar, T.; Baruah, A.; Shanker, V. Synthesis of a Novel and Stable g-C_3N_4-Ag_3PO_4 Hybrid Nanocomposite Photocatalyst and Study of the Photocatalytic Activity under Visible Light Irradiation. *J. Mater. Chem. A* **2013**, *1*, 5333-5340.

35. Pan, L.; Zou, J.; Liu, X.; Liu, X.; Wang, S.; Zhang, X.; Wang, L. Visible-Light-Induced Photodegradation of Rhodamine B over Hierarchical TiO_2: Effects of Storage Period and Water-Mediated Adsorption Switch. *Ind. Eng. Chem. Res.* **2012**, *51*, 12782-12786.

36. Zhao, J.; Wu, T.; Wu, K.; Oikawa, K.; Hidaka, H.; Serpone, N. Photoassisted Degradation of Dye Pollutants. 3. Degradation of the Cationic Dye Rhodamine B in Aqueous Anionic Surfactant/TiO_2 Dispersions under Visible Light Irradiation: Evidence for the Need of Substrate Adsorption on TiO_2 Particles. *Environ. Sci. Technol.* **1998**, *38*, 2394-2400.

37. Sayed, F. N.; Grover, V.; Mandal, B. P.; Tyagi, A. K. Influence of La^{3+} Substitution on Electrical and Photocatalytic Behavior of Complex $Bi_2Sn_2O_7$ Oxides. *J. Phys. Chem. C* **2013**, *117*, 10929-10938.

CHAPTER -5

New Five-Layer Aurivillius Perovskites for Sunlight-Driven Selective Dye Degradation

New Five-Layer Aurivillius Perovskites for Sunlight-Driven Selective Dye Degradation

5.1 INTRODUCTION

Efficient and selective removal of harmful pollutants from wastewaters in presence of other less harmful ones is a challenging task and such studies are rare in the current literature. Few reports of selective photocatalytic oxidation of organic compounds and contaminants with TiO_2 based oxides are known in the literature [1-5]. The photocatalytic selectivity was reported to be achieved by nanostructured rutile TiO_2 [1], base-modified anatase TiO_2 nanocrystals [5], mesoporous TiO_2 [2] and by constructing molecular recognition sites on TiO_2 [4]. In all above selective photocatalysis the catalysts utilize UV light. With respect to selectivity in dye degradation studies, there is a very recent report on sorption mediated visible-light-driven dye degradation by nano $CuWO_4$ and $Cu_3Mo_2O_9$ [6]. Moreover, the only other report of selective Methylene Blue (MB) degradation over $CuFe_2O_4$ nanoparticles was mediated by $NaBH_4$ [7]. Considering MB as a worldwide water contaminant, its selective removal from water is imperative. So, the development novel photocatalysts working under sunlight will be highly desirable for selective removal of MB.

There is considerable research attention in Bi-containing Aurivillius family of oxides due to their high efficiency in visible-light-driven photocatalysis. The role of Bi in enhanced photocatalysis has already been discussed in preceding chapters. During our search for new layered perovskites for efficient sunlight-driven photocatalysis, we have demonstrated excellent Rhodamine B degradation over four layer (n = 4) and five layer (n = 5) Aurivillius perovskites (in Chapters 3 & 4, respectively). Thus, research interests in Aurivillius phase photocatalysts continue to grow as single semiconductor oxide catalysts without heterojunction or co-catalyst loading for superior photocatalytic performances [8-12]. Moreover, it was realized that the degradation was facilitated by dye adsorption that varied with pH to a large extent. Based on this, it was imagined that it may be possible to demonstrate selective degradation of dyes with variable pH.

In this chapter, we have envisaged new members of five layered Aurivillius perovskites by both *A* and *B*-site co-substitution through cationic charge manipulation. The

replacement of one of the Fe^{3+} by Ti^{4+} in the parent composition, $Bi_6Ti_3Fe_2O_{18}$, makes the B-site cationic charge 1+ unit higher which is compensated by substituting one trivalent Bi by any divalent cations, such as, Ca^{2+}, Sr^{2+}, Ba^{2+} or Pb^{2+} resulting new Aurivillius perovskite compositions, $Bi_5ATi_4FeO_{18}$ (*A* = divalent cation). We thought it would be interesting to investigate the phase formation and structures of these new compositions and study their optical and photocatalytic properties.

The solid-states synthesis and characterization of a new series of Aurivillius layered perovskites, $Bi_5ATi_4FeO_{18}$ (*A* = Ca, Sr and Pb) are reported. Selective photocatalytic degradation of RhB and MB from a mixed RhB-MB solution at different pH has been investigated under sunlight-irradiation. In addition, the photocatalytic degradation of individual RhB and MB at different pH is also studied. Moreover, the reusability and stability of the photocatalysts are evaluated by performing five successive dye degradation cycles and a post-catalysis PXD pattern analysis, respectively. Further, for the detection of reactive species and elucidation of plausible mechanism of selective dye degradation, PL, adsorption, zeta-potential and scavenger tests are performed. The details of the investigation are presented in subsequent sections of this chapter.

5.2 EXPERIMENTAL SECTION

5.2.1 Materials and Synthesis

Bi_2O_3 (≥ 98%), $CaCO_3$ (≥ 99%), $SrCO_3$ (≥ 99.9%), PbO (≥ 99%), TiO_2 (99.8%) and $FeC_2O_4{\cdot}2H_2O$ (99%) were purchased from Sigma-Aldrich and used as received. The other reagents employed in our experiments were of analytical grade and used without any further purification. All the dye solutions were prepared freshly in Millipore water (Bedford, MA, USA).

Polycrystalline samples of $Bi_5ATi_4FeO_{18}$ (*A* = Ca, Sr, Pb) were prepared by solid-state reactions. For this, stoichiometric quantities of Bi_2O_3, ACO_3 (A = Ca, Sr) / PbO, TiO_2 and $FeC_2O_4{\cdot}2H_2O$ were well ground in an agate mortar for 1 h and heated at 780 °C for 2 h. Afterwards, the powders obtained after initial heating was thoroughly reground, pelletized and heated at 1000 °C for 2 h.

5.2.2 Adsorption Test

Adsorption tests were carried out for individual RhB and MB solutions together with a mixed solution of RhB and MB. For this, 50 mg of $Bi_5ATi_4FeO_{18}$ (*A* = Ca, Sr, Pb) catalyst (adsorbent) was dispersed in 50 mL of 1×10^{-5} M dye solution at appropriate pH (2, 7 and 11). For the mixed dye adsorption experiment, 25 mL each of RhB and MB of 2×10^{-5} M concentration were mixed to maintain the same catalyst to individual dye ratio. After magnetic stirring at a rate of 350 rpm for 6 h in the dark, the suspensions were centrifuged and a small amount of filtrates were used for absorption measurements on a Shimadzu 2450 UV-visible spectrophotometer. The percentage of dye adsorption was calculated using the following expression.

$$\text{Adsorption (\%)} = (1 - C/C_0) \times 100 \qquad (5.1)$$

where C is the concentration of the dye after 6 h stirring, C_0 is the initial dye concentration.

5.2.3 Photocatalysis

The photocatalytic dye degradation studies were carried out with individual RhB, MB and a mixture of RhB and MB under sunlight-irradiation at different pH (2, 7 and 11). All the photocatalytic experiments were carried out at IIT Roorkee (29°51′ N; 77°53′ E) under similar conditions in the month of October, 2015 (solar Direct Normal Irradiance ~ 212 W/m^2). For this, 0.1 g of the catalysts, $Bi_5ATi_4FeO_{18}$ (*A* = Ca, Sr, Pb), were suspended in 100 mL of 1×10^{-5} M dye solution of appropriate pH. Prior to irradiation, the catalyst-dye suspensions were magnetically stirred for 1 h under dark to ensure the establishment of adsorption-desorption equilibrium between the catalyst and dye molecules. For monitoring the dye degradation with time, an aliquot (~ 3 mL) from the dye-catalyst suspension was periodically sampled, and centrifuged at 8200 rpm (to remove the catalyst particles) for absorbance measurements on a Shimadzu 2450 UV-visible spectrophotometer. A blank experiment was always performed on the dye solutions in absence of the catalyst under identical experimental conditions.

5.2.4 Catalyst Dosage Experiment

To know the optimum catalyst concentration for maximum efficiency of dye degradation, photocatalytic experiments were carried out with different quantities of catalysts in a fixed volume of dye solution. For this purpose, 2.5, 5, 7.5, 10, 12.5, 15 and 17.5 mg of catalysts were used in 10 mL of 1×10^{-5} M RhB or MB solution. The required amounts of dye-catalyst suspensions were taken in test tubes and each test tube was sonicated for about 15 minutes for well dispersion of the catalysts in the dye solution. Then the dye-catalyst suspensions were exposed to the natural sunlight. After 10 minutes of irradiation, the suspensions were centrifuged to remove the catalysts and the solutions were employed for absorption measurements with a UV–vis spectrophotometer.

5.2.5 Analysis of Reactive Species

To understand the role of the reactive species for the degradation of RhB or MB over $Bi_5SrTi_4FeO_{18}$ under sunlight-irradiation, appropriate scavengers were added into the RhB or MB solution and the degradation experiments were carried out in a similar fashion as described in Chapter 4. In these experiments, ammonium oxalate (AO), benzoquinone (BQ) and tertiary butyl alcohol (*t*-BuOH) were used as scavengers for holes (h^+), superoxide radical anion ($O_2^{\bullet-}$) and hydroxyl radicals ($^{\bullet}OH$), respectively.

5.2.6 Chemical Oxygen Demand (COD) Test

Mineralization of the dye during and after photocatalysis was monitored by using a digestion unit (DRB 200, HACH, USA) and UV-visible spectrophotometer. For this, multiple degradation experiments were carried out with the same set of dye and catalyst. The dye-catalyst suspensions were exposed to different time intervals and the aliquots were collected for COD analysis. The photodegradation efficiency was calculated by using the following equation.

$$\text{Potodegradation efficiency} = \frac{\text{Initial COD}-\text{Final COD}}{\text{Initial COD}} \times 100 \qquad (5.2)$$

5.3 RESULTS AND DISCUSSION

5.3.1 PXD Analysis

The PXD patterns of $Bi_5ATi_4FeO_{18}$ (*A* = Ca, Sr, Pb) are shown in Figure 5.1. A comparison of the PXD pattern with standard JCPDS files reported in the literature indicated the formation of five-layer Aurivillius phases similar to $Bi_6Ti_3Fe_2O_{18}$ (JCPDS PDF # 21-0101). The unit cell parameters of $Bi_5ATi_4FeO_{18}$ (*A* = Ca, Sr, Pb) are determined by least-squares refinement of all the observed diffraction lines in the orthorhombic *F*2*mm* (No. 42) space group using the PROSZKI program. Table 5.1 shows the least-squares refined lattice parameters for all the compounds. The indexed PXD data for $Bi_5CaTi_4FeO_{18}$, $Bi_5SrTi_4FeO_{18}$ and $Bi_5PbTi_4FeO_{18}$ is given in Tables 5.2, 5.3 and 5.4, respectively. A close look at the lattice parameters of $Bi_5ATi_4FeO_{18}$ (*A* = Ca, Sr, and Pb) series shows an expansion in the *c*-parameter when A varies from Sr to Pb, while a slight contraction is observed for A = Ca analogue as compared to the parent $Bi_6Ti_3Fe_2O_{18}$ (see Chapter 4).

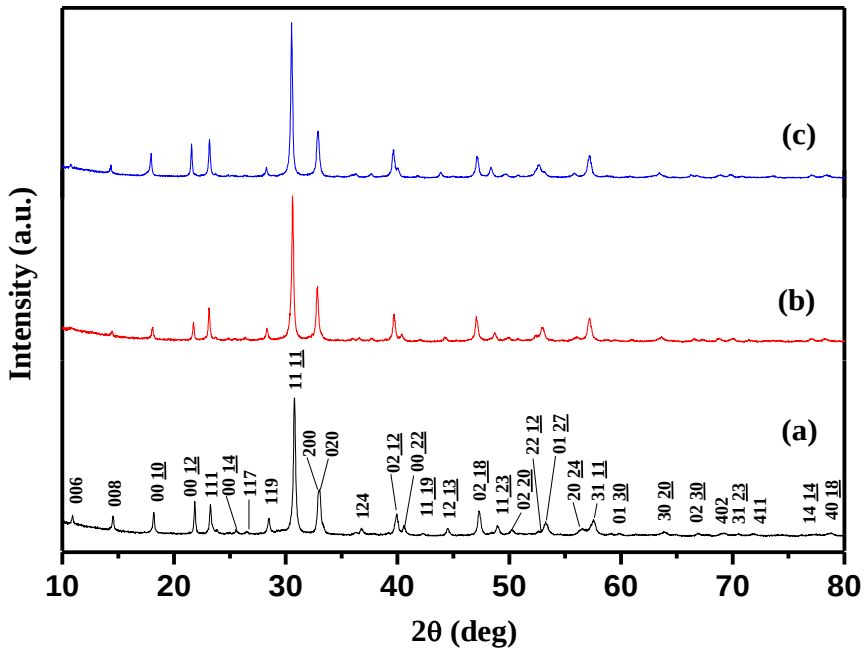

Figure 5.1 PXD patterns of (a) $Bi_5CaTi_4FeO_{18}$, (b) $Bi_5SrTi_4FeO_{18}$, and (c) $Bi_5PbTi_4FeO_{18}$.

Table 5.1 Lattice Parameters and Band Gap Energies of $Bi_5ATi_4FeO_{18}$ (*A* = Ca, Sr, Pb)

Compound	Lattice parameters (Å)			Band Gap (eV)	
	a	*b*	*c*	E_g (1)	E_g (2)
$Bi_5CaTi_4FeO_{18}$	5.451(1)	5.438(1)	49.10(1)	2.09	2.61
$Bi_5SrTi_4FeO_{18}$	5.475(1)	5.466(1)	49.29(1)	2.12	2.72
$Bi_5PbTi_4FeO_{18}$	5.472(1)	5.462(1)	49.69(1)	2.11	2.66

We have determined the crystal structure of $Bi_5ATi_4FeO_{18}$ (*A* = Ca, Sr, Pb) by Rietveld refinement of PXD data using the Fullprof program. The initial model for the refinement of the structure of $Bi_5SrTi_4FeO_{18}$ was constructed using the atomic coordinates of $Bi_6Ti_3Fe_2O_{18}$ (*F*2*mm* space group) wherein Fe^{3+} completely occupy the central octahedral layer and rest of the octahedral layers are occupied by Ti^{4+}. Moreover, the Sr^{2+} is distributed statistically over all the Bi^{3+}-sites in the perovskite block keeping the $[Bi_2O_2]^{2+}$ layer exclusively occupied by Bi^{3+}. The observed, calculated and difference profiles of Rietveld refinement are shown in Figure 5.2. The refined atomic positions, occupancies and thermal parameters are given in Table 5.5. Figure 5.3 shows the structure of $Bi_5SrTi_4FeO_{18}$ drawn using the refined atomic positions. Trial refinement runs with other models, where the Fe^{3+} was distributed over all the perovskite blocks and Sr over the perovskite *A*-site and $[Bi_2O_2]^{2+}$ layers, resulted in higher reliability factors. However, for more accurate determination of oxygen position and bond distances a neutron diffraction would be necessary.

A similar refinement of the PXD data for $Bi_5CaTi_4FeO_{18}$ and $Bi_5PbTi_4FeO_{18}$ based on same model structure gave a satisfactory fit (Figure 5.4). The refined atomic positions, occupancies and thermal factors are given in Tables 5.6 and 5.7.

Table 5.2 Indexed PXD Data for $Bi_5CaTi_4FeO_{18}$

h k l	d_{obs}(Å)	d_{calc} (Å)	I_{obs}
0 0 6	8.186	8.167	7
0 0 8	6.133	6.125	13
0 0 10	4.906	4.900	17
0 0 12	4.082	4.083	27
1 1 1	3.842	3.838	21
0 0 14	3.500	3.500	3
1 1 7	3.375	3.373	2
1 1 9	3.148	3.144	11
1 1 11	2.913	2.913	100
0 2 0	2.719	2.719	35
1 2 4	2.386	2.387	5
0 2 12	2.262	2.263	16
0 0 22	2.228	2.227	7
1 1 19	2.143	2.143	1
1 2 13	2.043	2.044	6
0 2 18	1.925	1.924	20
1 1 23	1.865	1.864	6
0 2 20	1.821	1.820	4
2 2 12	1.742	1.741	8
0 1 27	1.722	1.721	10
2 0 24	1.634	1.634	5
3 1 11	1.606	1.607	10
0 1 30	1.563	1.564	2
3 0 20	1.459	1.459	2
0 2 30	1.400	1.400	2

a = 5.451(1), b = 5.438(1), c = 49.10(1) Å.

Table 5.3 Indexed PXD Data for $Bi_5SrTi_4FeO_{18}$

h k l	d_{obs}(Å)	d_{calc} (Å)	I_{obs}
0 0 6	8.231	8.214	2
0 0 8	6.179	6.161	4
0 0 10	4.932	4.929	10
0 0 12	4.109	4.107	12
1 1 1	3.864	3.856	22
1 1 14	3.523	3.520	2
1 1 7	3.391	3.390	2
1 1 9	3.162	3.159	8
1 1 11	2.929	2.928	100
0 2 0	2.737	2.733	40
1 2 4	2.398	2.399	3
0 2 12	2.275	2.275	17
0 0 22	2.240	2.240	5
1 1 19	2.154	2.154	3
1 2 13	2.054	2.055	3
0 2 18	1.934	1.934	17
1 1 23	1.874	1.874	5
0 2 20	1.830	1.830	3
2 2 12	1.750	1.750	3
0 1 27	1.732	1.731	11
2 0 24	1.643	1.643	2
3 1 11	1.614	1.614	17
4 0 2	1.367	1.367	2

a = 5.475(1), b= 5.466(1), c = 49.29(1) Å.

Table 5.4 Indexed PXD Data for $Bi_5PbTi_4FeO_{18}$

h k l	d_{obs}(Å)	d_{calc} (Å)	I_{obs}
0 0 6	8.331	8.281	2
0 0 8	6.230	6.211	5
0 0 10	4.983	4.969	13
0 0 12	4.142	4.141	18
1 1 1	3.858	3.854	23
0 0 14	3.551	3.549	1
1 1 7	3.397	3.395	2
1 1 9	3.171	3.167	6
1 1 11	2.940	2.937	100
0 2 0	2.735	2.731	31
1 2 4	2.397	2.398	3
0 2 12	2.280	2.280	18
0 0 22	2.258	2.259	6
1 1 19	2.168	2.166	1
1 1 23	1.886	1.886	6
0 2 20	1.837	1.838	3
2 2 12	1.751	1.751	9
0 1 27	1.744	1.744	4
2 0 24	1.651	1.651	2
3 1 11	1.616	1.615	16
4 0 2	1.367	1.366	2

a = 5.472(1), b = 5.462(1), c = 49.69(1) Å.

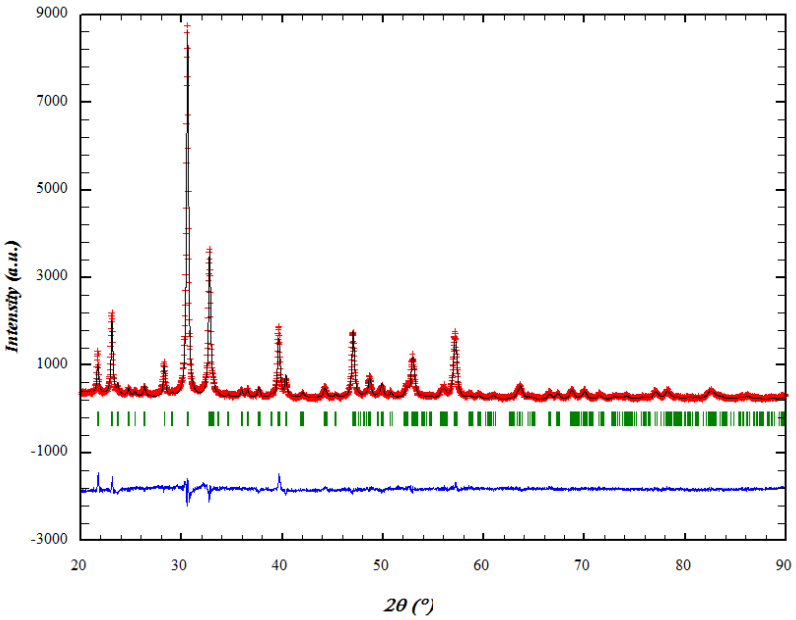

Figure 5.2 Rietveld refinement of the structure $Bi_5SrTi_4FeO_{18}$ from PXD data. Observed (+), calculated (–) and difference (bottom) profiles are shown. The vertical bars represent the Bragg positions.

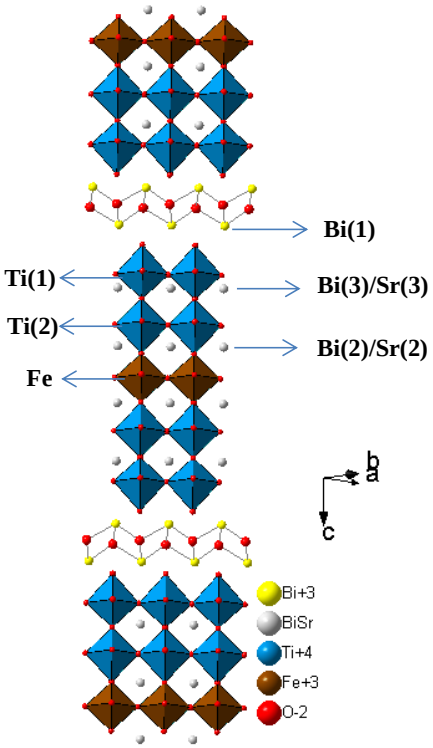

Figure 5.3 Crystal structure of $Bi_5SrTi_4FeO_{18}$ drawn from the refined atomic positions.

Table 5.5 Atomic Position, Site Occupancy and Thermal Parameters used for Structure Refinement of $Bi_5SrTi_4FeO_{18}$

Atom	*x*	*y*	*z*	B_{iso}	Occ.
Bi(1)	0.5490(1)	0	0.7247(1)	1.32(3)	2
Bi(2)/Sr(2)	0.5528(1)	0	0.5425(1)	1.32(3)	1.5/0.5
Bi(3)/Sr(3)	0.5418(2)	0	0.6301(2)	1.32(3)	1.5/0.5
Ti(1)	0.5155(1)	0	0.8301(1)	0.83(1)	2
Ti(2)	0.5115(3)	0	0.9171(1)	0.83(1)	2
Fe	0.5	0	0	0.83(1)	1
O(1)	0.25	0.75	0	3.1(2)	2
O(2)	0.75	0.25	0.25	3.1(2)	2
O(3)	0.5	0	0.7998(3)	3.1(2)	2
O(4)	0.5	0	0.8806(1)	3.1(2)	2
O(5)	0.5	0	0.9635(1)	3.1(2)	2
O(6)	0.25	0.25	0.4202(1)	3.1(2)	4
O(7)	0.25	0.25	0.3445(1)	3.1(2)	4

Space group *F*2*mm*, a = 5.4685(5), b = 5.4579(5), c = 49.166(3) Å, R_{Bragg} = 7.4%, R_f = 6.5%, R_p = 6.2%, R_{WP} = 7.9%, and χ^2 = 2.6

Table 5.6 Atomic Position, Site Occupancy and Thermal Parameters used for Structure Refinement of $Bi_5CaTi_4FeO_{18}$

Atom	*x*	*y*	*z*	B_{iso}	Occ.
Bi(1)	0.5791(1)	0	0.7219(4)	1.32(3)	2
Bi(2)/Ca(2)	0.5423(1)	0	0.5405(1)	1.32(3)	1.5/0.5
Bi(3)/Ca(3)	0.5572(2)	0	0.6299(2)	1.32(3)	1.5/0.5
Ti(1)	0.5555(1)	0	0.8259(4)	0.83(1)	2
Ti(2)	0.4991(3)	0	0.9184(1)	0.83(1)	2
Fe	0.5	0	0	0.83(1)	1
O(1)	0.25	0.75	0	3.1(2)	2
O(2)	0.75	0.25	0.25	3.1(2)	2
O(3)	0.5	0	0.7922(1)	3.1(2)	2
O(4)	0.5	0	0.8841(2)	3.1(2)	2
O(5)	0.5	0	0.9659(3)	3.1(2)	2
O(6)	0.25	0.25	0.4263(1)	3.1(2)	4
O(7)	0.25	0.25	0.3633(4)	3.1(2)	4

Space group *F*2*mm*, a = 5.4450(8), b = 5.4242(8), c = 48.872(7) Å, R_{Bragg} = 9.3%, R_f = 7.3%, R_p = 7.8%, R_{WP} = 10.2%, and χ^2 = 5.05

Table 5.7 Atomic Position, Site Occupancy and Thermal Parameters used for Structure Refinement of $Bi_5PbTi_4FeO_{18}$

Atom	*x*	*y*	*z*	B_{iso}	Occ.
Bi(1)	0.5669(7)	0	0.7240(1)	1.32(3)	2
Bi(2)/Pb(2)	0.5298(1)	0	0.5424(1)	1.32(3)	1.5/0.5
Bi(3)/Pb(3)	0.5325(1)	0	0.6298(1)	1.32(3)	1.5/0.5
Ti(1)	0.5100(1)	0	0.8238(1)	0.83(1)	2
Ti(2)	0.5100(1)	0	0.9158(1)	0.83(1)	2
Fe	0.5	0	0	0.83(1)	1
O(1)	0.25	0.75	0	3.1(2)	2
O(2)	0.75	0.25	0.25	3.1(2)	2
O(3)	0.5	0	0.8030(7)	3.1(2)	2
O(4)	0.5	0	0.8817(2)	3.1(2)	2
O(5)	0.5	0	0.9576(6)	3.1(2)	2
O(6)	0.25	0.25	0.4400(3)	3.1(2)	4
O(7)	0.25	0.25	0.3333(6)	3.1(2)	4

Space group *F*2*mm*, a = 5.4659(5), b = 5.4497(4), c = 49.623(3) Å, R_{Bragg} = 7.3%, R_f = 5.3%, R_p = 7.5%, R_{WP} = 9.6%, and χ^2 = 4.1

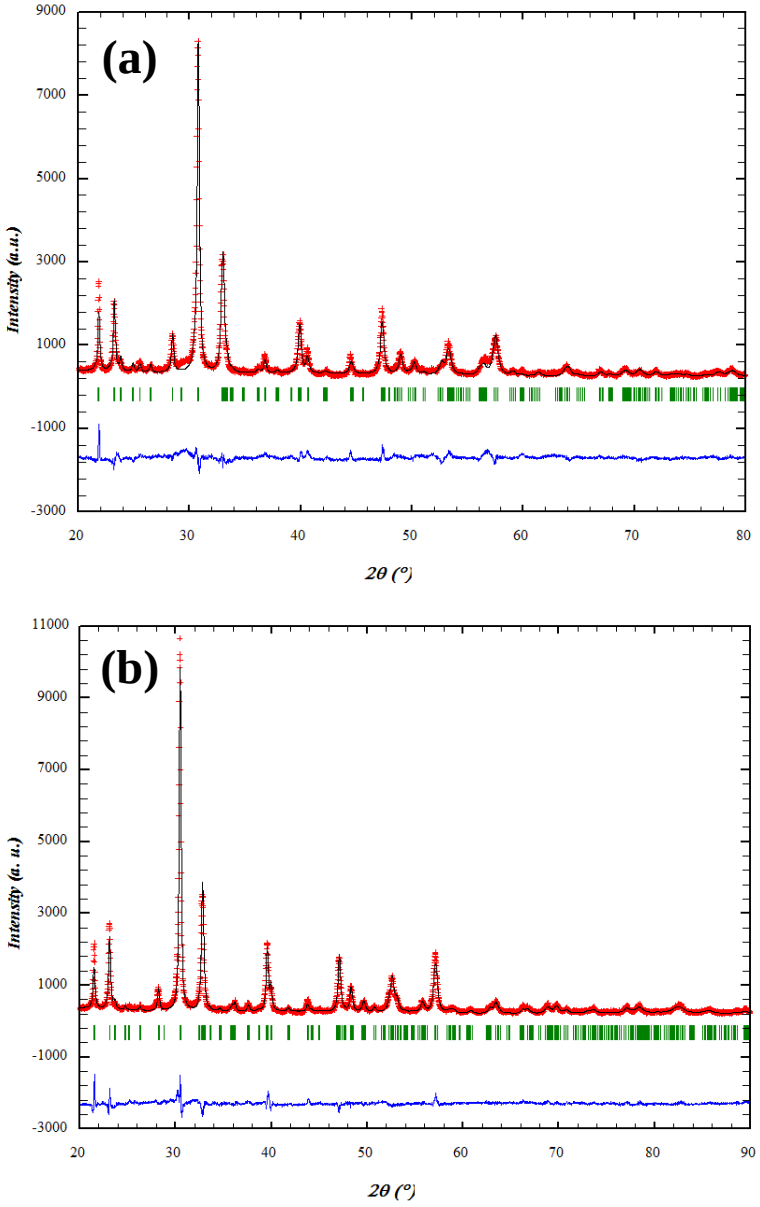

Figure 5.4 Rietveld refinement of the structures of (a) $Bi_5CaTi_4FeO_{18}$ and (b) $Bi_5PbTi_4FeO_{18}$. Observed (+), calculated (–) and difference (bottom) profiles are shown. The vertical bars represent the Bragg positions.

5.3.2 FE-SEM and EDS Analysis

FE-SEM and corresponding EDS spectra of $Bi_5ATi_4FeO_{18}$ (*A* = Ca, Sr, Pb) are shown in Figure 5.5. All the compounds show morphological homogeneity in the entire region of image prevailing plate-like morphology with a fairly large extent of particle aggregation.

Moreover, there is a large variation in the size of platelets ranging from several hundred nanometers to few micrometers. Elemental composition obtained from EDS at several crystallites of the imaged area shows excellent compositional uniformity with the nominal elemental composition.

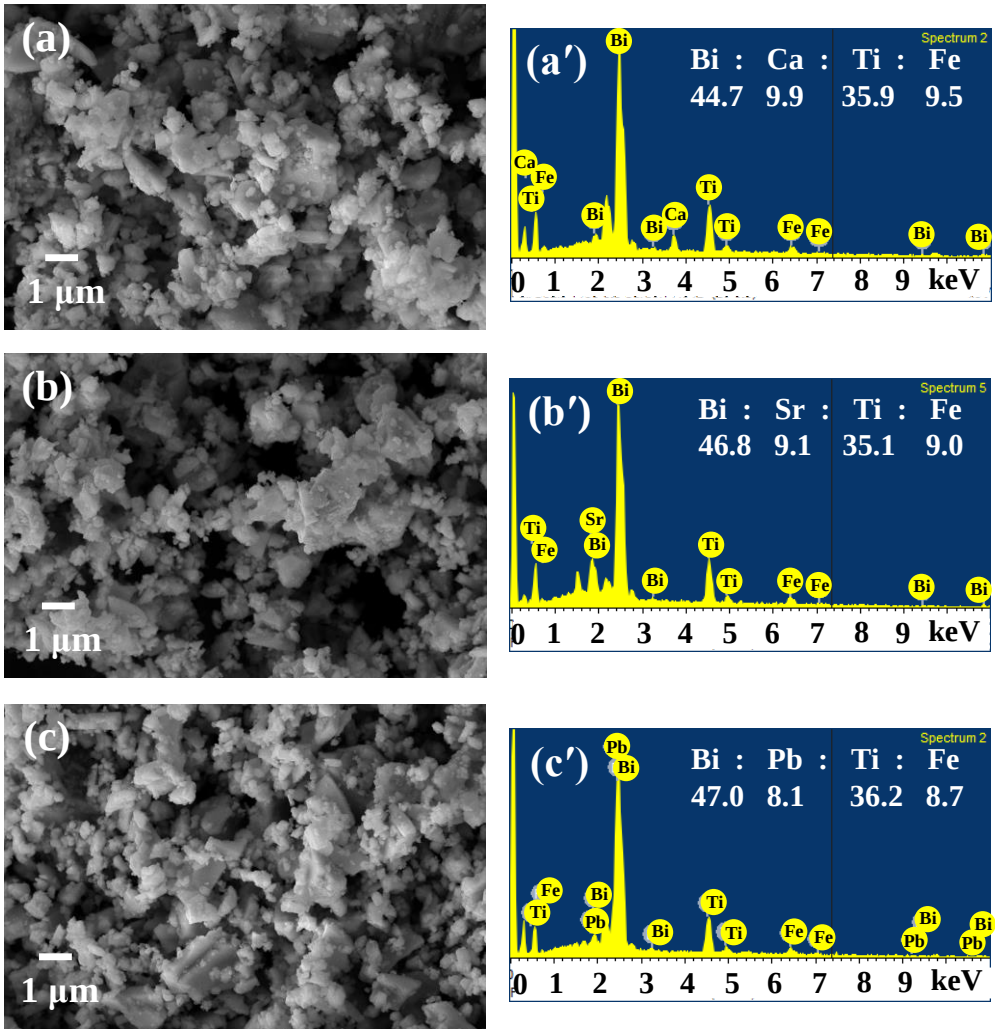

Figure 5.5 FE-SEM/EDX analysis of (a, a′) $Bi_5CaTi_4FeO_{18}$, (b, b′) $Bi_5SrTi_4FeO_{18}$, and (c, c′) $Bi_5PbTi_4FeO_{18}$.

5.3.3 FE-SEM-EDS Elemental Mapping Analysis

To investigate the elemental distribution in a selected rectangular area of $Bi_5ATi_4FeO_{18}$ (*A* = Ca, Sr, and Pb), EDS elemental mapping was conducted. The elemental

mapping (Figure 5.6) results indicate homogeneous and uniform distribution of all the elements in the selected rectangular area of FE-SEM image.

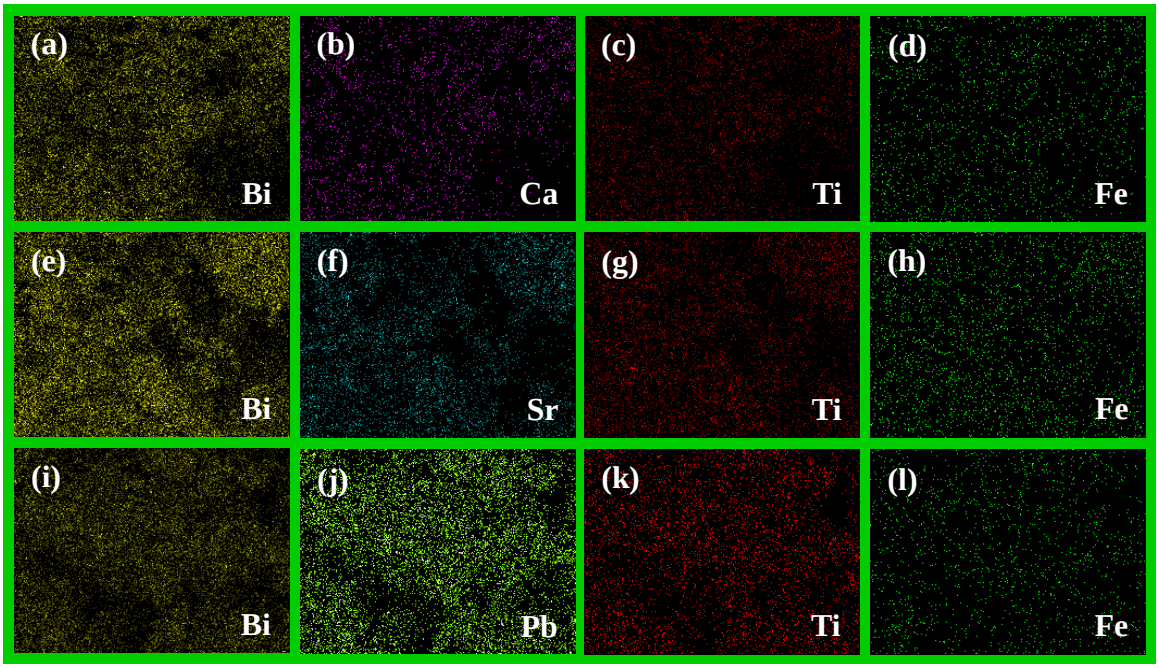

Figure 5.6 EDS elemental mapping of (a) Bi, (b) Ca, (c) Ti and (d) Fe in $Bi_5CaTi_4FeO_{18}$, (e-h) and (i-l) represent elemental mapping for $Bi_5ATi_4FeO_{18}$ (*A* = Sr and Pb) in the same order where the second panel represents the A cations, Sr and Pb, respectively.

5.3.4 TEM Analysis

The crystalline nature of $Bi_5SrTi_4FeO_{18}$ was confirmed by TEM and high resolution TEM studies (HR-TEM). The HR-TEM image (Figure 5.7 (a)) clearly revealed the layer intergrowth nature of the Aurivillius phases repeating with perovskite blocks and $[Bi_2O_2]^{2+}$ layers. Moreover, the HR-TEM shown in Figure 5.7 (b) clearly shows lattice fringes and the distance between the fringes indicated is calculated to be 4.925 nm, which is consistent with the *c*-parameter of the unit cell. The SAED pattern is indexable in the orthorhombic space group and consistent with the lattice parameters obtained from PXD data analysis. Indexing of few representative spots in the SAED pattern are shown in Figure 5.7 (c).

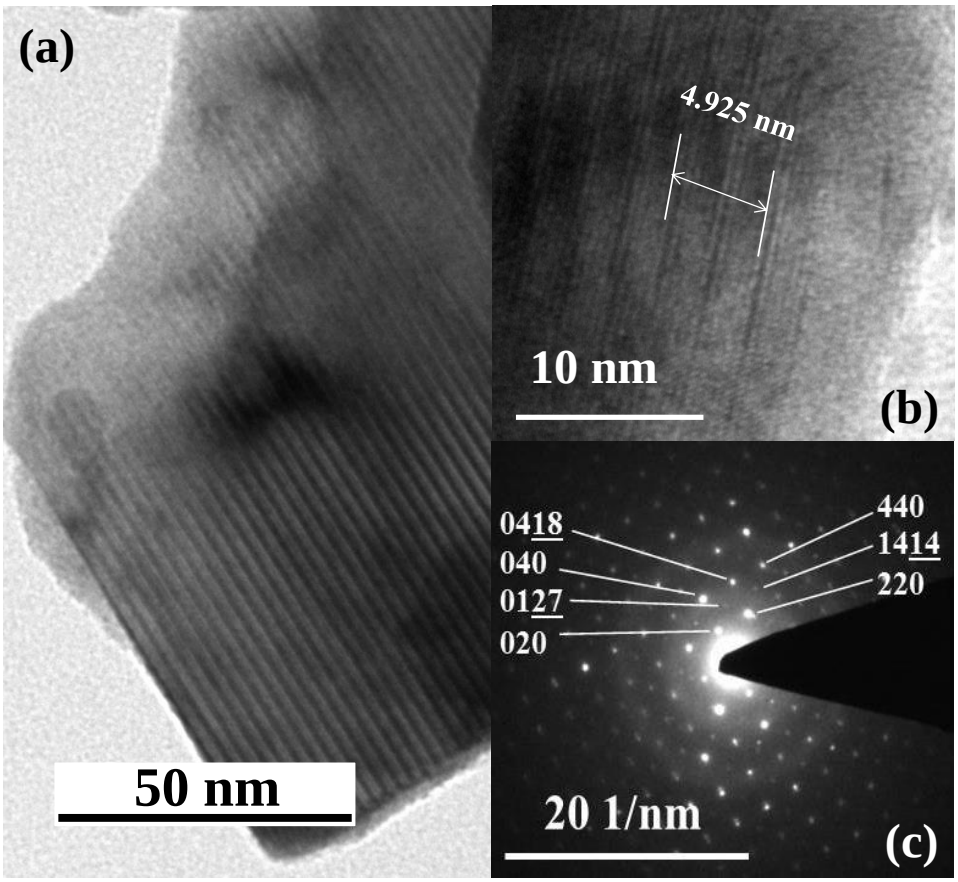

Figure 5. 7 (a) Transmission electron microscopy (TEM) image, (b) high-resolution TEM (HR-TEM) image and (c) Selected SAED patterns of $Bi_5SrTi_4FeO_{18}$.

5.3.5 UV-vis DRS Analysis

The optical absorption spectra of the $Bi_5ATi_4FeO_{18}$ (*A* = Ca, Sr, and Pb) are shown in Figure 5.8 (a). All the compounds show visible-light absorption and two absorption edges similar to those reported in previous chapters (Chapter 3 & 4) for $Bi_{5-x}La_xTi_3FeO_{15}$ (x = 1, 2) and $Bi_{6-x}La_xTi_3Fe_2O_{18}$ (x = 0, 1). The exact band gap energies of these compounds are calculated from the Tauc plots shown in Figure 5.8 (b). The best fit for $(\alpha h\nu)^{1/n}$ versus $h\nu$ was obtained for n = 2, suggesting probably to an indirect band gap transition. The calculated band gap energies of the compounds are given in Table 5.1. The fact that all the compounds are visible light absorber, lead us to believe in their potential for sunlight-driven photocatalysis.

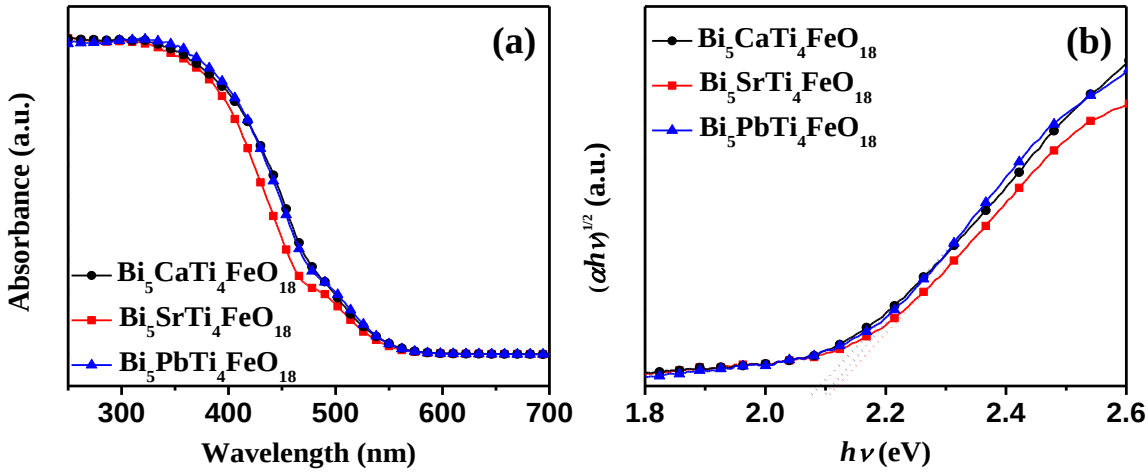

Figure 5.8 (a) UV-vis DRS of $Bi_5ATi_4FeO_{18}$ (*A* = Ca, Sr, and Pb). (b) Corresponding Tauc plots for calculation of band gap.

5.3.6 PL Analysis

In order to compare the e^--h^+ recombination rate or efficiencies of photogenerated charge carrier separation in $Bi_5ATi_4FeO_{18}$ (*A* = Ca, Sr, Pb), PL spectra were recorded at an excitation wavelength of 350 nm. As it is known and discussed in previous chapters (Chapters 3 & 4), a lower PL intensity indicates slow recombination and longer lifetime of charge carriers, an indicator for higher photocatalytic activity [13]. As portrayed in Figure 5.9, all the compounds show broad emission spectra ranging from 400 to 600 nm with a peak around 470 nm. According to the PL spectra, one would expect the activity order as $Bi_5CaTi_4FeO_{18}$ < $Bi_5PbTi_4FeO_{18}$ < $Bi_5SrTi_4FeO_{18}$, though the difference in PL intensities are very subtle and may depend on several other factors. However, a higher activity for $Bi_5SrTi_4FeO_{18}$ as compared to that of the Ca-analogue (see next section) can clearly be expected from the PL data.

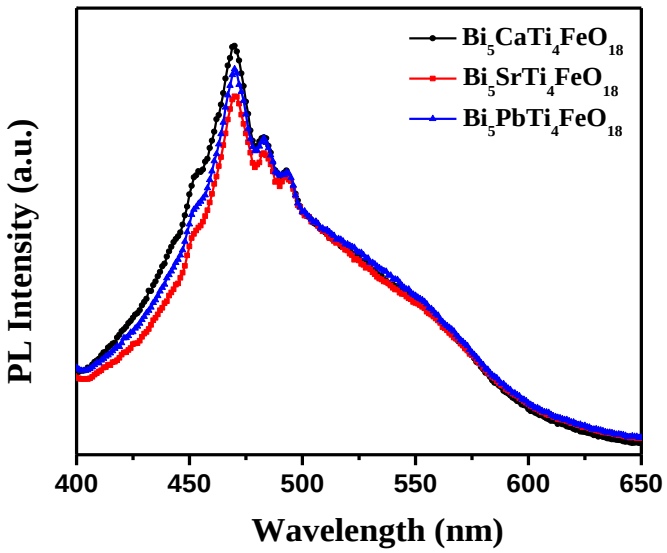

Figure 5.9 PL spectra of $Bi_5ATi_4FeO_{18}$ (*A* = Ca, Sr, Pb) at an excitation wavelength of 350 nm at room temperature.

5.3.7 Photocatalytic Activity

To evaluate the activity of $Bi_5ATi_4FeO_{18}$ (*A* = Ca, Sr, Pb) toward dye removal from contaminated waters, aqueous solutions of RhB (zwitterionic), MB (cationic), and a mixture of RhB and MB were selected as model systems for photocatalytic degradation experiments. The UV-vis spectral measurements (Figure 5.10) recorded with time show a decrease in the characteristic absorption peak intensity for the MB dye leaving the absorption peak intensity for RhB nearly unchanged on sunlight-irradiation of the mixed dye solution at pH 7 and 11. This indicates selective degradation of MB from the aqueous mixture of MB and RhB solution. The selective degradation of MB over these catalysts is faster at pH 11 as compared to that at pH 7. The inset of Figure 5.10 (e) clearly shows the selective degradation through a clear color changeover from purple (for mixed MB-RhB solution) to pink (for pure RhB solution). It is clear that $Bi_5SrTi_4FeO_{18}$ exhibited excellent selective degradation (within 80 min) of MB from the aqueous mixture of MB and RhB at pH 11, whereas $Bi_5PbTi_4FeO_{18}$ and $Bi_5CaTi_4FeO_{18}$ showed relatively lower activity (within 110 and 120 min, respectively). Conversely, it has also been observed (Figure 5.10 (a-c)) that at pH 7, for $Bi_5CaTi_4FeO_{18}$, $Bi_5SrTi_4FeO_{18}$ and $Bi_5PbTi_4FeO_{18}$, the selective degradations are up to 75, 79 and 79%, respectively, in 180 min of solar illumination. Therefore, it is concluded that all the compounds, $Bi_5ATi_4FeO_{18}$ (*A* = Ca, Sr, and Pb), are active toward selective

degradation of MB from a mixture of MB and RhB in neutral and alkaline media. The strategy may well be applied to extend in selectively degrading a harmful pollutant and recovery of precious dyes/chemicals from a mixed solution of pollutants.

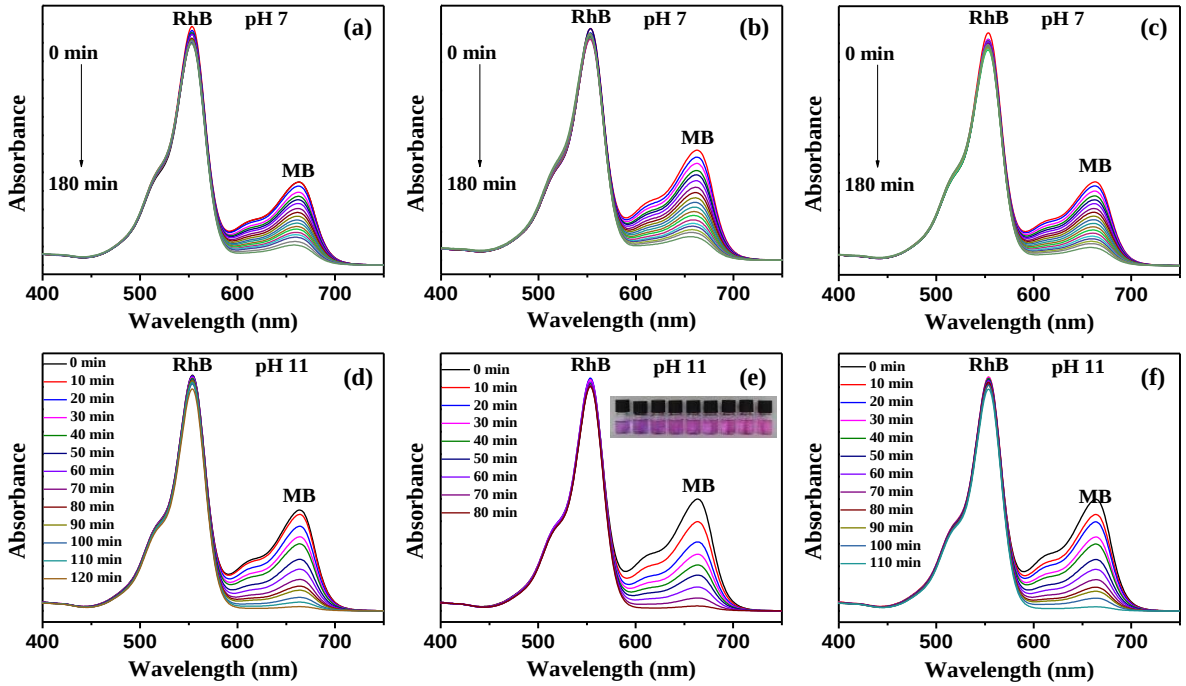

Figure 5.10 UV-vis absorption spectra for selective degradation of MB from aqueous mixture of MB and RhB at pH 7 (a - c) and pH 11 (d - f) over $Bi_5CaTi_4FeO_{18}$ (a, d), $Bi_5SrTi_4FeO_{18}$ (b, e) and $Bi_5PbTi_4FeO_{18}$ (c, f) under sunlight-irradiation. Inset of (e) shows representative color change during photocatalytic degradation of mixed dyes with time.

Interestingly, a complete degradation of both MB and RhB (Figure 5.11) from a mixture is also achieved at pH 2 within 160 min over $Bi_5SrTi_4FeO_{18}$. However, $Bi_5PbTi_4FeO_{18}$ showed a complete degradation of MB and up to 69 % degradation of RhB, whereas the corresponding Ca-analogue exhibited only up to 65 % of MB and 40 % of RhB degradation within 180 min solar irradiation at pH 2. In the later cases, the λ_{max} of RhB undergoes a hypsochromic shift indicating de-ethylation of RhB during the degradation [14].

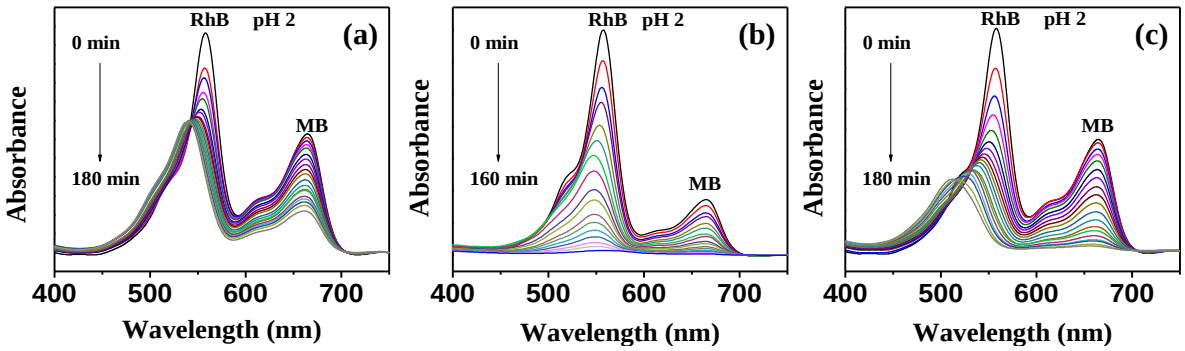

Figure 5.11 UV-vis absorption spectra for degradation of MB, RhB from aqueous mixture of MB, RhB at pH 2 over (a) $Bi_5CaTi_4FeO_{18}$ (b) $Bi_5SrTi_4FeO_{18}$ and (c) $Bi_5PbTi_4FeO_{18}$ under sunlight-irradiation.

To further confirm whether these catalysts have potential for degradation of individual MB and RhB, a series of experiments were conducted under sunlight-irradiation at different pH with single dye solutions as well. The RhB degradation and % COD removal with time as shown in Figure 5.12 (a), unveiled that the RhB was degraded completely within 30-60 min of sunlight-irradiation at pH 2. The % COD removal data for RhB degradation at pH 2 further confirmed the complete mineralization of the dye within 30-60 min of irradiation. Interestingly, the % COD removal is in agreement with the degradation kinetics (Figure 5.12 (a)) indicating excellent dye mineralization and that it is more or less concordant with the decoloration kinetics.

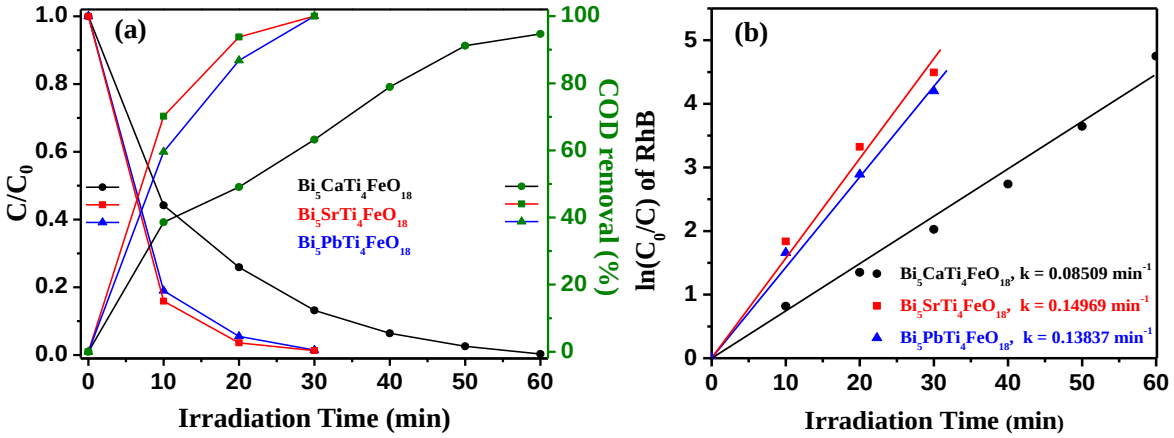

Figure 5.12 (a) Photocatalytic degradation of RhB and % COD removal (b) Plot of $\ln(C_0/C)$ as a function of irradiation time over $Bi_5ATi_4FeO_{18}$ (*A* = Ca, Sr, and Pb).

The photocatalytic RhB degradation kinetics over $Bi_5ATi_4FeO_{18}$ (*A* = Ca, Sr, Pb) were fitted with Languir-Hinshelwood model:

$$\ln(C_0/C) = kt \quad (5.3)$$

where, C_0 is the initial RhB concentration, C is the actual concentration of RhB at time t and k is the rate constant. The plot between $\ln(C_0/C)$ and time were linear (Figure 5.12 (b)), which indicates that the degradation of RhB follows a pseudo-first-order kinetics. The degradation rate constant (k) is calculated to be 0.08509, 0.14969 and 0.13837 min^{-1} for $Bi_5CaTi_4FeO_{18}$, $Bi_5SrTi_4FeO_{18}$ and $Bi_5PbTi_4FeO_{18}$, respectively.

Despite, complete RhB degradation at pH 2, the catalysts did not show RhB degradation to any significant extent at pH 7 and pH 11, indicating zero photocatalysis in neutral and alkaline media (Figure 5.13). All the photocatalytic activities were compared with blank tests (without catalysts) carried out at same pH and under identical experimental conditions to ensure self-degradation (if any) of the dye (Figure 5.13).

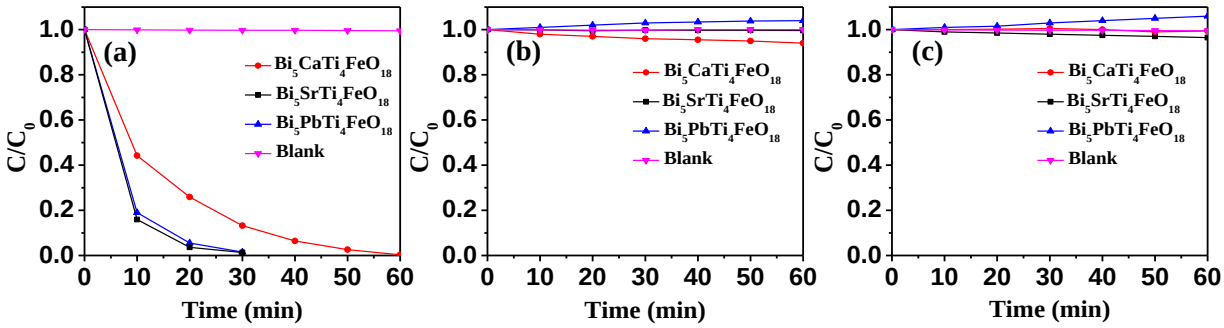

Figure 5.13 Photocatalytic degradation of RhB over $Bi_5ATi_4FeO_{18}$ (*A* = Ca, Sr, and Pb) at (a) pH 2 (b) pH 7 and (c) pH 11 under sunlight-irradiation.

Figure 5.14 shows MB degradation with time over $Bi_5ATi_4FeO_{18}$ (*A* = Ca, Sr, and Pb) unveiling fastest degradation at pH 11, moderate degradation at pH 2 and very slow degradation at pH 7. The complete degradation of MB over the as synthesized compounds is observed at pH 11 within 50-60 min of sunlight-irradiation and the % COD removal indicates good dye mineralization ability (Figure 5.15 (a)). The rate constants (k) for MB degradation (Figure 5.15 (b)) at pH 11 are calculated to be 0.06899, 0.11272 and 0.07667 min^{-1} for $Bi_5CaTi_4FeO_{18}$, $Bi_5SrTi_4FeO_{18}$ and $Bi_5PbTi_4FeO_{18}$, respectively. Interestingly, at

pH 2, $Bi_5SrTi_4FeO_{18}$ and $Bi_5PbTi_4FeO_{18}$ show complete degradation of MB within 130-150 min and $Bi_5CaTi_4FeO_{18}$ shows only up to 55 % degradation within 180 min of solar irradiation (Figure 5.14 (a)). But at pH 7 only up to 30, 45, and 37 % of MB is degraded by $Bi_5CaTi_4FeO_{18}$, $Bi_5SrTi_4FeO_{18}$ and $Bi_5PbTi_4FeO_{18}$, respectively, in 180 min of solar illumination. Moreover, the MB did not show any self-degradation in the blank test (without catalysts) under similar experimental conditions of photocatalysis (Figure 5.14). The order of photocatalytic activity for degradation of individual MB and RhB over the as synthesized compounds is $Bi_5CaTi_4FeO_{18} < Bi_5PbTi_4FeO_{18} < Bi_5SrTi_4FeO_{18}$.

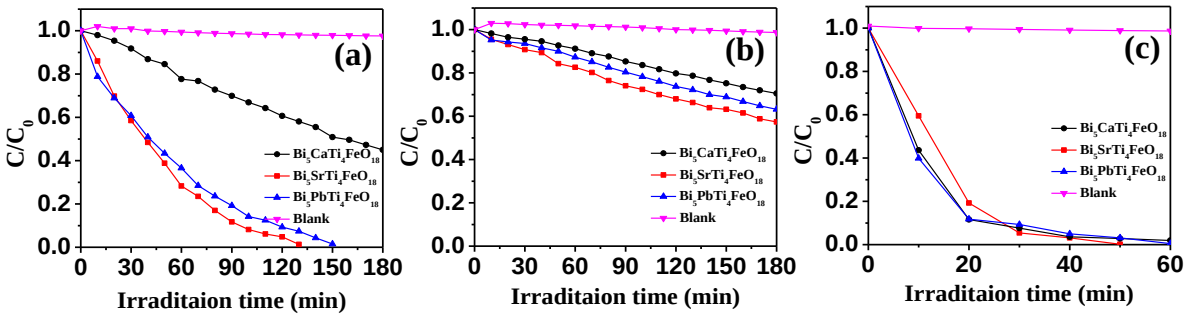

Figure 5.14 Photocatalytic degradation of MB over $Bi_5ATi_4FeO_{18}$ (*A* = Ca, Sr, and Pb) at (a) pH 2 (b) pH 7 and (c) pH 11 under sunlight-irradiation.

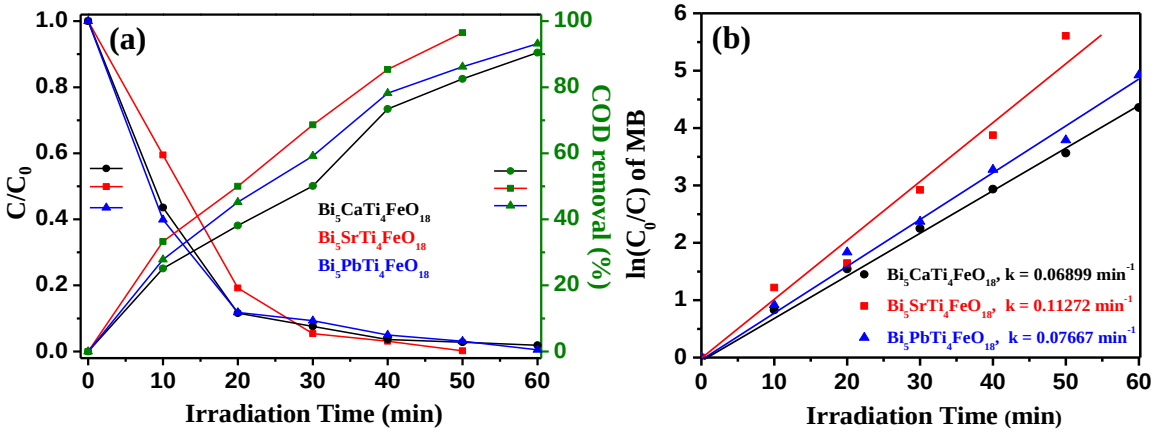

Figure 5.15 (a) Photocatalytic degradation of MB and % COD removal (b) Plot of $\ln(C_0/C)$ as a function of irradiation time over $Bi_5ATi_4FeO_{18}$ (*A* = Ca, Sr, Pb).

5.3.8 Dosage Test

The effect of catalyst dosage on the rate of photocatalytic degradation was investigated by taking different quantities of $Bi_5SrTi_4FeO_{18}$ powder in10 mL of 1×10^{-5} M RhB solution and irradiating them for 10 min under sunlight. The degradation efficiency of RhB at pH 2 with catalyst dosage for $Bi_5SrTi_4FeO_{18}$ is shown in Figure 5.16 (a). The degradation rate of RhB gradually increased with increasing the catalyst dosage from 2.5 mg/10 mL up to 10 mg/10 mL and the increment in rate is less beyond this concentration. This could be due to the "shielding effect" which is caused by suspended catalyst layer located near the top of the solution (or closer to the radiation sources) and agglomeration of catalyst particles at higher catalyst concentration. From the above findings, we concluded that 10 mg/10 mL is the optimum concentration for RhB degradation by these catalysts. The degradation of MB over $Bi_5SrTi_4FeO_{18}$ at pH 11 is also shown as a function of catalyst dosage in Figure 5.16 (b). The gradual increase of MB degradation may probably be related to the extent of MB adsorption on the catalyst surface with increasing catalyst dosage (see section 5.3.12).

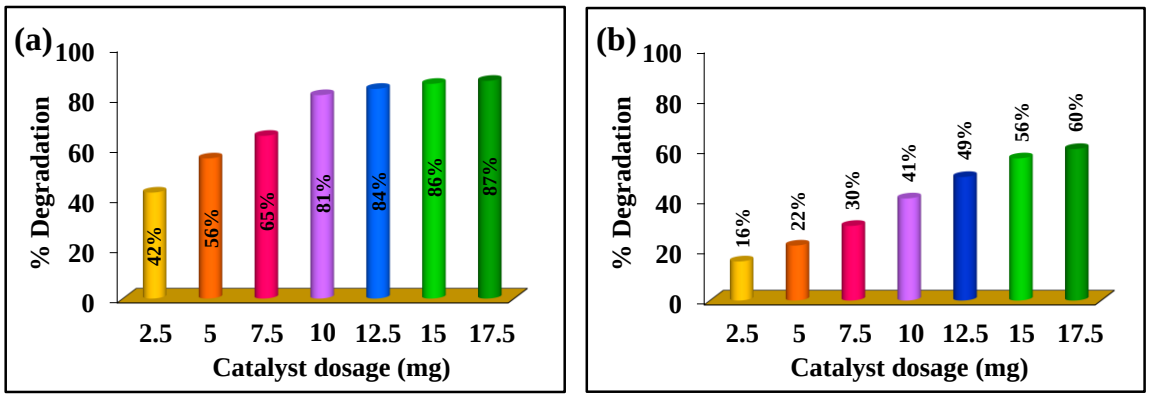

Figure 5.16 Effect of catalyst dosage for degradation of (a) RhB at pH 2, and (b) MB at pH 11, over $Bi_5SrTi_4FeO_{18}$ under solar irradiation for 10 min.

5.3.9 Detection of Reactive Species

To identify the dominant reactive species responsible for the photocatalytic dye degradation over $Bi_5SrTi_4FeO_{18}$, a series of scavenger tests were performed. While Benzoquinone (BQ) was used as $O_2^{\bullet-}$ scavenger, ammonium oxalate (AO) and *tert*-butanol (*t*-BuOH) were employed for scavenging h^+, $^{\bullet}OH$, respectively. The quenchers / scavengers

were introduced to the dye solution prior to the start of photocatalysis experiments. The presence of scavengers retards the dye degradation to different extents. The more the retardation in presence of a particular scavenger, more efficient is the role of the corresponding species that it scavenges. The photocatalytic degradation of RhB over $Bi_5SrTi_4FeO_{18}$ in presence of scavengers is shown in Figure 5.17. The addition of AO (h^+ scavenger) to dye-catalyst suspension, RhB degradation was substantially reduced as compared to that of no scavenger. A moderate extent of retardation phenomenon is noticed with the introduction of BQ ($O_2^{\bullet-}$ scavenger) on the photocatalytic degradation of RhB. However, the addition of *t*-BuOH ($^{\bullet}OH$ scavenger) caused retardation in the photodegradation of RhB only to a small extent.

Based on the above findings of the scavenger experiments, we concluded that h^+ and $O_2^{\bullet-}$ are active contributors in the photocatalytic degradation of RhB over $Bi_5SrTi_4FeO_{18}$ in the acidic medium, whereas an assistant role of $^{\bullet}OH$ cannot be completely ruled out. Moreover, the same reactive species are active for the degradation of MB at pH 11 (Figure 5.18).

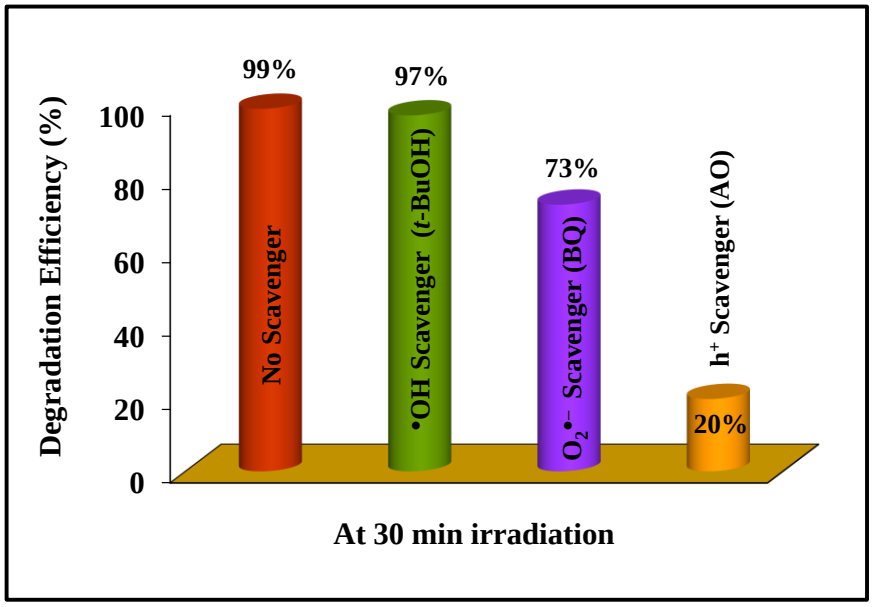

Figure 5.17 Effect of different scavengers on the degradation of RhB over $Bi_5SrTi_4FeO_{18}$ under sunlight-irradiation.

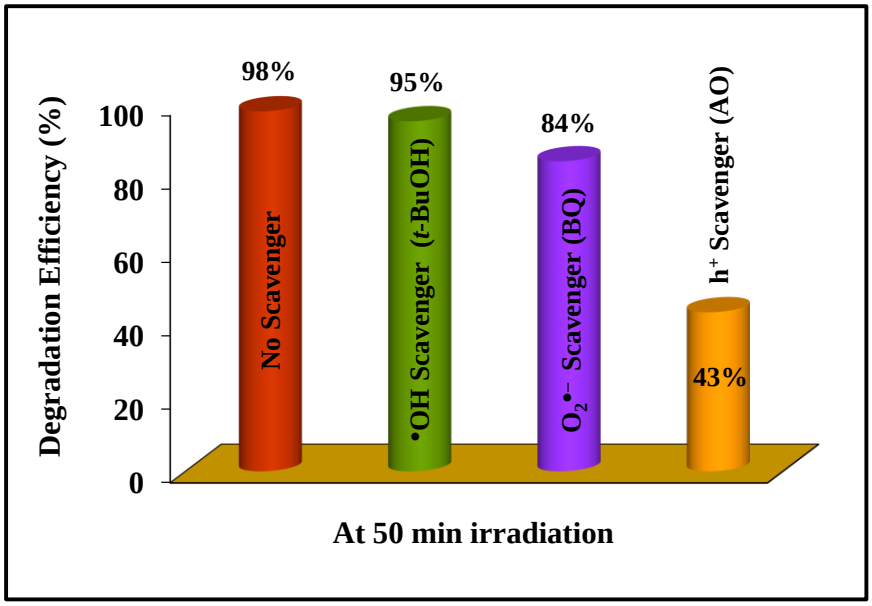

Figure 5.18 Effect of different scavengers on the degradation of MB over $Bi_5SrTi_4FeO_{18}$ under sunlight-irradiation.

5.3.10 Catalyst Reusability and Stability

The stability and reusability of the catalysts are important parameters to be assessed for making the semiconductor photocatalysis attractive and cost-effective for dye wastewater treatment. To test the stability and reusability of the catalysts, five consecutive cyclic photocatalytic dye degradation experiments were performed over $Bi_5SrTi_4FeO_{18}$. The photocatalytic cycles carried out over $Bi_5SrTi_4FeO_{18}$ for RhB degradation under sunlight-irradiation are represented in Figure 5.19 (a). The catalyst show excellent recyclability up to 4 cycles and show only a minor decrease (~ 3 %) in the activity during the fifth cycle, which is attributed to the unavoidable loss of catalysts during recycling. The recycling study strongly suggests that there is no noticeable loss in the activity of the photocatalyst. The stability of the catalyst was assessed by PXD analysis of $Bi_5SrTi_4FeO_{18}$ recovered after five cyclic runs. The PXD pattern indicates excellent phase purity and crystallinity indicating no photocorrosion or photoleaching of the oxide while maintaining its structural integrity during the photocatalysis (Figure 5.19 (b)). Moreover, the cycle test for the degradation of MB over $Bi_5SrTi_4FeO_{18}$ also indicates excellent recyclability at pH 11 (Figure 5.20). The

post-catalysis PXD patterns for the Ca and Pb analogues also demonstrated good stability under the reaction conditions (Figure 5.21).

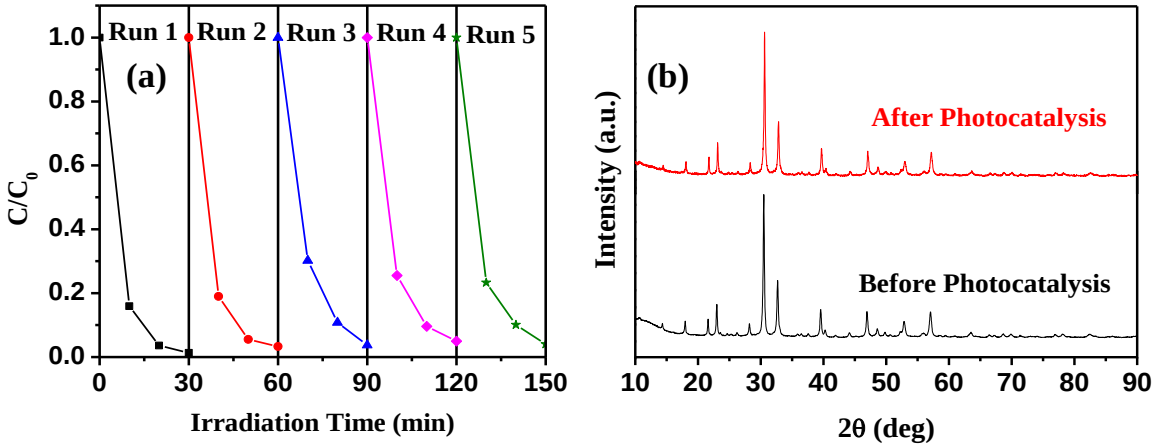

Figure 5.19 (a) Reusability of $Bi_5SrTi_4FeO_{18}$ in five successive cycles for the degradation of RhB. (b) PXD patterns of $Bi_5SrTi_4FeO_{18}$ recorded before and after five successive photocatalytic RhB degradation.

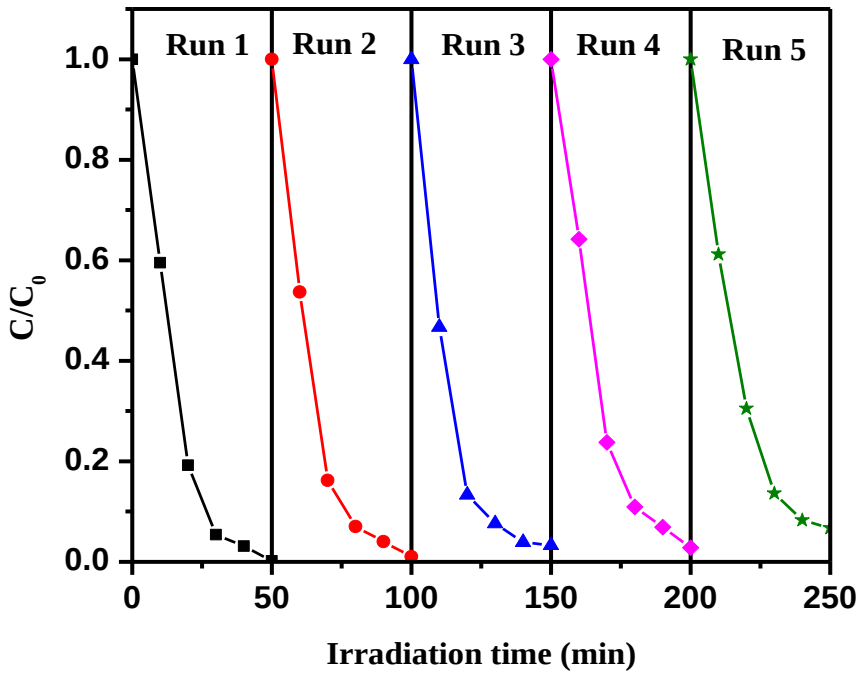

Figure 5.20 Reusability of $Bi_5SrTi_4FeO_{18}$ in five successive cycles for the degradation of MB at pH 11.

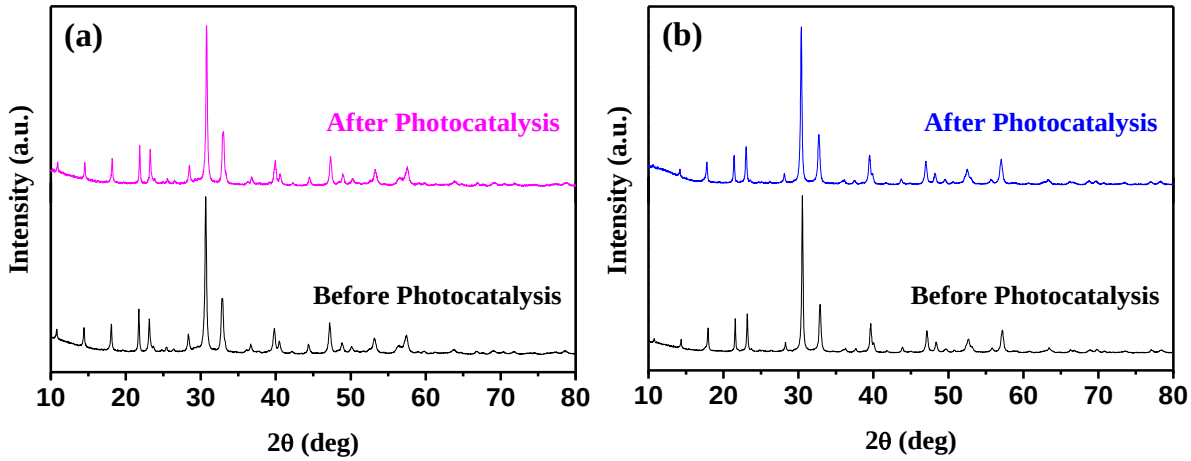

Figure 5.21 PXD patterns of (a) $Bi_5CaTi_4FeO_{18}$ and (b) $Bi_5PbTi_4FeO_{18}$ before and after the photocatalysis.

5.3.11 Mechanism for Enhanced Photocatalytic Activity

It is believed from our previous studies (Chapters 3 & 4) that dye adsorption on the surface of the photocatalyst plays a crucial role in photocatalysis in addition to other well-known factors such as, creation of electron-hole pairs on photoexcitation and generation of reactive oxygen species (ROS) followed by oxidative degradation of the dye on action of ROS generated. In general, firstly on absorption of light photons by a photocatalyst, electrons from valence band (VB) get excited to the conduction band (CB) and leave holes at the VB. In the second step, the electrons-hole pairs thus generated get separated from each other and migrate to the surface of the photocatalyst where they participate in the reactive species generation/redox reaction. In most cases, electrons in the CB reduces dissolved oxygens to yield superoxide radical anions ($O_2^{\bullet-}$) and holes in the VB oxidizes water to give $^{\bullet}OH$ radicals, which further takes part in the dye degradation. In addition, the photogenerated holes in the VB of the semiconductors may also oxidize adsorbed dye molecules into CO_2 and H_2O.

To explain the enhanced photocatalysis, the relative band edge positions of the photocatalysts were calculated using the following empirical formula [15] and a similar procedure as described in Chapter 3.

$$E_{CB} = \chi(A_aB_bC_c) - \tfrac{1}{2} E_g + E_0 \qquad (5.4)$$

$$E_{VB} = E_{CB} + E_g \quad (5.5)$$

Using the above equations, the CB (E_{CB}) and VB (E_{VB}) positions of $Bi_5ATi_4FeO_{18}$ (*A* = Ca, Sr, and Pb) are calculated and summarized in Table 5.8. The potential for generation of $^{\bullet}OH$ ($E_{\bullet OH/H2O}$= + 2.68 eV *vs. NHE*), $O_2^{\bullet-}$ ($E_{O2/O2\bullet-}$= + 0.13 eV *vs*. *NHE*) and HOMO-LUMO levels of RhB (E_{HOMO} = 0.95 eV and E_{LUMO} = – 1.42 eV) and MB (E_{HOMO} = 1.76 eV and E_{LUMO} = – 0.05 eV) as reported in the literature were used [16-18].

Since the conduction band potential of $Bi_5SrTi_4FeO_{18}$ E_{CB} (2) (– 0.15 eV *vs. NHE*) is higher than the potential for generation of $O_2^{\bullet-}$ ($E_{O2/O2\bullet-}$ = + 0.13 eV *vs. NHE*), the photoinduced electrons in E_{CB} (2) could react with dissolved O_2 to produce $O_2^{\bullet-}$ radicals (Figure 5.22). Meanwhile, the holes generated in the VB of the catalyst could transfer to the adsorbed dye and thereby degrade it. Moreover, the photogenerated holes are not in favor to form $^{\bullet}OH$ radicals by oxidizing H_2O because the valence band potential (E_{VB} = + 2.39 eV *vs. NHE*) is higher than the potential for $^{\bullet}OH$ radical generation from H_2O ($E_{\bullet OH/H2O}$ = + 2.68 eV *vs. NHE*). Therefore, $O_2^{\bullet-}$ and h^+ are the major reactive species that actively contribute to the dye degradation. This is also evidenced by the scavenger test results. Moreover, the electrons at the LUMO of RhB are in a favorable position for its degradation through a photosensitization mechanism.

Table 5.8 Calculated Values of Valence and Conduction Band Positions of $Bi_5ATi_4FeO_{18}$ (*A* = Ca, Sr, Pb)

compound	valence band (eV)	conduction band-1 (eV)	conduction band-2 (eV)
$Bi_5CaTi_4FeO_{18}$	2.40	0.31	– 0.21
$Bi_5SrTi_4FeO_{18}$	2.39	0.27	– 0.33
$Bi_5PbTi_4FeO_{18}$	2.52	0.41	– 0.14

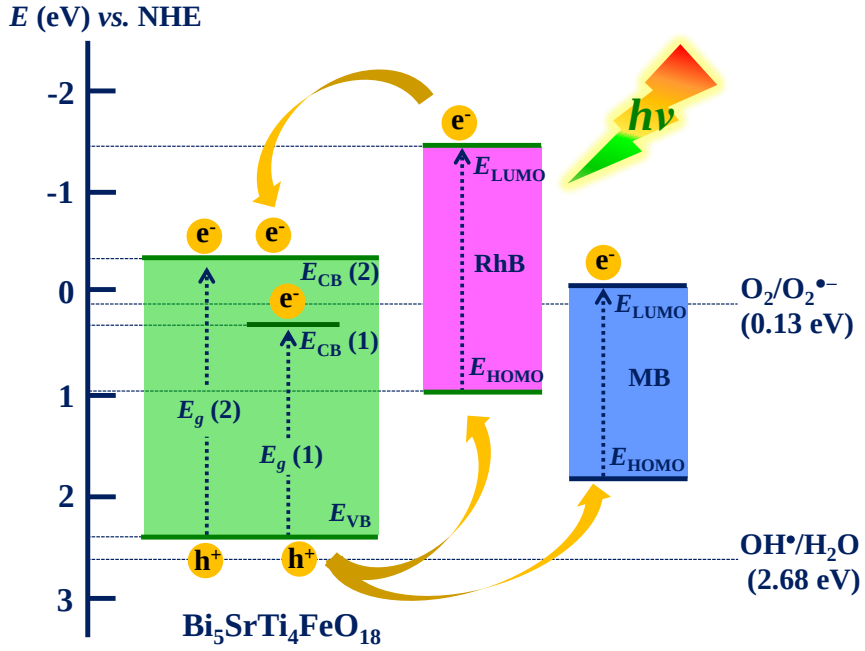

Figure 5.22 Schematic energy level diagram of $Bi_5SrTi_4FeO_{18}$ with respect to potential (vs *NHE*) for generation of $^{\bullet}OH$ ($E_{\bullet OH/H2O}$), $O_2^{\bullet-}$ ($E_{O2/O2\bullet-}$) radicals and the HOMO-LUMO levels of the dyes (RhB and MB).

5.3.12 Adsorption and ζ–potential

As we have established, the attachment of the dye molecule with the catalyst surface plays a crucial role in h^+ mediated dye degradation and we believe that the preferential adsorption of MB over RhB is one of the reasons for selective degradation. For this purpose, we have performed adsorption tests over $Bi_5ATi_4FeO_{18}$ (*A* = Ca, Sr, Pb) at different pH in the dark. Interestingly, the adsorption results in mixed dye solutions indicate selective adsorption of MB in neutral and alkaline media (Figure 5.23) for all the catalysts. However, it shows both MB and RhB adsorption in the acidic medium. The maximum adsorption of MB took place in the alkaline medium for all the catalysts. These results are consistent with the selective degradation of MB in the neutral and alkaline media, and mixed dye degradation (both MB and RhB) in the acidic medium. The selective degradation is faster in the alkaline medium because of maximum adsorption of MB. Moreover, the individual adsorption of MB and RhB in different media over these catalysts under dark is shown in Figure 5.24. The photocatalytic activity of the catalysts follows the adsorption order making

$Bi_5SrTi_4FeO_{18}$ as the most efficient and decreases in the order $Bi_5SrTi_4FeO_{18}$ > $Bi_5PbTi_4FeO_{18}$ > $Bi_5CaTi_4FeO_{18}$.

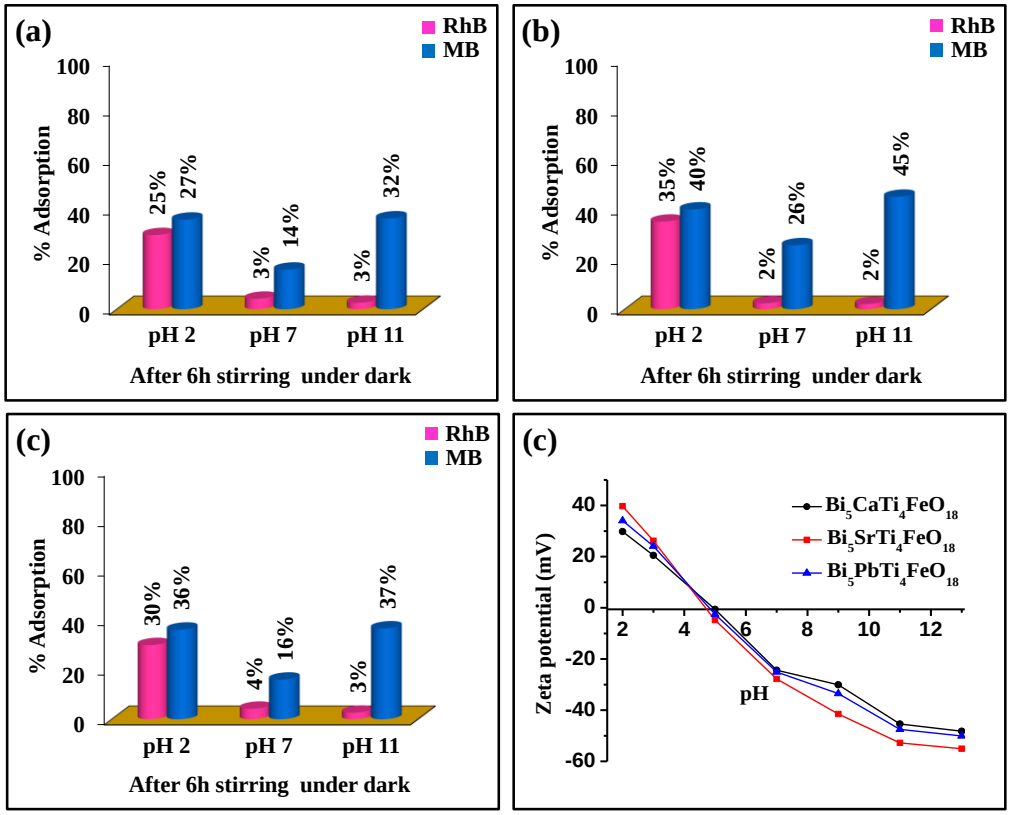

Figure 5.23 Influence of pH on preferential adsorption of dye from aqueous mixtures of MB and RhB on (a) $Bi_5CaTi_4FeO_{18}$, (b) $Bi_5SrTi_4FeO_{18}$, and (c) $Bi_5PbTi_4FeO_{18}$. (d) ζ- potential of $Bi_5ATi_4FeO_{18}$ (*A* = Ca, Sr, and Pb) catalysts at different pH.

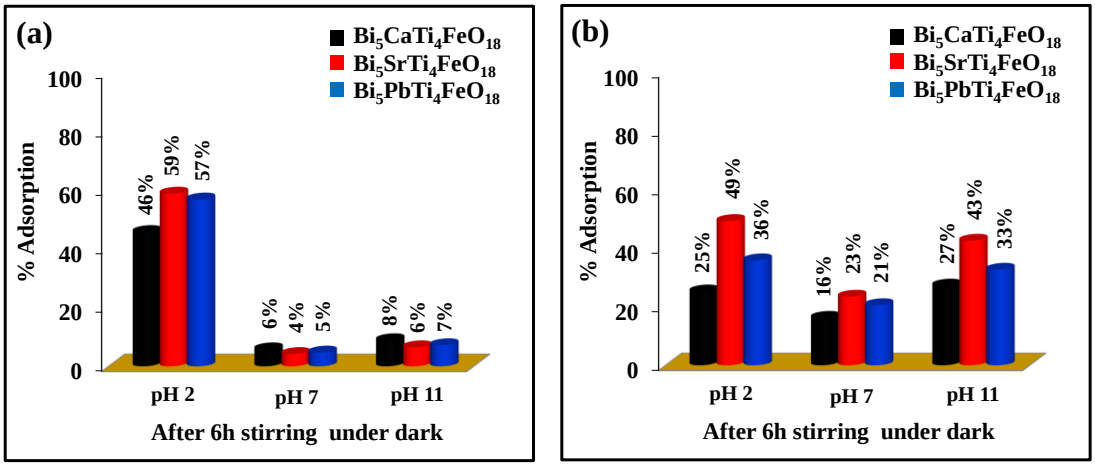

Figure 5.24 Influence of pH on adsorption of (a) RhB, (b) MB over $Bi_5ATi_4FeO_{18}$ (*A* = Ca, Sr, and Pb) catalyst surfaces.

The catalyst surface charge plays a vital role in the dye adsorption process. The ζ-potential measurements were performed to know the surface charge of the catalysts at different pH, and the results are shown in Figure 5.23 (d). The highest negative ζ–potentials are observed at pH 11. As the pH is decreased, the ζ– potential decreases from more negative potentials to less negative potentials and finally to reach positive potentials in the acidic medium. This trend is mostly due to the action of H^+ and OH^- ions on the surface hydroxyl groups of the oxide catalyst and has been discussed in Chapter 3.

Interestingly, the ζ–potential of the catalysts was mirrored in the selective dye adsorption and degradation. At pH 11, only MB adsorption took place on $Bi_5SrTi_4FeO_{18}$, which had highest negative ζ– potential (– 55.1 mV) followed by $Bi_5PbTi_4FeO_{18}$ and $Bi_5CaTi_4FeO_{18}$, which had ζ- potentials of – 50.1 and – 48.2 mV, respectively. Moreover, selective MB adsorption to a moderate extent was also noticed at pH 7. This has also been attributed to negative ζ– potentials of the catalysts at this pH. The selective adsorption of MB in neutral and alkaline media is due to electrostatic interaction of negatively charged catalyst surfaces with the cationic MB molecules, while a negligible adsorption of RhB is attributed to the electrostatic repulsion between the negatively charged carboxylic acid groups of RhB molecules and a negatively charged catalyst surface. Moreover, all the catalysts reported here show the adsorption of both MB and RhB in the acidic medium. The biggest adsorption of both dyes took place over $Bi_5SrTi_4FeO_{18}$, which had more positive ζ-potential (+ 39.7 mV) among all the catalysts at pH 2. The ζ- potential for $Bi_5PbTi_4FeO_{18}$ and $Bi_5CaTi_4FeO_{18}$ were + 34.1 and + 29.8 mV, respectively. The adsorption of both dyes is due to a positively charged catalyst surface that electrostatically interacts with negatively charged carboxylic acid group of RhB and probably the co-adsorption of MB over RhB. Indeed, the adsorption of the dyes over catalyst surface is in good agreement with the ζ-potential.

In summary, new five-layer Aurivillius perovskites, $Bi_5ATi_4FeO_{18}$ (*A* = Ca, Sr, Pb), are synthesized and characterized for the first time, to the best of our knowledge. The UV-vis DRS confirmed that all the catalysts have principal band gap in the visible ranging from ~ 2.61–2.72 eV. These catalysts showed fully selective degradation of MB from aqueous mixture of MB and RhB in alkaline as well as neutral medium (pH 11 and 7). However, the catalysts degrade MB and RhB simultaneously in the acidic medium (pH 2). The

photocatalytic activity tests indicated $Bi_5SrTi_4FeO_{18}$ as the most active catalyst among all the Aurivillius oxides reported in this chapter. The improved photocatalysis of $Bi_5SrTi_4FeO_{18}$ is attributed to a sluggish recombination of photoinduced e^-–h^+ pairs, higher surface charge and corresponding enhanced adsorption of dye on the catalyst surface. Scavenger tests indicated h^+ and $O_2^{\bullet-}$ as major reactive species contributing toward photocatalytic RhB and MB degradation in presence of $Bi_5SrTi_4FeO_{18}$. The valence and conduction band edge positions of $Bi_5SrTi_4FeO_{18}$ with respect to potentials of $^{\bullet}OH/H_2O$, $O_2/O_2^{\bullet-}$ and HOMO–LUMO levels of RhB and MB also supports the involvement h^+ and $O_2^{\bullet-}$ radicals in the photocatalysis. Moreover, the photocatalytic cycle tests and post-catalysis PXD pattern analysis confirmed the cycleability and stability of the catalysts under the reactions conditions.

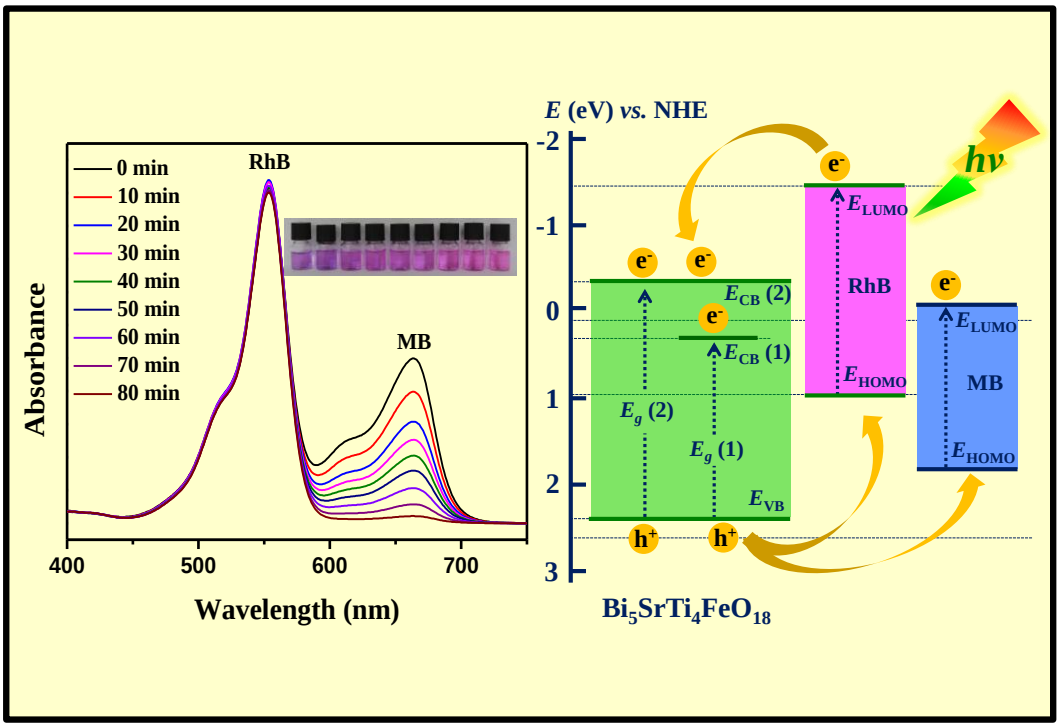

REFERENCES

1. Yurdakal, S.; Palmisano, G.; Loddo, V.; Augugliaro, V.; Palmisano, L. Nanostructured Rutile TiO_2 for Selective Photocatalytic Oxidation of Aromatic Alcohols to Aldehydes in Water *J. Am. Chem. Soc.* **2008**, *130*, 1568-1569.

2. Shiraishi, Y.; Saito, N.; Hirai, T. Adsorption–Driven Photocatalytic Activity of Mesoporous Titanium Dioxide. *J. Am. Chem. Soc.* **2005**, *127*, 12820-12822.

3. Robert, D.; Piscopo, A.; Weber, J. V. First Approach of the Selective Treatment of Water by Heterogeneous Photocatalysis. *Environ. Chem. Lett.* **2004**, *2*, 5-8.

4. Ghosh-Mukerji, S.; Haick, H.; Schvartzman, M.; Paz, Y. Selective Photocatalysis by Means of Molecular Recognition *J. Am. Chem. Soc.* **2001**, *123*, 10776-10777.

5. Lazar, M. A.; Daoud, W. A. Selective adsorption and photocatalysis of low-temperature base-modified anatase nanocrystals. *RSC Advances* **2012**, *2*, 447-452.

6. Dutta, D. P.; Rathore, A.; Ballal, A.; Tyagi, A. K. Selective sorption and subsequent photocatalytic degradation of cationic dyes by sonochemically synthesized nano CuWO4 and Cu3Mo2O9. *RSC Advances* **2015**, *5*, 94866-94878.

7. Wang, L.; Hu, G.; Wang, Z.; Wang, B.; Song, Y.; Tang, H. Highly efficient and selective degradation of methylene blue from mixed aqueous solution by using monodisperse CuFe2O4 nanoparticles. *RSC Advances* **2015**, *5*, 73327-73332.

8. Shimodaira, Y.; Kato, H.; Kobayashi, H.; Kudo, A. Photophysical Properties and Photocatalytic Activities of Bismuth Molybdates under Visible Light Irradiation. *J. Phys. Chem. B* **2006**, *110*, 17790-17797.

9. Kim, H. G.; Borse, P. H.; Jang, J. S.; Jeong, E. D.; Lee, J. S. Enhanced Photochemical Properties of Electron Rich W-Doped $PbBi_2Nb_2O_9$ Layered Perovskite Material under Visible-Light Irradiation. *Mater. Lett.* **2008**, *62*, 1427-1430.

10. Muktha, B.; Priya, M. H.; Madras, G.; Guru Row, T. N. Synthesis, Structure, and Photocatalysis in a New Structural Variant of the Aurivillius Phase: $LiBi_4M_3O_{14}$ (M = Nb, Ta). *J. Phys. Chem. B* **2005**, *109*, 11442-11449.

11. Zhou, L.; Yu, M.; Yang, J.; Wang, Y.; Yu, C. Nanosheet-Based $Bi_2Mo_xW_{1-x}O_6$ Solid Solutions with Adjustable Band Gaps and Enhanced Visible-Light-Driven Photocatalytic Activities. *J. Phys. Chem. C* **2010**, *114*, 18812-18818.

12. Zhang, L.; Man, Y.; Zhu, Y. Effects of Mo Replacement on the Structure and Visible-Light-Induced Photocatalytic Performances of Bi_2WO_6 Photocatalyst. *ACS Catal.* **2011**, *1*, 841-848.

13. Fujihara, K.; Izuni, S.; Ohno, S.; Matsumura, M. Time-resolved Photoluminescence of Particulate TiO_2 Photocatalysts Suspended in Aqueous Solution. *J. Photochem. Photobiol. A* **2000**, *132*, 99-104.

14. Watanabe, T.; Takizawa, T.; Honda, K. Photocatalysis through excitation of Adsorbates. 1. Highly Efficient N-deethylation of Rhodamine B Adsorbed to Cadmium Sulfide. *J. Phys. Chem.* **1977**, *81*, 1845-1851.

15. Lv, J.; Kako, T.; Zou, Z.; Ye, J. Band Structure Design and Photocatalytic Activity of In_2O_3/N−$InNbO_4$ Composite. *Appl. Phys. Lett.* **2009**, *95*, 032107-032109.

16. Kumar, S.; Surendar, T.; Baruah, A.; Shanker, V. Synthesis of a Novel and Stable g-C_3N_4-Ag_3PO_4 Hybrid Nanocomposite Photocatalyst and Study of the Photocatalytic Activity under Visible Light Irradiation. *J. Mater. Chem. A* **2013**, *1*, 5333-5340.

17. Pan, L.; Zou, J.; Liu, X.; Liu, X.; Wang, S.; Zhang, X.; Wang, L. Visible-Light-Induced Photodegradation of Rhodamine B over Hierarchical TiO_2: Effects of Storage Period and Water-Mediated Adsorption Switch. *Ind. Eng. Chem. Res.* **2012**, *51*, 12782-12786.

18. Shen, J-S.; Yu, T.; Xie, J-W.; Jiang, Y-B. Photoluminescence of CdTe Nanocrystals Modulated by Methylene Blue and DNA. A Label-Free Luminescent Signaling Nanohybride Platform. *Phys. Chem. Chem. Phys.* **2009**, *11*, 5062-5069.

CHAPTER -6

Layered Oxyhalide Perovskites: New Members of Sillén-Aurivillius Hybrids and their Sunlight-Driven Selective Dye Degradation

Layered Oxyhalide Perovskites: New Members of Sillén-Aurivillius Hybrids and their Sunlight-Driven Selective Dye Degradation

6.1 INTRODUCTION

Synthetic dyes are widely used in several industries such as paper, textiles, plastics, printing, cosmetics, coatings, and rubber [1, 2]. It has been estimated that more than 11% of these dyes were discharged into environment during manufacture and application process [3]. Some of these dyes are toxic and even carcinogenic for the entire ecosystem. So, degradation/complete mineralization of these dyes are essential before these are disposed off to the environment.

In recent years, various transition metal oxide based photocatalysts, such as Fe_2O_3, ZnO, TiO_2 and many others have been extensively explored for environmental remediation [4-6, 7, 8]. In particular, TiO_2 has been widely investigated as an efficient photocatalyst because of its excellent photostability, non-toxicity and inexpensive nature [4-6, 9, 10]. But, the major disadvantage associated with TiO_2 is its utilization of UV-light and non-selective photocatalysis. Some examples of selective catalysis by TiO_2 have been discussed before in Chapter 5. In addition, few other surface modified TiO_2 systems for selective degradation [11, 12], microporous titanosilicates for shape-selective photocatalytic degradation [13, 14] and organic conversion [15, 16] have been reported. In the light of very limited research on selective MB degradation as pointed out in Chapter 5, there is immense potential in developing solar photocatalysts for selective dye degradation.

As already discussed in the previous chapters, the research attention in utilizing solar energy by visible-light-induced photocatalysis employing Aurivillius layered perovskites continue to grow [17-25]. Recently, Bi-containing layered Sillén-Aurivillius intergrowth phases have been reported for their excellent visible-light-induced photocatalytic activity [26-30] and ferroelectric properties [31-33]. Moreover, the Sillén-Aurivillius intergrowth phases have been researched as efficient photocatalysts with effective separation of photogenerated electrons and holes due to the presence of internal electric fields between

$[Bi_2O_2]$ and [Cl] blocks [26]. The family of Sillén-Aurivillius intergrowth phases originates from the regular intergrowth of two structurally similar families, namely, the Aurivillius and the Sillén phases. Both the family consists of common fluorite-like $[Bi_2O_2]$ blocks that alternately stack with either a perovskite-like block, $[A_{n-1}B_nO_{3n+1}]$, (as in Aurivillius phases) or a halide block $[X_m]$ (as in Sillén phases). The Sillén-Aurivillius intergrowth phases have the general formula, $[M_2O_2][A_{n-1}B_nO_{3n+1}][M_2O_2][X_m]$. The nomenclature A*n*X*m* is used for these phases to express the number of perovskite octahedral [A*n*] layers and halide [X*m*] layers, typical examples being Bi_4NbO_8Cl [A1X1] [34], $Bi_3Pb_2Nb_2O_{11}Cl$ [A2X1] [32] and $Bi_5PbTi_3O_{14}Cl$ [A3X1] [33].

In previous chapters we have dealt with new member of Aurivillius phases where the perovskite layer thickness varied from four to five. Moreover, anion and cation manipulations were carried out and their effect on phase stability, structure and photocatalytic activity was investigated. Although there are recent reports on the visible-light-driven photocatalytic activity by Sillén-Aurivillius intergrowths, the studies were limited to the simplest members of the series where the perovskite block was single layer thick. In the present endeavor, we have undertaken a systematic study on the exploration of new Sillén-Aurivillius intergrowths where the perovskite layer thickness is three. In this chapter, we report for the first time, the synthesis, characterization and photocatalytic activity of a new series of Sillén-Aurivillius intergrowth layered perovskites, $Bi_{5-x}La_xBaTi_3O_{14}Cl$ (x = 0 – 2). Selective and collective photodegradation of dyes from aqueous mixture of MB-RhB at different pH have been studied under solar irradiation. Moreover, the individual photodegradation of RhB and MB at different pH is also explored over these hybrid phases. The efficiency of photoinduced e^-–h^+ separation in these semiconductors was compared with the aid of PL and EIS. A mechanistic study of the photocatalytic dye degradation over these compounds have been carried out with the help of scavenger tests and corroborated with the aid of an energy level diagram.

6.2 EXPERIMENTAL SECTION

6.2.1 Materials and Synthesis

Bi_2O_3 (≥ 98%), La_2O_3 (99.99%), $BaCO_3$ (≥ 99%), and TiO_2 (99.8%) were purchased from Sigma-Aldrich and used as received. The other reagents used in our experiments were

of analytical grade and used without any further purification. Millipore water (Bedford, MA, USA) was used for preparation of all dye solutions.

Polycrystalline samples of $Bi_{5-x}La_xBaTi_3O_{14}Cl$ (x = 0 – 2) were synthesized by solid-state reactions. For this, stoichiometric quantities of $Bi_{4-x}La_xTi_3O_{12}$ (x = 0 – 2) and $BiBaO_2Cl$ were ground thoroughly in an agate mortar for 1 h and heated at 820 °C for 20 h under Argon flow. The compounds, $Bi_{4-x}La_xTi_3O_{12}$ (x = 0 – 2) and $BiBaO_2Cl$, were synthesized by conventional solid-state reaction method, similar to that reported in the literature [35].

6.2.2 Photocatalysis

All the photocatalytic dye degradation experiments were carried out in IIT Roorkee (29°51′ N; 77°53′ E) under identical conditions in the month of December, 2014 (having solar Direct Normal Irradiance ~ 137 W/m^2 during the month). In a typical degradation study, 100 mg catalyst suspended in 100 mL 1×10^{-5} M dye solution (in a 250 mL beaker) of appropriate pH was first magnetically stirred in the dark for 1 h, and then exposed to sunlight-irradiation. At given intervals, small aliquots (3 mL) of suspensions were withdrawn, centrifuged and the absorbance of the supernatant was measured on a UV-vis spectrophotometer. The degradation efficiency was evaluated by using the absorption data. A blank test was also conducted with the same dye solution of appropriate pH without catalyst under identical conditions to assess the self-degradation of the dye. The remaining procedure that was followed to monitor the dye degradation was same as reported in the previous chapter (Chapter 5). The COD removal efficiency was calculated by the following expression.

$$\text{Potodegradation efficiency} = \frac{\text{Initial COD} - \text{Final COD}}{\text{Initial COD}} \times 100 \qquad (6.1)$$

To understand the role of reactive species (h^+, $^\bullet OH$ and $O_2^{\bullet-}$) on the photocatalytic activity, different scavenger tests were conducted. In this experiment, 10 mM of an appropriate scavenger was added to the catalyst-dye suspension and degradation was carried out in a similar fashion to that described in the previous chapters. For this purpose, ammonium oxalate (AO), benzoquinone (BQ) and tertiary butyl alcohol (*t*-BuOH) were used as h^+, $O_2^{\bullet-}$ and $^\bullet OH$ scavengers, respectively [36, 37].

6.3 RESULTS AND DISCUSSION

6.3.1 PXD Analysis

The PXD patterns of $Bi_{5-x}La_xBaTi_3O_{14}Cl$ (x = 0 – 2) are shown in Figure 6.1. The PXD pattern indicated formation of pure Sillén-Aurivillius hybrid perovskite phase similar to orthorhombic $Bi_5PbTi_3O_{14}Cl$ (JCPDS card # 35-0454) reported in the literature. All the peaks observed in the PXD pattern are indexable in the orthorhombic *P*2*an* space group. The lattice parameters of all the newly synthesized compounds are least-square refined by the PROSZKI program and are given in Table 6.1. The indexed PXD data for $Bi_5BaTi_3O_{14}Cl$, $Bi_4LaBaTi_3O_{14}Cl$ and $Bi_3La_2BaTi_3O_{14}Cl$ are given in Tables 6.2, 6.3 and 6.4, respectively.

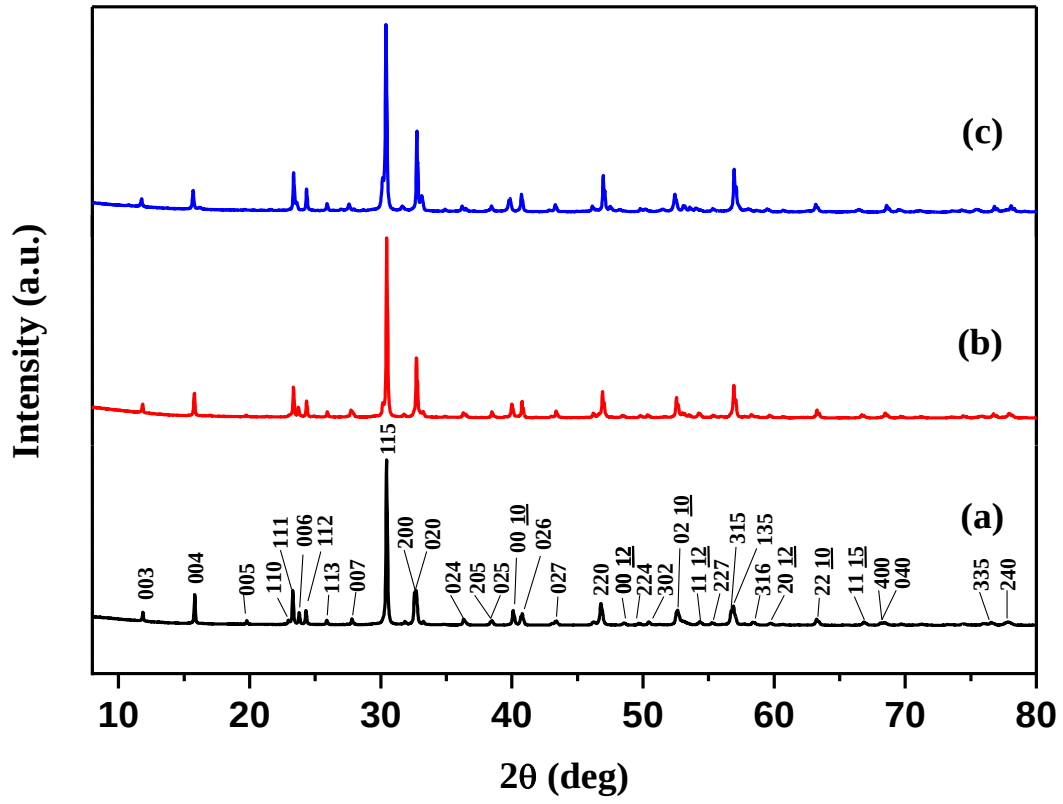

Figure 6.1 PXD patterns of (a) $Bi_5BaTi_3O_{14}Cl$, (b) $Bi_4LaBaTi_3O_{14}Cl$, and (c) $Bi_3La_2BaTi_3O_{14}Cl$.

The trend in the lattice parameter variation of the La-substituted analogs $Bi_{5-x}La_xBaTi_3O_{14}Cl$ (x = 1 – 2) are consistent with those observed with four layer Aurivillius phases described in Chapter 3. The lattice parameters show a marginal increase in the *c*-direction while the difference in the in-plane lattice parameters (*a* and *b*) decreases gradually with La-substitution. This indicates a decrease in orthorhombic distortion with progressive replacement of lone-pair active Bi^{3+} by La^{3+} and adoption of nearly tetragonal structure in the end member, $Bi_3La_2BaTi_3O_{14}Cl$, which has been stabilized in this study. It has been reported that the incorporation of La in the A-site of the perovskite decreases the out-of-center distortion [38] which results in an increase in the *c*-parameter with increasing La-substitution. The lattice parameter variation is consistent with the above fact.

Table 6.1 Lattice Parameters and Band Gap Energies of $Bi_{5-x}La_xBaTi_3O_{14}Cl$ (x = 0 - 2)

Compound	Lattice parameters (Å)			Band Gap (eV)
	a	*b*	*c*	E_g
$Bi_5BaTi_3O_{14}Cl$	5.499(1)	5.478(1)	22.472(5)	2.66
$Bi_4LaBaTi_3O_{14}Cl$	5.477(1)	5.463(1)	22.530(6)	2.74
$Bi_3La_2BaTi_3O_{14}Cl$	5.471(1)	5.468(1)	22.627(4)	2.87

Table 6.2 Indexed PXD Data for $Bi_5BaTi_3O_{14}Cl$

h k l	d_{obs}(Å)	d_{calc} (Å)	I_{obs}
0 0 3	7.459	7.490	5
0 0 4	5.601	5.618	18
0 0 5	4.485	4.494	2
1 1 0	3.873	3.881	2
1 1 1	3.817	3.824	21
0 0 6	3.740	3.745	7
1 1 2	3.662	3.668	8
1 1 3	3.442	3.446	3
0 0 7	3.207	3.210	4
1 1 5	2.934	2.937	100
2 0 0	2.747	2.749	19
0 2 0	2.737	2.739	21
2 0 5	2.343	2.345	3
0 2 5	2.338	2.339	3
0 0 10	2.247	2.247	9
0 2 6	2.210	2.211	7
0 2 7	2.084	2.084	3
2 2 0	1.940	1.941	13
0 0 12	1.874	1.873	2
2 2 4	1.834	1.834	1
3 0 2	1.808	1.809	2
0 2 10	1.738	1.737	9
1 1 12	1.687	1.687	2
3 1 5	1.622	1.621	8
1 3 5	1.617	1.617	11
3 1 6	1.580	1.577	2
2 0 12	1.547	1.548	1
2 2 10	1.469	1.469	4
1 1 15	1.398	1.398	2
4 0 0	1.375	1.375	1
0 4 0	1.369	1.369	2
3 3 5	1.244	1.243	2
2 4 0	1.226	1.226	2

a = 5.499(1), b = 5.478(1), c = 22.472(5) Å.

Table 6.3 Indexed PXD Data for $Bi_4LaBaTi_3O_{14}Cl$

h k l	d_{obs}(Å)	d_{calc} (Å)	I_{obs}
0 0 3	7.472	7.510	5
0 0 4	5.609	5.632	13
0 0 5	4.498	4.506	1
1 1 0	3.865	3.868	1
1 1 1	3.808	3.812	16
0 0 6	3.749	3.755	5
1 1 2	3.654	3.659	9
1 1 3	3.435	3.438	3
0 0 7	3.215	3.219	4
1 1 5	2.933	2.935	100
2 0 0	2.735	2.739	33
0 2 0	2.734	2.732	33
0 2 4	2.458	2.458	3
2 0 5	2.338	2.340	3
0 2 5	2.332	2.336	3
0 0 10	2.252	2.253	7
0 2 6	2.211	2.209	9
0 2 7	2.085	2.083	4
2 2 0	1.935	1.934	15
0 0 12	1.878	1.878	1
2 2 4	1.830	1.829	1
3 0 2	1.804	1.802	2
0 2 10	1.736	1.738	11
1 1 12	1.689	1.689	2
3 1 5	1.616	1.616	18
1 3 5	1.612	1.613	18
3 1 6	1.582	1.573	2
2 0 12	1.549	1.549	1
2 2 10	1.469	1.468	4
1 1 15	1.401	1.400	2
4 0 0	1.369	1.369	3
0 4 0	1.366	1.366	2
3 3 5	1.241	1.240	2
2 4 0	1.225	1.222	2

a = 5.477(1), b= 5.463(1), c = 22.530(6) Å.

Table 6.4 Indexed PXD Data for $Bi_3La_2BaTi_3O_{14}Cl$

h k l	d_{obs}(Å)	d_{calc} (Å)	I_{obs}
0 0 3	7.520	7.542	4
0 0 4	5.642	5.656	10
0 0 5	4.520	4.525	1
1 1 1	3.806	3.812	20
0 0 6	3.770	3.771	4
1 1 2	3.654	3.659	11
1 1 3	3.437	3.441	4
0 0 7	3.230	3.232	4
1 1 5	2.938	2.940	100
2 0 0	2.734	2.735	43
0 2 0	2.732	2.734	43
0 2 4	2.479	2.462	3
2 0 5	2.341	2.341	3
0 2 5	2.339	2.340	3
0 0 10	2.260	2.263	7
0 2 6	2.213	2.214	9
0 2 7	2.087	2.087	4
2 2 0	1.933	1.934	19
0 2 10	1.743	1.743	9
1 1 12	1.696	1.695	3
3 1 5	1.615	1.616	22
1 3 5	1.612	1.615	22
3 1 6	1.573	1.572	1
2 0 12	1.553	1.553	1
2 2 10	1.471	1.470	4
1 1 15	1.405	1.405	1
4 0 0	1.367	1.368	4
2 4 0	1.223	1.223	3

a = 5.471(1), b = 5.468(1), c = 22.627(1) Å.

6.3.2 FE-SEM and EDS Analysis

FE-SEM images and corresponding EDS spectra for $Bi_{5-x}La_xBaTi_3O_{14}Cl$ (x = 0 – 2) are shown in Figure 6.2. All the compounds show plate-like morphology having aggregated platelets with particle sizes ranging from several hundred nanometers to few micrometers. The EDS analysis carried out at several regions of the image shows excellent compositional uniformity of the compounds with the experimental elemental ratio closely matching with the nominal compositions.

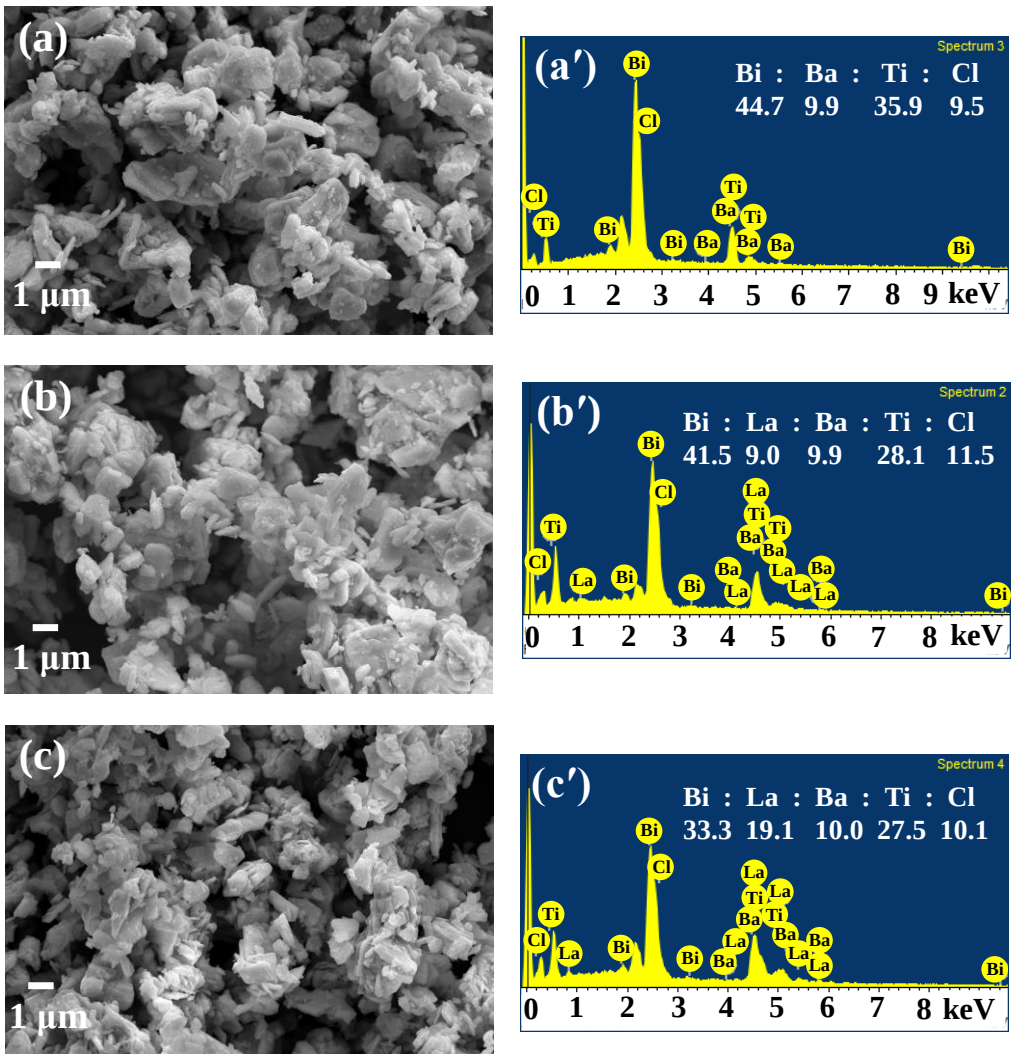

Figure 6.2 FE-SEM/EDX analysis of $Bi_5BaTi_3O_{14}Cl$ (a, a′), $Bi_4LaBaTi_3O_{14}Cl$ (b, b′), and $Bi_3La_2BaTi_3O_{14}Cl$ (c, c′).

6.3.3 FE-SEM-EDS Elemental Mapping Analysis

To investigate the elemental distribution in $Bi_{5-x}La_xBaTi_3O_{14}Cl$ (x = 0 – 2), EDS elemental mapping was performed at different areas of the samples. The EDS elemental mapping results are shown in Figure 6.3, which indicates homogeneous distribution of all the elements in these compounds. Moreover, an increase in La quantity and decrease in Bi quantity as x varies from 0 – 2, while the quantity of Ba, Ti and Cl remained largely unaltered as expected for nominal compositions is clearly evident in the elemental mapping.

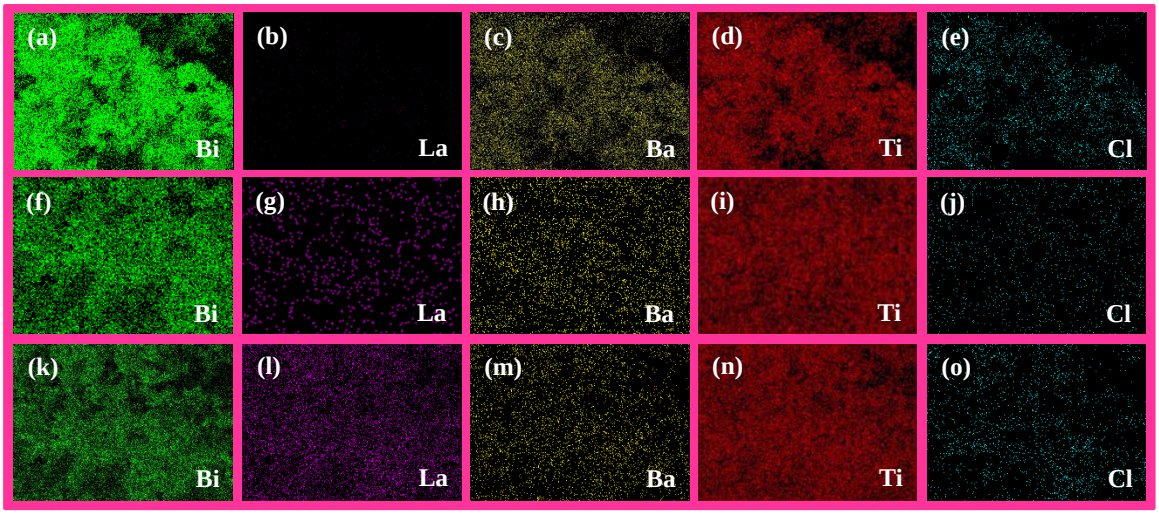

Figure 6.3 EDS mapping of (a) Bi, (b) La, (c) Ba, (d) Ti, and (e) Cl in $Bi_5BaTi_3O_{14}Cl$, (f–j) and (k–o) are elemental mapping for $Bi_4LaBaTi_3O_{14}Cl$ and $Bi_3La_2BaTi_3O_{14}Cl$, respectively.

6.3.4 UV-vis DRS Analysis

The UV-vis DRS spectra of the parent Aurivillius ($Bi_{4-x}La_xTi_3O_{12}$; x = 0 – 2), Sillén ($BaBiO_2Cl$), and the hybrid phases, $Bi_{5-x}La_xBaTi_3O_{14}Cl$ (x = 0 – 2) are shown in Figure 6.4. The precursor compounds, $Bi_{4-x}La_xTi_3O_{12}$ and $BaBiO_2Cl$, show absorption edges in the UV (< 400 nm) while the Sillén-Aurivillius intergrowth phases, $Bi_{5-x}La_xBaTi_3O_{14}Cl$ (x = 0 – 2), show absorption edges in the visible region (> 400 nm). These results indicate that intergrowth of the Sillén and Aurivillius is an effective strategy to transform the UV active wide gap semiconductors into the visible-light-active semiconductors. The parent compound of the series, namely, $Bi_5BaTi_3O_{14}Cl$, shows an absorption edge at ~ 479 nm, whilst the absorption edge is found to be blue-shifted with increasing La-content. The exact band gaps (E_g) of the semiconductors are calculated from the Tauc plots portrayed in Figure 6.5. The

estimated E_g of $Bi_{5-x}La_xBaTi_3O_{14}Cl$ (x = 0 – 2) are given in Table 6.1. All the intergrowth phases show absorption in the visible, thereby indicating their potential in sunlight-driven photocatalytic activity.

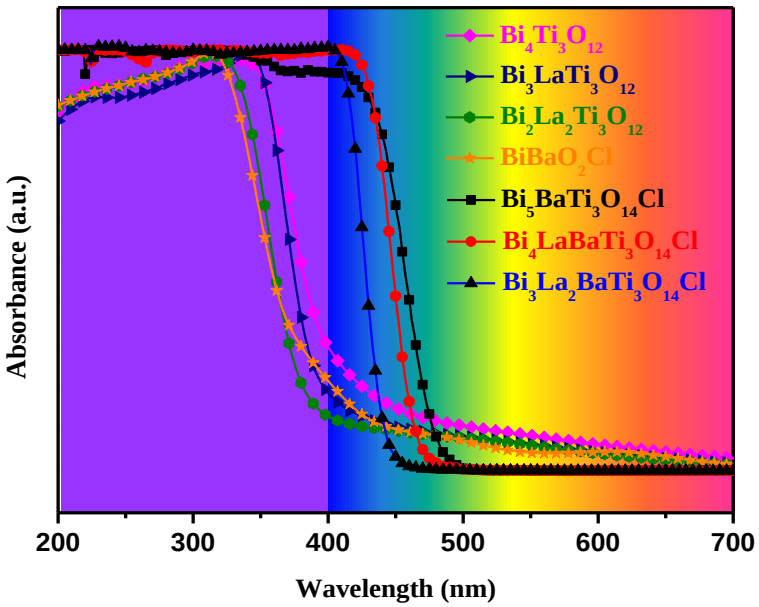

Figure 6.4 UV-vis DRS of $Bi_{4-x}La_xTi_3O_{12}$ (x = 0 – 2), $BiBaO_2Cl$ and $Bi_{5-x}La_xBaTi_3O_{14}Cl$ (x = 0 – 2).

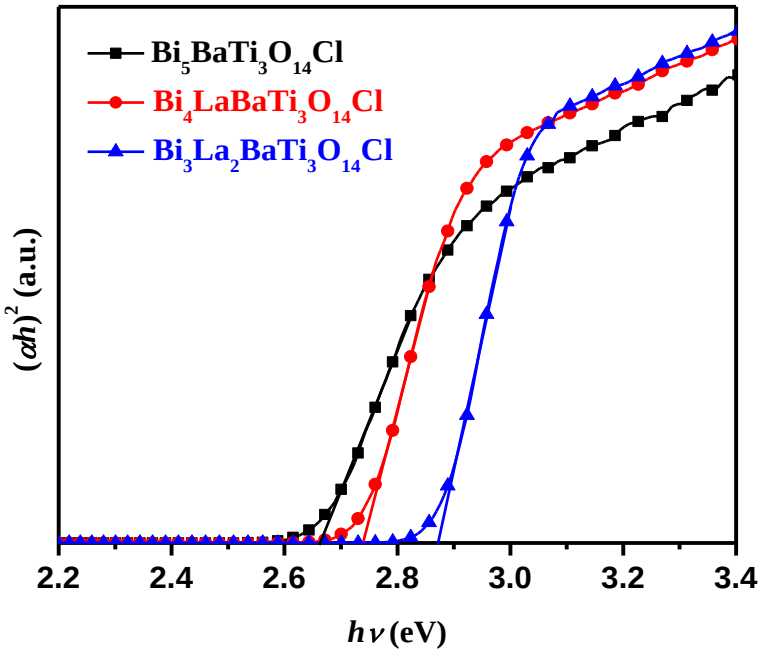

Figure 6.5 Tauc plots for calculation of band gap of $Bi_{5-x}La_xBaTi_3O_{14}Cl$ (x = 0 – 2).

6.3.5 PL Analysis

To compare the e^-–h^+ recombination rate and effectiveness of photoinduced e^-–h^+ separation in $Bi_{5-x}La_xBaTi_3O_{14}Cl$ (x = 0 – 2), PL spectra were recorded with an excitation wavelength of 350 nm. The PL intensity being an indirect measure of the e^-–h^+ recombination rate, a lower PL intensity indicates slow recombination and therefore better separation of the photogenerated e^- and h^+ pairs [39]. All the compounds showed broad emission spectra (Figure 6.6 (a)) ranging from 402 to 558 nm with a peak around 470 nm. According to the PL intensity, the expected activity order would be $Bi_5BaTi_3O_{14}Cl$ < $Bi_4LaBaTi_3O_{14}Cl$ < $Bi_3La_2BaTi_3O_{14}Cl$, if all other factors are considered to remain fixed.

6.3.6 EIS Analysis

The EIS studies were carried out to investigate the charge transfer resistance (R_{CT}) and the separation efficiency of the photogenerated charge carriers. The R_{CT} for $Bi_5BaTi_3O_{14}Cl$, $Bi_4LaBaTi_3O_{14}Cl$, and $Bi_3La_2BaTi_3O_{14}Cl$ were found to be 35.85, 30.99 and 27.86 kΩ, respectively. As shown in Figure 6.6 (b), the diameter of the Nyquist semicircle for $Bi_3La_2BaTi_3O_{14}Cl$ is smaller than that for $Bi_4LaBaTi_3O_{14}Cl$ and $Bi_5BaTi_3O_{14}Cl$, which indicates a lower charge transfer resistance for $Bi_3La_2BaTi_3O_{14}Cl$ as compared to $Bi_5BaTi_3O_{14}Cl$ and $Bi_4LaBaTi_3O_{14}Cl$. These results demonstrate that the separation of photogenerated e^-–h^+ pairs is more efficient in $Bi_3La_2BaTi_3O_{14}Cl$ than that in the other two compounds investigated here. The results are consistent with the PL data.

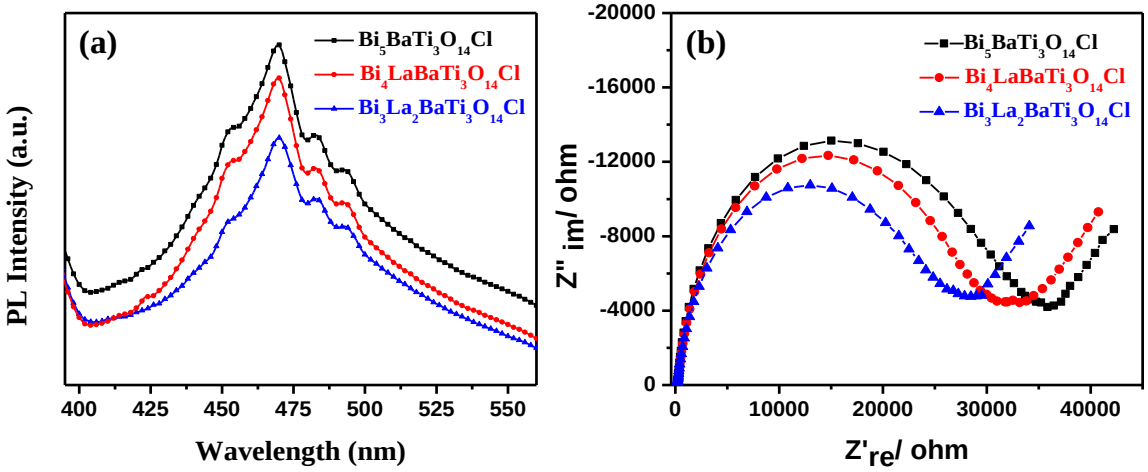

Figure 6.6 (a) PL spectra of $Bi_{5-x}La_xBaTi_3O_{14}Cl$ (x = 0 – 2) at room temperature with an excitation wavelength of 350 nm. (b) EIS profiles of $Bi_{5-x}La_xBaTi_3O_{14}Cl$ (x = 0 – 2).

6.3.7 Photocatalysis

To evaluate the catalysts, $Bi_{5-x}La_xBaTi_3O_{14}Cl$ (x = 0 – 2), toward selective dye degradation under sunlight-irradiation model dye systems comprising of individual RhB, MB and an equimolar mixture of RhB and MB aqueous solutions were used. Figure 6.7 shows the dye degradation study of a mixture of RhB and MB over $Bi_{5-x}La_xBaTi_3O_{14}Cl$ (x = 0 – 2) at pH 7 and 11. The steady decrease in the absorbance at 664 nm (λ_{max} of MB) and a very little or insignificant change in the absorbance at 558 nm (λ_{max} of RhB) with time clearly indicates a preferential degradation of MB over RhB at both the pH for all the compounds. While $Bi_3La_2BaTi_3O_{14}Cl$ took 135 min, $Bi_5BaTi_3O_{14}Cl$ and $Bi_4LaBaTi_3O_{14}Cl$ took 150 and 180 min, respectively, for complete degradation of MB at pH 11 (Figure 6.7 (d - f)). However, the selective MB degradation in neutral medium is found to be 85, 83, and 95 % over $Bi_5BaTi_3O_{14}Cl$, $Bi_4LaBaTi_3O_{14}Cl$ and $Bi_3La_2BaTi_3O_{14}Cl$, respectively, with a little decrease in the RhB (11-27%) concentration during 240 min of sunlight-irradiation (Figure 6.7 (a-c)).

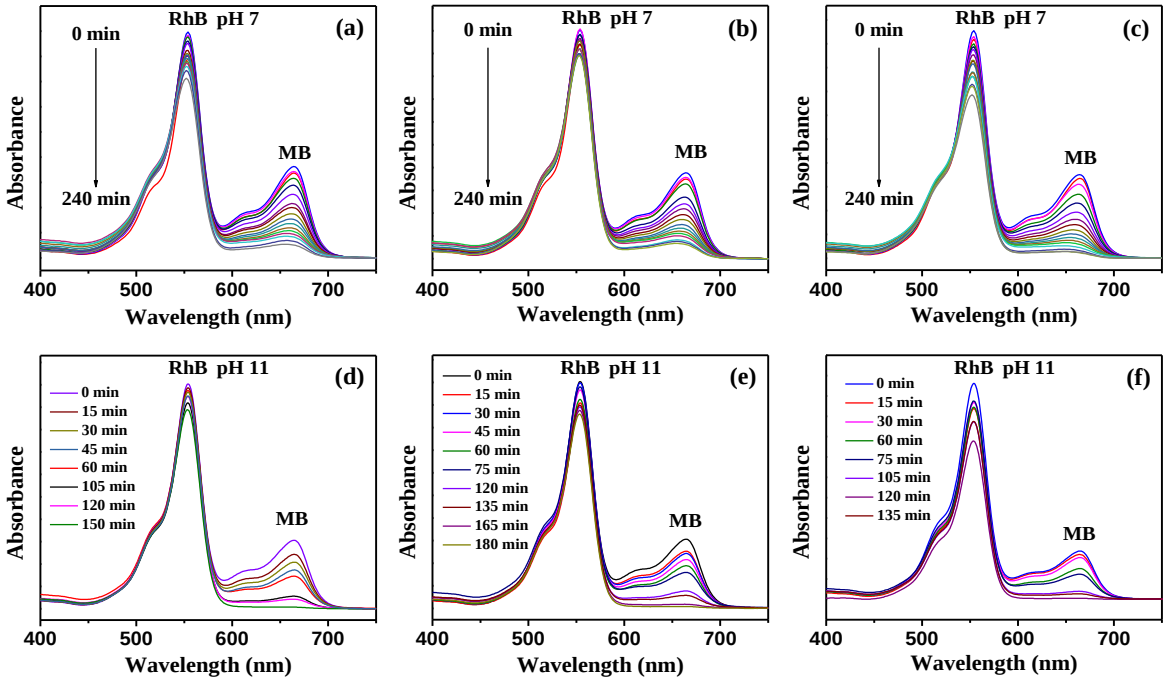

Figure 6.7 UV-vis absorption spectra for the selective degradation of MB from aqueous mixture of MB and RhB at (a - c) pH 7 and (d - f) pH 11 over $Bi_5BaTi_3O_{14}Cl$ (a, d), $Bi_4LaBaTi_3O_{14}Cl$ (b, e) and $Bi_3La_2BaTi_3O_{14}Cl$ (c, f) under sunlight-irradiation.

The selective MB degradation in the alkaline medium over these compounds is found to be faster as compared to that observed in the neutral medium. This is probably due to the presence of higher negative charge (see ζ- potential section later) on the catalysts so that they interact more strongly with the cationic MB in the alkaline medium. Thus, the selective degradation of cationic dyes, such as, MB from the mixture of cationic (MB) and zwitterionic (RhB) dyes is possible under neutral and alkaline media using these catalysts. Moreover, the compound shows simultaneous degradation of RhB and MB in the acidic medium from the mixture of RhB and MB. The degradation of RhB and MB in the acidic medium as a function of time is shown in Figure 6.8, unveiling complete degradation of both the dyes after 165 min sunlight-irradiation in presence of $Bi_3La_2BaTi_3O_{14}Cl$, while $Bi_5BaTi_3O_{14}Cl$ and $Bi_4LaBaTi_3O_{14}Cl$ took 255 and 345 min, respectively. The degradation of both dyes can be explained by the adsorption results, which is discussed later in the adsorption section.

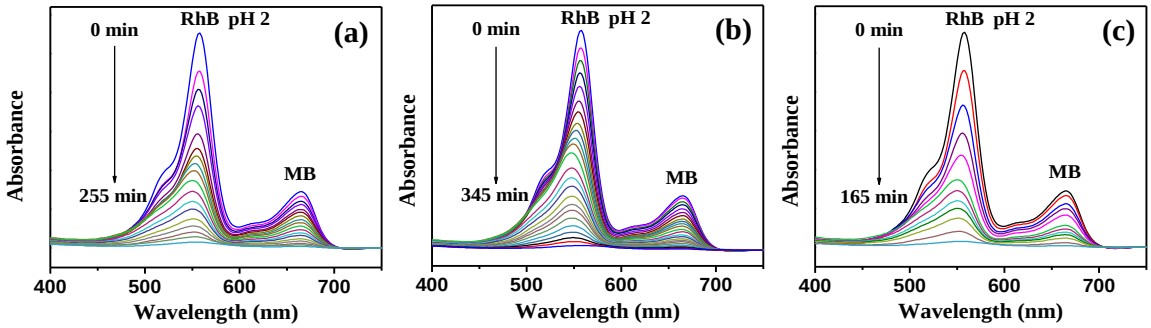

Figure 6.8 UV-vis absorption spectra for the degradation of MB and RhB from aqueous mixture of MB and RhB at pH 2 over (a) $Bi_5BaTi_3O_{14}Cl$, (b) $Bi_4LaBaTi_3O_{14}Cl$ and (c) $Bi_3La_2BaTi_3O_{14}Cl$ under sunlight-irradiation.

The photocatalytic activities for the degradation of individual dyes over these compounds were also studied at different pH. Figure 6.9 (a) shows complete degradation within 15-25 min of sunlight- irradiation at pH 2. The blank test conducted under the identical condition without catalyst did not show any RhB degradation, indicating no self-degradation under sunlight-irradiation.

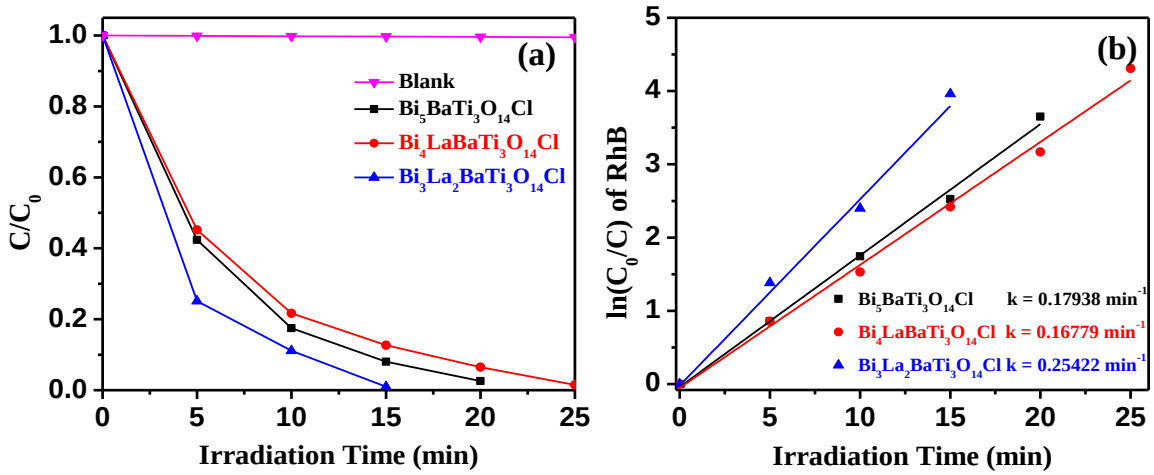

Figure 6.9 (a) Photodegradation of RhB with irradiation time over $Bi_{5-x}La_xBaTi_3O_{14}Cl$ (x = 0 – 2). (b) Plot of $\ln(C_0/C)$ as a function of irradiation time for $Bi_{5-x}La_xBaTi_3O_{14}Cl$ (x = 0 – 2).

The RhB degradation kinetics over $Bi_{5-x}La_xBaTi_3O_{14}Cl$ (x = 0 – 2) photocatalysts in acidic medium were fitted with the Langmuir-Hinshelwood model [40]:

$$\ln(C_0/C) = kt \qquad (6.2)$$

where, C_0 is the initial concentration, C is concentration of RhB at time interval t and k is the rate constant. The linear plot between $\ln(C_0/C)$ and time indicates the photodegradation of RhB to follow a pseudo-first-order kinetics. The degradation rate constant (k) is calculated to be 0.17938, 0.16779 and 0.25422 min^{-1} for $Bi_5BaTi_3O_{14}Cl$, $Bi_4LaBaTi_3O_{14}Cl$ and $Bi_3La_2BaTi_3O_{14}Cl$, respectively (Figure 6.9 (b)). The rate of RhB degradation over these compounds in alkaline medium is higher than those observed for four-layer Aurivillius compounds discussed in Chapter 3.

Moreover, the % COD removal data for RhB degradation in the acidic medium was further confirmed by excellent mineralization of the dye within 15-25 min light irradiation (Figure 6.10). Figure 6.11 shows the sunlight-driven RhB degradation with time over all the three catalysts at pH 7 and 11. At pH 7, complete degradation of RhB is achieved only over $Bi_3La_2BaTi_3O_{14}Cl$ within 180 min of sunlight-irradiation. The RhB degradation over $Bi_5BaTi_3O_{14}Cl$ and $Bi_4LaBaTi_3O_{14}Cl$ are only up to 49 % and 64 %, respectively after 180 min. Therefore, the RhB degradation is far less efficient over $Bi_5BaTi_3O_{14}Cl$ and

$Bi_4LaBaTi_3O_{14}Cl$ than that over $Bi_3La_2BaTi_3O_{14}Cl$ at pH 7. However, less than 10% of RhB degradation is observed in alkaline pH for all the catalysts after 180 min irradiation (Figure 6.11).

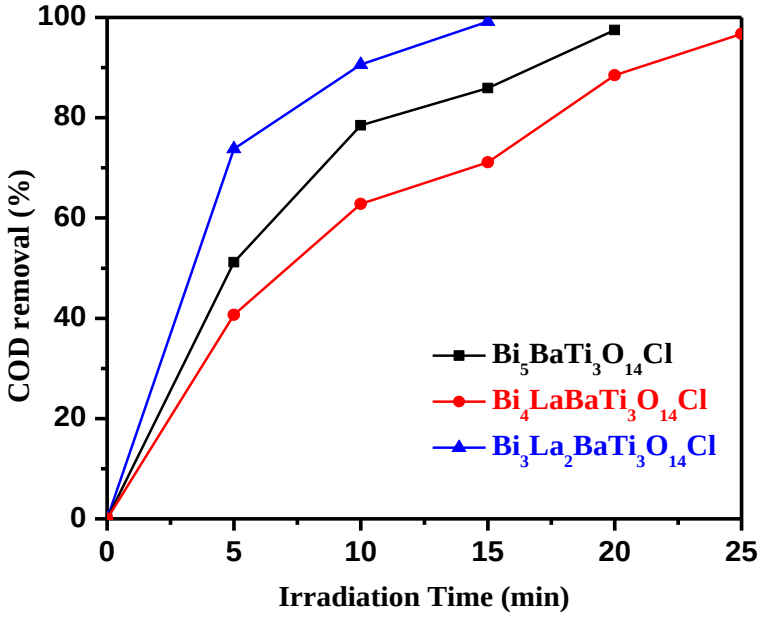

Figure 6.10 COD removal efficiency during photodegradation of RhB with time over $Bi_{5-x}La_xBaTi_3O_{14}Cl$ (x = 0 – 2) under sunlight-irradiation.

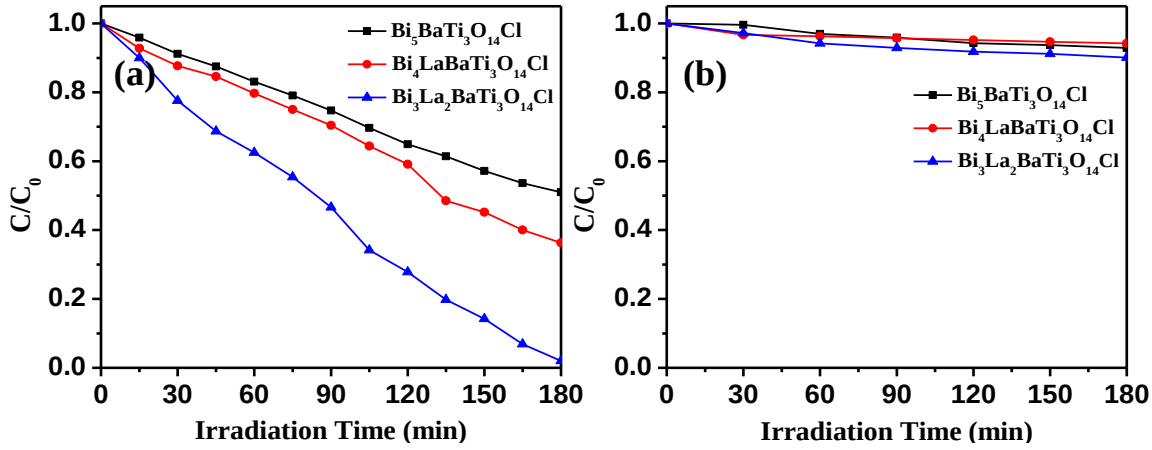

Figure 6.11 Photodegradation of RhB with time over $Bi_{5-x}La_xBaTi_3O_{14}Cl$ (x = 0 – 2) at (a) pH 7 and (b) pH 11 under sunlight-irradiation.

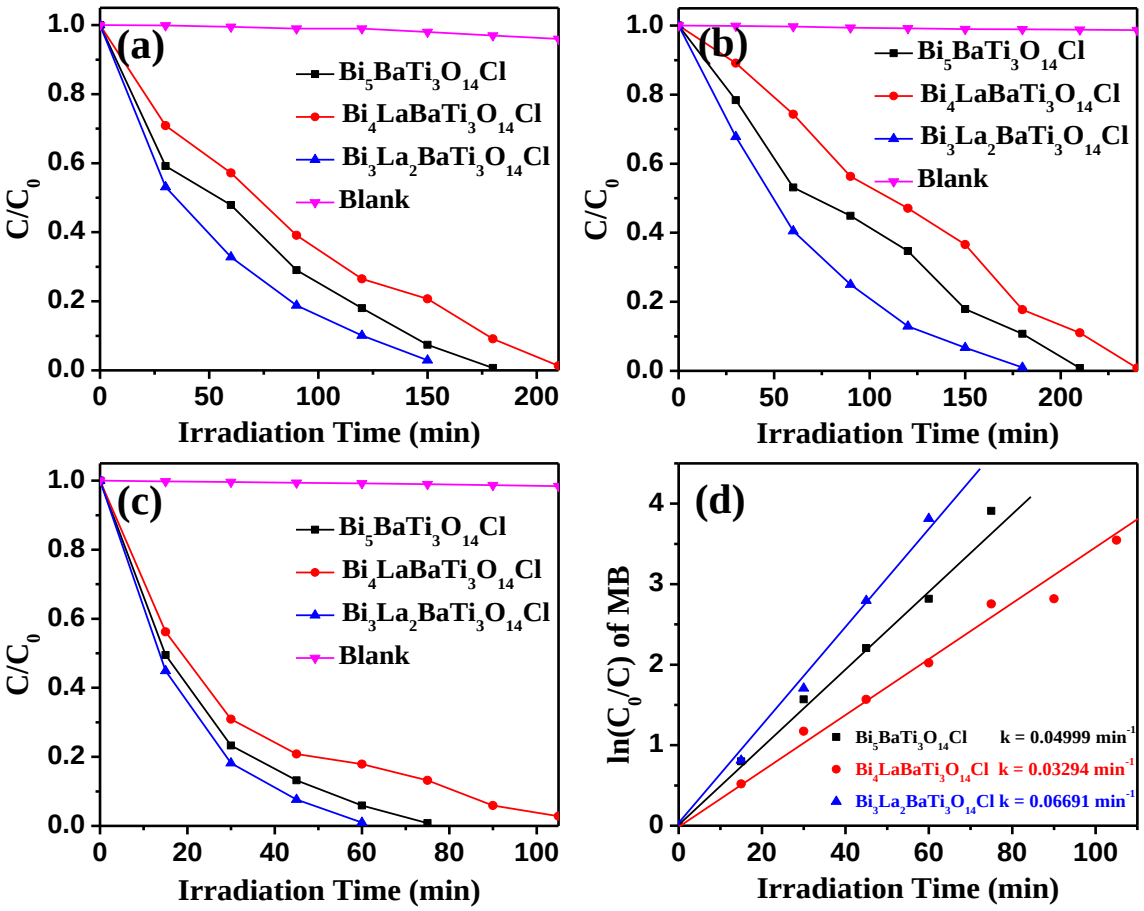

Figure 6.12 Photodegradation of MB with irradiation time at (a) pH 2, (b) pH 7 and (c) pH 11 over $Bi_{5-x}La_xBaTi_3O_{14}Cl$ (x = 0 – 2). (d) Plot of $\ln(C_0/C)$ as a function of time at pH 11 over $Bi_{5-x}La_xBaTi_3O_{14}Cl$ (x = 0 – 2).

Besides, selective and simultaneous dye degradation experiments, the compounds have also been investigated for the degradation of individual MB at different pH conditions. Figure 6.12 (a – c) shows the MB degradation with time in presence of $Bi_{5-x}La_xBaTi_3O_{14}Cl$ (x = 0 – 2) under sunlight-irradiation at different pH. As shown in Figure 6.12 (c), the concentration of MB decreases rapidly with the exposure time, and degrades completely within 60-105 min in the alkaline medium (pH 11). A linear fit of MB degradation kinetics data at pH 11 with the Langmuir-Hinshelwood model, resulted in rate constants, k, of 0.04999, 0.03294 and 0.06691 min^{-1} for $Bi_5BaTi_3O_{14}Cl$, $Bi_4LaBaTi_3O_{14}Cl$ and $Bi_3La_2BaTi_3O_{14}Cl$, respectively (Figure 6.12 (d)). A similar trend has also been noticed for the degradation of MB in the acidic and neutral media (Figure 6.12). However, the degradation activity for the latter two cases (pH 2 and 7) is slower than the former one (pH

11), with the degradation time of 150-210 in acidic and 180-240 min in neutral medium. Moreover, the % COD removal indicates good mineralization of MB in the alkaline medium within the degradation time (Figure 6.13).

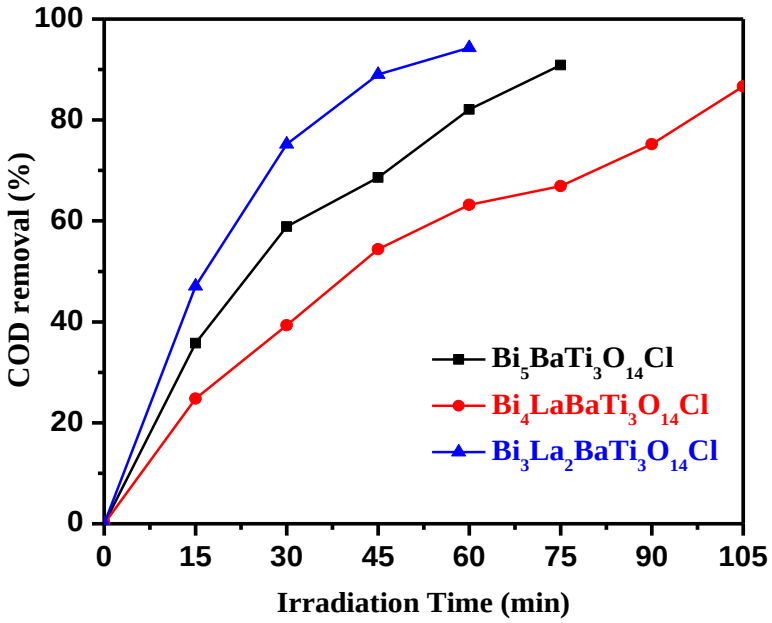

Figure 6.13 COD removal efficiency during photodegradation of MB with irradiation time over $Bi_{5-x}La_xBaTi_3O_{14}Cl$ (x = 0 – 2) at pH 11 under sunlight-irradiation.

6.3.8 Scavenger Study

To understand the role of reactive species ($O_2^{\bullet-}$, $^{\bullet}OH$ and h^+) in the degradation mechanism over $Bi_3La_2BaTi_3O_{14}Cl$, scavenger tests were conducted. A series of controlled experiments using various scavengers, benzoquinone (BQ), ammonium oxalate (AO), and *tert*-butanol (*t*-BuOH) for $O_2^{\bullet-}$, h^+ and $^{\bullet}OH$, respectively, have been carried out in order to understand the role of reactive species in the degradation. As shown in Figure 6.14, the photodegradation of MB over $Bi_3La_2BaTi_3O_{14}Cl$ was remarkably retarded by 57% - 65% when AO was added as scavenger in the reaction carried out at different pH. This observation highlights the predominant role of photogenerated holes in the degradation of MB at different pH. The decline in the photodegradation efficiency of MB by 22% - 30% with the addition of BQ points toward moderate role of $O_2^{\bullet-}$ in all pH conditions. Interestingly, ≤ 7% reduction in the photodegradation efficiency is observed with the

addition of *t*-BuOH in neutral and alkaline media, while ~ 19% reduction in photodegradation efficiency is noticed in the acidic pH. This indicates, while •OH played an almost insignificant role in the neutral and alkaline media, a minor role is evident in the acidic medium. Moreover, same reactive species are also active for the photodegradation of RhB in the acidic and neutral media (Figure 6.15).

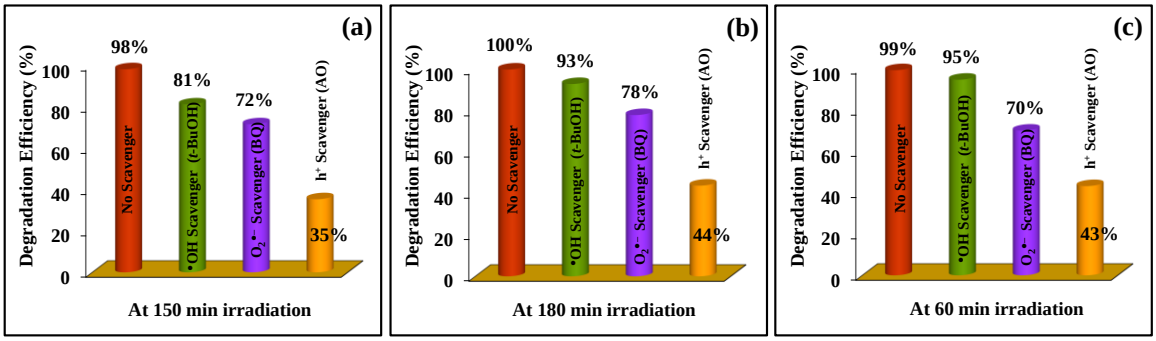

Figure 6.14 Effect of different scavengers on the degradation of MB at (a) pH 2, (b) pH 7 and (c) pH 11 over $Bi_3La_2BaTi_3O_{14}Cl$ under sunlight-irradiation.

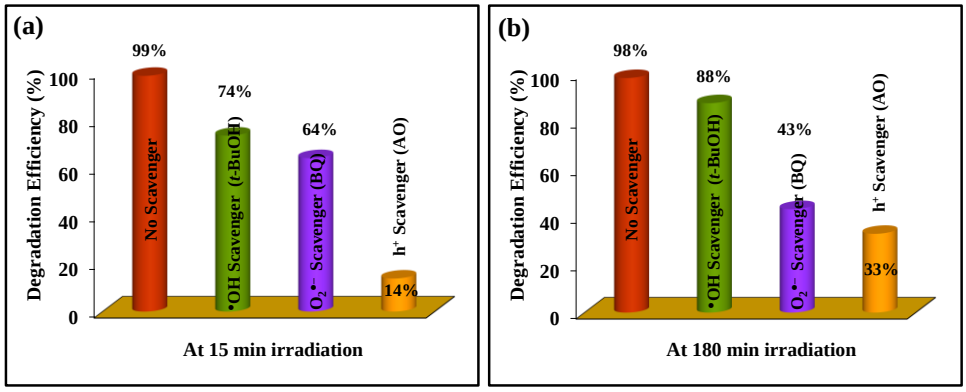

Figure 6.15 Effect of different scavengers on the degradation of RhB over $Bi_3La_2BaTi_3O_{14}Cl$ catalyst at (a) pH 2 and (b) pH 7 under sunlight-irradiation.

6.3.9 Reusability and Stability

Recyclability and stability of the catalyst is important parameter to make photocatalyst to be viable in environmental remediation. To evaluate the recyclability performance of $Bi_3La_2BaTi_3O_{14}Cl$, five consecutive degradation cycles were carried out with individual RhB and MB at pH 2 and 11 under sunlight-irradiation (Figure,6.16 (a)). As seen in the figure, the catalyst did not show any significant loss in the activity even in the fifth run for the degradation of RhB. A small lose (≤ 5%) in the activity during fifth cycle is

due probably to unpreventable loss of the catalyst in the course of centrifugation. The photostability of $Bi_3La_2BaTi_3O_{14}Cl$, after five cyclic runs is also evident from the PXD patter analysis, indicating excellent phase stability devoid of any photoleaching during the photodegradation (Figure 6.16 (b)). Moreover, the photocatalytic cycles for MB degradation over $Bi_3La_2BaTi_3O_{14}Cl$ also signify excellent reusability at pH 11 (Figure 6.17). The PXD pattern analysis of $Bi_5BaTi_3O_{14}Cl$ and $Bi_4LaBaTi_3O_{14}Cl$ before and after the photocatalytic RhB degradation in acidic medium also indicates good stability of the catalysts (Figure 6.18).

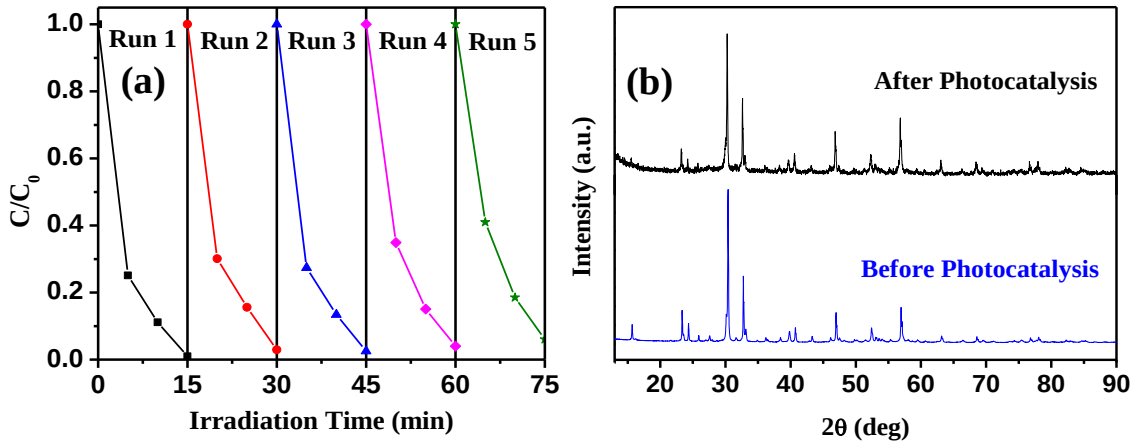

Figure 6.16 (a) Time profile of RhB photodegradation for five successive cycles over $Bi_3La_2BaTi_3O_{14}Cl$ in acidic medium. (b) PXD pattern of $Bi_3La_2BaTi_3O_{14}Cl$ before and after five successive cycles of photodegradation.

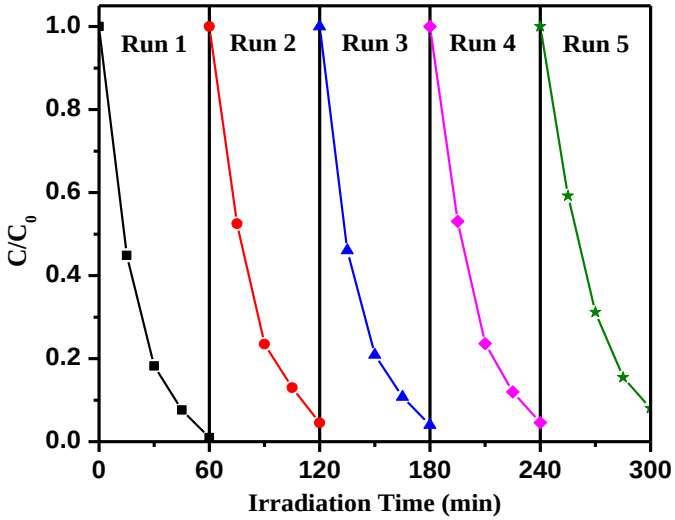

Figure 6.17 Reusability of $Bi_3La_2BaTi_3O_{14}Cl$ in five successive cycles for the degradation of MB at pH 11.

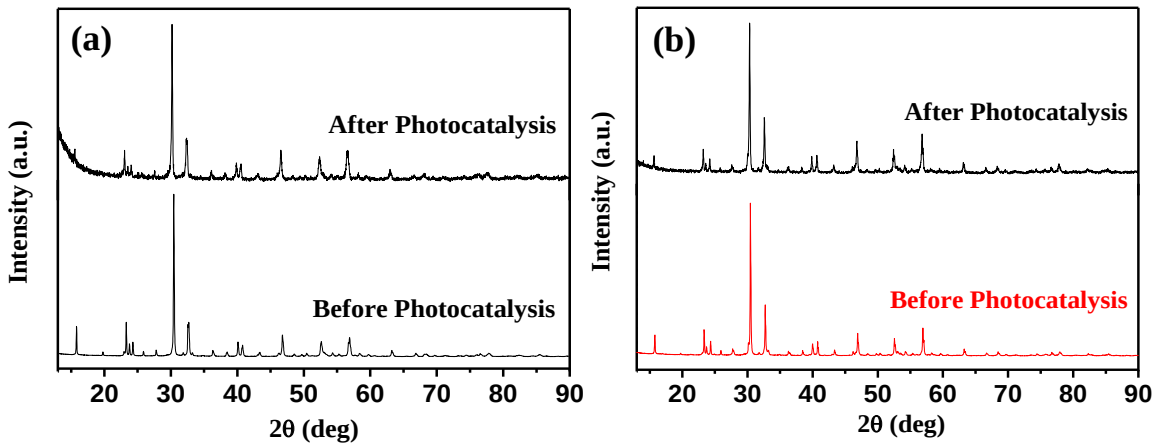

Figure 6.18 PXD patterns of (a) $Bi_5BaTi_3O_{14}Cl$ and (b) $Bi_4LaBaTi_3O_{14}Cl$ before and after the photocatalytic RhB degradation in the acidic medium.

6.3.10 Energy Level Diagram (ELD)

To understand the enhanced photodegradation, we calculated the relative band edge positions of $Bi_{5-x}La_xBaTi_3O_{14}Cl$ (x = 0 – 2) at different pH, using the following empirical formula [41]:

$$E_{CB} = -(\chi_M^a \chi_X^b)^{1/(a+b)} - \tfrac{1}{2} E_g + 0.059(pH_{ZPC} - pH) + E_0 \quad (6.3)$$

$$E_{VB} = E_{CB} + E_g \quad (6.4)$$

where, E_{CB} is the conduction band potential, E_g refers to the band gap of the photocatalyst, pH_{ZPC} is the zero point of charge for the compound taken by the zeta potential values, E_0 signifies the scale factor taken as – 4.5 eV with respect to *NHE* scale, E_{VB} is the valence band potential, χ_M and χ_X are absolute electronegativity of the atoms M and X, respectively, for the compound M_aX_b. Using above mentioned equations, conduction and valence band positions at various pH are calculated for $Bi_{5-x}La_xBaTi_3O_{14}Cl$ (x = 0 – 2) and are given in Table 6.5.

Table 6.5 Calculated Values of Valence and Conduction Band Positions of $Bi_{5-x}La_xBaTi_3O_{14}Cl$ (x = 0 – 2) at Different pH

Compound		pH 2	pH 7	pH 11
$Bi_5BaTi_3O_{14}Cl$	CB (eV)	0.13	– 0.16	– 0.40
	VB (eV)	2.79	2.50	2.26
$Bi_4LaBaTi_3O_{14}Cl$	CB (eV)	–0.02	– 0.31	– 0.55
	VB (eV)	2.72	2.43	2.19
$Bi_3La_2BaTi_3O_{14}Cl$	CB (eV)	– 0.10	– 0.40	– 0.63
	VB (eV)	2.77	2.47	2.24

The HOMO-LUMO energy levels of the dyes are calculated from the cyclic voltammograms recorded at different pH (Figure 6.19) by using the following equations [42].

From oxidation potential,

$$E_{HOMO} = E_{ox} + 4.8 \quad (6.5)$$

$$E_{LUMO} = E_{HOMO} - E_g \quad (6.6)$$

From reduction potential,

$$E_{LUMO} = E_{red} - 4.8 \quad (6.7)$$

$$E_{HOMO} = E_{LUMO} + E_g \quad (6.8)$$

$$E_{(NHE)} = - E_{(AVS)} - 4.5 \quad (6.9)$$

where, E_{HOMO} is HOMO level potential, E_{ox} refers to oxidation potential, E_{red} is the reduction potential taken from CV of the dyes at different pH, E_{LUMO} stands for LUMO level potential, $E_{(NHE)}$ is the potential with respect to normal hydrogen electrode and $E_{(AVS)}$ is the potential with respect to absolute vacuum scale. The HOMO-LUMO potentials of RhB and

MB at different pH are summarized in Table 6.6. The potentials of MB and RhB in neutral medium are found to be in fairly good agreement with the literature reported values [43, 44]. Moreover, the potential energy for the generation of $^{\bullet}OH$ ($E_{\bullet OH/H2O}$= + 2.68 eV *vs. NHE*) and $O_2^{\bullet-}$ ($E_{O2/O2\bullet-}$= + 0.13 eV *vs. NHE*) was taken from the literature [45].

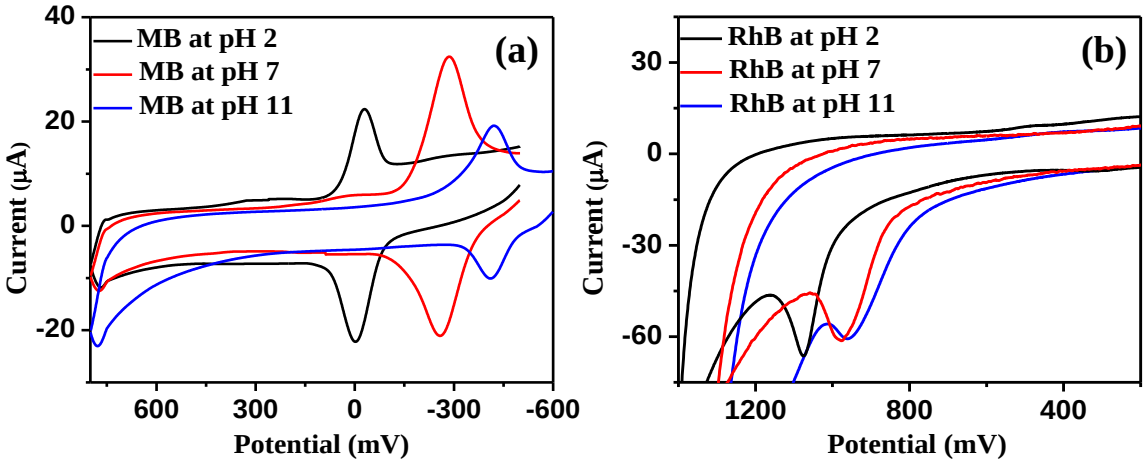

Figure 6.19 Cyclic voltammograms of (a) MB and (b) RhB at different pH.

Table 6.6 Calculated HOMO-LUMO Positions of RhB and MB at Different pH

Dye		pH 2	pH 7	pH 11
RhB	LUMO (eV)	– 0.88	– 1.02	– 1.35
	HOMO (eV)	1.36	1.22	0.89
MB	LUMO (eV)	0.28	0.02	– 0.12
	HOMO (eV)	2.15	1.89	1.75

Figure 6.20 represents an energy level diagram showing the band edge positions of $Bi_3La_2BaTi_3O_{14}Cl$ with respect to the potential for generation of $^{\bullet}OH$, $O_2^{\bullet-}$ and HOMO-LUMO levels of different dyes at various pH. According to the ELD, the photogenerated electrons in the CB of $Bi_3La_2BaTi_3O_{14}Cl$ at different pH could produce $O_2^{\bullet-}$ radicals from dissolved O_2 because the E_{CB} at different pH (≥ – 0.10 eV *vs. NHE*) is higher than $E_{O2/O2\bullet-}$

(+ 0.13 eV *vs. NHE*). Moreover, the holes in the valence band are in a favorable position to generate •OH radical from H_2O only at pH 2 because the E_{VB} (+ 2.77 eV *vs. NHE*) is below the potential of $E_{•OH/H2O}$ (+ 2.68 eV *vs. NHE*). Interestingly, the valence band holes at pH 7 and 11 are not in favor of •OH radical formation because the E_{VB} (≤ + 2.47 eV *vs. NHE*) at these pH values is above $E_{•OH/H2O}$ (+ 2.68 eV *vs. NHE*). Although, the holes in valence band could migrate to the adsorbed dye molecules and thereby degrade the dye at all pH, since the HOMO levels are always above the E_{VB} of $Bi_3La_2BaTi_3O_{14}Cl$.

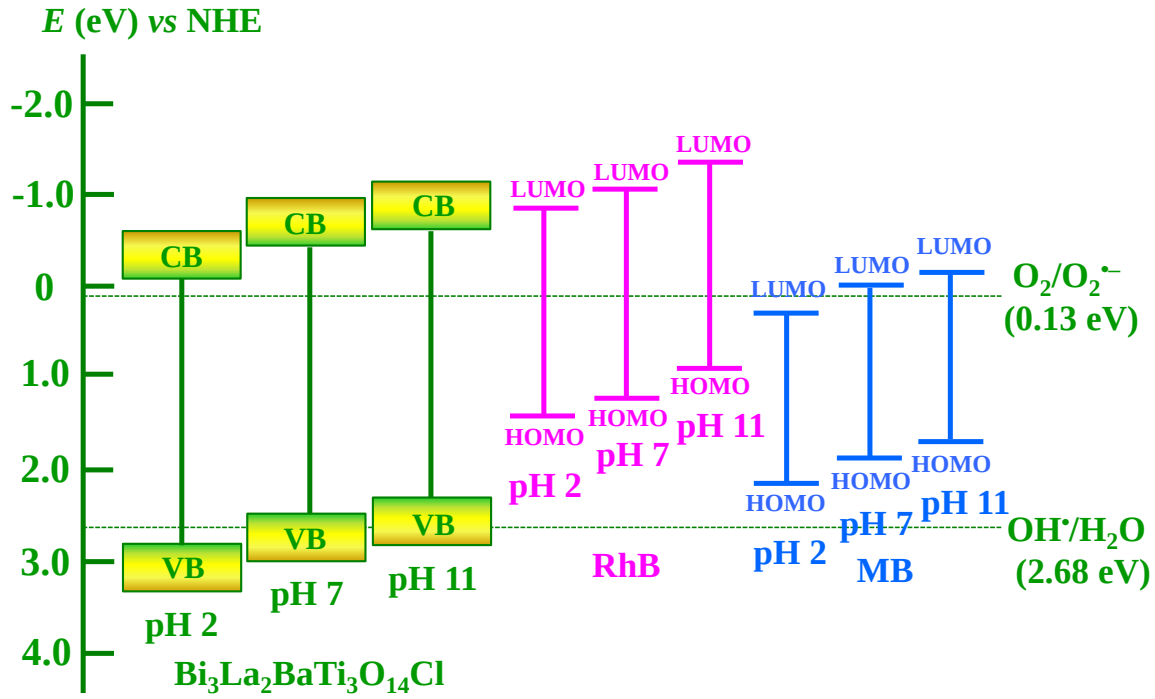

Figure 6.20 Schematic energy level diagram of $Bi_3La_2Ti_3O_{14}Cl$ showing HOMO−LUMO levels of RhB and MB at different pH with respect to the potential (vs NHE) of •OH/H_2O and $O_2/O_2^{\bullet-}$.

The information of band edge positions is in good agreement with the scavenger study of $Bi_3La_2BaTi_3O_{14}Cl$ at different pH. Based on this a mechanism for dye degradation at different pH is proposed.

$Bi_3La_2BaTi_3O_{14}Cl + h\nu \rightarrow Bi_3La_2BaTi_3O_{14}Cl\ (e^-_{CB} \cdots h^+_{VB})$

At pH 2,

$$Bi_3La_2BaTi_3O_{14}Cl\ (e^-_{CB}) + O_2 \rightarrow O_2^{\bullet-} + Bi_3La_2BaTi_3O_{14}Cl$$

$$Bi_3La_2BaTi_3O_{14}Cl\ (h^+_{VB}) + H_2O \rightarrow {}^{\bullet}OH + Bi_3La_2BaTi_3O_{14}Cl$$

$$Dye + O_2^{\bullet-} \rightarrow CO_2 + H_2O$$

$$Dye + {}^{\bullet}OH \rightarrow CO_2 + H_2O$$

$$Dye + Bi_3La_2BaTi_3O_{14}Cl\ (h^+_{VB}) \rightarrow CO_2 + H_2O$$

At pH 7 and 11,

$$Bi_3La_2BaTi_3O_{14}Cl\ (e^-_{CB}) + O_2 \rightarrow O_2^{\bullet-} + Bi_3La_2BaTi_3O_{14}Cl$$

$$Dye + O_2^{\bullet-} \rightarrow CO_2 + H_2O$$

$$Dye + Bi_3La_2BaTi_3O_{14}Cl\ (h^+_{VB}) \rightarrow CO_2 + H_2O$$

where, e^-_{CB} is the conduction band electron and h^+_{VB} refers to the valence band hole.

Under visible-light irradiation, generation of electrons and holes takes place in the CB and VB, respectively. The photogenerated electrons in the CB of the catalyst reduce dissolved O_2 to yield $O_2^{\bullet-}$ anions in all pH conditions. Only at pH 2, holes in the VB can oxidize water to produce ${}^{\bullet}OH$ radicals. Moreover, the photogenerated holes in the VB can also degrade the dye molecules directly. Thus, at pH 2, all the reactive species such as $O_2^{\bullet-}$, ${}^{\bullet}OH$ and holes are active players in the dye degradation (Figure 6.21). While at pH 7 and 11, only $O_2^{\bullet-}$ and holes are involved in the dye degradation (Figure 6.22).

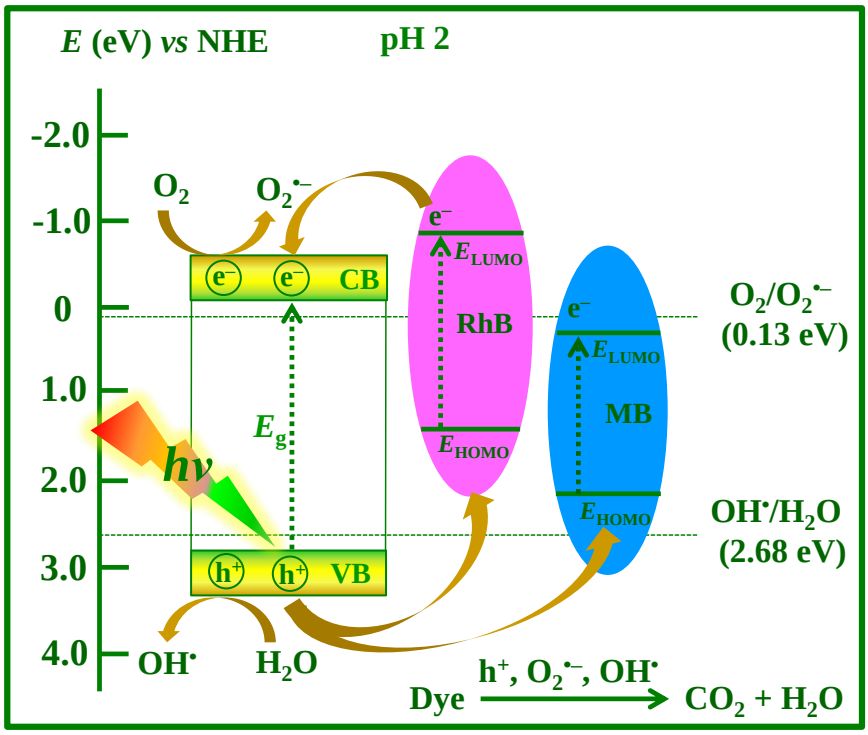

Figure 6.21 Schematic diagram showing the generation of reactive species and dye degradation over $Bi_3La_2Ti_3O_{14}Cl$ at pH 2 under sunlight-irradiation.

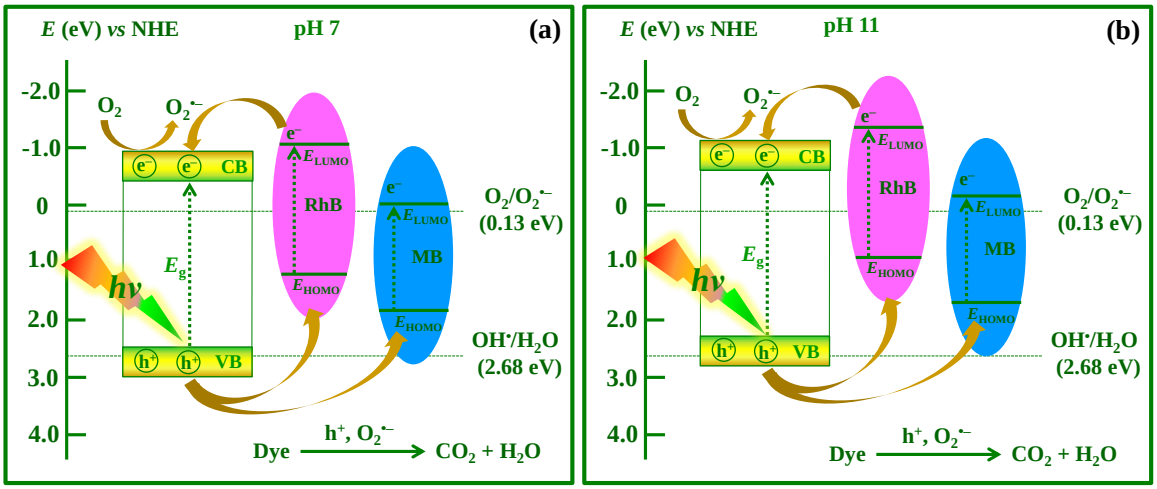

Figure 6.22 Schematic diagram showing the generation of reactive species and dye degradation over $Bi_3La_2Ti_3O_{14}Cl$ at (a) pH 7, (b) pH 11 under sunlight-irradiation.

6.3.11 Role of Adsorption and ζ– potential

It has been observed that the attachment of the dye molecule with catalyst surface plays crucial role in degradation, where h^+ is the main reactive species. To evaluate the role of dye adsorption on the selective and individual degradation, we have conducted adsorption tests of catalysts in a mixture of RhB and MB together with individual RhB and MB solutions at different pH in the dark. These compounds show selective adsorption of MB over RhB in neutral and alkaline media, where as in the acidic medium both MB and RhB get adsorbed. The maximum adsorption of MB over RhB is noticed in the alkaline medium than the neutral one, which corroborate with the fast degradation of these compounds in alkaline medium. The compound, $Bi_3La_2BaTi_3O_{14}Cl$, show greater dye adsorption than those of the other two compounds in all pH conditions, supportive of enhanced activity of the compound. Moreover, the degradation of individual RhB and MB over these compounds follows the adsorption order making $Bi_3La_2BaTi_3O_{14}Cl$ as the most active as shown in Figure 6.23 (a – c). The activity for selective and individual degradation of the catalysts conforms to the adsorption order as follows: $Bi_3La_2BaTi_3O_{14}Cl$ > $Bi_5BaTi_3O_{14}Cl$ > $Bi_4LaBaTi_3O_{14}Cl$.

To understand the role of catalyst surface charge in dye adsorption process, ζ-potential measurements of the catalysts were carried out at different pH. As shown in Figure 6.23 (d), the ζ–potentials are more negative in the alkaline medium, passing through less negative potentials with lowering in pH to neutral and finally to positive potentials in the acidic medium. This trend is because of H^+ and OH^- ions action on the catalyst surface hydroxyl groups as discussed in Chapter 3.

In alkaline medium, the compound $Bi_3La_2BaTi_3O_{14}Cl$ had more negative ζ–potential (– 40.0 mV) than those of the other two compounds (Figure 6.23 (d)). So, maximum selective adsorption of cationic MB took place over more negatively charged surface of $Bi_3La_2BaTi_3O_{14}Cl$, followed by $Bi_5BaTi_3O_{14}Cl$ (– 37.3 mV) and $Bi_4LaBaTi_3O_{14}Cl$ (– 34.8 mV). Moreover, the moderate extent of selective MB adsorption in neutral medium, follows the ζ– potential order having – 23.9, – 21.0 and – 7.6 mV for $Bi_3La_2BaTi_3O_{14}Cl$, $Bi_5BaTi_3O_{14}Cl$ and $Bi_4LaBaTi_3O_{14}Cl$, respectively. Therefore, in neutral and alkaline media selectivity is achieved because of selective adsorption of cationic MB on the negatively

charged catalyst by electrostatic interaction. The negligible amount of RhB adsorption is because of electrostatic repulsion of the negatively charged carboxylic acid groups of RhB with negatively charged catalyst.

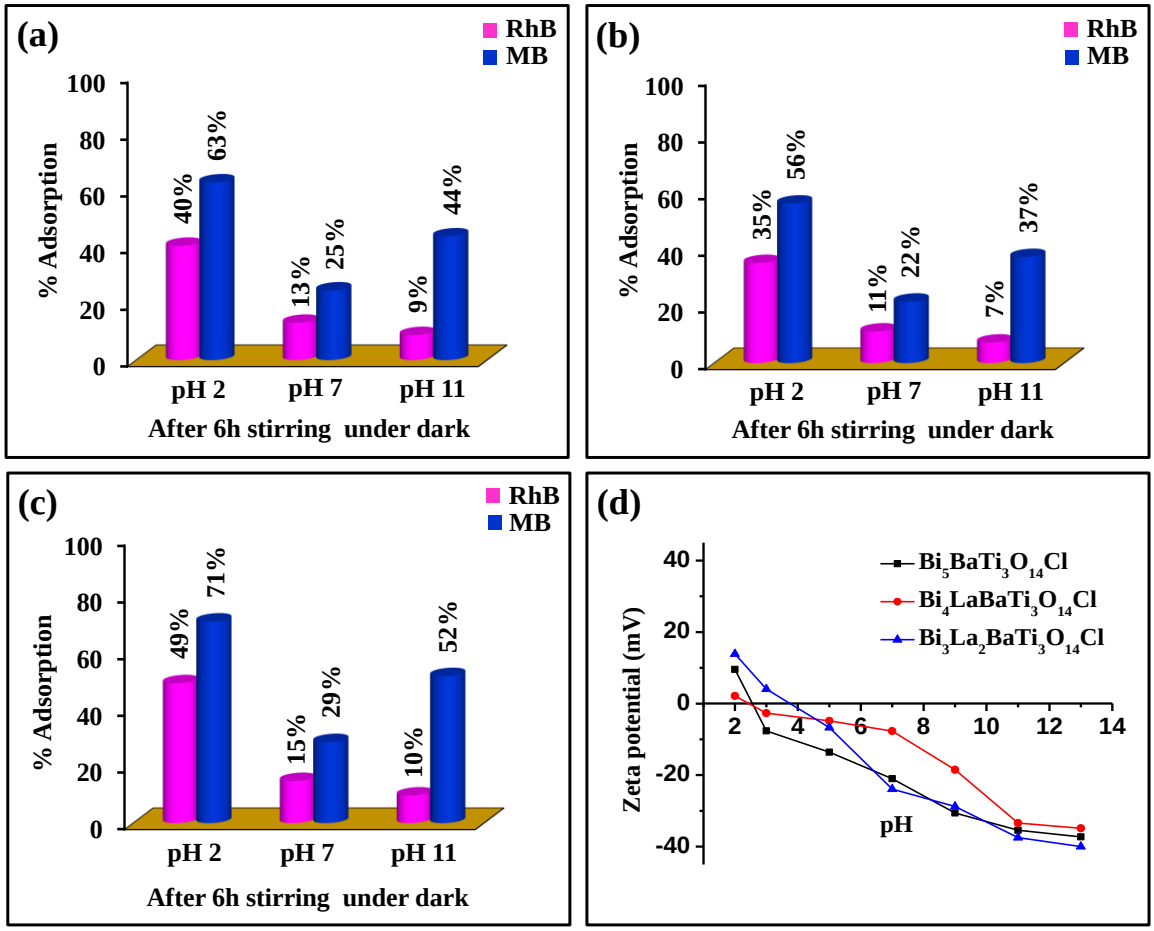

Figure 6.23 Influence of pH on preferential adsorption of dye from aqueous mixture of MB and RhB on (a) $Bi_5BaTi_3O_{14}Cl$, (b) $Bi_4LaBaTi_3O_{14}Cl$, and (c) $Bi_3La_2BaTi_3O_{14}Cl$ catalyst surface. (d) ζ- potential of $Bi_{5-x}La_xBaTi_3O_{14}Cl$ (x = 0 – 2) at different pH.

Interestingly in acidic medium, both MB and RhB were adsorbed on the catalyst surface and the adsorption follows the ζ- potential order. The ζ- potential for $Bi_3La_2BaTi_3O_{14}Cl$, $Bi_5BaTi_3O_{14}Cl$ and $Bi_4LaBaTi_3O_{14}Cl$ were + 13.9, + 9.7 and + 2.2 mV respectively, at pH 2. The adsorption of both dyes in acidic medium is because of electrostatic interaction between positively charged catalyst and negatively charged carboxylic acid group of RhB. Moreover, the cationic MB is probably co-adsorbed on

adsorbed RhB. Indeed, the adsorption of the individual RhB and MB dyes (Figure 6.24) over these catalyst surfaces is in line with the ζ- potential values.

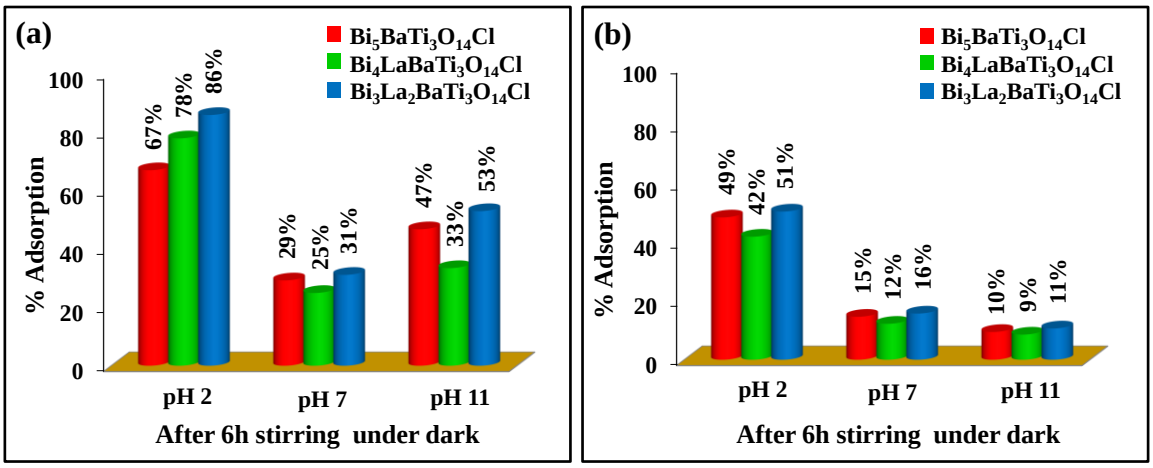

Figure 6.24 Influence of pH on adsorption of (a) MB, (b) RhB over $Bi_{5-x}La_xBaTi_3O_{14}Cl$ (x = 0 – 2) catalyst surfaces.

In summary, we have devised a new strategy to make visible-light active compounds from UV-active compounds by synthesizing new Sillén-Aurivillius intergrowth phases, $Bi_{5-x}La_xBaTi_3O_{14}Cl$ (x = 0 – 2). A multistep reaction strategy was adopted to prepare the hybrid phases. The compounds exhibited selective degradation of MB in neutral and alkaline media, whereas simultaneous RhB and MB degradation was noticed in the acidic medium with a mixed RhB-MB dye solution. Furthermore, the compounds showed excellent photodegradation of individual RhB and MB at different pH conditions under sunlight-irradiation. Among the three catalysts reported here, $Bi_3La_2BaTi_3O_{14}Cl$ showed enhanced activity because of slower recombination of photogenerated e^-–h^+ pairs and greater adsorption of dye. Analysis of band edge position of $Bi_3La_2BaTi_3O_{14}Cl$, HOMO-LUMO levels of the dyes and scavenger test result indicated $^{\bullet}OH$, $O_2^{\bullet-}$ and h^+ as reactive species for dye degradation under acidic condition, whereas only $O_2^{\bullet-}$ and h^+ were mostly responsible for dye degradation in the neutral and alkaline media.

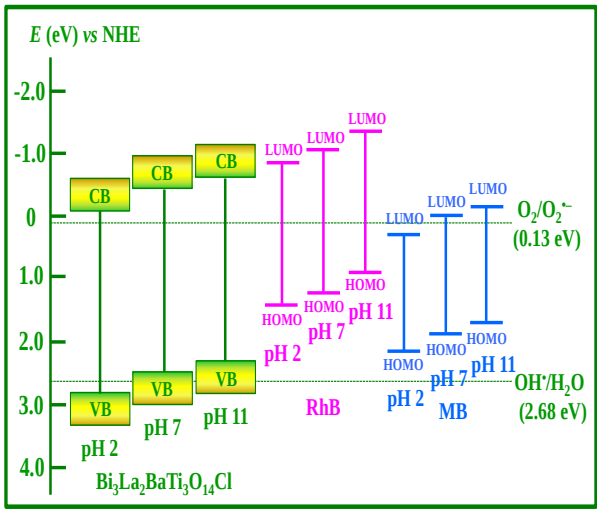
E (eV) vs NHE
-2.0
-1.0
0
1.0
2.0
3.0
4.0
CB
VB
pH 2
pH 7
pH 11
Bi3La2BaTi3O14Cl
LUMO
HOMO
RhB
MB
O2/O2•−
(0.13 eV)
OH•/H2O
(2.68 eV)

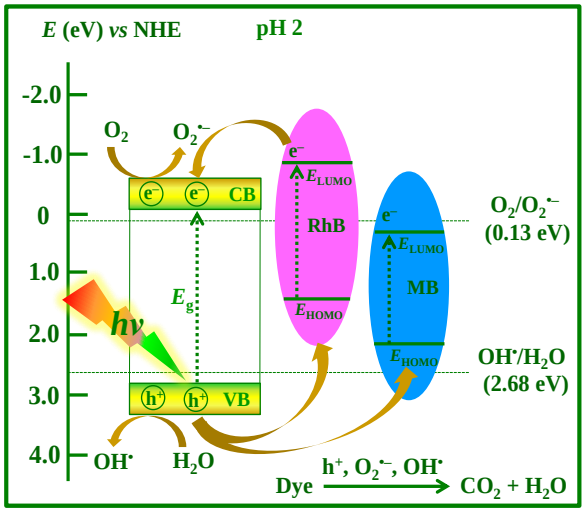
E (eV) vs NHE
pH 2
-2.0
-1.0
0
1.0
2.0
3.0
4.0
O2
O2•−
e−
CB
VB
h+
Eg
hν
ELUMO
EHOMO
RhB
MB
O2/O2•−
(0.13 eV)
OH•/H2O
(2.68 eV)
OH•
H2O
Dye
h+, O2•−, OH•
CO2 + H2O

REFERENCES

1. Sinha, A. K.; Pradhan, M.; Sarkar, S.; Pal, T. Large-Scale Solid−State Synthesis of Sn−SnO_2Nanoparticles from Layered SnO by Sunlight: a Material for Dye Degradation in Water by Photocatalytic Reaction. *Environ. Sci. Technol.* **2013**, *47*, 2339−2345.

2. Subramanian, V.; Kamat, P. V.; Wolf, E. E. Mass−Transfer and Kinetic Studies during the Photocatalytic Degradation of an Azo Dye on Optically Transparent Electrode Thin Film. *Ind. Eng. Chem. Res.* **2003**, *42*, 2131−2138.

3. Forgacs, E.; Cserhati, T.; Oros, G. Removal of Synthetic Dyes from Wastewaters: a Review. *Environ. Int.* **2004**, *30*, 953–971.

4. Hoffmann, M. R.; Martin, S. T.; Choi, W.; Bahnemann, D. W. Environmental Applications of Semiconductor Photocatalysis. *Chem. Rev.* **1995**, *95*, 69-96.

5. Zhang, H.; Chen, G.; Bahnemann, D. W. Photoelectrocatalytic Materials for Environmental Applications. *J. Mater. Chem.* **2009**, *19*, 5089-5121.

6. Ravelli, D.; Dondi, D.; Fagnoni, M.; Albini, A. Photocatalysis. A Multi-Faceted Concept for Green Chemistry. *Chem. Soc. Rev.* **2009**, *38*, 1999-2011.

7. Li, L.; Chu, Y.; Liu, Y.; Dong, L. Template-Free Synthesis and Photocatalytic Properties of Novel Fe_2O_3 Hollow Spheres *J. Phys. Chem. C* **2007**, *111*, 2123-2127.

8. Ye, C.; Bando, Y.; Shen, G.; Golberg, D. Thickness-Dependent Photocatalytic Performance of ZnO Nanoplatelets. *J. Phys. Chem. B* **2006**, *110*, 15146-15151.

9. Dong, S.; Feng, J.; Fan, M.; Pi, Y.; Hu, L.; Han, X.; Liu, M.; Sun, J.; Sun, J. Recent Developments in Heterogeneous Photocatalytic Water Treatment using Visible Light Responsive Photocatalysts: A Review. *RSC Adv.* **2015**, *5*, 14610-14630.

10. Zhang, D.; Li, G.; Yu, J. C. Inorganic Materials for Photocatalytic Water Disinfection. *J. Mater. Chem.* **2010**, *20*, 4529-4536.

11. Ghosh-Mukerji, S.; Haick, H.; Schvartzman, M.; Paz, Y. Selective Photocatalysis by Means of Molecular Recognition. *J. Am. Chem. Soc.* **2001**, *123*, 10776-10777.

12. Inumaru, K.; Kasahara, T.; Yamanaka, S. Direct Nanocomposite of Crystalline TiO_2 Particles and Mesoporous Silica as a Molecular Selective and Highly Active Photocatalyst. *Chem. Commun.* **2005**, 2131-2133.

13. Calza, P.; Paze ´, C.; Pelizzetti, E.; Zecchina, A. Shape-Selective Photocatalytic Transformation of Phenols in an Aqueous Medium. *Chem. Commun.* **2001**, 2130-2131.

14. Xamena, F. X. L.; Calza, P.; Lamberti, C.; Prestipino, C.; Damin, A.; Bordiga, S.; Pelizzetti, E.; Zecchina, A. Enhancement of the ETS-10 Titanosilicate Activity in the Shape-Selective Photocatalytic Degradation of Large Aromatic Molecules by Controlled Defect Production *J. Am. Chem. Soc.* **2003**, *125*, 2264-2271.

15. Shiraishi, Y.; Saito, N.; Hirai, T. Titanosilicate Molecular Sieve for Size-Screening Photocatalytic Conversion. *J. Am. Chem. Soc.* **2005**, *127*, 8304-8306.

16. Shiraishi, Y.; Tsukamoto, D.; Hirai, T. Selective Photocatalytic Transformations on Microporous Titanosilicate ETS-10 Driven by Size and Polarity of Molecules. *Langmuir* **2008**, *24*, 12658-12663.

17. Osterloh, F. E. Inorganic Materials as Catalysts for Photochemical Splitting of Water. *Chem. Mater.* **2008**, *20*, 35-54.

18. Kudo, A.; Miseki, Y. Heterogeneous Photocatalyst Materials for Water Splitting. *Chem. Soc. Rev.* **2009**, *38*, 253-278.

19. Chen, X.; Shen, S.; Guo, L.; Mao, S. S. Semiconductor-Based Photocatalytic Hydrogen Generation. *Chem. Rev.* **2010**, *110*, 6503-6570.

20. Kim, H. G.; Hwang, D. W.; Lee, J. S. An Undoped, Single-Phase Oxide Photocatalyst Working under Visible Light. *J. Am. Chem. Soc.* **2004**, *126*, 8912-8913.

21. Tang, J.; Zou, Z.; Ye, J. Photocatalytic Decomposition of Organic Contaminants by Bi_2WO_6 under Visible Light Irradiation. *Catal. Lett.* **2004**, *92*, 53-56.

22. Muktha, B.; Priya, M. H.; Madras, G.; Guru Row, T. N. Synthesis, Structure, and Photocatalysis in a New Structural Variant of the Aurivillius Phase: $LiBi_4M_3O_{14}$ (M = Nb, Ta) *J. Phys. Chem. B* **2005**, *109*, 11442-11449.

23. Yoshimura, J.; Ebana, Y.; Kondo, J.; Domen, K.; Tanaka, A. Visible Light Induced Photocatalytic Behavior of a Layered Perovskite Type Niobate, $RbPb_2Nb_3O_{10}$. *J. Phys. Chem.* **1993**, *97*, 1970-1973.

24. Arney, D.; Maggard, P. A. Effect of Platelet-Shaped Surfaces and Silver-Cation Exchange on the Photocatalytic Hydrogen Production of $RbLaNb_2O_7$. *ACS Catal.* **2012**, *2*, 1711-1717.

25. Boltersdorf, J.; Maggard, P. A. Silver Exchange of Layered Metal Oxides and Their Photocatalytic Activities. *ACS Catal.* **2013**, *3*, 2547-2555.

26. Lin, X.; Huang, T.; Huang, F.; Wang, W.; Shia, J. Photocatalytic Activity of a Bi-based Oxychloride Bi_4NbO_8Cl. *J. Mater. Chem*. 2007, *17*, 2145-2150.

27. Fan, J.; Hu, X.; Xie, Z.; Zhang, K.; Wang, J. Photocatalytic Degradation of Azo Dye by Novel Bi-based Photocatalyst Bi_4TaO_8I under Visible-Light Irradiation. *Chem. Eng. J.* 2012, *179*, 44-51.

28. Bhat, S. S. M.; Sundaram, N. G. Efficient Visible Light Photocatalysis of Bi_4TaO_8Cl Nanoparticles Synthesized by Solution Combustion Technique. *RSC Adv.* 2013, *3*, 14371-14378.

29. He, Y.; Zhang, Y.; Huang, H.; Tian, N.; Guo, Y.; Luo, Y. A Novel Bi-based Oxybromide Bi_4NbO_8Br: Synthesis, Characterization and Visible-Light-Active Photocatalytic Activity. *Colloids and Surfaces A* 2014, *462*, 131-136.

30. Bhat, S. S. M.; Sundaram, N. G. Photocatalysis of Bi_4NbO_8Cl Hierarchical Nanostructure for Degradation of Dye under Solar/UV Irradiation. *New J. Chem.* 2015, *39*, 3956.

31. Liu, S.; Miiller, W.; Liu, Y.; Avdeev, M.; Ling, C. D. Sillen−Aurivillius Intergrowth Phases as Templates for Naturally Layered Multiferroics. *Chem. Mater.* **2012**, *24*, 3932−3942.

32. Kusainova, A. M.; Lightfoot, P.; Zhou, W.; Stefanovich, S. Y.; Mosunov, A. V.; Dolgikh, V. A. Ferroelectric Properties and Crystal Structure of the Layered Intergrowth Phase $Bi_3Pb_2Nb_2O_{11}Cl$. *Chem. Mater.* **2001**, *13*, 4731-4737.

33. Kusainova, A. M.; Stefanovich, S. Y.; Irvine, J. T. S.; Lightfoot, P. Structure–Property Correlations in the New Ferroelectric $Bi_5PbTi_3O_{14}Cl$ and Related Layered Oxyhalide Intergrowth Phases. *J. Mater. Chem.* **2002**, *12*, 3413–3418.

34. Ackerman, J. F. The Structures of Bi_3PbWO_8Cl and Bi_4NbO_8Cl and the Evolution of the Bipox Structure Series. *J. Solid State Chem.* **1986**, *62*, 92-104.

35. Hervoches, C. H.; Lightfoot, P. Cation Disorder in Three-Layer Aurivillius Phases: Structural Studies of $Bi_{2-x}Sr_{2+x}Ti_{1-x}Nb_{2+x}O_{12}$ ($0 < x < 0.8$) and $Bi_{4-x}La_xTi_3O_{12}$ ($x = 1$ and 2). *J. Solid State Chem.* **2002**, *153*, 66-73.

36. Wang, Y.; Deng, K.; Zhang, L. Visible Light Photocatalysis of BiOI and Its Photocatalytic Activity Enhancement by in Situ Ionic Liquid Modification. *J. Phys. Chem. C* **2011**, *115*, 14300-14308.

37. Kumar, S.; Khanchandani, S.; Thirumal, M.; Ganguli, A. K. Achieving Enhanced Visible-Light-Driven Photocatalysis Using Type-II $NaNbO_3$/CdS Core/Shell Heterostructures. *ACS Appl. Mater. Interfaces* **2014**, *6*, 13221-13233.

38. Halasyamani, P. S. Asymmetric Cation Coordination in Oxide Materials: Influence of Lone-Pair Cations on the Intra-Octahedral Distortion in d^0 Transition Metals. *Chem. Mater.* **2004**, *16*, 3586-3592.

39. Fujihara, K.; Izuni, S.; Ohno, S.; Matsumura, M. Time-resolved Photoluminescence of Particulate TiO_2 Photocatalysts Suspended in Aqueous Solution. *J. Photochem. Photobiol. A* **2000**, *132*, 99-104.

40. Fu, H.; Pan, C.; Yao, W.; Zhu, Y. Visible−Light−Induced Degradation of Rhodamine B by Nanosized Bi_2WO_6. *J. Phys. Chem. B* **2005**, *109*, 22432-22439.

41. Xu, Y.; Schoonen, M. A. A. The Absolute Energy Positions of Conduction and Valence Bands of Selected Semiconducting Minerals. *Am. Mineral.* **2000**, *85*, 543-556.

42. Kumar, D.; Thomas, K. R. J.; Chen, Y-L.; Jou, Y-C. Synthesis, Optical Properties, and Electroluminescence of Fluorene Derivatives Containing Multiple Imidazoles Bearing Polyaromatic Hydrocarbons. *Tetrahedron* **2013**, *69*, 2594-2602.

43. Pan, L.; Zou, J.; Liu, X.; Liu, X.; Wang, S.; Zhang, X.; Wang, L. Visible-Light-Induced Photodegradation of Rhodamine B over Hierarchical TiO_2: Effects of Storage Period and Water-Mediated Adsorption Switch. *Ind. Eng. Chem. Res.* **2012**, *51*, 12782-12786.

44. Shen, J-S.; Yu, T.; Xie, J-W.; Jiang, Y-B. Photoluminescence of CdTe Nanocrystals Modulated by Methylene Blue and DNA. A Label-Free Luminescent Signaling Nanohybride Platform. *Phys. Chem. Chem. Phys.* **2009**, *11*, 5062-5069.

45. Kumar, S.; Surendar, T.; Baruah, A.; Shanker, V. Synthesis of a Novel and Stable g-C_3N_4-Ag_3PO_4 Hybrid Nanocomposite Photocatalyst and Study of the Photocatalytic Activity under Visible Light Irradiation. *J. Mater. Chem. A* **2013**, *1*, 5333-5340.

CHAPTER -7

Conclusions and Future Prospects

Conclusions and Future Prospects

The aim of the present investigation was to develop new layered oxides and oxyhalides for visible-light-driven photocatalysis. During the course of this investigation we recognized that the layered perovskites especially the Aurivillius and related type of oxides could be promising class of materials for solar photocatalysis. The research direction was a natural choice based on increasing reports of Bi-based layered oxides toward visible-light-driven photocatalysis. As already mentioned in earlier chapters, the presence of Bi in these oxides plays a crucial role not only in band gap variation but, in charge carrier mobility as well. Moreover, most of the work related to Aurivillius oxides in photocatalysis were based on the starting members of the Aurivillius family with only a few higher order members and their chemically substituted congeners. Therefore, there were immense opportunity in developing a variety of complex and higher order members of the Aurivillius and related type of oxides that are largely unexplored. Based on these observations, we have basically undertaken a systematic exploration of higher order members of Aurivillius phases, namely, the four- and five-layer Aurivillius perovskite titanates. Moreover, with compositional variation by means of both *A* and *B* cation manipulation, we have explored new five-layer Aurivillius perovskite titanates. Finally, a new series of hybrid Sillén-Aurivillius phases with three layer perovskite titanates has been investigated. The study gives an insight into the phase formation, structure and sunlight-driven photocatalytic activity toward dye degradation by these Aurivillius and Sillén-Aurivillius oxides and oxychlorides. Moreover, based on our current understanding on enhanced photocatalytic dye degradation, we have also developed and demonstrated a pH mediated strategy for selective dye degradation from a mixture of dye solution.

In the four-layer series of Aurivillius phases, we have reported for the first time, to the best of our knowledge, the solid-state bulk synthesis of $Bi_{5-x}La_xTi_3FeO_{15}$ (x = 1, 2). The compounds were thoroughly characterized by PXD, FE-SEM, EDS, PL and UV-vis DRS. The lattice parameters analysis indicated a slight increase in the *c*-parameter as x varied from 0 – 2 in the $Bi_{5-x}La_xTi_3FeO_{15}$ series, while *a* and *b*-parameter approached each other and became nearly equal in $Bi_3La_2Ti_3FeO_{15}$. This clearly indicated a decrease in the orthorhombic distortion present in the parent compound. This was attributed to the diminishing effect of out-of-center octahedral distortion with gradual replacement of Bi^{3+} by

La^{3+}. Due to the compositional and structural changes, there was a slight and steady increase in the principal band gap of the resulting oxides with progressive La-substitution. The UV-vis DRS data revealed the compounds as visible-light absorbing semiconductors with the principal band gap varying from 2.62 – 2.71 eV. All the compounds showed excellent photocatalytic Rhodamine B degradation activity under sunlight-irradiation in the acidic medium (pH 2). The activity of the catalysts toward RhB degradation is comparable or higher than many of the single and composite catalysts with Aurivillius and perovskite related structures in the bulk or nanostructured form reported recently. The highest activity in this series of oxides was exhibited by $Bi_4LaTi_3FeO_{15}$. This has been attributed to slow e^- - h^+ recombination, efficient h^+ transport and enhanced dye adsorption irrespective of the degradation mechanisms involved. Scavenger test experiments clearly indicated the dominant role of holes in the degradation process involving the Aurivillius layered oxides reported here. The positioning of VB and CB edges with respect to potentials of $^{\bullet}OH/H_2O$, $O_2/O_2^{\bullet-}$ and HOMO-LUMO levels of RhB clearly corroborated with the scavenger test results indicating no major role of hydroxyl species in the degradation.

In our next endeavor, we explored the solid-state synthesis of five layer Aurivillius perovskites, $Bi_{6-x}La_xTi_3Fe_2O_{18}$ (x = 0, 4). However, only x = 0 and 1, members of the family was stabilized into a single phase under the synthesis conditions we adopted. Our structural investigation indicated very similar structural changes that occurred in the four layer perovskite with La^{3+} substitution. It was attributed to a complex interplay between cation disorder and concomitant octahedral tilting distortion. Here, the La-substitution appeared to help in the suppression of photogenerated e^-–h^+ recombination as evidenced by PL spectra. The photocatalytic Rhodamine B degradation in the acidic medium under sunlight-irradiation indicated $Bi_5LaTi_3Fe_2O_{18}$ as the most active catalyst among the two five layered Aurivillius compounds reported here. The enhanced activity of $Bi_5LaTi_3Fe_2O_{18}$ was similarly attributed to an effective e^-–h^+ separation and improved dye adsorption in the acidic medium. The predominant role of photogenerated holes in the RhB degradation has been established by reactive species trapping experiments in this case as well. The compounds showed an excellent COD removal efficiency that was concomitant with the dye decoloration.

Extending our idea in developing new members of the five-layer perovskites, we envisaged divalent alkaline earth (Ca, Sr, Ba) and Pb substitutions in the *A*-site of $Bi_6Ti_3Fe_2O_{18}$. This required a simultaneous *B*-cation substitution as well to obtain a charge balanced composition, $Bi_5ATi_4FeO_{18}$ (*A* = divalent cation). The compounds were synthesized for the first time and only the Ca, Sr and Pb analogs of the series were stabilized as single-phase. All the compounds were visible band gap semiconductors with principal band gaps ranging from 2.61 – 2.72 eV as confirmed by UV-vis DRS analysis. These catalysts exhibited fully selective degradation of MB from an aqueous mixture of MB and RhB in alkaline as well as neutral medium. Among these, $Bi_5SrTi_4FeO_{18}$ showed the maximum activity attributable to a sluggish recombination of photoinduced e^-–h^+ pairs and enhanced dye adsorption. Scavenger tests indicated dominant role of h^+ and $O_2^{\bullet-}$ similar to those observed in the four-layer and five-layer Aurivillius phases described earlier.

Finally, in our effort to synthesize new layered hybrid phases, we explored Sillén-Aurivillius intergrowth of a single-layer Sillén with three-layer Aurivillius perovskite. This has enabled us to prepare a series on new layered hybrid phases of general composition, $Bi_{5-x}La_xBaTi_3O_{14}Cl$ (x = 0 – 2). For the synthesis of these hybrid phases a multi-step solid state reaction strategy was adopted, where the precursor oxides, namely, a series of three layer Aurivillius, $Bi_{4-x}La_xTi_3O_{12}$ (x = 0 – 2) and a Sillén, $BiBaO_2Cl$, were first synthesized. Then in a second step each member of the Aurivillius was further reacted with the Sillén phase to prepare the hybrid phases. All the Sillén-Aurivillius phases reported here were visible-light absorbers with band gaps ranging from 2.66 to 2.87 eV. The compounds exhibited excellent RhB and MB degradation at different pH conditions. Moreover, the hybrid catalysts were highly active toward selective degradation of MB as well from mixed RhB-MB dye solutions in neutral and alkaline media. Among the three catalysts, $Bi_3La_2BaTi_3O_{14}Cl$ showed enhanced activity which was attributed to slow recombination of photogenerated e^-–h^+ pairs and superior dye adsorption. Based on the band edge position of $Bi_3La_2BaTi_3O_{14}Cl$ and HOMO-LUMO levels of the dyes, $^{\bullet}OH$, $O_2^{\bullet-}$ and h^+ were perceived as active species at pH 2, whereas participation of only $O_2^{\bullet-}$ and h^+ were realized at pH 7 and 11. This was further supported by scavenger test results where retardations were noticed with $^{\bullet}OH$, $O_2^{\bullet-}$ and h^+ scavengers at pH 2, while almost negligible retardation was observed with $^{\bullet}OH$ scavenger only at pH 7 and 11. These catalysts were reusable and stable after five photocatalytic cycles without showing any appreciable loss of activity. Lastly, this work

opened up a new way of making visible-light harvesting compounds from UV active compounds by intergrowth of Sillén and Aurivillius phases.

In summary, all the compounds that are reported in the present investigation are visible light absorbers and active under natural sunlight-irradiation. Exceptional sunlight-driven photocatalytic activity of these bulk oxides toward dye degradation in a wide range of pH (2-11) has been demonstrated. The catalysts showed excellent stability and recyclability after five successive cycle of dye degradation. Moreover, the five-layer Aurivillius perovskites have showed excellent COD removal efficiency that is more or less concomitant with the dye decoloration from pollutant dye water system under sunlight-irradiation. By various scavenger experiments it was also established that the sunlight-driven photocatalytic degradation is largely mediated by hole (h^+) transfer from the photocatalyst to the dye pollutant unlike conventional ROS ($^{\bullet}OH$, $O_2^{\bullet}$) mediated degradations. This has further been supported by an energy level diagram involving valence and conduction band positions of the semiconductors with respect to the potentials of $^{\bullet}OH/H_2O$, $O_2/O_2^{\bullet-}$ and HOMO-LUMO levels of the dye. Furthermore, a pH mediated strategy for selective dye degradation has also been demonstrated. This has been achieved with the new five-layer Aurivillius perovskites, $Bi_5ATi_4FeO_{18}$ (A = Ca, Sr, Pb), and Sillén-Aurivillius hybrids, $Bi_{5-x}La_xBaTi_3O_{14}Cl$ (x = 0 - 2). Comparing the activity of all the semiconductors toward RhB degradation in the acidic medium, the Sillén-Aurivillius hybrid phases have turned out as the most active ones despite having a low solar direct normal irradiance at the time of dye degradation experiments. Moreover, the degradation efficiency seemed to be slightly higher in case of four layer Aurivillius compounds as compared to the five layer compounds reported here under similar experimental conditions. Realizing the robustness of the single semiconductor catalyst systems under various pH conditions and their high dye degradation efficiency with natural sunlight, we believe our work will have a great impact in the area of catalysis using solar radiation.

The present work has tremendous potential and gives insight for the development of various new types of layered oxides for sunlight-driven photocatalysis not only in the area of dye pollutant degradation but many other organic pollutant degradation, selective degradation and recovery of precious chemicals etc. Our idea can further be extended for the development of new oxides with other lanthanides and transition metal cations involving 3d

as well as 4d and 5d elements. Further, the Sillén-Aurivillius hybrid series can be extended toward other halides and perovskites of varied layers. The future work will help in deeper understanding of structural dependence on specific factors responsible for high photocatalytic activity and such structure-property correlation may be used for tailor-made design and synthesis of new generation of photocatalysts.